

AEDC-TR-76-102

72

16

ADA030852



3330

**EVALUATION OF BOATTAIL GEOMETRY AND EXHAUST PLUME
TEMPERATURE EFFECTS ON NOZZLE AFTERBODY DRAG
AT TRANSONIC MACH NUMBERS**

**PROPELLION WIND TUNNEL FACILITY
ARNOLD ENGINEERING DEVELOPMENT CENTER
AIR FORCE SYSTEMS COMMAND
ARNOLD AIR FORCE STATION, TENNESSEE**

October 1976

Final Report for Period July 1974 - June 1975

Approved for public release; distribution unlimited.

Prepared for

**DIRECTORATE OF TECHNOLOGY
ARNOLD ENGINEERING DEVELOPMENT CENTER
ARNOLD AIR FORCE STATION, TENNESSEE 37389**

72
16
Approved for public release; distribution unlimited.

NOTICES

When U. S. Government drawings specifications, or other data are used for any purpose other than a definitely related Government procurement operation, the Government thereby incurs no responsibility nor any obligation whatsoever, and the fact that the Government may have formulated, furnished, or in any way supplied the said drawings, specifications, or other data, is not to be regarded by implication or otherwise, or in any manner licensing the holder or any other person or corporation, or conveying any rights or permission to manufacture, use, or sell any patented invention that may in any way be related thereto.

Qualified users may obtain copies of this report from the Defense Documentation Center.

References to named commercial products in this report are not to be considered in any sense as an endorsement of the product by the United States Air Force or the Government.

This report has been reviewed by the Information Office (OI) and is releasable to the National Technical Information Service (NTIS). At NTIS, it will be available to the general public, including foreign nations.

APPROVAL STATEMENT

This technical report has been reviewed and is approved for publication.

FOR THE COMMANDER

ELTON R. THOMPSON
Research & Development
Division
Directorate of Technology

ROBERT O. DIETZ
Director of Technology

57
SIGHTS
DATA
A

UNCLASSIFIED

| REPORT DOCUMENTATION PAGE | | READ INSTRUCTIONS BEFORE COMPLETING FORM |
|---------------------------------------------------------------------------------------------------------------------------------------------------------------------------------------------------------------------------------------------------------------------------------------------------------------------------------------------------------------------------------------------------------------------------------------------------------------------------------------------------------------------------------------------|-----------------------|---------------------------------------------------------------------------------------|
| 14) 1) REPORT NUMBER AEDC-TR-76-102 | 2) GOVT ACCESSION NO. | 3) RECIPIENT'S CATALOG NUMBER 9) |
| 4) TITLE (and Subtitle) EVALUATION OF BOATTAIL GEOMETRY AND EXHAUST PLUME TEMPERATURE EFFECTS ON NOZZLE AFTERBODY DRAG AT TRANSONIC MACH NUMBERS. | | 5) TYPE OF REPORT & PERIOD COVERED Final Report, July 1974 - June 1975 |
| 7) AUTHOR(s) L. L. Galigher, S. F. Yaros and R. C. Bauer ARO, Inc. | | 6) PERFORMING ORG REPORT NUMBER |
| 9) PERFORMING ORGANIZATION NAME AND ADDRESS Arnold Engineering Development Center (DY) Air Force Systems Command Arnold Air Force Station, TN 37389 | | 10) PROGRAM ELEMENT, PROJECT, TASK AREA & WORK UNIT NUMBERS Program Element 65807F |
| 11) CONTROLLING OFFICE NAME AND ADDRESS Arnold Engineering Development Center (DYFS), Air Force Systems Command, Arnold Air Force Station, TN 37389 | | 12) REPORT DATE Oct 1976 |
| 14) MONITORING AGENCY NAME & ADDRESS (if different from Controlling Office) | | 13) NUMBER OF PAGES 141 |
| 16) DISTRIBUTION STATEMENT (of this Report) | | 15) SECURITY CLASS (of this report) UNCLASSIFIED |
| | | 15a) DECLASSIFICATION/DOWNGRADING SCHEDULE N/A |
| 17) DISTRIBUTION STATEMENT (of the abstract entered in Block 20, if different from Report) 16) ARO - PH411, - P41T - 011 | | |
| 18) SUPPLEMENTARY NOTES Available in DDC. | | |
| 19) KEY WORDS (Continue on reverse side if necessary and identify by block number) wind tunnels flow fields turbojet exhaust nozzles pressure drag exhaust plume flow temperature nozzles afterbodies | | |
| 20) ABSTRACT (Continue on reverse side if necessary and identify by block number) An experimental program was conducted to investigate the interaction effects which occur between the nozzle exhaust flow and the external flow field associated with isolated nozzle afterbody configurations at transonic Mach numbers. Pressure data were obtained for three afterbody geometries with boattail angles of 10, 15, and 25 deg at Mach numbers from 0.6 to 1.5 at zero angles of attack and sideslip. Cold (high-pressure air) and hot | | |

UNCLASSIFIED

20. ABSTRACT (Continued)

(air/ethylene combustion) jet test techniques were used to simulate and duplicate, respectively, the nozzle exhaust flow for a sonic jet installation. Nozzle exhaust temperature was varied from 540 to approximately 2,900°R. The most significant results pertain to those effects on boattail pressure drag caused by exhaust plume temperature and flow asymmetry (model support strut induced). The differences obtained in boattail pressure drag between the cold jet simulation and hot jet duplication results were significant at nozzle pressure ratios representative for turbofan and turbojet engines at subsonic Mach numbers. Adjusting the cold jet nozzle pressure ratio to correct for changes in the exhaust plume specific heat ratio with temperature did not account for the differences observed. Flow asymmetry effects were Mach number and nozzle pressure ratio dependent and increased in severity as the boattail angle was increased.

UNCLASSIFIED

PREFACE

The work reported herein was conducted by the Arnold Engineering Development Center (AEDC), Air Force Systems Command (AFSC), under Program Element 65807F. The results of the tests were obtained by ARO, Inc. (a subsidiary of Sverdrup & Parcel and Associates, Inc.), contract operator of AEDC, AFSC, Arnold Air Force Station, Tennessee, under ARO Project Number PA411 in support of Research Project Number PF430 and under ARO Project Number P41T-80A in support of Research Project Numbers P32P-11B and P32P-AOA. The authors of this report were L. L. Galigher, S. F. Yaros, and R. C. Bauer, ARO, Inc. The manuscript (ARO Control No. ARO-PWT-TR-76-28) was submitted for publication on March 9, 1976.

CONTENTS

| | <u>Page</u> |
|----------------------------------------------------------|-------------|
| 1.0 INTRODUCTION | 7 |
| 2.0 APPARATUS | |
| 2.1 Test Facility | 7 |
| 2.2 Experimental Hardware and Model Support System | 8 |
| 2.3 Instrumentation | 9 |
| 3.0 PROCEDURE | |
| 3.1 Experimental Conditions and Technique | 9 |
| 3.2 Data Reduction | 10 |
| 3.3 Precision of Measurements | 11 |
| 4.0 EXPERIMENTAL RESULTS | |
| 4.1 Flow Duct and Nozzle Entrance Characteristics | 12 |
| 4.2 Nozzle Pressure Ratio Effects | 13 |
| 4.3 Mach Number Effects | 13 |
| 4.4 Flow Asymmetry Effects | 14 |
| 4.5 Exhaust Plume Temperature Effects | 15 |
| 4.6 Nozzle Base Area Effects | 16 |
| 5.0 THEORETICAL ANALYSIS | |
| 5.1 Physical Statement of Problem | 17 |
| 5.2 Computational Techniques | 19 |
| 5.3 Results of the Analysis | 21 |
| 6.0 CONCLUDING REMARKS | 22 |
| REFERENCES | 23 |

ILLUSTRATIONS

Figure

| | |
|-----------------------------------------------------------------------------------------------|----|
| 1. Basic Model Dimensions and Location in Test Section | 25 |
| 2. Model/Strut Cross-Sectional Area Distribution | 26 |
| 3. Nozzle Boattail Geometry | 27 |
| 4. Model Installation Photograph | 30 |
| 5. Cold Flow Nozzle Assembly | 31 |
| 6. Hot Flow Nozzle Assembly | 32 |
| 7. Hot Flow Nozzle Installation Photograph | 33 |
| 8. Nozzle Flow Duct Total Pressure Profile | 34 |
| 9. Comparison between Primary and Secondary Measurements of Nozzle Total Pressure Ratio | 35 |

| <u>Figure</u> | <u>Page</u> |
|-----------------------------------------------------------------------------------------------------------|-------------|
| 10. Nozzle Discharge Coefficient for Cold Flow Model | 36 |
| 11. Hot Flow Model Exhaust Total Temperature | 37 |
| 12. Effect of Boattail Geometry on Boattail Pressure Drag Coefficient | 38 |
| 13. Nozzle Pressure Ratio Effects on 10-deg Boattail Pressure Distribution | 44 |
| 14. Nozzle Pressure Ratio Effects on 15-deg Boattail Pressure Distribution | 50 |
| 15. Nozzle Pressure Ratio Effects on 25-deg Boattail Pressure Distribution | 56 |
| 16. Schlieren Photographs of 10-, 15-, and 25-deg Boattail Geometries at Selected Mach Numbers | 62 |
| 17. Variation of Boattail Pressure Drag Coefficient with Mach Number | 65 |
| 18. Subsonic Mach Number Effects on Boattail Pressure Distribution | 66 |
| 19. Supersonic Mach Number Effects on Boattail Pressure Distribution | 69 |
| 20. Flow Asymmetry Effects on 10-deg Boattail Pressure Drag Coefficient | 72 |
| 21. Flow Asymmetry Effects on 15-deg Boattail Pressure Drag Coefficient | 75 |
| 22. Flow Asymmetry Effects on 25-deg Boattail Pressure Drag Coefficient | 78 |
| 23. Flow Asymmetry Effects as a Function of Mach Number | 81 |
| 24. Flow Asymmetry Effects on 10-deg Boattail Pressure Distribution | 84 |
| 25. Flow Asymmetry Effects on 15-deg Boattail Pressure Distribution | 87 |
| 26. Flow Asymmetry Effects on 25-deg Boattail Pressure Distribution | 90 |
| 27. Exhaust Plume Temperature Effects on 15-deg Boattail Configuration | 93 |
| 28. Exhaust Plume Temperature Effects on 25-deg Boattail Configuration | 99 |
| 29. Exhaust Plume Temperature Effects on 15-deg Boattail as a Function of Jet Inclination Angle | 105 |
| 30. Exhaust Plume Temperature Effects on 25-deg Boattail as a Function of Jet Inclination Angle | 111 |
| 31. Nozzle Base Area Effects on 15- and 25-deg Boattail Configurations | 117 |
| 32. Schematic of the Various Flow Regions Involved in the Afterbody Problem | 123 |
| 33. Schematic of the Various Flow Regions Involved in the Modeling of the Afterbody Problem | 124 |
| 34. General Iteration Flow Plan | 125 |

| <u>Figure</u> | <u>Page</u> |
|--------------------------------------------------------------------------------------------------------------|-------------|
| 35. Comparison of Computed and Measured Boundary Layer at Mach Number 0.9, Model Station 115.46 | 126 |
| 36. Characteristic Plume Shapes | 127 |
| 37. Comparison of Computed and Measured Boattail Pressure Distribution for the 15-deg Boattail Configuration | 128 |

TABLES

| | |
|----------------------------------------------|-----|
| 1. External Pressure Orifice Locations | 131 |
| 2. Cold Flow Nozzle Assembly Instrumentation | 134 |
| 3. Hot Flow Nozzle Assembly Instrumentation | 135 |

APPENDIX

| | |
|---------------------------------------------|-----|
| A. Plume Displacement Thickness Calculation | 137 |
|---------------------------------------------|-----|

| | |
|--------------|-----|
| NOMENCLATURE | 139 |
|--------------|-----|

1.0 INTRODUCTION

The technical challenge associated with exhaust system integration is formidable in view of the complex interactions which occur between the exhaust plume, the local free stream, and the afterbody surfaces. The flow interactions between the exhaust plume and the free stream can be categorized as either inviscid or viscous in nature. Inviscid interactions result if the jet exhaust is not fully expanded and the local external flow does not match the jet exhaust Mach number and flow angle - a plume displacement effect. Viscous interactions result from mixing at the interface of the local external flow and the jet exhaust. For simulation of the flow field about the nozzle afterbody, wind tunnel test programs normally use high-pressure air to simulate nozzle exhaust flow - not only for economic reasons but also to simplify testing requirements. The cold jet technique can be used to match either the initial inclination angle or the maximum diameter of the inviscid plume boundary of the hot jet. However, viscous interaction effects for a cold jet differ from those for a hot jet since mixing between the nozzle exhaust and local external flow depends largely on temperature and velocity gradients.

The purpose of the experimental program reported herein was to investigate the interaction effects which occur between the nozzle exhaust flow and the external flow field associated with isolated nozzle/afterbody (NAB) installations in the transonic Mach number range. Configuration variables included nozzle boattail geometry and internal nozzle geometry. A cold jet and hot jet test technique was used to simulate and duplicate, respectively, the nozzle exhaust flow. High-pressure air served as the simulation fluid, and an air/ethylene combustor provided the means for duplicating the exhaust flow for the hot jet installation. The experimental program concerning the NAB geometry effects was initiated in response to a request by the Advisory Group for Aeronautical Research and Development (AGARD) of NATO for member nations to participate in a research project on improved nozzle testing techniques in transonic flow. The overall objective of the AGARD program is to parametrically develop the influences of exhaust nozzle flows on the external afterbody flow and, conversely, show the effect of external afterbody flow on nozzle internal flow characteristics. The hot jet duplication experiments were conducted by AEDC as part of an effort to investigate hot versus cold jet effects on boattails of different geometries.

2.0 APPARATUS

2.1 TEST FACILITY

The transonic Propulsion Wind Tunnel (16T) is a continuous flow, closed-circuit wind tunnel capable of operating within a Mach number range from 0.2 to 1.6. The tunnel can be operated within a stagnation pressure range from 120 to 4,000 psfa depending

on the Mach number. The stagnation temperature can be varied from an average minimum of about 80 to a maximum of 160°F depending on the cooling water temperature. The specific humidity of the air in the tunnel is controlled by exchanging tunnel air for conditioned makeup air from an atmospheric drier.

2.2 EXPERIMENTAL HARDWARE AND MODEL SUPPORT SYSTEM

An existing axisymmetric cone-cylinder model was modified to satisfy requirements for both cold and hot exhaust testing with three external afterbody configurations having boattail angles of 10, 15, and 25 deg. The model had a length of approximately 147 in., a maximum diameter of 9.86 in., and a 14-deg, half-angle conical nose. A boundary-layer trip consisting of 0.055-in.-diam steel spheres spot welded to a trip ring at a circumferential spacing of four sphere diameters was located 12 in. aft of the cone vertex. The model was mounted on a tapered strut with an average aft sweep angle of 35 deg. The strut thickness-to-chord ratio varied from 0.053 at the model to 0.088 at the tunnel floor. The maximum cross-sectional area of the model/strut arrangement was equivalent to 0.88 percent of the wind tunnel test section cross-sectional area. A dimensioned sketch of the model is presented in Fig. 1, and the cross-sectional area distribution of the model/strut arrangement is shown in Fig. 2. A dimensioned sketch of each of the three nozzle boattail configurations (10-, 15-, and 25-deg boattail angle) is presented in Fig. 3. An installation photograph of the model installed in Tunnel 16T is presented in Fig. 4.

2.2.1 Cold Flow Nozzle Assembly

High-pressure air was used to simulate the jet exhaust for the cold flow portion of the experiments. The high-pressure air was ducted through the model support strut to a plenum in the model forebody. The air continued aft through a flow-conditioning section prior to entering the convergent nozzle assembly. The nozzle assembly, which had a contraction ratio of 3.28 and an exit diameter of 3.982 in., is sketched in Fig. 5.

2.2.2 Hot Flow Nozzle Assembly

An ethylene/air combustor was used to provide hot jet exhaust flow duplication. Ethylene (C_2H_4) is a gaseous hydrocarbon fuel which, when burned in air, produces exhaust products that very closely duplicate the exhaust products of JP-4 burned in air. The water-cooled combustor assembly was fabricated from copper and had an inside diameter of 6.15 in. and a wall thickness of 0.125 in. The combustor terminated with a convergent nozzle with an exit diameter of 3.228 in. and a contraction ratio of 3.63. The flame holder consisted of four doughnut rings interconnected with fuel flow passages, but only

the forward doughnut ring served as the ethylene injection ring. Ignition was accomplished by injecting a small quantity of tri-ethyl borane (TEB, a pyrophoric fuel) into a retainer mounted on the flame holder. Flow mixers were placed at the rear of the flame holder to mix the hot flow from the combustion zone with the air around the outside of the flame holder. A sketch of the hot flow nozzle assembly is shown in Fig. 6. An installation photograph of the hot flow model is presented in Fig. 7. The nozzle base area depicted in the preceding photograph was seven times larger than that for the cold flow model (4.968 in.² compared to 0.709 in.²). This difference in nozzle base area resulted from imposing water cooling requirements on the hot flow nozzle assembly.

2.3 INSTRUMENTATION

External pressure instrumentation was common for both the cold and hot flow model configurations; only the instrumentation within the nozzle flow chambers was different. Rows of static pressure orifices were located along the model centerbody and on the nozzle boattails at various circumferential stations as shown in Table 1. Pressure and temperature instrumentation in the nozzle flow chambers of the cold and hot flow model configurations are presented in Tables 2 and 3, respectively. Air and ethylene flow rates were determined from pressure, temperature, and area measurements in critical flow venturi metering sections external to the models.

3.0 PROCEDURE

3.1 EXPERIMENTAL CONDITIONS AND TECHNIQUE

The data presented in this report were obtained at nominal free-stream Mach numbers of 0.6, 0.8, 0.9, 0.95, 1.1, and 1.5 at a free-stream Reynolds number of 2.5×10^6 per foot. Data on the influence of Reynolds number for the range from 1 to 50×10^6 per foot are reported in Ref. 1. Angle of attack was zero at all test conditions. Nozzle total pressure-to-free-stream static pressure ratio (NPR) was varied from jet-off conditions to a maximum of 22 depending on the free-stream Mach number. Nozzle pressure ratio surveys for the hot flow model were conducted primarily at constant fuel/air ratios of 0, 0.015, 0.025, and 0.040. The 10-, 15-, and 25-deg boattail configurations were tested on the cold flow model, but only the 15- and 25-deg boattail configurations were tested on the hot flow model. Schlieren photographs were obtained at selected nozzle pressure ratios for both the cold and hot flow models.

The data acquisition procedure consisted of (1) setting desired free-stream Mach number, (2) obtaining jet-off data, (3) setting desired fuel/air ratio, if applicable, and varying nozzle total pressure ratio, and (4) obtaining schlieren photographs as required.

3.2 DATA REDUCTION

The primary performance parameter presented in this report is the nozzle boattail pressure drag coefficient obtained from integration of the experimental pressure distributions. The data reduction technique employed was based on using the measurements of each individual row of pressure orifices located at circumferential stations of 0, 180, and 270 deg and assuming that each of these pressure distributions was imposed on all of the boattail projected area. Thus, pressure drag coefficients based on the top, side, and bottom row of pressure orifices were calculated as follows:

$$CDPX = \left(-\frac{1}{A} \right) \sum_i^{i_{max}-1} \left(\frac{CP_i + CP_{i+1}}{2} \right) \left(\pi R_i^2 - \pi R_{i+1}^2 \right)$$

(Note: X = top, side, or bottom)

where "A" is the reference area based on the maximum diameter of the model, "CP_i" is the pressure coefficient for orifices identified in Table 1, and "R_i" is the radius of the boattail surface relative to the nozzle centerline. The drag coefficient values, as calculated, pertain to the pressure drag on the nozzle boattail projected area aft of model station 130.471 in. (see Fig. 1).

| Boattail Configuration | Top | | Side | | Bottom | |
|------------------------|-----|------------------|------|------------------|--------|------------------|
| | i | i _{max} | i | i _{max} | i | i _{max} |
| 10-deg | 401 | 422 | 464 | 485 | 442 | 463 |
| 15-deg | 401 | 425 | 464 | 483 | 442 | 461 |
| 25-deg | 401 | 423 | 464 | 478 | 442 | 456 |

For the cold flow nozzle assembly, the nozzle total pressure, PTJ, was calculated from one-dimensional relationships using measured nozzle mass flow and nozzle flow duct static pressure, total temperature, and cross-sectional area. Nozzle discharge coefficient, CDND, was calculated by the following equation:

$$CDND = 1.8803 \frac{M_a}{(PTJ)(AT)(TTJ)^{-0.5}}$$

For the hot flow nozzle assembly, static pressure orifices located within the flow duct and just forward of the start of the throat contraction were used to calculate the nozzle total pressure, PTJ, in the following manner:

$$PTJ = P_{wall} \left(\frac{P_T}{P} \right)_I$$

where $(PT/P)_1$ is the subsonic isentropic pressure ratio based on the nozzle contraction ratio of 3.63 and the ratio of specific heats, γ , of the exhaust products based on 100-percent combustion efficiency. Since PT/P is an extremely weak function of γ (PT/P decreases approximately 0.15 percent for a change in γ from 1.40 to 1.26), use of γ based on 100-percent combustion efficiency introduces no significant error in the calculation of PTJ . Exhaust total temperature was calculated from mass flow relationship in the following manner:

$$TTJ = \left[\frac{K_\gamma (PTJ)(AT)(CDND)}{\dot{M}_a + \dot{M}_f} \right]^2$$

where K_γ is a function of γ , AT is the measured throat area, CDND is the nozzle discharge coefficient (0.9902) determined from cold flow tests of the hot flow nozzle, and \dot{M}_a and \dot{M}_f are air and ethylene mass flow rates, respectively.

3.3 PRECISION OF MEASUREMENTS

The uncertainty of the major test parameters is tabulated below. The uncertainty in these parameters includes the inaccuracies in the tunnel reference systems, the recording systems, and the pressure transducers themselves. Uncertainty is defined as

$$U = \pm (B + 2S)$$

where "B" is the bias and "S" is an estimate of the standard deviation, both values being determined from the Taylor series propagation-of-error method.

UNCERTAINTY

| Parameter | Mach Number | | | | | |
|------------|-------------|---------|---------|---------|---------|---------|
| | 0.6 | 0.8 | 0.9 | 0.95 | 1.1 | 1.5 |
| M_∞ | 0.00320 | 0.00300 | 0.00300 | 0.00290 | 0.00300 | 0.00360 |
| CDPX | 0.00056 | 0.00046 | 0.00043 | 0.00038 | 0.00035 | 0.00031 |
| CP | 0.00460 | 0.00330 | 0.00290 | 0.00270 | 0.00240 | 0.00200 |
| NPR | 0.00380 | 0.00510 | 0.00600 | 0.00630 | 0.00760 | 0.01290 |

4.0 EXPERIMENTAL RESULTS

The experimental results are presented in the following order:

- 4.1 Flow Duct and Nozzle Entrance Characteristics
- 4.2 Nozzle Pressure Ratio Effects
- 4.3 Mach Number Effects

- 4.4 Flow Asymmetry Effects
- 4.5 Exhaust Plume Temperature Effects
- 4.6 Nozzle Base Area Effects

The cold flow model data are presented to illustrate the effects of nozzle pressure ratio, Mach number, and flow asymmetry on boattail pressure distribution and drag coefficient since experiments on all three boattail configurations were conducted during the cold flow phase. As stated previously, experiments were conducted only on the 15- and 25-deg boattail configurations with the hot flow model. The exhaust temperature effects were determined by comparing data from the hot flow model operated with and without the combustor in operation.

The boattail pressure drag coefficient, as presented in this report, was nondimensionalized with the model maximum cross-sectional area and should not be construed as being equal in magnitude to aircraft drag counts (one drag count = 0.0001 in drag coefficient), which are based on wing area. (Generally an aircraft drag count for an aircraft similar to a lightweight fighter is equivalent to approximately 15 "body" drag counts.)

4.1 FLOW DUCT AND NOZZLE ENTRANCE CHARACTERISTICS

Nozzle total pressure for the cold flow model was determined by two methods: one from one-dimensional relationships using the measured mass flow and flow duct static pressure, total temperature, and cross-sectional area, and the other from a ten-probe, area-weighted, total pressure rake installed in the flow duct. The flow duct total pressure profiles shown in Fig. 8 were representative of those profiles established for various flow duct pressure levels. The total pressure distortion was approximately 5.4 percent and was independent of flow duct pressure level. The difference between the calculated total pressure value and the measured total pressure value obtained from the rake was less than 1 percent. The data presented in Fig. 9 show the excellent agreement obtained between the two methods used to obtain flow duct total pressure. For this test, the calculated flow duct total pressure was considered the primary measurement, and the average total pressure, as determined from the pressure rake, was considered as the backup measurement.

The discharge coefficient (CDND) for the cold flow model is presented in Fig. 10 as a function of throat Reynolds number (RET). The discharge coefficient generally varied from approximately 0.994 at a throat Reynolds number of 1×10^6 to approximately 0.998 at a throat Reynolds number of 5×10^6 . For the hot flow model, the nozzle discharge coefficient had an average value of 0.99.

The calculated values of exhaust total temperature for the hot flow model are presented in Fig. 11 as a function of flow duct total pressure. These data indicate that

combustion efficiency is pressure level dependent, especially at a fuel/air ratio of 0.04. The average exhaust total temperatures at fuel/air ratios of 0.015, 0.025, and 0.04 were approximately 1,600, 2,100, and 2,900°R, respectively.

4.2 NOZZLE PRESSURE RATIO EFFECTS

The basic data showing the effects of nozzle pressure ratio on the pressure drag and pressure distributions for the 10-, 15-, and 25-deg boattail configurations are presented in Figs. 12 through 15. The data presented in these figures represent the data obtained from the top row of pressure orifices. In general, the drag trend with nozzle pressure ratio (NPR), as well as the drag level, for the 25-deg boattail configuration differed significantly from that for the 10- and 15-deg boattail configurations at subsonic Mach numbers; however, as the Mach number increased supersonically, all three boattail configurations exhibited similar drag trends, and the differences in drag level decreased noticeably.

The pressure distribution data presented for the 10- and 15-deg boattail configurations are characteristic of these distributions usually encountered with small angle boattails at subsonic Mach numbers - flow expansion around the boattail shoulder followed by a well-behaved flow recompression to a pressure level above free-stream ambient. The pressure distributions for the 25-deg boattail configuration at similar Mach numbers differed radically from those obtained for the 10- and 15-deg configurations in that significantly more flow expansion occurred and was followed by an abrupt flow recompression to a pressure level approaching the ambient. It is difficult to discern from the schlieren photographs presented in Fig. 16 if the very adverse pressure gradient ($\Delta P/\Delta X > 0$) imposed on the 25-deg boattail configuration at subsonic Mach numbers resulted in flow separation; however, it is suspected that the adverse pressure gradient imposed on the 25-deg boattail configuration was of sufficient magnitude to cause separation of the turbulent boundary layer.

At supersonic Mach numbers, only the pressure distribution data for the 10-deg boattail configuration show flow recompression above free-stream static pressure, and compared with the subsonic data, the flow recompression was much less. The schlieren photographs obtained at Mach number 1.5 show quite clearly the shock wave structure in the flow region near the 10- and 15-deg boattail surfaces. Flow separation is visible in the schlieren photograph for the 25-deg boattail configuration at Mach number 1.5.

4.3 MACH NUMBER EFFECTS

The data presented to show Mach number effects on boattail drag coefficient and pressure distribution are for scheduled nozzle pressure ratio values of 3 at all subsonic Mach numbers and 5 and 7 for $M_\infty = 1.1$ and 1.5, respectively. The most obvious aspect

of the drag coefficient data presented in Fig. 17 was the onset of drag rise characteristic exhibited for each of the boattail configurations. As boattail angle was increased from 10 to 25 deg, the Mach number at which the drag rise occurred decreased. The drag rise occurred at $M_{\infty} = 0.9$ for the 10-deg boattail configuration, at $M_{\infty} = 0.8$ for the 15-deg boattail configuration, and at a Mach number equal to or less than 0.6 for the 25-deg boattail configuration.

Before the onset of drag rise for the 10- and 15-deg boattail configurations, the drag coefficient levels were essentially at a constant value. The pressure distributions for the 10- and 15-deg boattail configurations, as shown in Figs. 18 and 19, at Mach numbers less than that corresponding to the onset of drag rise show that although flow expansion around the shoulder of the boattails increased as Mach number was increased, flow recompression also increased. The net result was that no change in pressure drag occurred.

4.4 FLOW ASYMMETRY EFFECTS

Flow asymmetry effects were determined from independent calculations of boattail pressure drag based on the pressure distribution as measured from the (1) top row of pressure orifices, (2) side row of pressure orifices, and 3) bottom row of pressure orifices. The bottom row of pressure orifices was in the flow field of the model support strut wake. Any differences obtained in the drag values calculated in the above manner were the result of flow asymmetry. Nozzle pressure ratio effects on flow asymmetry are shown in Figs. 20 through 22 for the 10-, 15-, and 25-deg boattail configurations, respectively. The drag coefficient data presented in Fig. 23 summarize flow asymmetry results as a function of Mach number (at the NPR schedule defined in Section 4.3). Pressure distribution data for each of the boattail configurations are presented in Figs. 24 through 26.

In general, flow asymmetry effects were Mach number and NPR dependent; this was especially true for the 25-deg boattail configuration, less so for the 15-deg boattail configuration, and practically not at all for the 10-deg boattail configuration. For a given NPR, flow asymmetry effects increased as boattail angle was increased. The drag coefficient, as determined from pressure integration of the bottom row of pressure orifices for the 25-deg boattail configuration, was significantly larger than that obtained for the top row of pressure orifices. For example, at $M_{\infty} = 0.95$ and for $NPR = 3$ the drag coefficient as determined from the bottom row of pressure orifices was approximately 16 percent larger than that for the top row of pressure orifices. This 16-percent difference, when translated into aircraft drag counts, is equivalent to approximately 7 percent of the aircraft drag based on a total drag of 250 counts. Similar analysis for the 15-deg boattail configuration at $M_{\infty} = 0.95$ would result in 4 percent of the aircraft drag. For the 10-deg

boattail configuration, the analysis would result in zero percent of the aircraft drag since the pressure drag coefficients based on the top and bottom row of pressure orifices were equal. The pressure distribution data for the 25-deg boattail configuration show a significant difference between the top and bottom rows of pressure orifices - on the order of 0.04 in pressure coefficient aft of the boattail shoulder. It should be noted that a 0.01 change in the average pressure coefficient for the boattails is equivalent to approximately 0.0085 in boattail pressure drag coefficient.

4.5 EXHAUST PLUME TEMPERATURE EFFECTS

The hot flow model data were obtained at fuel/air ratios of 0, 0.015, 0.025, and 0.04, which corresponded to exhaust gas temperatures of approximately 540, 1,600, 2,100, and 2,900°R, respectively. Over this temperature range, the ratio of specific heats (γ) varied from 1.4 to approximately 1.28. The exhaust plume temperature effects on the boattail drag for the 15- and 25-deg boattail configurations are shown in Figs. 27 and 28, respectively. These data illustrate the fact that "cold jet" test results must first be adjusted for exhaust temperature effects before they can be used to estimate nozzle boattail performance for a "live" engine installation. A procedure normally used to correct "cold jet" test results is based on the premise that the jet plume characteristics immediately downstream of the nozzle exit are functions primarily of nozzle geometry, nozzle total pressure ratio, and the ratio of specific heats. The effect of increasing the nozzle total pressure ratio is to increase the initial inclination angle of the jet and to increase the maximum plume diameter. The effect of increasing γ of the jet is to decrease the initial inclination angle of the jet and to decrease the maximum plume diameter. Simulation of a "hot jet" ($\gamma < 1.4$) plume operating at a given nozzle pressure ratio using cold air requires that the nozzle pressure ratio be increased to offset the effect of γ . For example, to simulate the initial inclination angle of a "hot jet" (with sonic exit conditions) operating at a nozzle total pressure ratio of 4.5 and with a value of γ of 1.286, the "cold jet" must be operated at a nozzle total pressure ratio of 5.

If the procedure as outlined above and described in Ref. 2 is correct, then the data presented in Figs. 27 and 28 for the 15- and 25-deg boattail configurations should collapse into one curve when plotted as a function of initial jet inclination angle (called "γ correction" herein). As shown in Figs. 29 and 30, the "γ correction" was dependent on Mach number, nozzle pressure ratio, and boattail configuration. In general, the data collapsed into one curve only at $M_\infty = 1.5$ over the range of nozzle pressure ratio tested. At Mach numbers of less than 1.5, the "γ correction" tended to collapse the data only at the higher nozzle pressure ratio values. For the 25-deg boattail configuration at subsonic Mach numbers, the data do not tend to collapse at any nozzle pressure ratios tested.

It should be noted that application of the " γ correction" to "cold jet" test results at nozzle pressure ratios representative of turbofan and turbojet engines can result in significant error if the "corrected cold jet" drag values are used to estimate boattail performance for "live" engine installations. For example, at $M_\infty = 0.8$ and $NPR = 3$, use of the " γ correction" technique to correct 15-deg boattail "cold jet" test results for application to a "live" engine operating with a plume temperature of $2,900^{\circ}\text{R}$ would result in a 45-percent error (increase) in boattail drag coefficient. When translated into aircraft drag counts, this increase is equivalent to approximately 3 percent of the total aircraft drag (based on a total aircraft drag of 250 drag counts). Additional results of correlating plume temperature effects are reported in Ref. 3.

4.6 NOZZLE BASE AREA EFFECTS

Water cooling requirements for the hot flow nozzle assembly resulted in a nozzle base area equivalent to 6.5 percent of the model maximum cross-sectional area, as compared to 0.93 percent for the cold flow nozzle assembly. The data presented in Fig. 31 for the 15- and 25-deg boattail configurations show that nozzle base area effects on boattail drag were significant and dependent on nozzle pressure ratio and Mach number. For the 15-deg boattail configuration, the drag coefficient as measured on the hot flow model was either equal to or significantly larger than that measured on the cold flow model through the Mach number range from 0.6 to 1.5. The 25-deg boattail configuration exhibited similar characteristics except at $M_\infty = 0.95$, where the drag as measured on the cold flow model at nozzle pressure ratios of less than 6 was significantly larger than that measured on the hot flow model. The following table summarizes base area effects on the drag coefficients for the 15- and 25-deg boattail configurations at the nozzle pressure ratio schedule defined previously in Section 4.3.

$$\text{Percent} = \frac{\text{CDPT (Hot Flow Model)} - \text{CDPT (Cold Flow Model)}}{\text{CDPT (Cold Flow Model)}} \times 100$$

| M_∞ | NPR | 15-deg Boattail, | |
|------------|-----|------------------|-----------------------------|
| | | percent | 25-deg Boattail, percent |
| 0.6 | 3 | 57.0 | 12.9 |
| 0.8 | 3 | 57.0 | 6.5 |
| 0.9 | 3 | 17.5 | - 7.9 |
| 0.95 | 3 | 6.7 | -12.0 |
| 1.1 | 5 | 3.8 | 1.9 |
| 1.5 | 7 | 20.0 | 15.0 |

5.0 THEORETICAL ANALYSIS

5.1 PHYSICAL STATEMENT OF PROBLEM

One of the main concerns of this analysis was the accurate description of the physical phenomena involved throughout the complex flow field. The analytical model chosen was a compromise between the requirements of the physical reality and the capabilities of the available analytical methods. Since much was discovered concerning both facets of this problem during the course of the analyses, the analytical model was constantly revised and is, indeed, still being modified. In general the model accurately represented a large portion of the flow and allowed fairly accurate predictions of the pressure distribution over the nozzle boattail. The following discussions of the actual flow characteristics and the analytical model should indicate the validity of the model and, to a certain extent, the areas of disagreement between theory and experiment.

5.1.1 Characteristics of the Actual Flow

The configurations that were analyzed were assumed to be nonseparated with thin boundary layers (relative to the reference maximum radius of the cone-cylinder model). Although this was the case for most of the experiments conducted with the 10-deg and 15-deg boattail configurations, it was not true for most of the experiments with the 25-deg boattail configuration, which had an extremely sharp shoulder.

If the flow is "well behaved," as in the former cases, the two separate flows and their mixing region are usually described as indicated in Fig. 32. The flow through the nozzle is divided into an inviscid core region (A) and a thin boundary layer (C), whereas the external flow is described in an analogous manner, the corresponding parts being (B) and (D).

Because of the length of the cylindrical portion of the model preceding the nozzle boattail pictured in Fig. 32, and because the external flow is usually tripped somewhere near the model nose, the boundary layer of the external flow (D) is considered to be turbulent. This assumption is also made for the inner boundary layer (C). Thus, region (E) is an area of turbulent mixing.

This relatively simple and straightforward model does not hold under some conditions, particularly those situations that produce separated flow. Large closure rates of the nozzle boattail will generate adverse pressure gradients which can easily cause flow separation. An increase in Mach number will aggravate the situation, particularly if it is sufficient to produce local shock waves. Such flows are common (particularly with the 25-deg boattail) but cannot be solved analytically at this time.

5.1.2 Analytical Model

The component flow as described in the previous section was modeled as closely as possible. Although each family of calculations will be covered in detail, it may be helpful here to describe the general solution procedure.

Because a great deal of the flow is subsonic in many cases, it would be preferable to treat the entire region of interest with the Navier-Stokes equations, thereby guaranteeing that the upstream influence of the plume would be included throughout the subsonic areas. This form of general solution is, however, not yet available for compressible turbulent flows, and thus it was decided to use the component flow model as shown in Fig. 33. It will be noted that the only difference in this model from that in Fig. 32 is the division of the mixing layer into two parts separated by the inviscid plume boundary.

5.1.3 Computational Procedure

The actual interaction between the plume and the external flow is so strong that it was deemed necessary to make the solution an iterative one, following the outline in Fig. 34. The procedure consists of an inviscid/inviscid (I/I) loop and a viscous/inviscid (V/I) loop, in essence each loop being an iteration within itself. The I/I loop is primarily concerned with the consistent solution between the internal inviscid plume flow and the external inviscid flow, (A) and (B) in Fig. 32. Any difference in pressure between the external inviscid solution and the previously specified plume boundary pressure requires recalculation first of the plume and then of the external inviscid flow using the new plume shape. In the I/I loop the displacement thicknesses in the boundary and shear layers, which usually exist in all but the first entry into this loop, are assumed constant and merely translate as the plume shape changes. When reasonable agreement is obtained between the two solutions, the V/I loop is entered.

The V/I loop is concerned with adjusting the displacement thicknesses on the nozzle boattail (D) and inviscid plume surface (E1) according to their compatibility with the external inviscid flow (B). The inviscid plume shape is assumed constant within this loop. The viscous analysis which is covered in Section 5.2.3 and Appendix A, provides the external displacement thicknesses. Any effect of the internal boundary layer on the afterbody flow is assumed to be sufficiently small to be ignored. Upon leaving this loop, further convergence may be obtained by reentering the I/I loop. In practice it has been found that this is rarely necessary.

Inherent in the procedures described above are the assumptions that the boundary layers are thin and that the supporting surfaces have little longitudinal curvature. These assumptions may not be strictly true for some of the data reported herein, but they are

for the most part valid for the configurations analyzed, as the flows remain attached. Further extension of this procedure is expected into the realm of separated flows, as will be further explained in Section 5.2.4.. Viscous Flows.

5.2 COMPUTATIONAL TECHNIQUES

A number of different techniques were available for the inviscid and viscous flows, and during the initial computations, most of the programs were used and the results compared. The strengths and weaknesses of each program gradually became apparent, and some programs were eliminated in the subsequent iterations. This was true in particular for the programs used in the analysis of the initial boundary layers and the inviscid flow. Pertinent details of the four main computations follow

5.2.1 Initial Boundary Layers

The viscous calculations in the V/I iterations were performed from station 130 of the model, a point approximately 3.4 radii ahead of the exit plane and one radius ahead of the initial point of curvature of the nozzle boattail. Although it was realized that the flow upstream as far as the nose of the model would be affected by what was happening at the nozzle exit, this station was assumed to be sufficiently upstream to be relatively unaffected when compared to the variation near the nozzle exit. Subsequently, during the course of the iterations, it was found that the displacement thicknesses and surface pressures calculated in the viscous and inviscid portions, respectively, of the iterations changed very little during the course of the iterations in spite of large variations of these quantities near the nozzle exit plane. Thus, it was felt that the choice of MS 130 was justified, although this would not necessarily be the case for the other boattail configurations.

In order to determine the boundary layer at that point, two boundary layer programs, Refs. 4 and 5, were used to calculate the boundary layer profiles at MS 115.46. The two computations agreed well with each other and the wind tunnel data, Fig. 35, and they were extended to MS 130.

5.2.2 Plume

The plumes were calculated using the Lockheed Method of Characteristics (MOC) Program, Refs. 6 through 9. The manner in which this program was used was to specify the Mach number distribution across the nozzle, sonic in this case, and the pressure distribution downstream from the nozzle, as well as stagnation properties of the internal nozzle flow. Calculations performed using the MOC program furnished the axisymmetric plume boundary, hereafter referred to as the inviscid reference line (JRL). This line will

become important in the discussion of the viscous flow calculations, Section 5.2.4. Characteristic plume shapes for nozzle pressure ratios of three and seven are shown in Fig. 36. For the purposes of the analysis, the plume was assumed to extend cylindrically past its point of maximum radius, as shown in the figure.

5.2.3 Inviscid Flow

Three digital computer programs were used initially in the inviscid flow calculations. The first program was the Pratt and Whitney Transonic Program, Ref. 10, which was available and had been used previously for similar analyses. Reference 11 describes the second program used, a finite-difference solution of the full transonic potential equation by South and Jameson. This program was modified slightly for our purposes so that the body shape could be input directly, a change which gave the opportunity to then compute the body derivatives using a number of polynomial or spline fits. The Douglas-Neumann Potential Flow Program was also used, even though it is primarily a subsonic calculation. It does, however, incorporate a Goethert similarity transformation for high subsonic flows.

In order to compare the accuracy, efficiency, and reliability of these three programs, a typical well-behaved case was chosen for the viscous/inviscid iterations, the 15-deg boattail at $M_\infty = 0.6$, $Re/\ell = 2.5 \times 10^6$ ft⁻¹ and $NPR = 3$. The iterations were run independently with the three programs using the same calculation procedure for the turbulent boundary-layer calculations. A comparison of the three "converged" solutions is shown in Fig. 37a.

The iteration technique used for all the iterations except the first, when the inviscid flow over the body and plume alone is calculated, was identical for all three programs. The pressure distribution from the previous iteration was input into the boundary-layer program, and the calculated displacement thicknesses were added to the body. The plume was treated as an effective body using a method which will be described in the next section. This new body shape was then input to the inviscid program. Any discrepancy between the resulting pressure distribution and the previous one was averaged and used for the starting distribution for the next iteration. This technique was used for subsequent calculations at different Mach numbers. All three programs converged within four or five iterations.

The general agreement among the three programs was good, as shown in Fig. 37a. The disagreement at the afterbody/plume junction and the Pratt and Whitney Program's tendency not to return to recovery pressure downstream are apparent. Because of this and because true transonic capability was desired in the inviscid analysis, all subsequent iterations were performed with the South-Jameson program, with occasional checks using the Douglas-Neumann program.

5.2.4 Viscous Flow

The displacement thickness over the boattail and, at first, over the plume (considered as a solid body) was calculated with the Kuhn-Nielsen Turbulent Separated Boundary Layer Program (Ref. 3). The program is an integral technique utilizing a law-of-the-wall/law-of-the-wake velocity profile and an eddy viscosity turbulent relationship. Its uniqueness lies in the fact that the mathematical singularity occurring in the approach to a point of flow separation is bypassed by rearrangement of the governing ordinary differential equations. Acquired for its separated flow capabilities, the program was not used in this mode for the present analysis, however, as the 15-deg boattail configuration and plume analyses resulted in flows which did not indicate separation, as determined by inspection of schlieren photographs.

The problem of how to handle the plume realistically, with both its displacement and entrainment characteristics, was accommodated somewhat with the mixing analysis presented in Appendix A. This analysis showed that a technically valid technique was to take the value of the displacement thickness calculated at the boattail/plume junction and add it to the inviscid reference line along its entire length. Although this method was not entirely satisfactory, it did eliminate the need to fair in a line of arbitrary shape from the afterbody boundary layer to some point on the inviscid reference line, or to assume the plume to be a solid body. Further work is continuing in this area to include the effects of longitudinal pressure gradients and transverse (y-direction) velocities.

5.3 RESULTS OF THE ANALYSIS

Figure 37 represents the analyses performed on the 15-deg boattail configuration, $Re/\ell = 2.5 \times 10^6 \text{ ft}^{-1}$, $NPR = 3$, at Mach numbers of 0.6, 0.8, and 0.9. As pointed out previously in Section 5.2.3, agreement between the three methods used for the inviscid calculations was good for the $M_\infty = 0.6$ case, Fig. 37a. It is apparent that overcompression is predicted near the end of the boattail, a characteristic of the flow calculation which would tend to make drag predictions highly optimistic.

Figures 37b and c, at Mach numbers 0.8 and 0.9, respectively, show a continuation of the overcompression characteristic. Although neither inviscid program accurately predicts the highly negative pressure at the shoulder of the boattail, the subsonic (rather than transonic) nature of the Douglas-Neumann program is apparent in the solution at $M_\infty = 0.9$ (Fig. 37c).

6.0 CONCLUDING REMARKS

An experimental program was conducted to investigate the interaction effects which occur between the nozzle exhaust flow and the external flow field associated with isolated nozzle/afterbody configurations at Mach numbers 0.6, 0.8, 0.9, 0.95, 1.1, and 1.5. Configuration variables included nozzle boattail geometries with boattail angles of 10, 15, and 25 deg. Cold and hot jet test techniques were used to both simulate and duplicate the nozzle exhaust flow for a sonic jet installation. High pressure air was used to simulate the nozzle exhaust, and an air/ethylene combustor provided the means to duplicate the nozzle exhaust. Nozzle exhaust temperature effects were evaluated over the temperature range from 540°R to approximately 2,900°R.

The significant results obtained from the experimental program pertain to those effects on boattail pressure drag coefficient caused by flow asymmetry (model support strut induced), nozzle base area, and exhaust plume temperature. These results are as follows:

1. Flow asymmetry effects were Mach number and nozzle pressure ratio dependent and increased in severity as the boattail angle was increased. For example, flow asymmetry effects on the 25-deg boattail configuration at Mach number 0.95 were equivalent to approximately 16 percent of the boattail drag level.
2. Nozzle base area effects were significant and dependent on Mach number, nozzle pressure ratios, and boattail configuration. Increasing the nozzle base area from 0.93 to 6.5 percent of the model maximum cross-sectional area resulted in increasing the boattail pressure drag as much as 57 percent for the 15-deg boattail at Mach number 0.6 and nozzle pressure ratio 3 and decreasing the boattail pressure drag as much as 12 percent for the 25-deg boattail at Mach number 0.95 and nozzle pressure ratio 3.
3. The differences obtained in boattail pressure drag between the cold jet simulation and hot jet duplication results were significant at nozzle pressure ratios representative of turbofan and turbojet engines at subsonic Mach numbers. Adjusting the cold jet nozzle pressure ratio to correct for the changes in the exhaust plume specific heat ratio with temperature did not account for the differences observed. At Mach number 0.8 and for a nozzle pressure ratio of 3, adjusting the 15-deg boattail, cold jet results to a result representative of an engine operating with a plume temperature of 2,900°R would result in a 45-percent error (increase in drag) in boattail drag.

In a continuing effort to improve nozzle afterbody-related theoretical prediction techniques, the experimentally measured pressure distribution (top row of pressure orifices) on the 15-deg boattail configuration at Mach numbers 0.6, 0.8, and 0.9 were compared with theoretical results obtained from the South-Jameson, Douglas-Neumann, and Pratt and Whitney inviscid programs in conjunction with the Kuhn-Nielson separated boundary-layer program. The analyses were limited to that for a cold jet operating at a nozzle total pressure ratio of 3 and were performed using a viscous/inviscid iterative procedure. All three computer programs predicted more recompression near the boattail/plume junction than was actually measured. Further work is continuing to remedy this problem, particularly through more sophisticated mixing analyses. The programs predict with reasonable accuracy the low pressures encountered at the boattail shoulder; the South-Jameson program was the preferred program since it predicted results nearer the actual measurements. Predictions of pressure level at other points along the boattail agreed reasonably well with the actual measurements with results improving as the free-stream Mach number was decreased from sonic conditions.

REFERENCES

1. Robinson, C. E. "Evaluation of Reynolds Number and Tunnel Wall Porosity Effects on Nozzle Afterbody Drag at Transonic Mach Numbers." AEDC-TR-76-70 (ADA027388), July 1976.
2. Robinson, C. E. and High, M. D. "Exhaust Plume Temperature Effects on Nozzle Afterbody Performance Over the Transonic Mach Number Range." AEDC-TR-74-9 (AD781377), July 1974.
3. Peters, W. L. "Air Evaluation of Jet Simulation Parameters for Nozzle Afterbody Testing at Transonic Mach Numbers." AEDC-TR-76-109, to be published.
4. Kuhn, G. D. and Nielsen, J. N. "Prediction of Turbulent Separated Boundary Layers in Subsonic and Transonic Flows." AIAA Paper No. 73-663, presented at the AIAA 6th Fluid and Plasma Dynamics Conference, Palm Springs, California, July 1973.
5. Whitfield, D. L. "Analytical, Numerical, and Experimental Results on Turbulent Boundary Layers." AEDC-TR-76-72 (ADA027588), July 1976.
6. Rathiff, A. W., Smith, S. D., and Penny, M. M. "Rocket Exhaust Plume Computer Program Improvement, Vol. 1: Summary Volume, Method of Characteristics Nozzle and Plume Programs." Technical Report LMSC/HREC D162220-1, January 1972.

7. Smith, S. D. and Penny, M. M. "Rocket Exhaust Plume Computer Program Improvement, Vol. II: User's Manual Method of Characteristics Plot Program." Technical Report LMSC/HREC D162220-II-A, July 1971.
8. Prozan, R. J. "Rocket Exhaust Plume Computer Program Improvement, Vol. III: Solution of Non-Isoenergetic Supersonic Flows by Method of Characteristics." Technical Report LMSC/HREC D162220-III-A, January 1972.
9. Smith, S. D. and Ratliff, A. W. "Rocket Exhaust Plume Computer Program Improvement, Vol. IV: User's Manual, Variable O/F Ratio Method of Characteristics Program for Nozzle and Plume Analysis." Technical Report LMSC/HREC D162220-IV-A, January 1972.
10. "Users Manual for the External Drag and Internal Nozzle Performance Deck (Deck XI) Transonic/External Flow Analysis (Applicable to Deck V)." Pratt and Whitney Aircraft PWA-3465, Supplement F, Part II, September 1968.
11. South, J. C. and Jameson, A. "Relaxation Solutions for Inviscid Axisymmetric Transonic Flow over Blunt or Pointed Bodies." Proceedings of AIAA Computational Fluid Dynamics Conference, Palm Springs, California, July 1973, pp. 8-17.

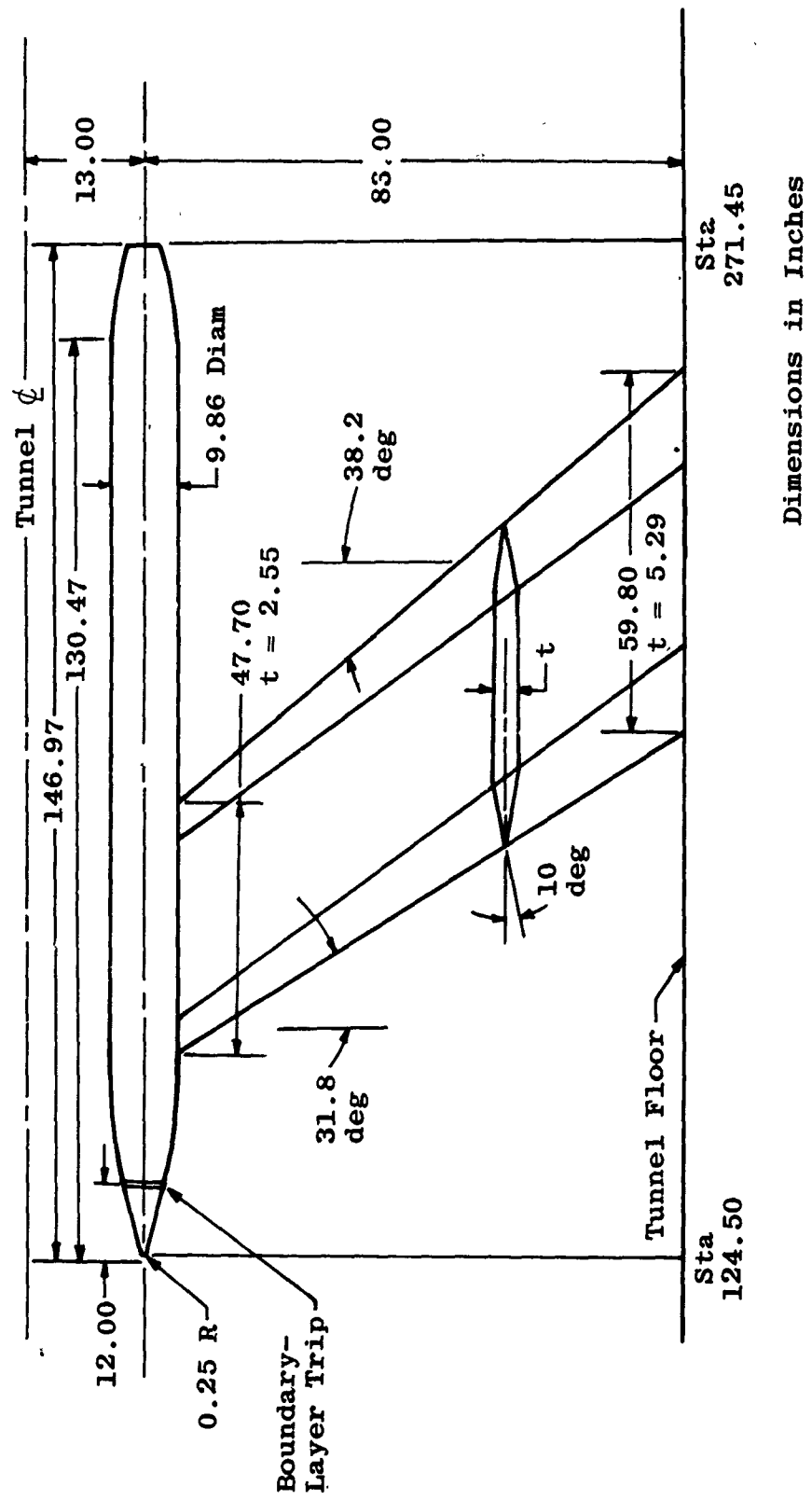


Figure 1. Basic model dimensions and location in test section.

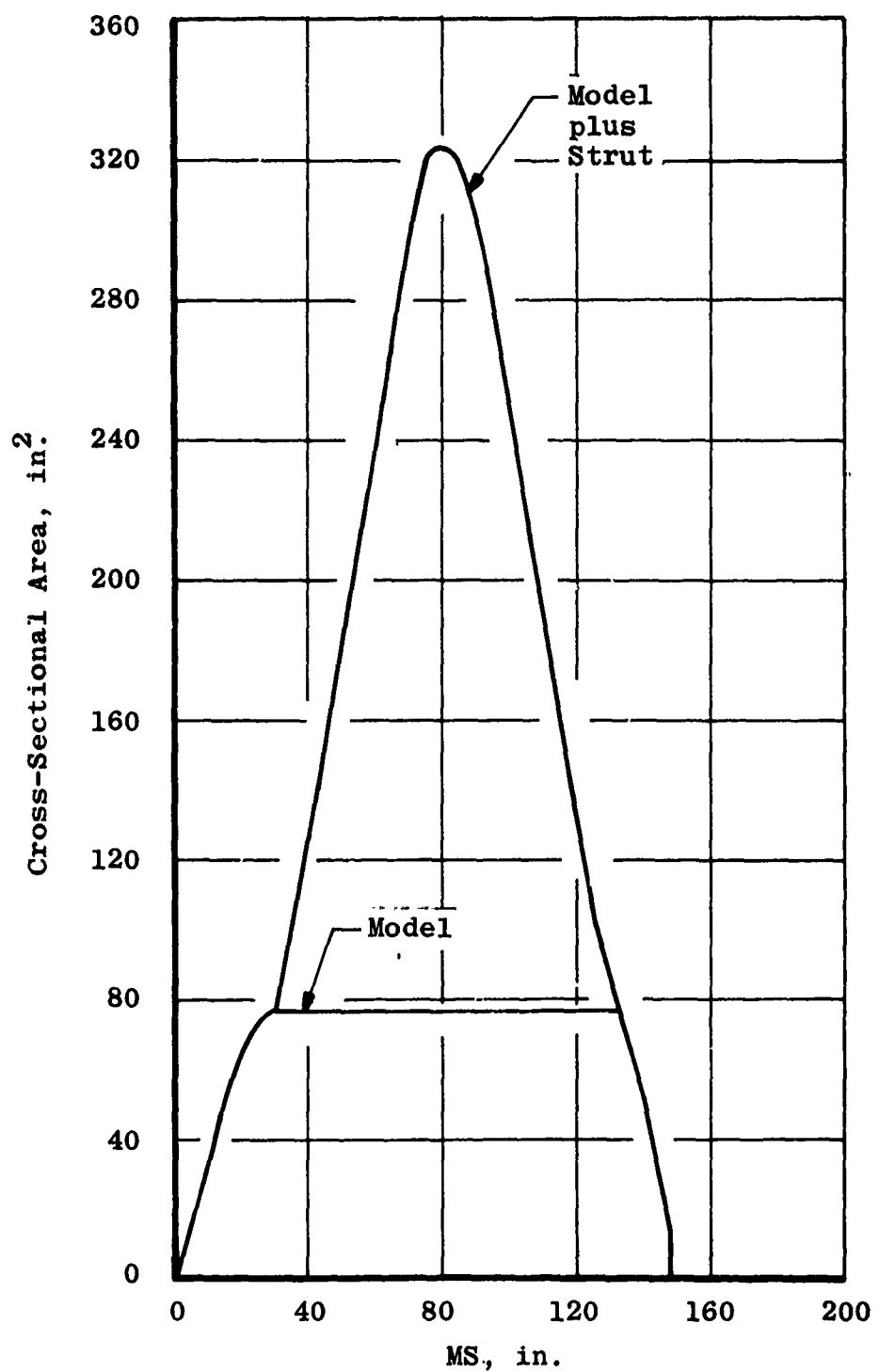
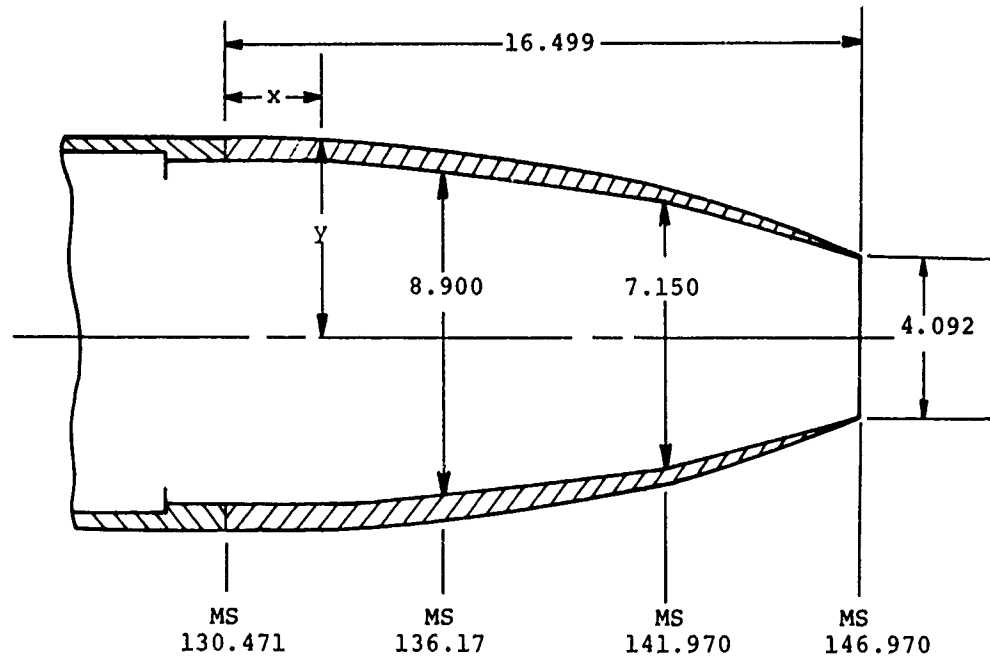


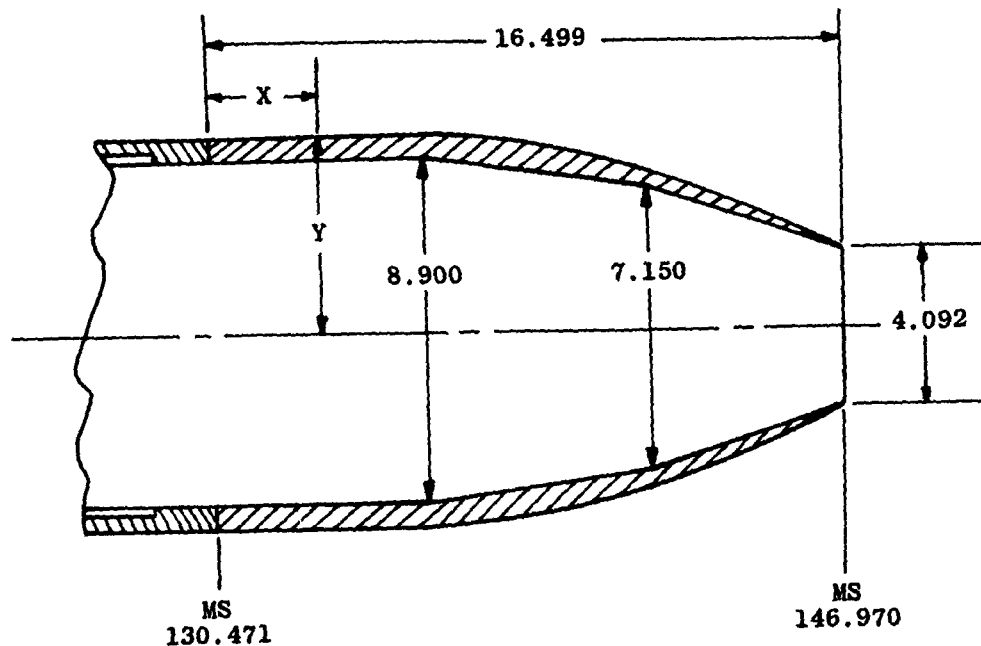
Figure 2. Model/strut cross-sectional area distribution.



Stations and Dimensions in Inches

| X | Y | X | Y | X | Y |
|-------|-------|--------|-------|--------|-------|
| 0 | 4.930 | 5.653 | 4.624 | 11.322 | 3.760 |
| 0.230 | 4.926 | 5.899 | 4.595 | 11.569 | 3.707 |
| 0.476 | 4.923 | 6.146 | 4.565 | 11.815 | 3.653 |
| 0.723 | 4.918 | 6.392 | 4.536 | 12.062 | 3.592 |
| 0.969 | 4.915 | 6.639 | 4.504 | 12.308 | 3.530 |
| 1.216 | 4.913 | 6.885 | 4.472 | 12.555 | 3.464 |
| 1.462 | 4.908 | 7.132 | 4.440 | 12.801 | 3.397 |
| 1.709 | 4.903 | 7.378 | 4.407 | 13.048 | 3.326 |
| 1.955 | 4.895 | 7.625 | 4.376 | 13.294 | 3.252 |
| 2.202 | 4.889 | 7.871 | 4.341 | 13.541 | 3.173 |
| 2.448 | 4.881 | 8.118 | 4.304 | 13.787 | 3.089 |
| 2.695 | 4.874 | 8.364 | 4.267 | 14.034 | 3.002 |
| 2.941 | 4.864 | 8.611 | 4.228 | 14.280 | 2.914 |
| 3.188 | 4.854 | 8.857 | 4.191 | 14.527 | 2.820 |
| 3.434 | 4.841 | 9.104 | 4.154 | 14.773 | 2.726 |
| 3.681 | 4.824 | 9.350 | 4.115 | 15.020 | 2.626 |
| 3.927 | 4.807 | 9.597 | 4.075 | 15.266 | 2.524 |
| 4.174 | 4.785 | 9.843 | 4.036 | 15.513 | 2.419 |
| 4.420 | 4.760 | 10.090 | 3.993 | 15.636 | 2.366 |
| 4.667 | 4.736 | 10.336 | 3.949 | 15.759 | 2.315 |
| 4.913 | 4.711 | 10.583 | 3.905 | 16.006 | 2.214 |
| 5.160 | 4.684 | 10.879 | 3.858 | 16.252 | 2.125 |
| 5.406 | 4.654 | 11.076 | 3.809 | 16.499 | 2.046 |

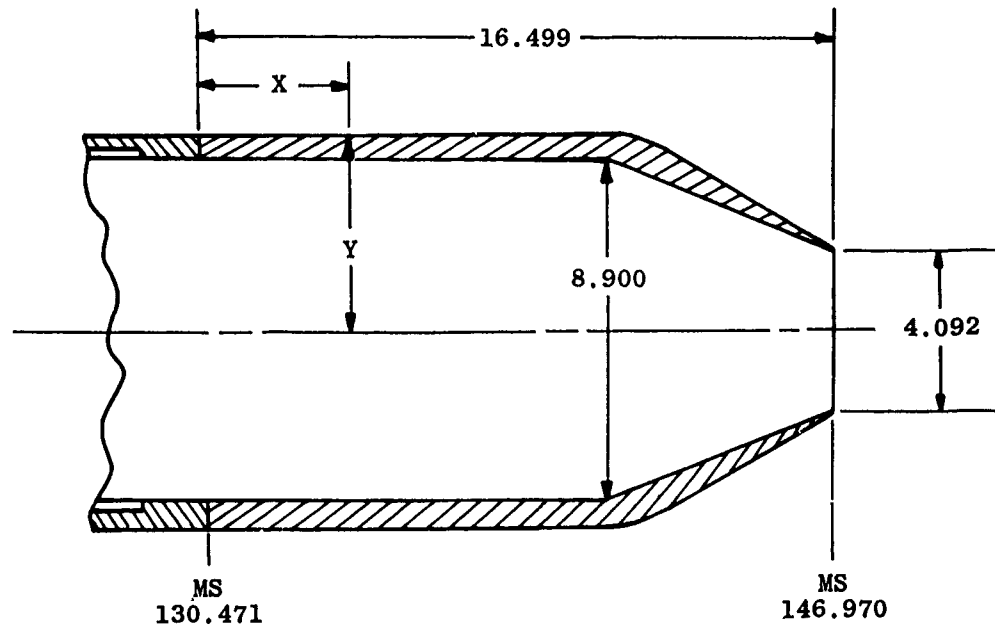
a. 10-deg boattail
 Figure 3. Nozzle boattail geometry.



Stations and Dimensions in Inches

| X | Y | X | Y |
|--------|-------|--------|-------|
| 0 | 4.930 | 11.322 | 3.977 |
| 6.146 | 4.930 | 11.569 | 3.903 |
| 6.392 | 4.920 | 11.815 | 3.826 |
| 6.639 | 4.908 | 12.062 | 3.747 |
| 6.895 | 4.884 | 12.308 | 3.666 |
| 7.132 | 4.859 | 12.555 | 3.579 |
| 7.378 | 4.829 | 12.801 | 3.495 |
| 7.625 | 4.795 | 13.048 | 3.410 |
| 7.871 | 4.760 | 13.294 | 3.321 |
| 8.118 | 4.721 | 13.541 | 3.229 |
| 8.364 | 4.677 | 13.787 | 3.135 |
| 8.611 | 4.629 | 14.034 | 3.043 |
| 8.857 | 4.580 | 14.280 | 2.946 |
| 9.103 | 4.531 | 14.527 | 2.848 |
| 9.350 | 4.479 | 14.773 | 2.749 |
| 9.597 | 4.427 | 15.020 | 2.641 |
| 9.843 | 4.373 | 15.266 | 2.532 |
| 10.090 | 4.313 | 15.513 | 2.423 |
| 10.336 | 4.252 | 15.759 | 2.315 |
| 10.583 | 4.189 | 16.006 | 2.214 |
| 10.830 | 4.120 | 16.252 | 2.125 |
| 11.076 | 4.050 | 16.499 | 2.046 |

b. 15-deg boat tail
Figure 3. Continued.



Stations and Dimensions in Inches

| X | Y | X | Y |
|--------|-------|--------|-------|
| 0 | 4.930 | 13.294 | 3.545 |
| 10.090 | 4.930 | 13.541 | 3.425 |
| 10.336 | 4.910 | 13.787 | 3.310 |
| 10.583 | 4.859 | 14.034 | 3.196 |
| 10.830 | 4.777 | 14.280 | 3.080 |
| 11.076 | 4.669 | 14.527 | 2.966 |
| 11.322 | 4.543 | 14.773 | 2.851 |
| 11.569 | 4.417 | 15.020 | 2.736 |
| 11.815 | 4.292 | 15.266 | 2.621 |
| 12.062 | 4.166 | 15.513 | 2.505 |
| 12.308 | 4.041 | 15.759 | 2.391 |
| 12.555 | 3.914 | 16.006 | 2.276 |
| 12.801 | 3.791 | 16.499 | 2.046 |

c. 25-deg boattail
 Figure 3. Concluded.

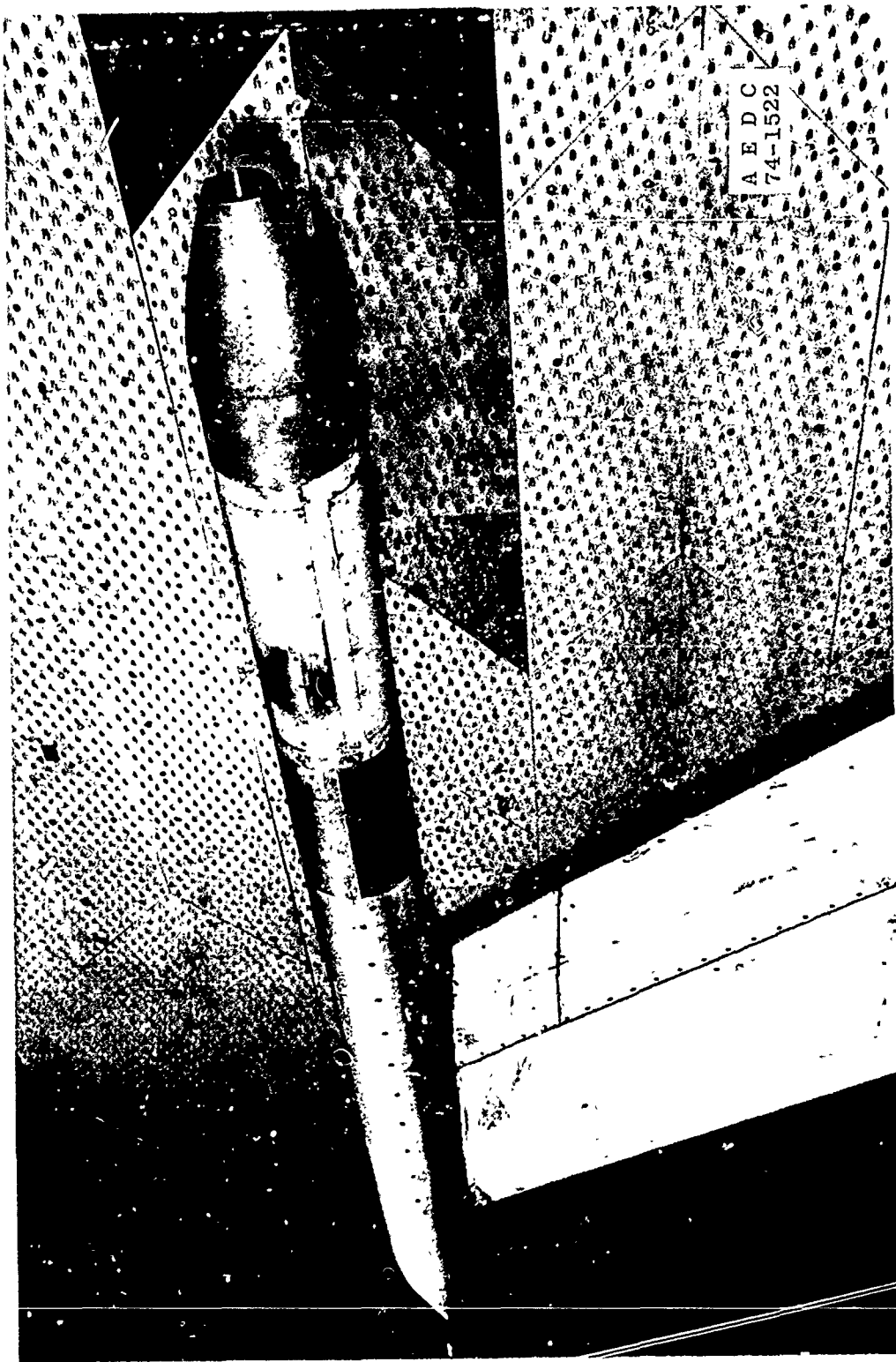


Figure 4. Model installation photograph.

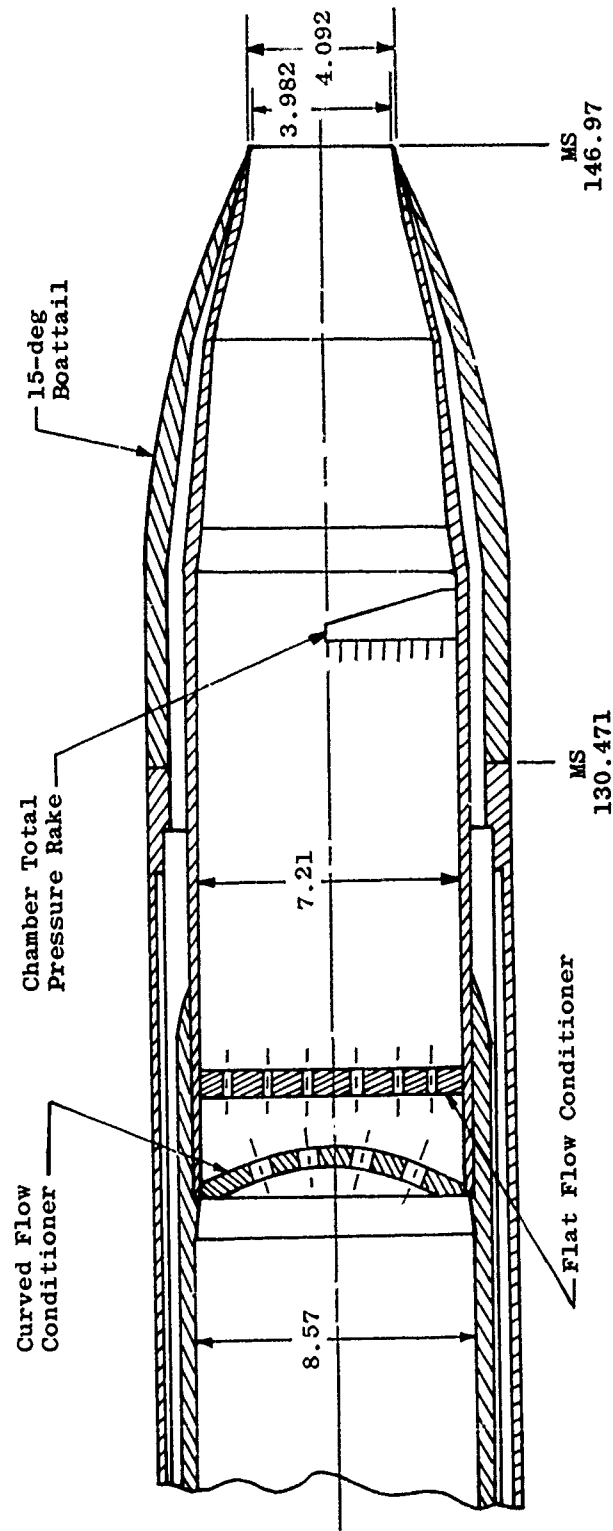


Figure 5. Cold flow nozzle assembly.

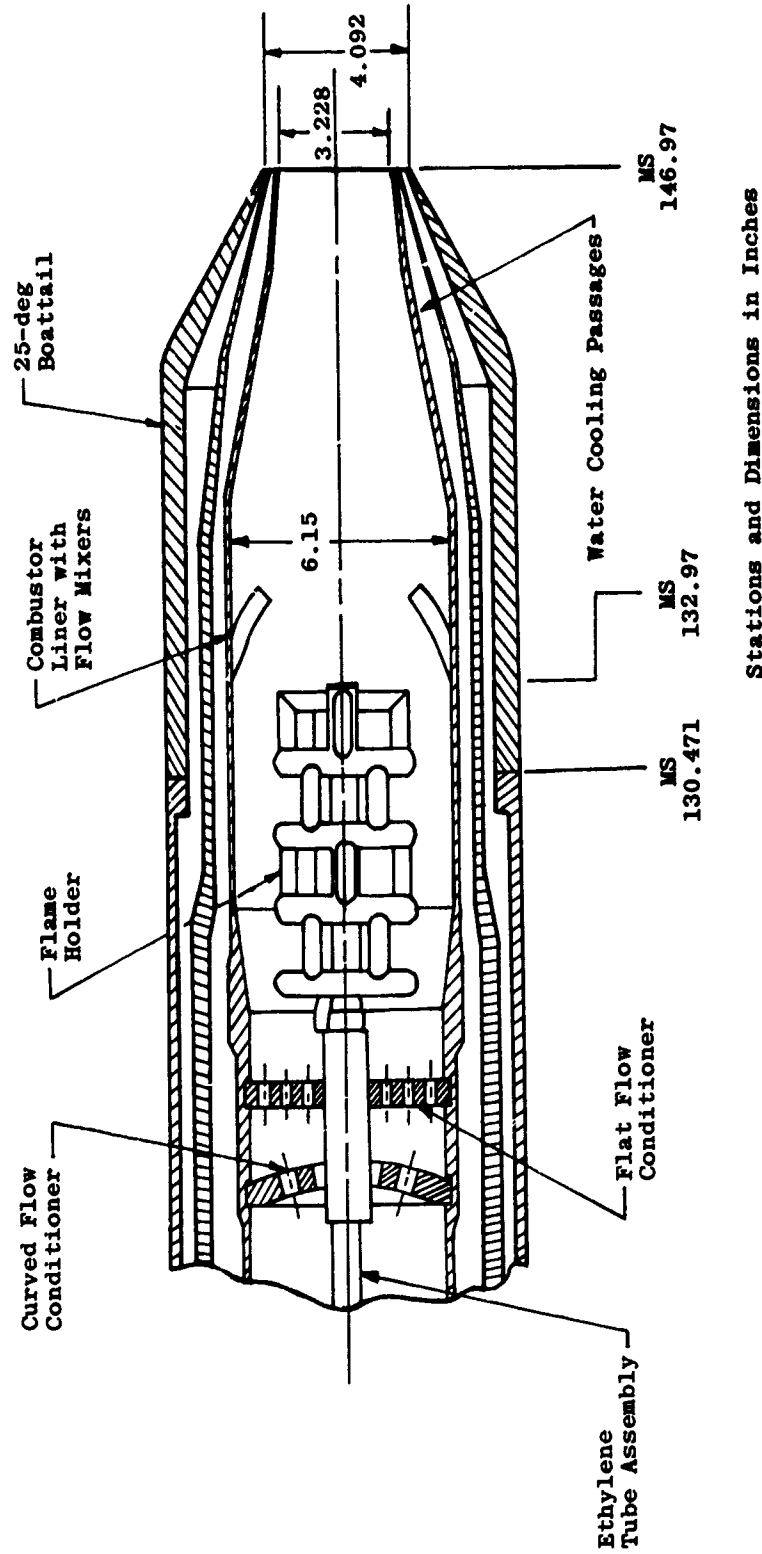


Figure 6. Hot flow nozzle assembly.



Figure 7. Hot flow nozzle installation photograph.

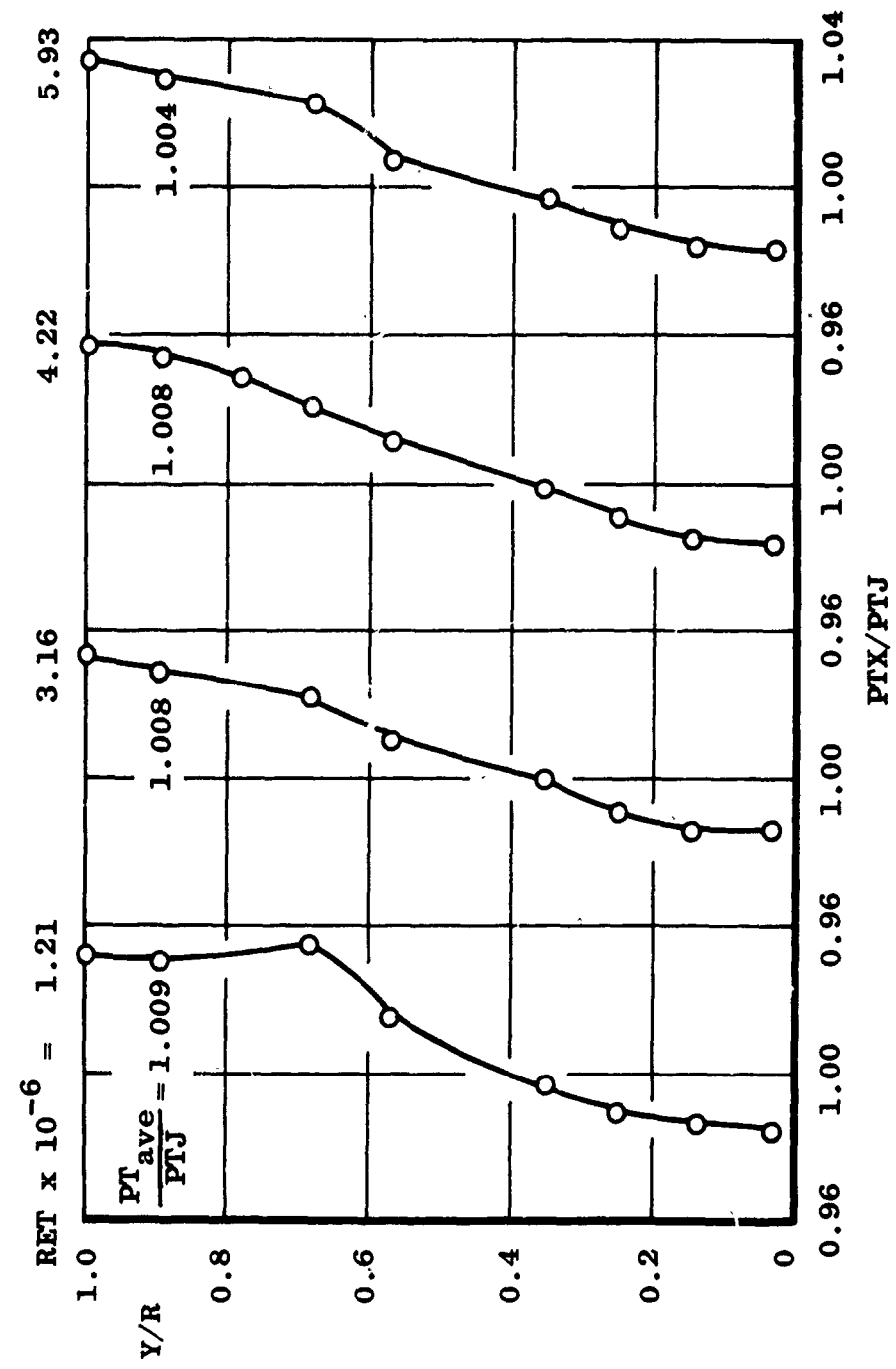


Figure 8. Nozzle flow duct total pressure profile.

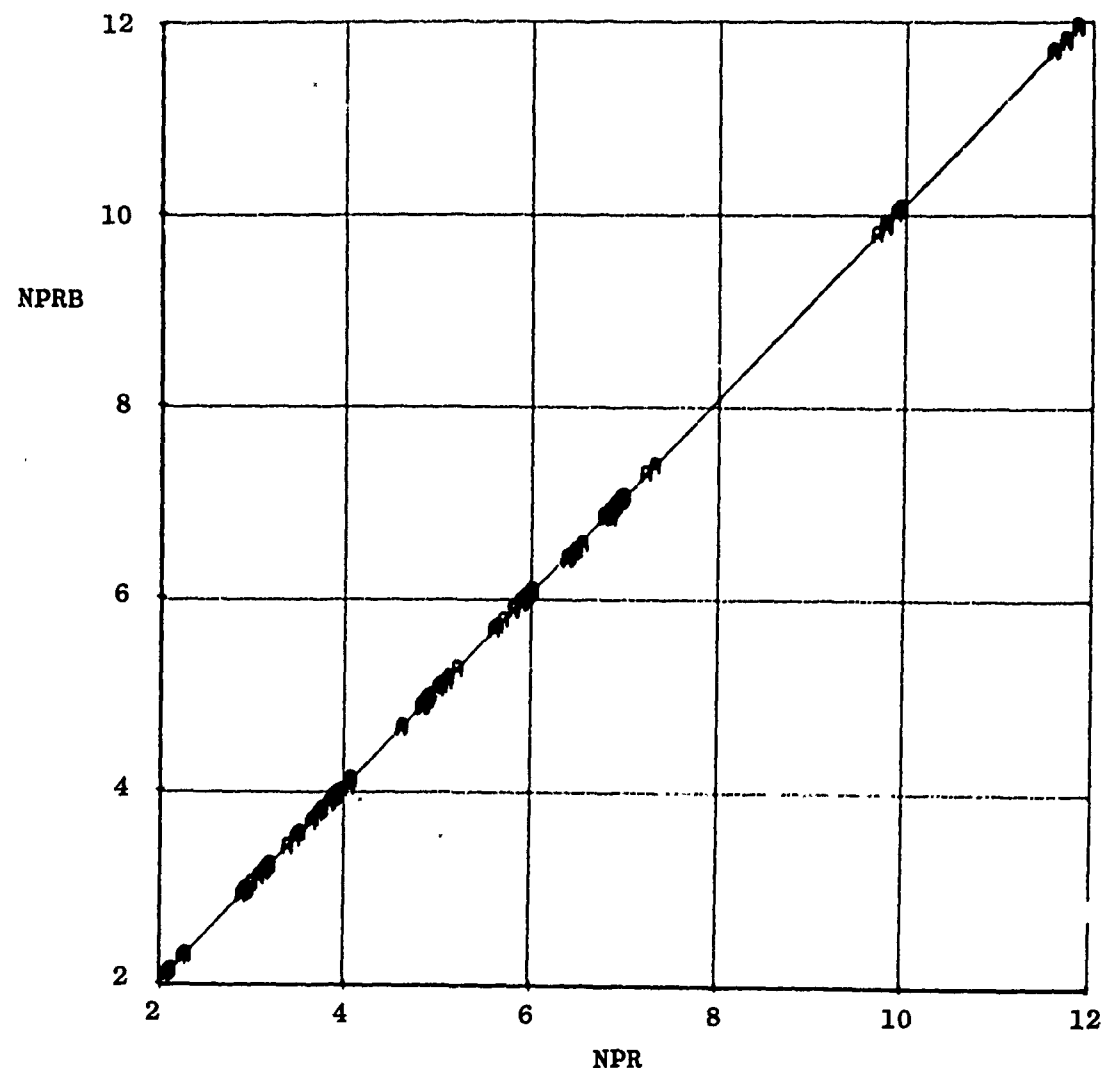


Figure 9. Comparison between primary and secondary measurements of nozzle total pressure ratio.

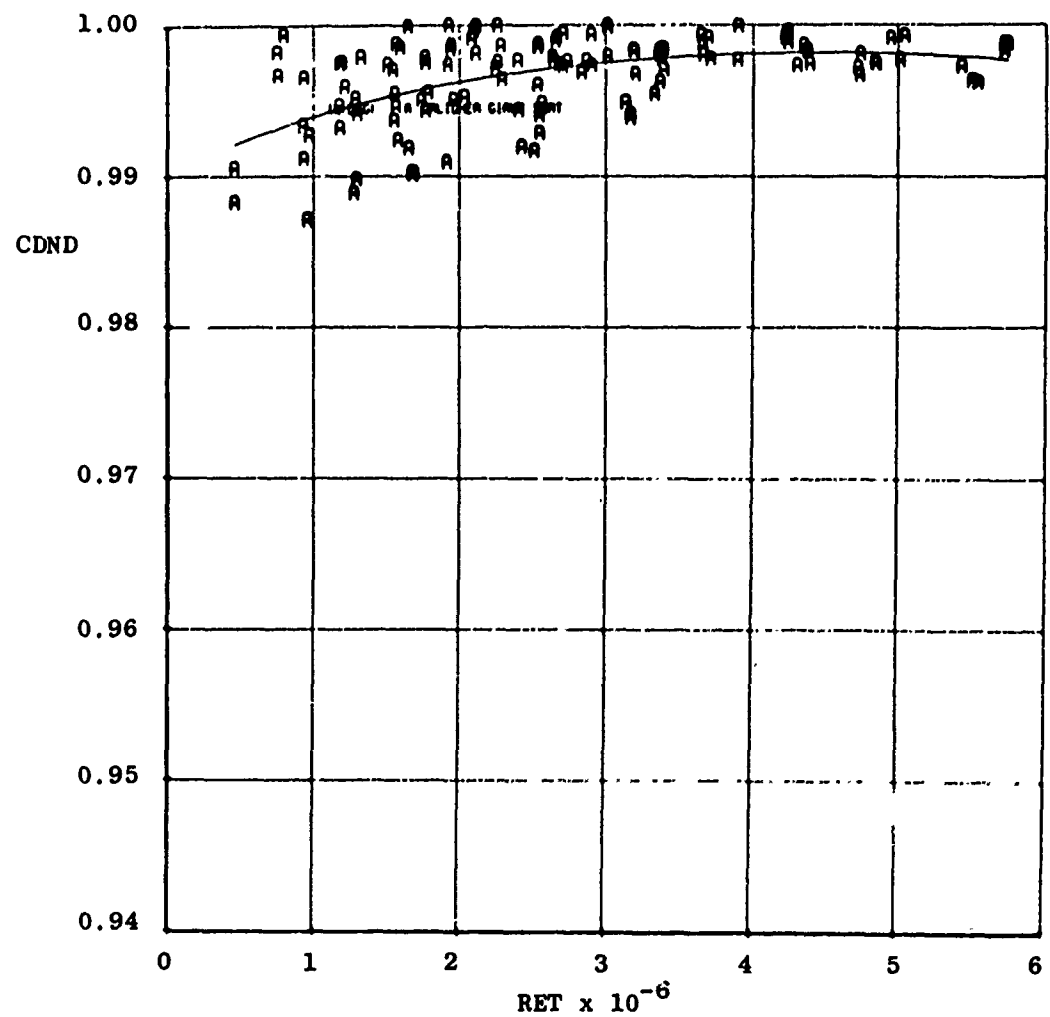


Figure 10. Nozzle discharge coefficient for cold flow model.

| Sym | FTA |
|-----|-------|
| A | 0.015 |
| B | 0.025 |
| C | 0.040 |

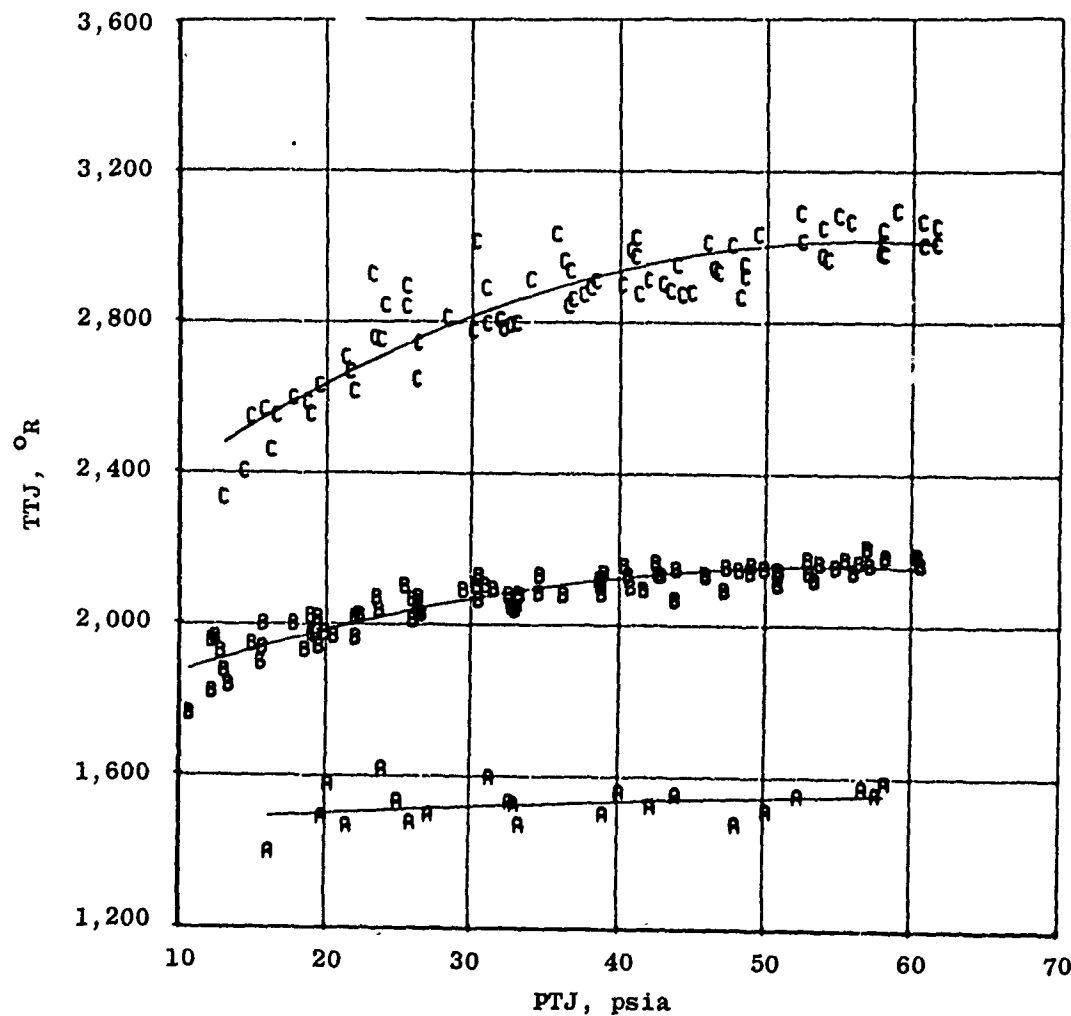


Figure 11. Hot flow model exhaust total temperature.

| Sym | <u>Config., deg</u> | <u>PN/TP</u> |
|-----|---------------------|--------------|
| A | 10 | 6101 |
| B | 15 | 1901 |
| C | 25 | 11301 |

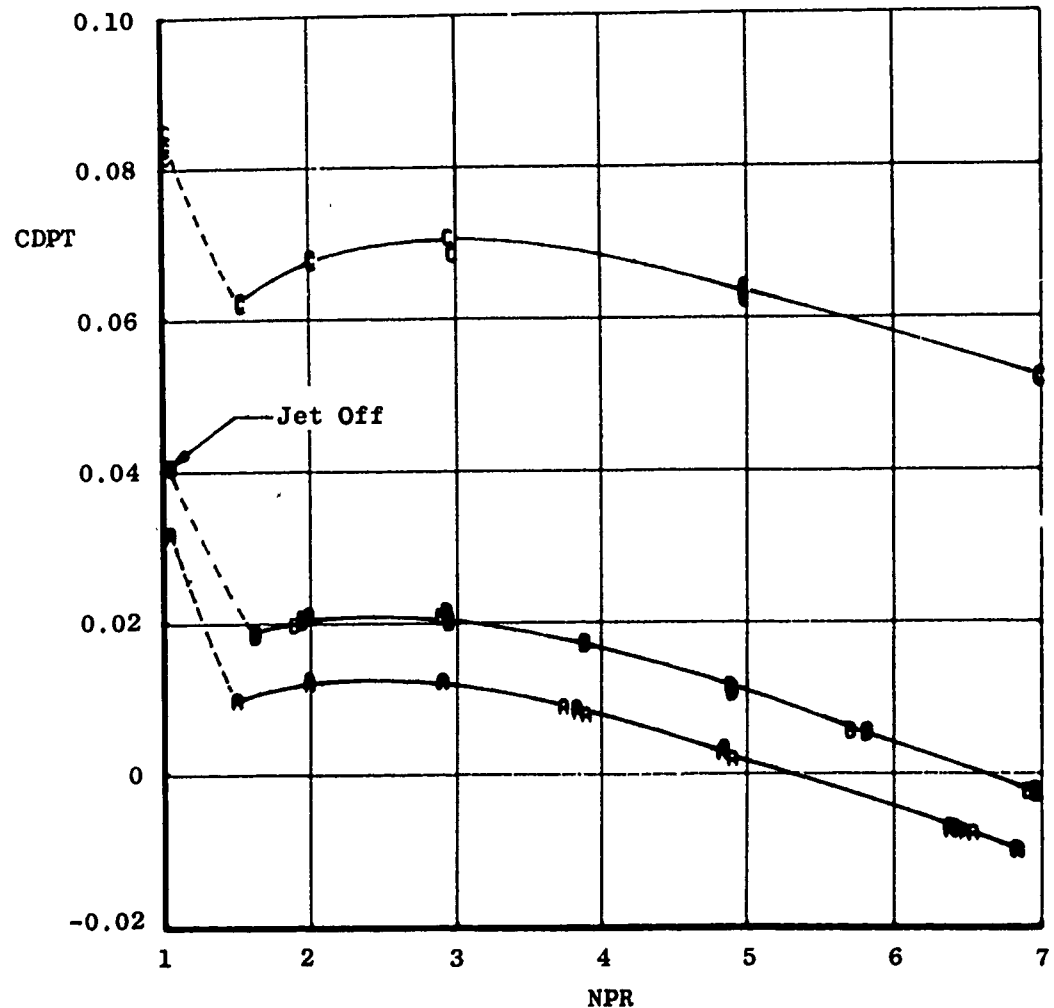
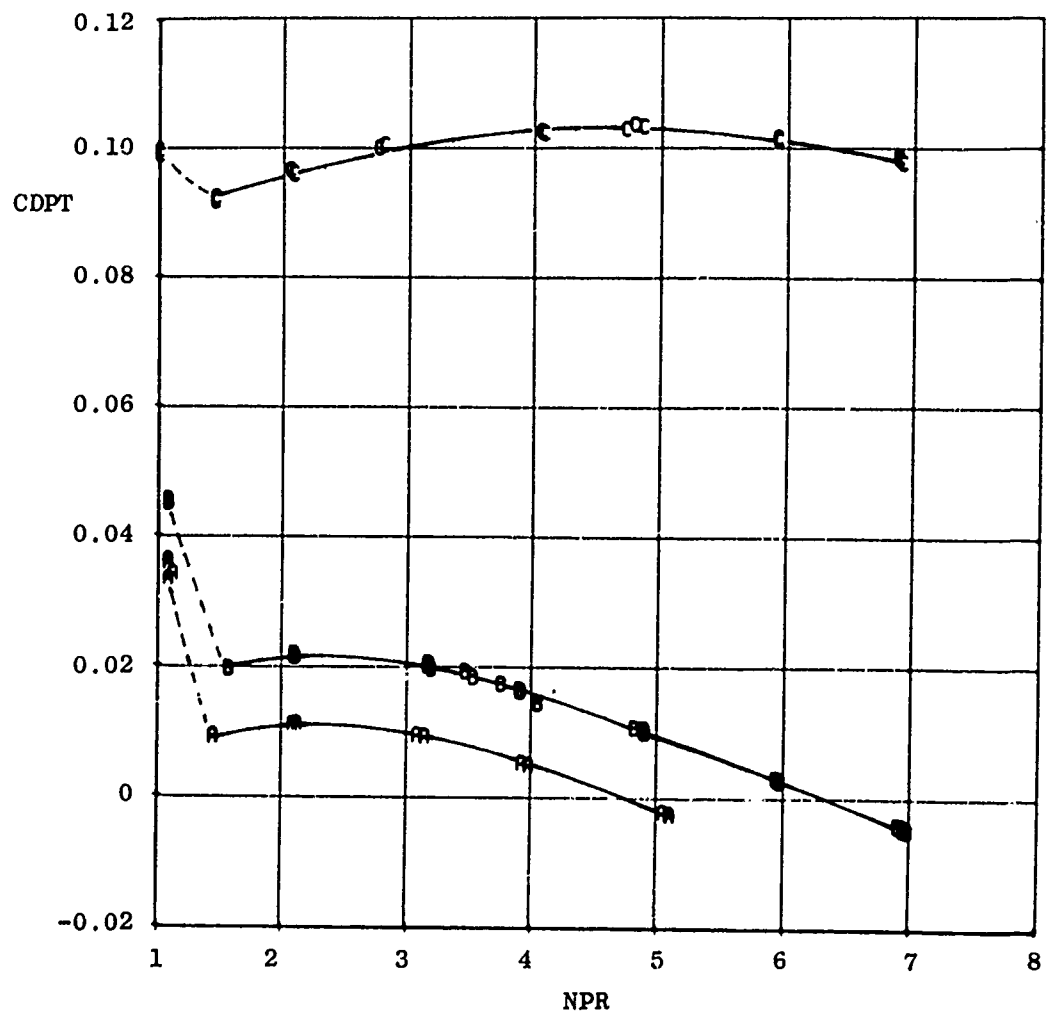
a. $M_{\infty} = 0.60$

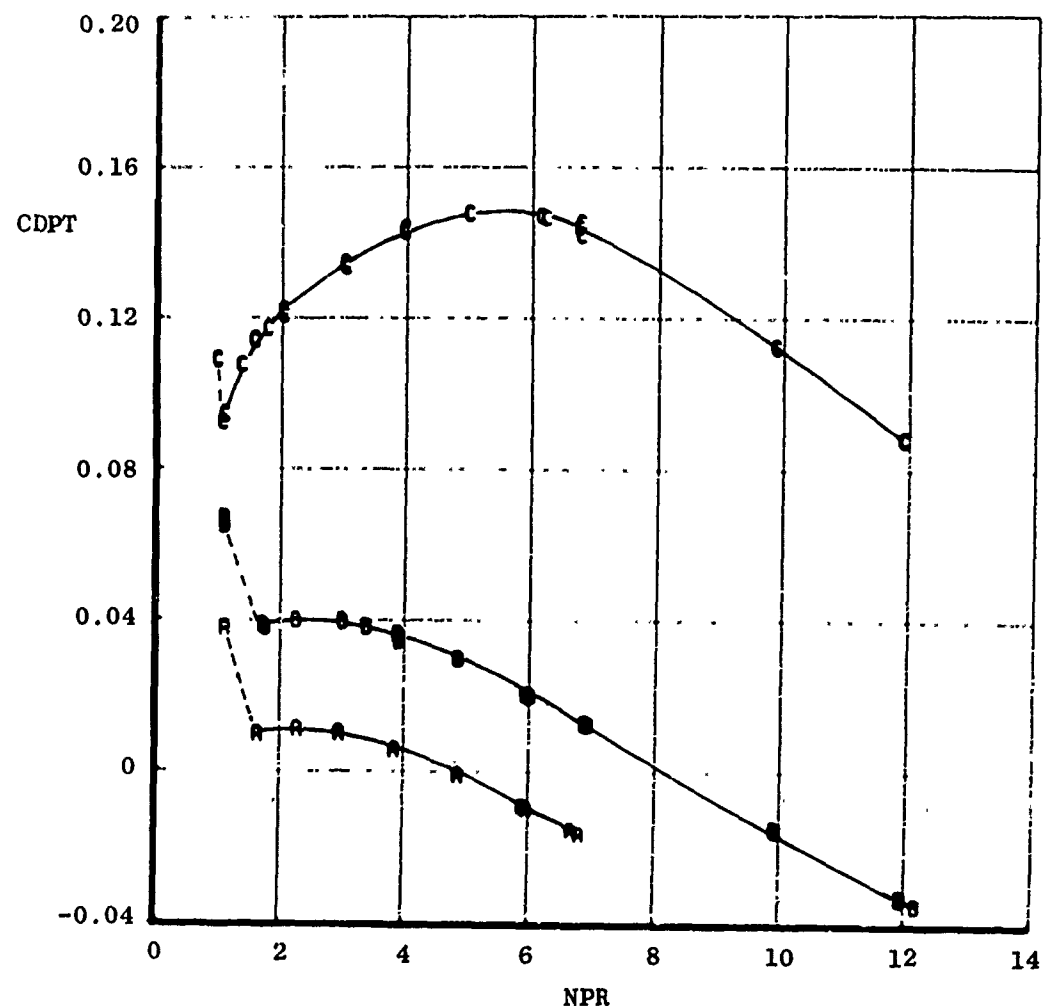
Figure 12. Effect of boattail geometry on boattail pressure drag coefficient.

| Sym | Config, deg | PN/TP |
|-----|-------------|-------|
| A | 10 | 6201 |
| B | 15 | 2001 |
| C | 25 | 11201 |



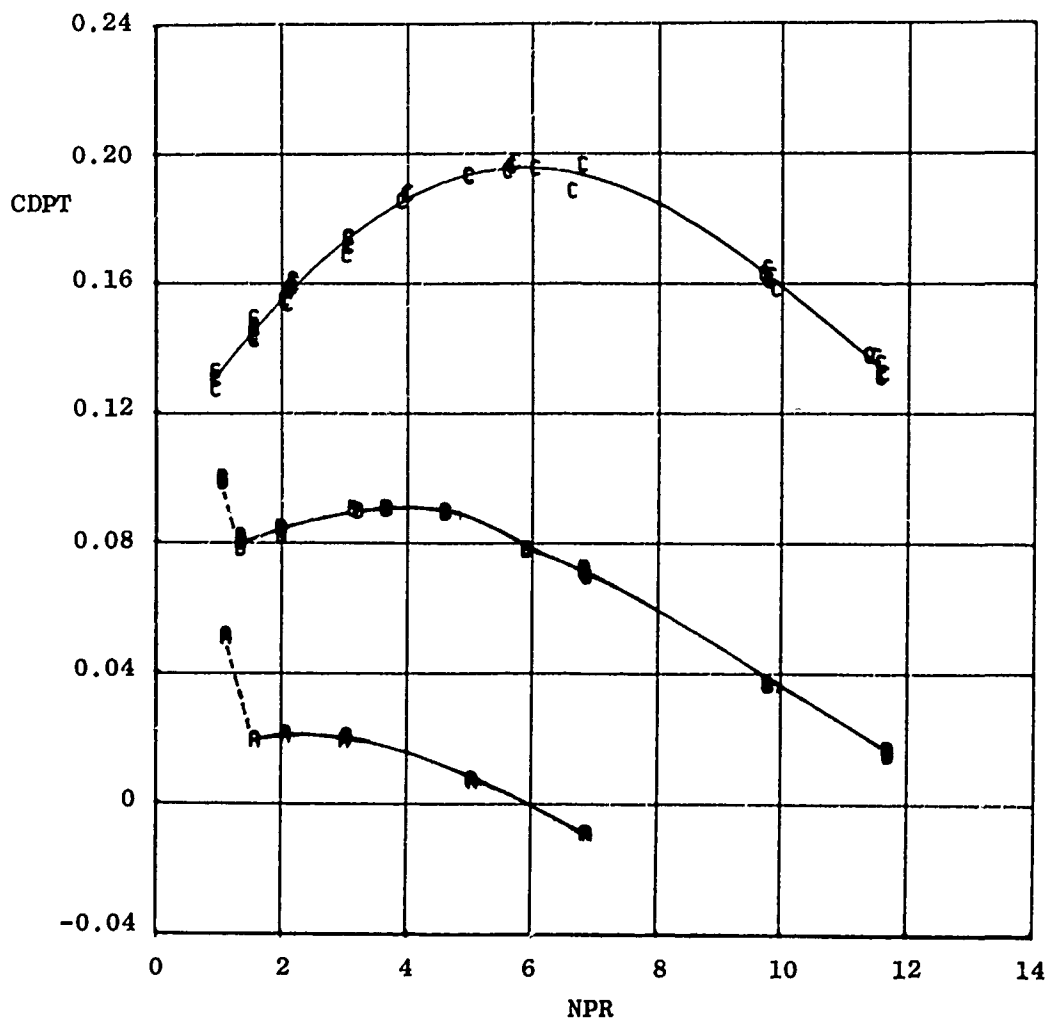
b. $M_{\infty} = 0.80$
 Figure 12. Continued.

| Sym | Config, deg | PN/TP |
|-----|-------------|-------|
| A | 10 | 6301 |
| B | 15 | 2101 |
| C | 25 | 11101 |



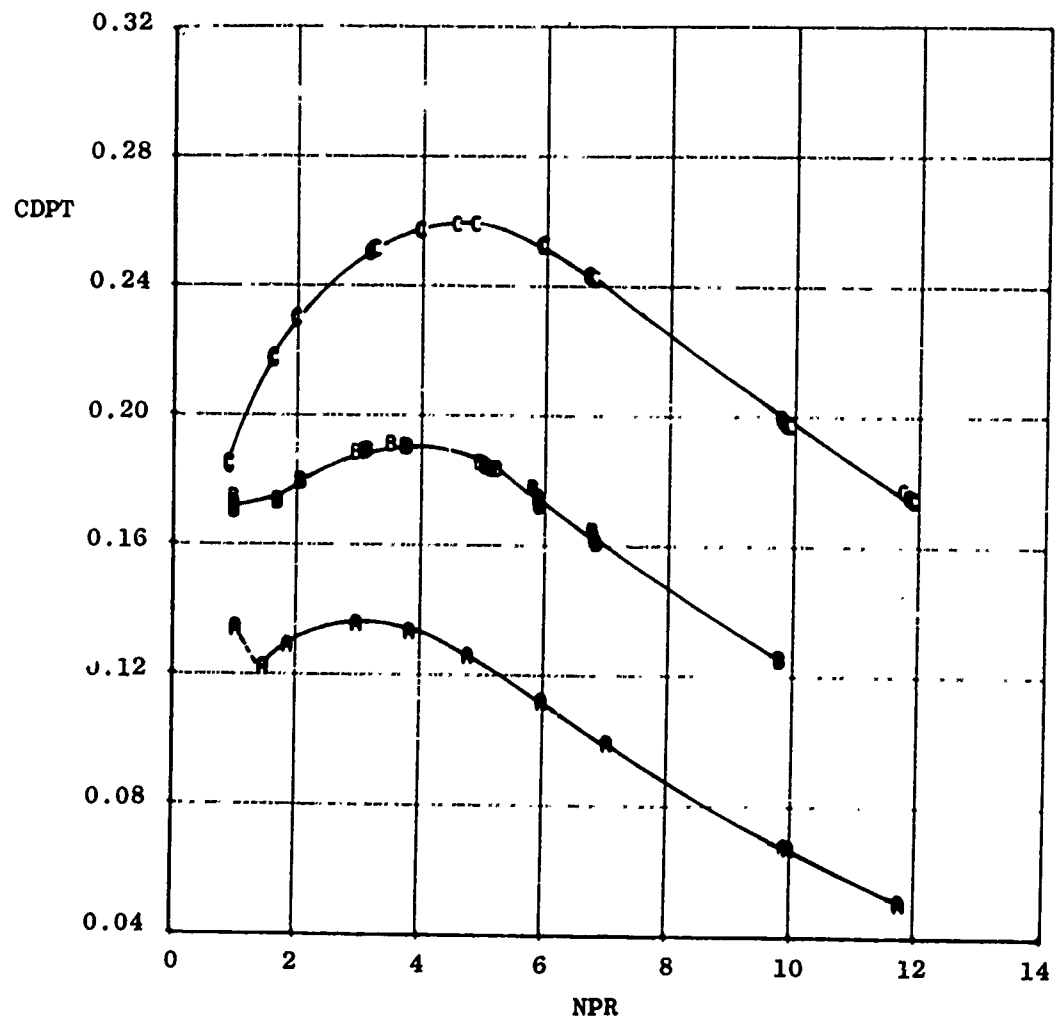
c. $M_{\infty} = 0.90$
 Figure 12. Continued.

| Sym | Config, deg | PN/TP |
|-----|-------------|-------|
| A | 10 | 6401 |
| B | 15 | 4901 |
| C | 25 | 11001 |



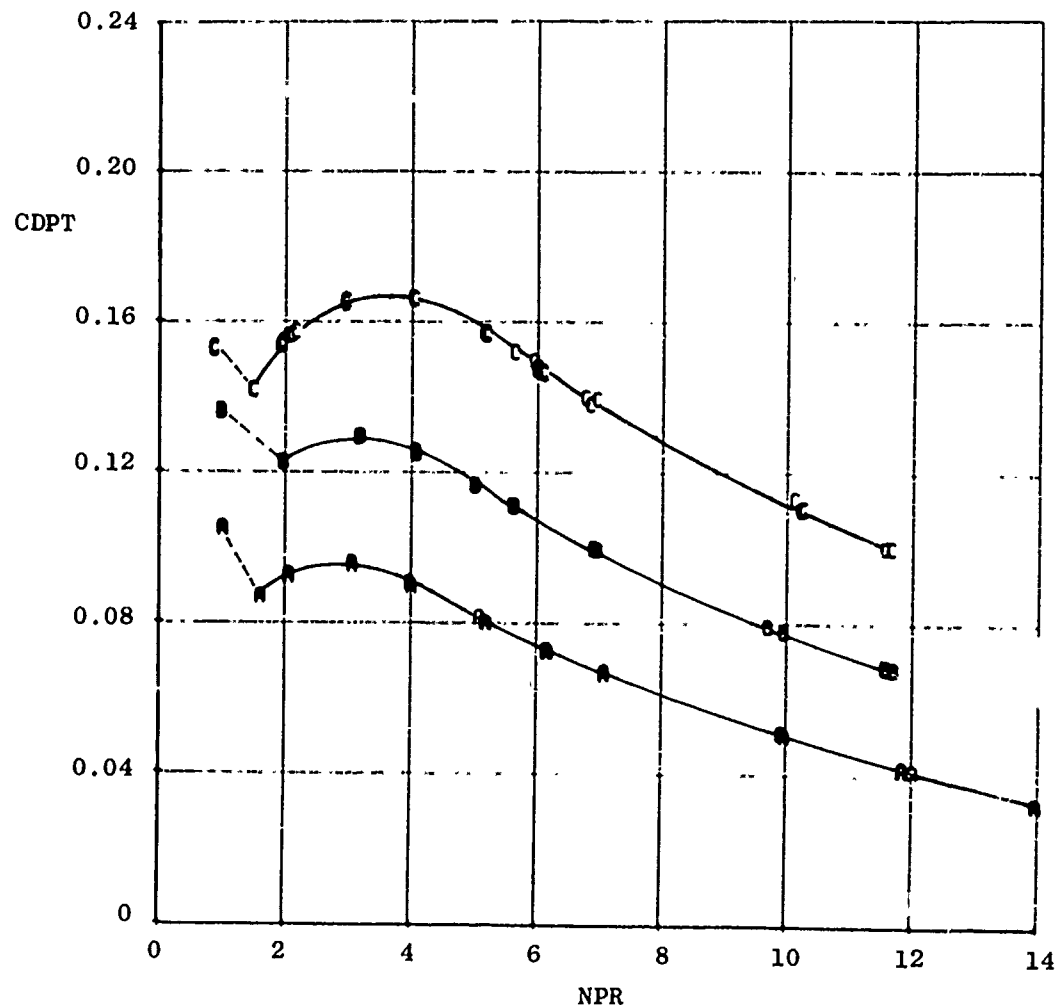
d. $M_{\infty} = 0.95$
Figure 12. Continued.

| <u>Sym</u> | <u>Config, deg</u> | <u>PN/TP</u> |
|------------|--------------------|--------------|
| A | 10 | 6502 |
| B | 15 | 3801 |
| C | 25 | 9801 |



e. $M_{\infty} = 1.10$
 Figure 12. Continued.

| <u>Sym</u> | <u>Config, deg</u> | <u>PN/TP</u> |
|------------|--------------------|--------------|
| A | 10 | 7501 |
| B | 15 | 4701 |
| C | 25 | 9901 |



f. $M_{\infty} = 1.50$
Figure 12. Concluded.

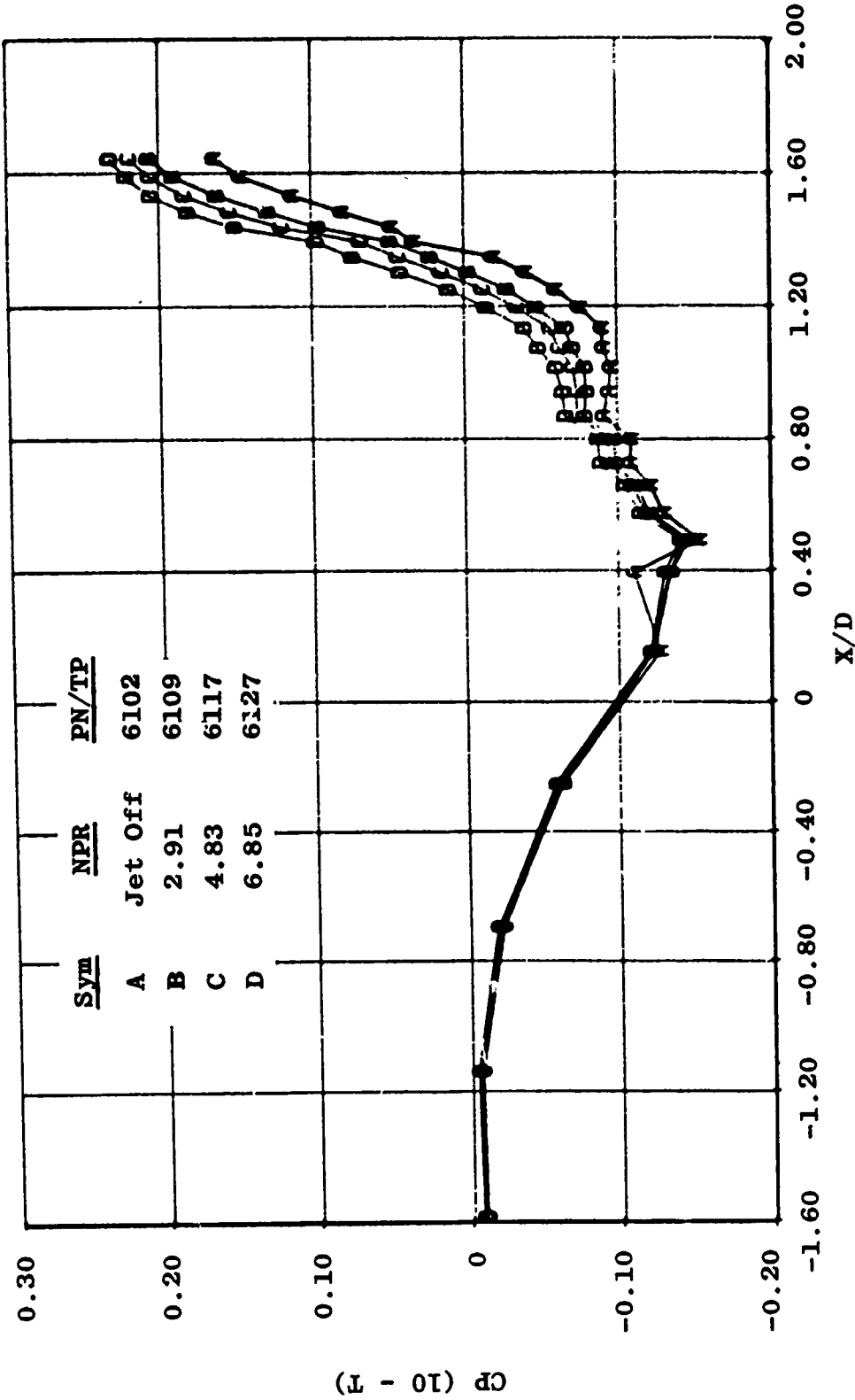
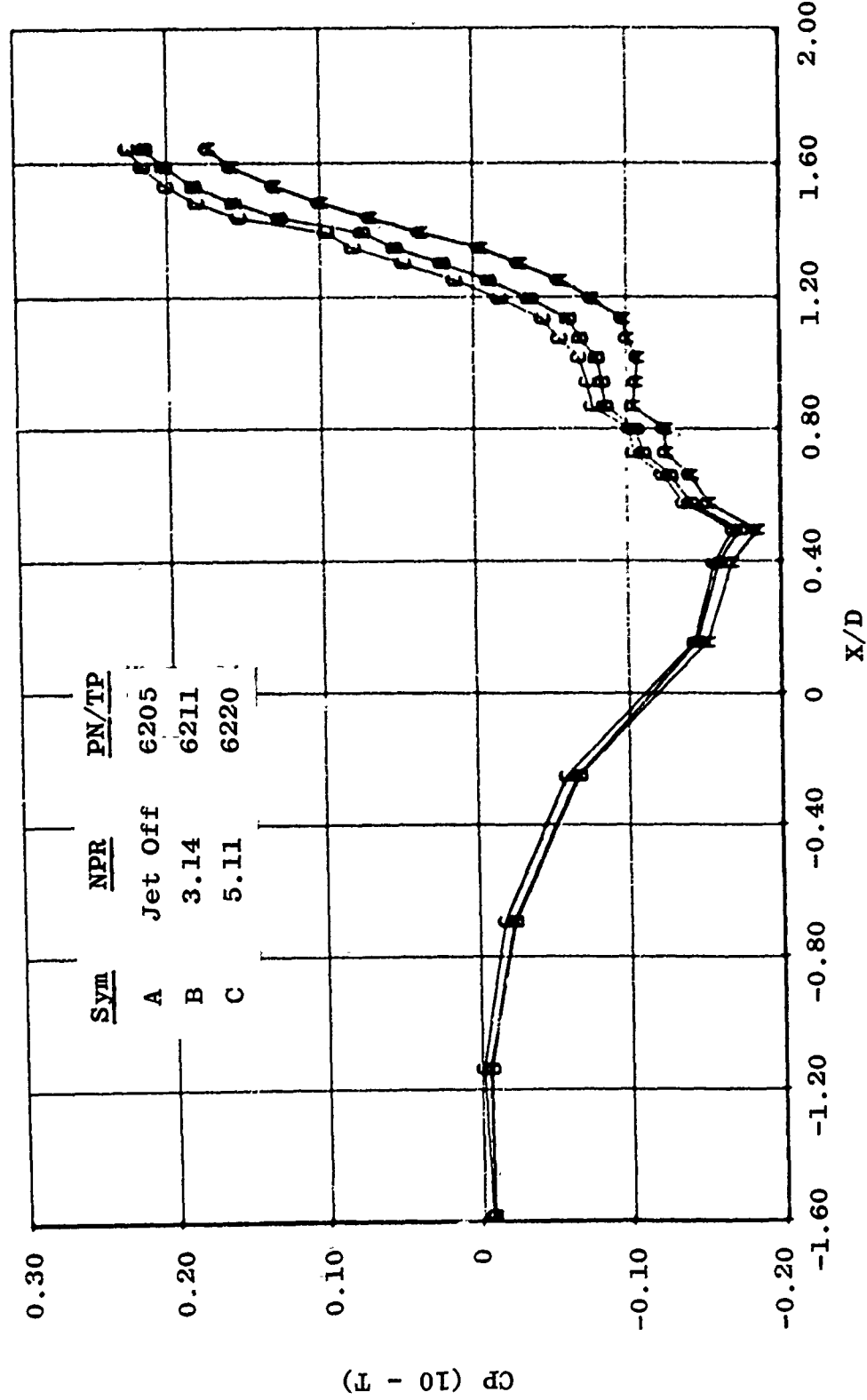
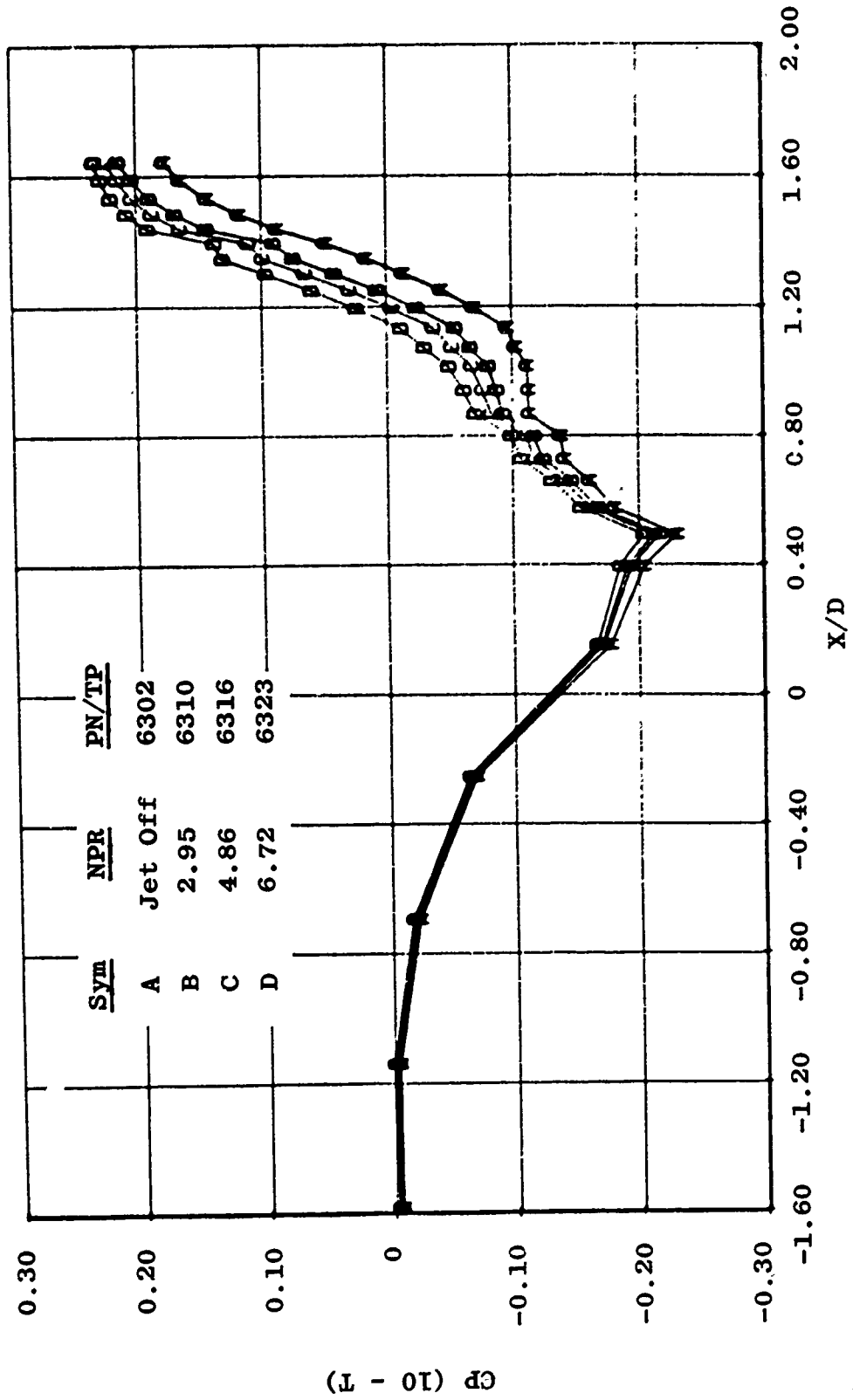


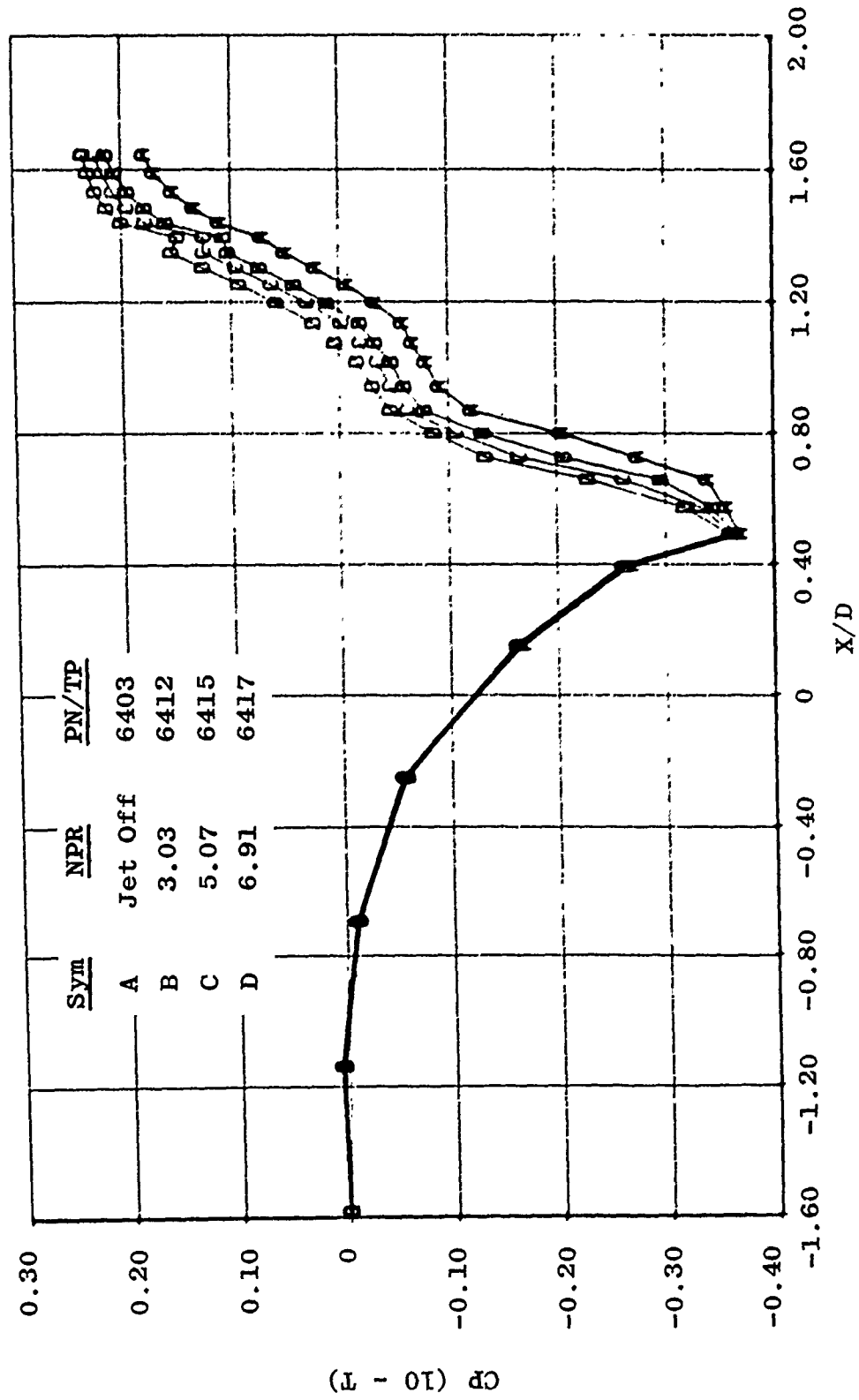
Figure 13. Nozzle pressure ratio effects on 10-deg boattail pressure distribution.
 a. $M_\infty = 0.60$



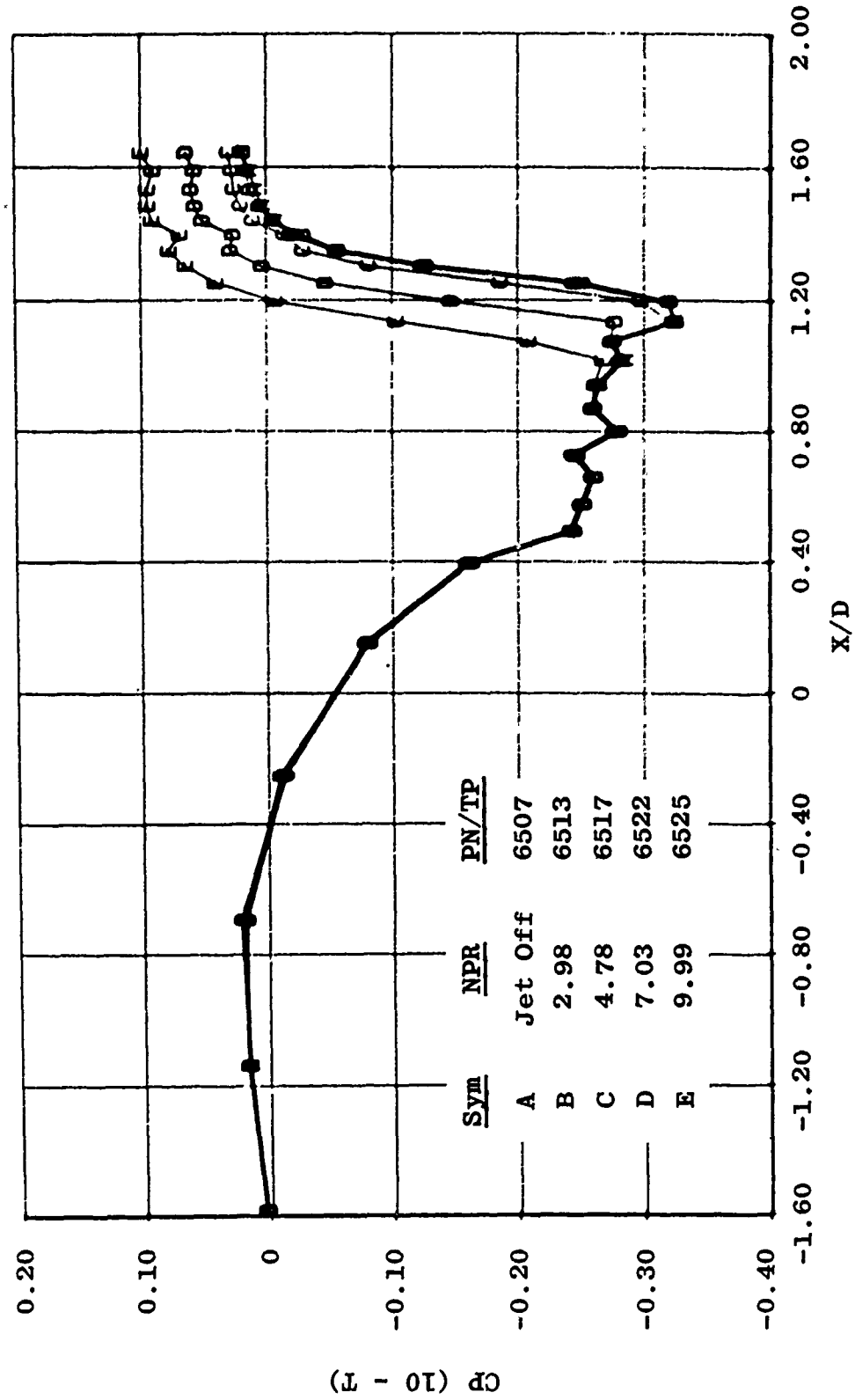
b. $M_\infty = 0.80$
Figure 13. Continued.



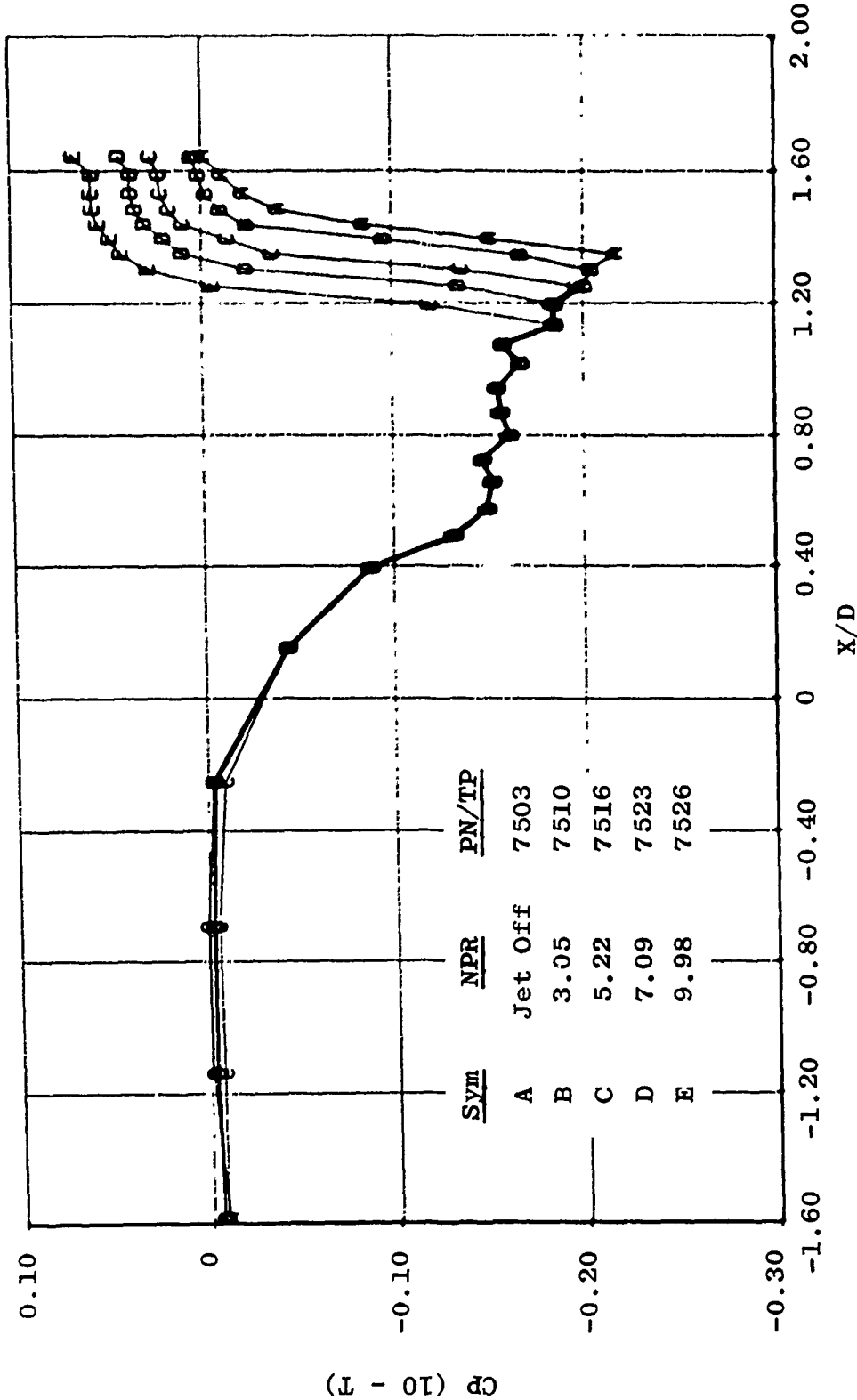
c. $M_{\infty} = 0.90$
Figure 13. Continued.



d. $M_{\infty} = 0.95$
Figure 13. Continued.



e. $M_\infty = 1.10$
Figure 13. Continued.



f. $M_{\infty} = 1.50$
Figure 13. Concluded.

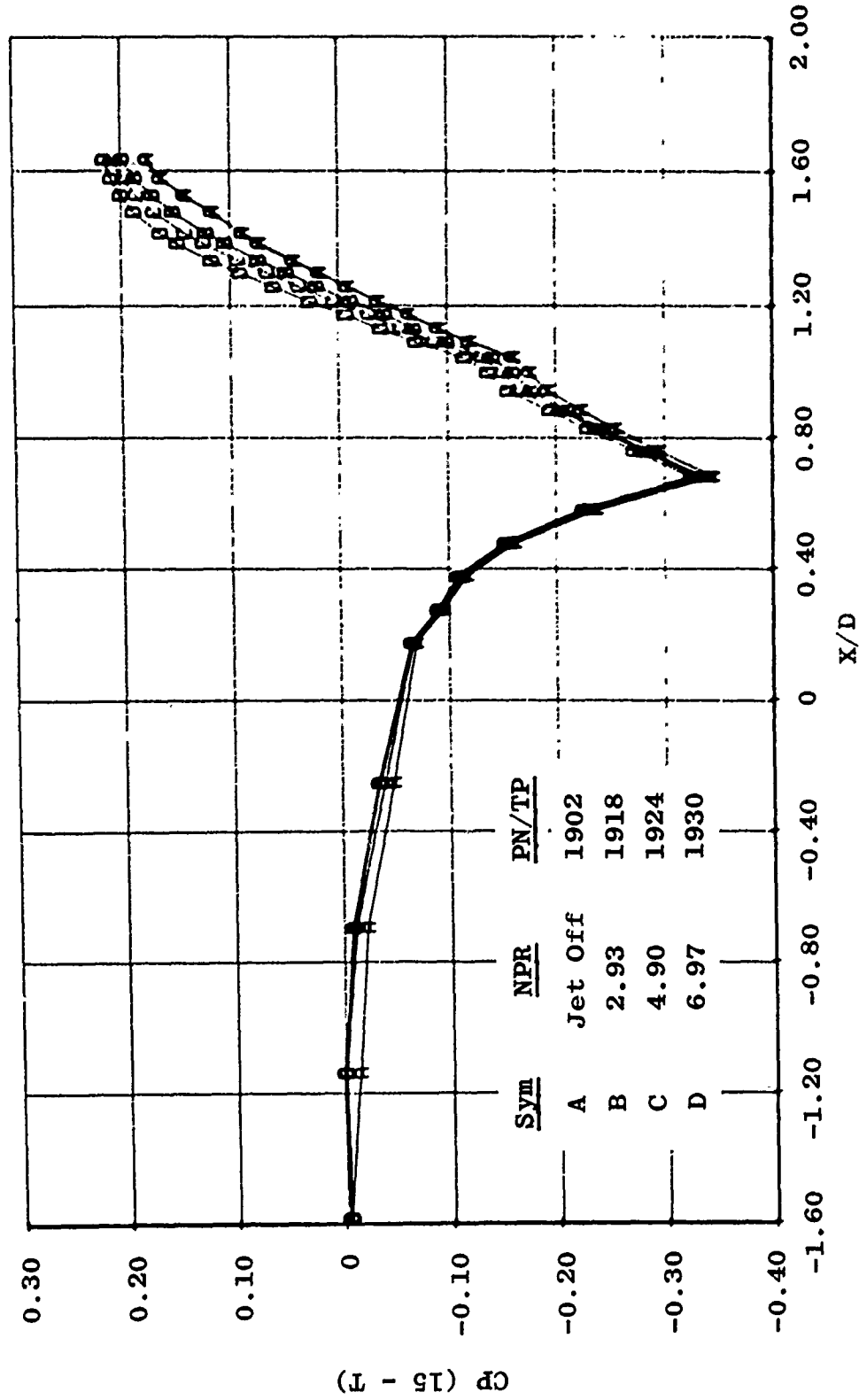
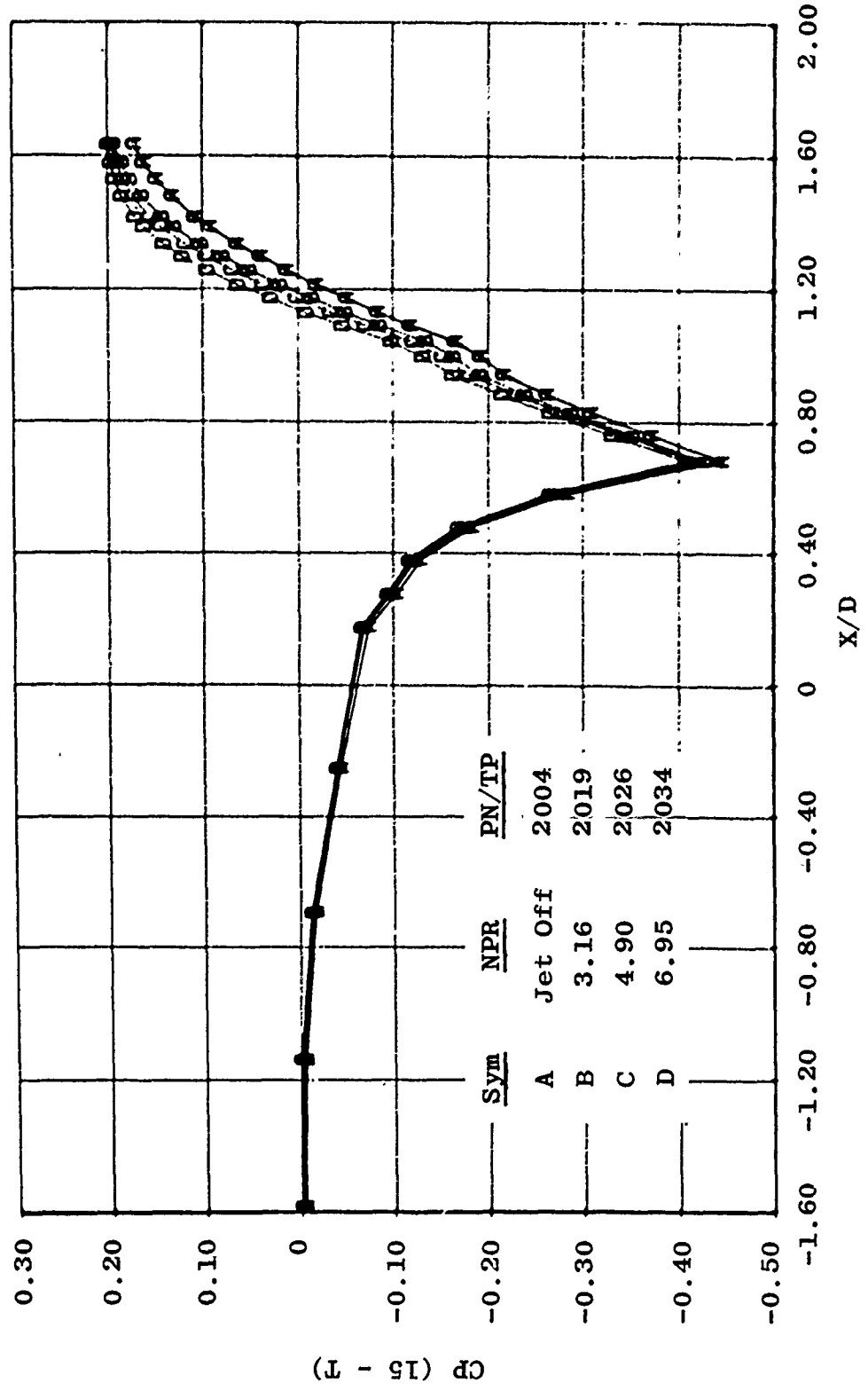
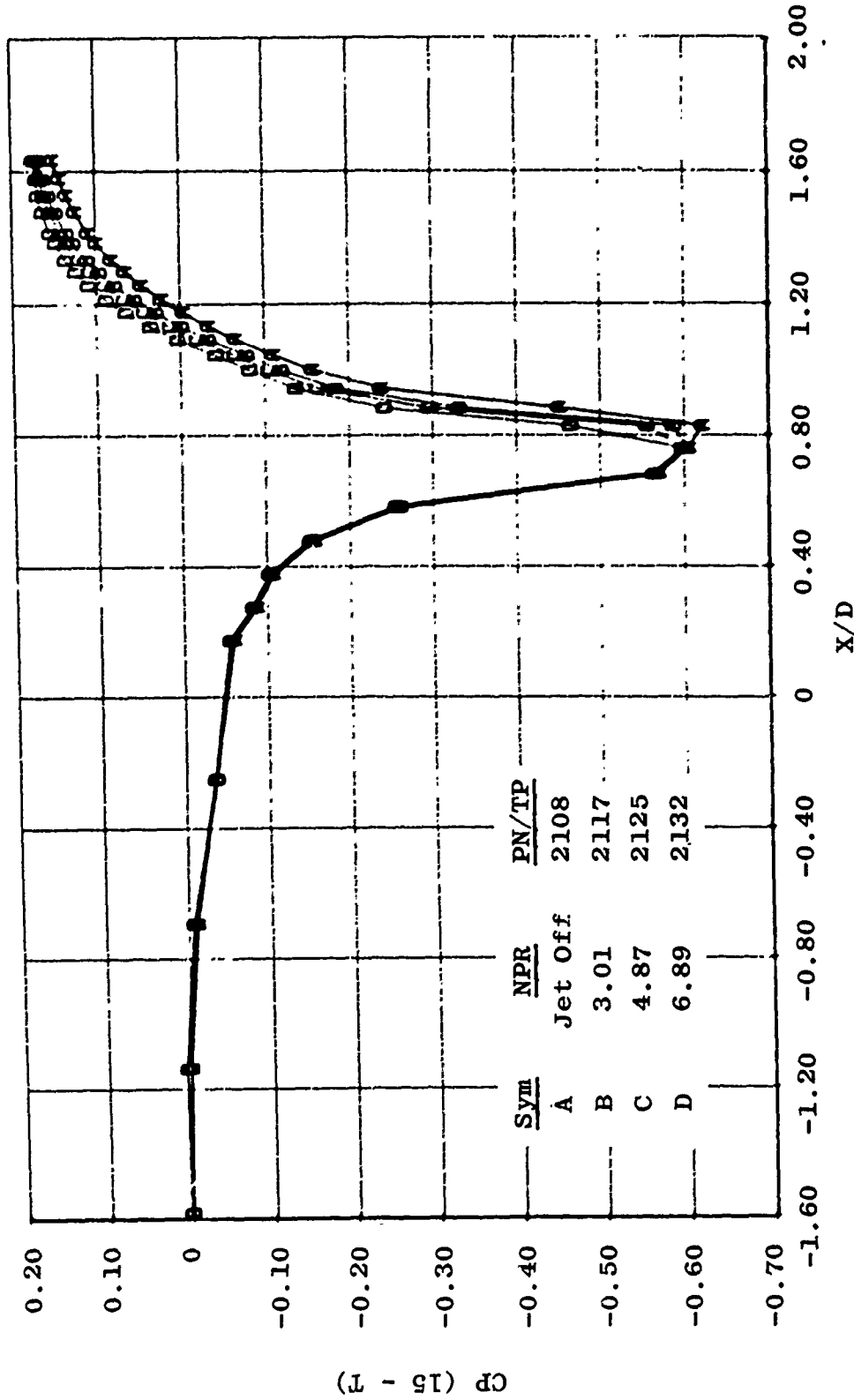


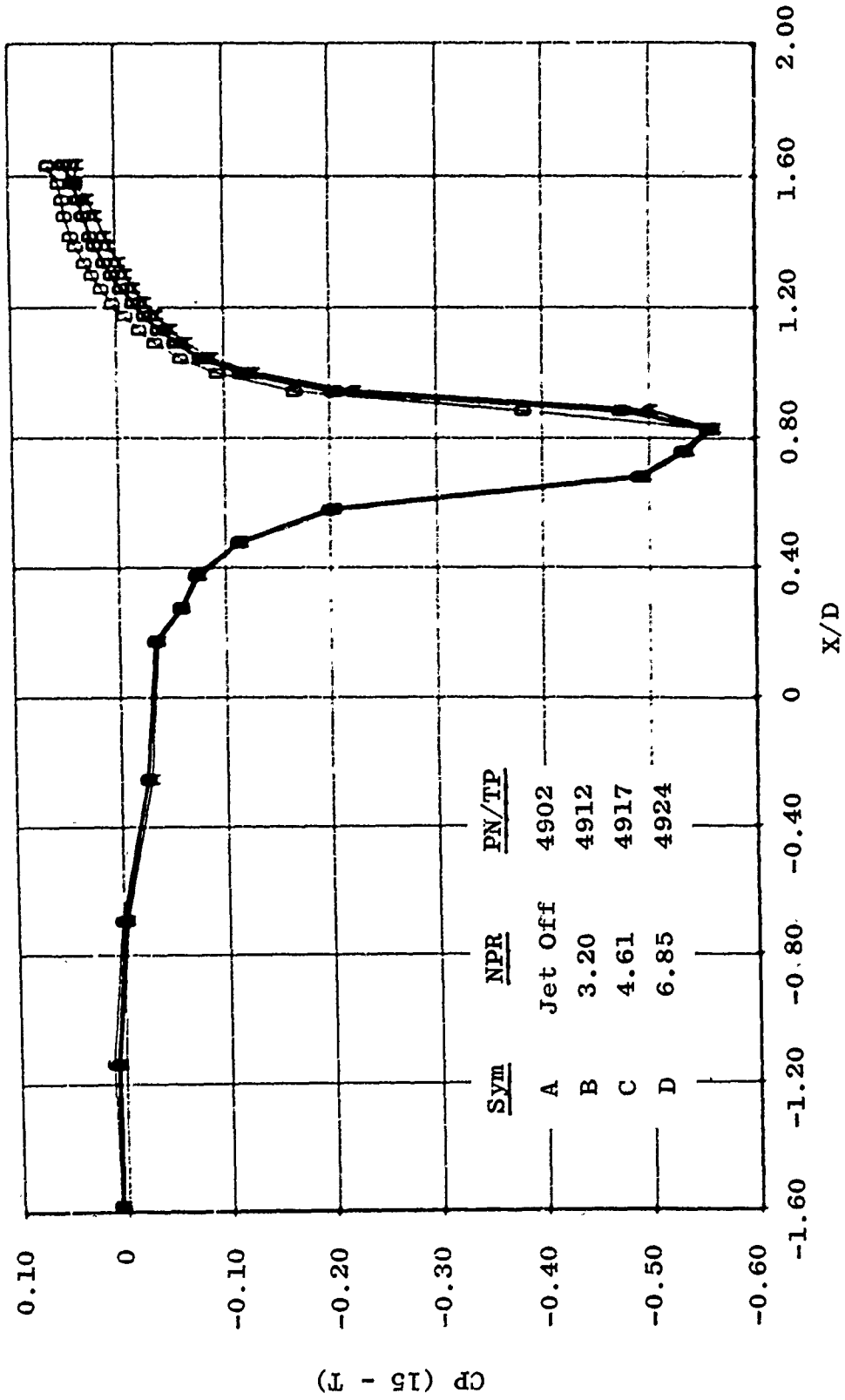
Figure 14. Nozzle pressure ratio effects on 15-deg boattail pressure distribution.
 a. $M_{\infty} = 0.60$



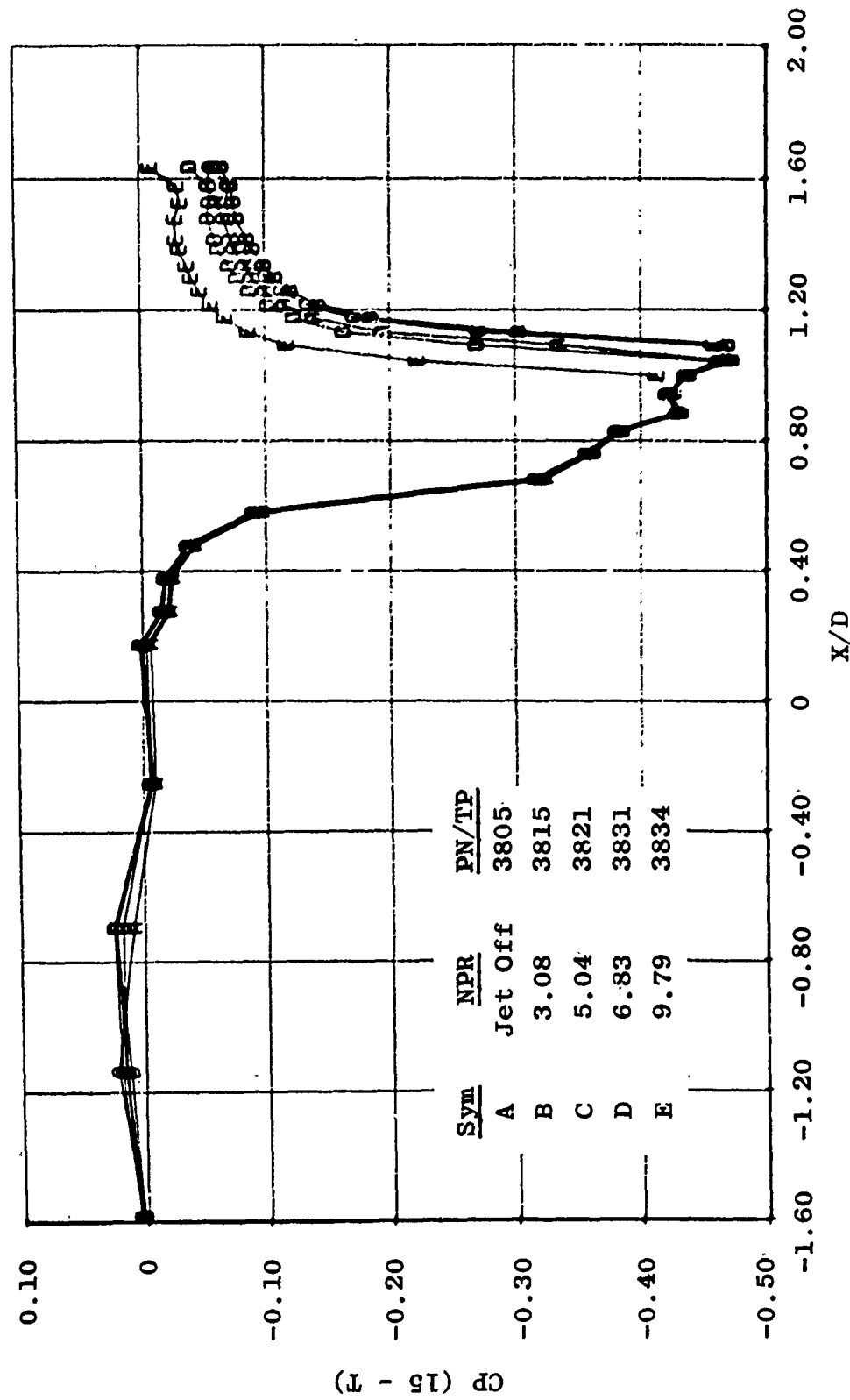
b. $M_\infty = 0.86$
Figure 14. Continued.



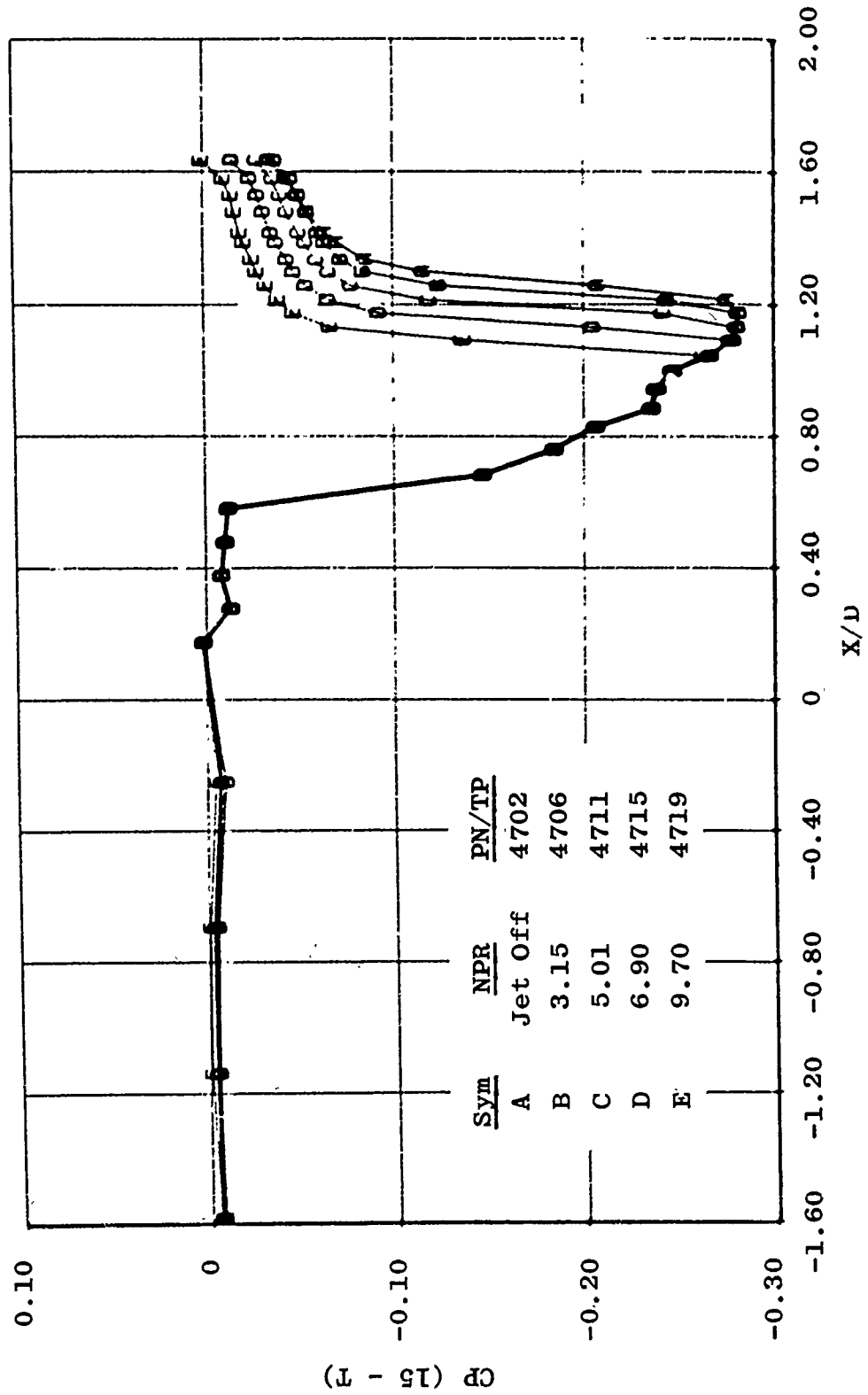
c. $M_{\infty} = 0.90$
Figure 14. Continued.



d. $M_{\infty} = 0.95$
 Figure 14. Continued.



e. $M_{\infty} = 1.10$
Figure 14. Continued.



f. $M_{\infty} = 1.50$
Figure 14. Concluded.

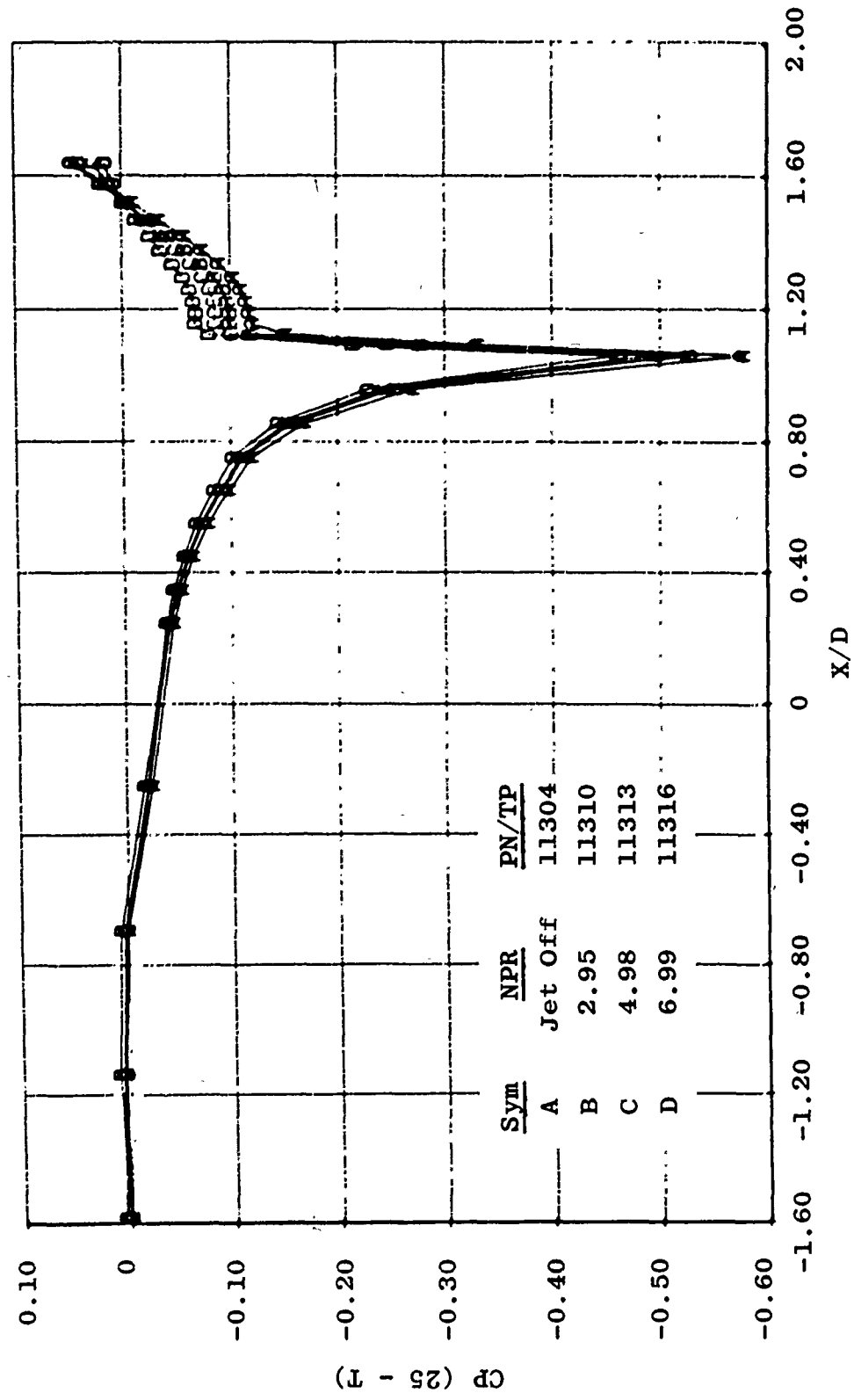
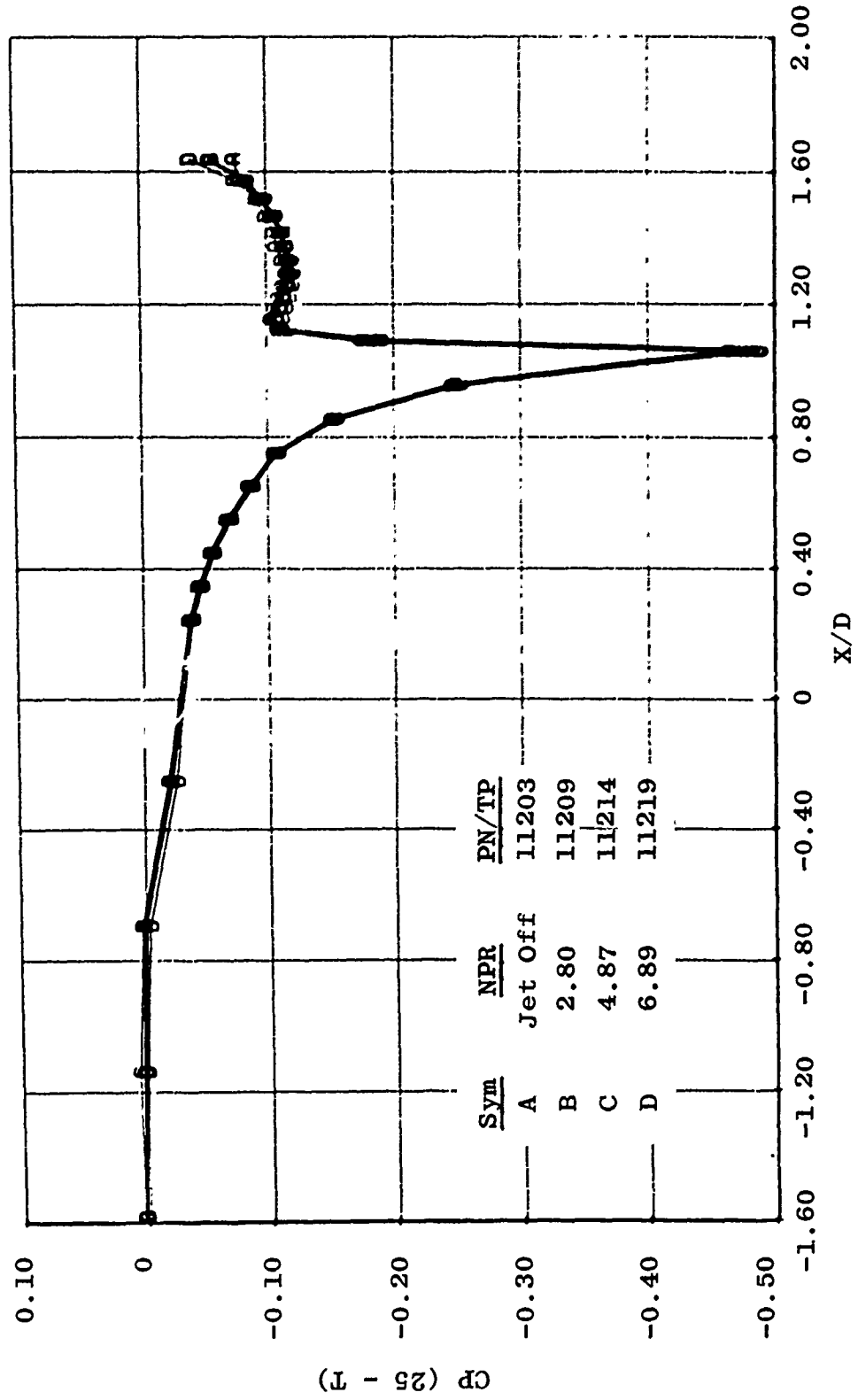
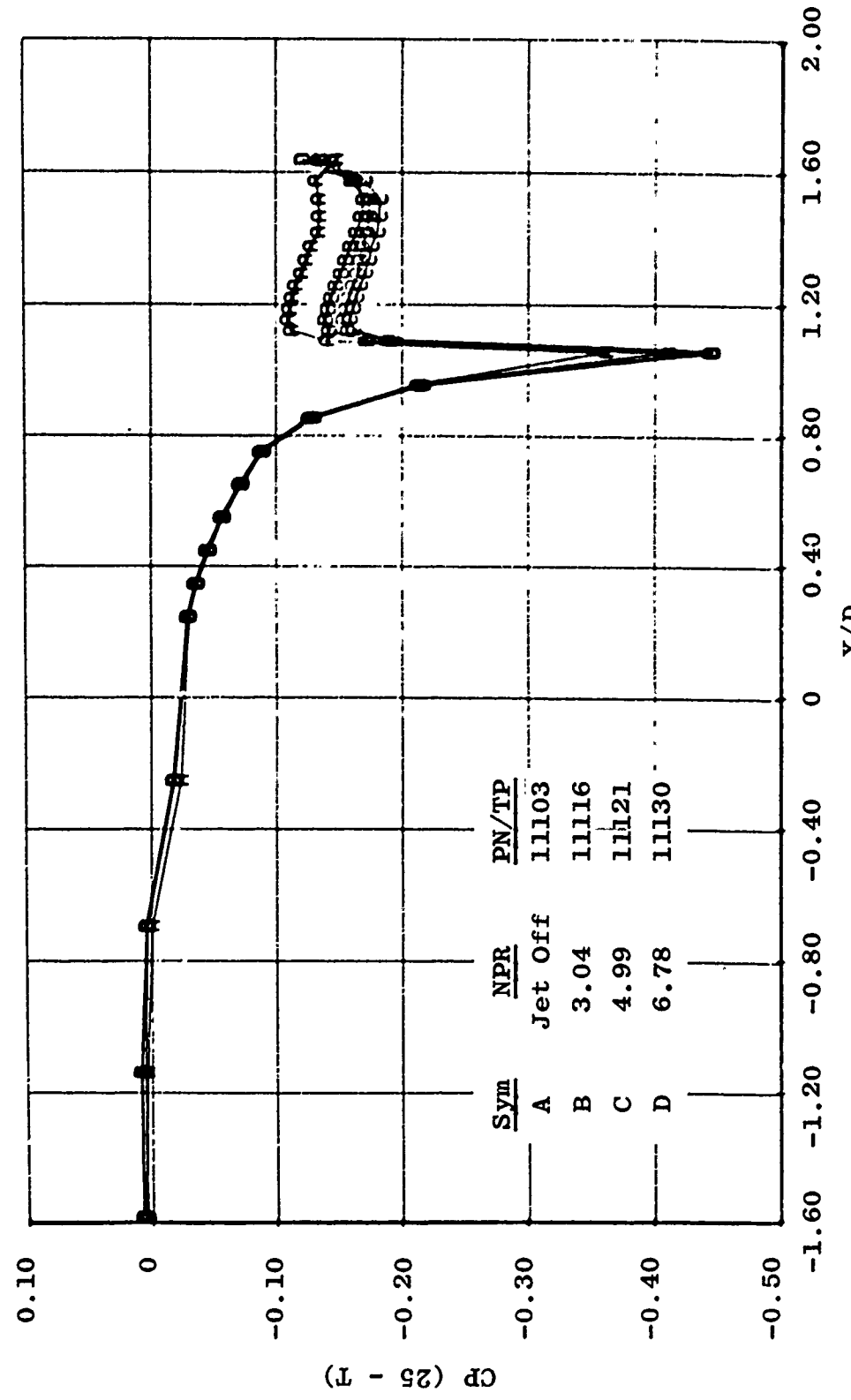


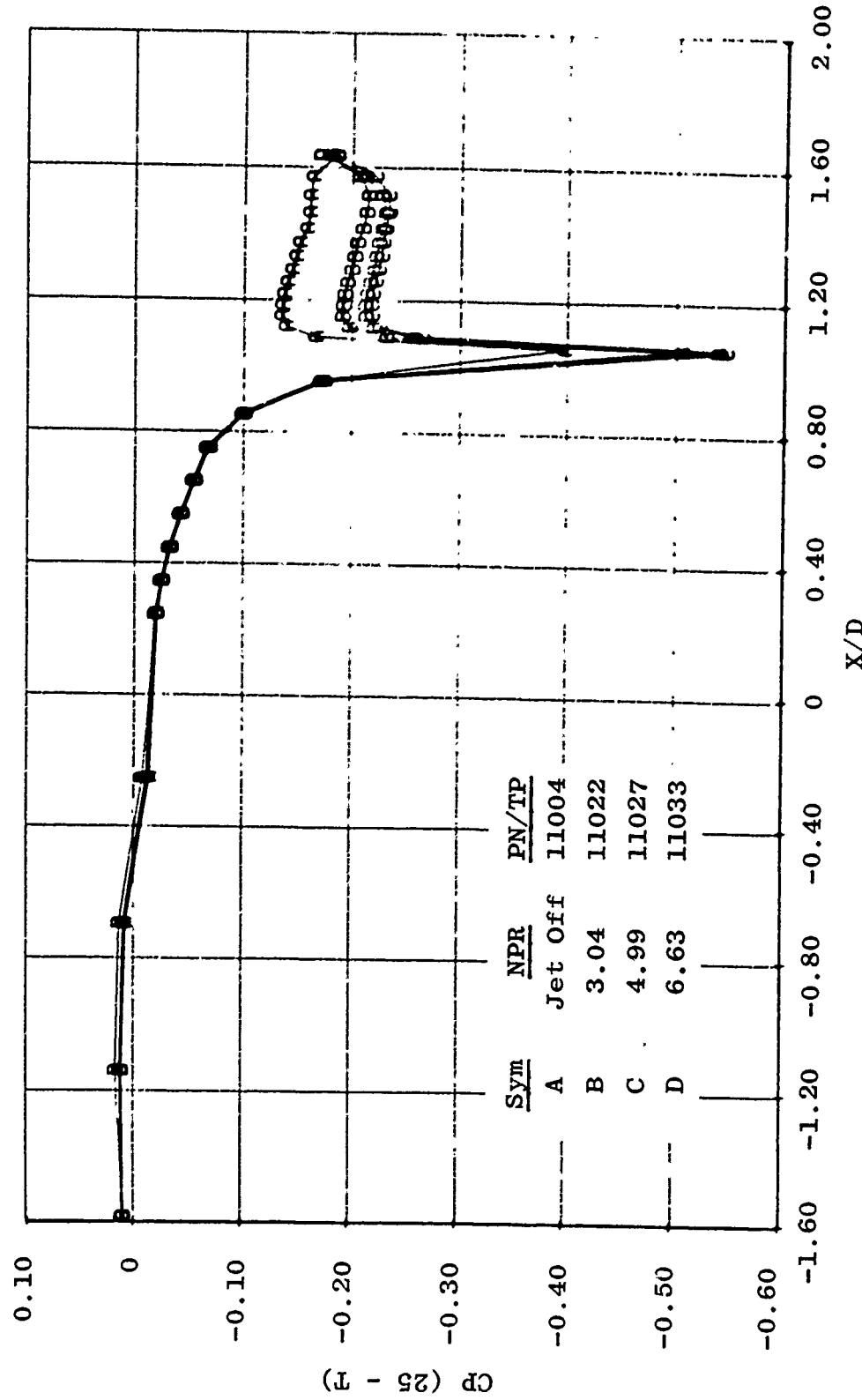
Figure 15. Nozzle pressure ratio effects on 25-deg boat-tail pressure distribution.
 a. $M_\infty = 0.60$



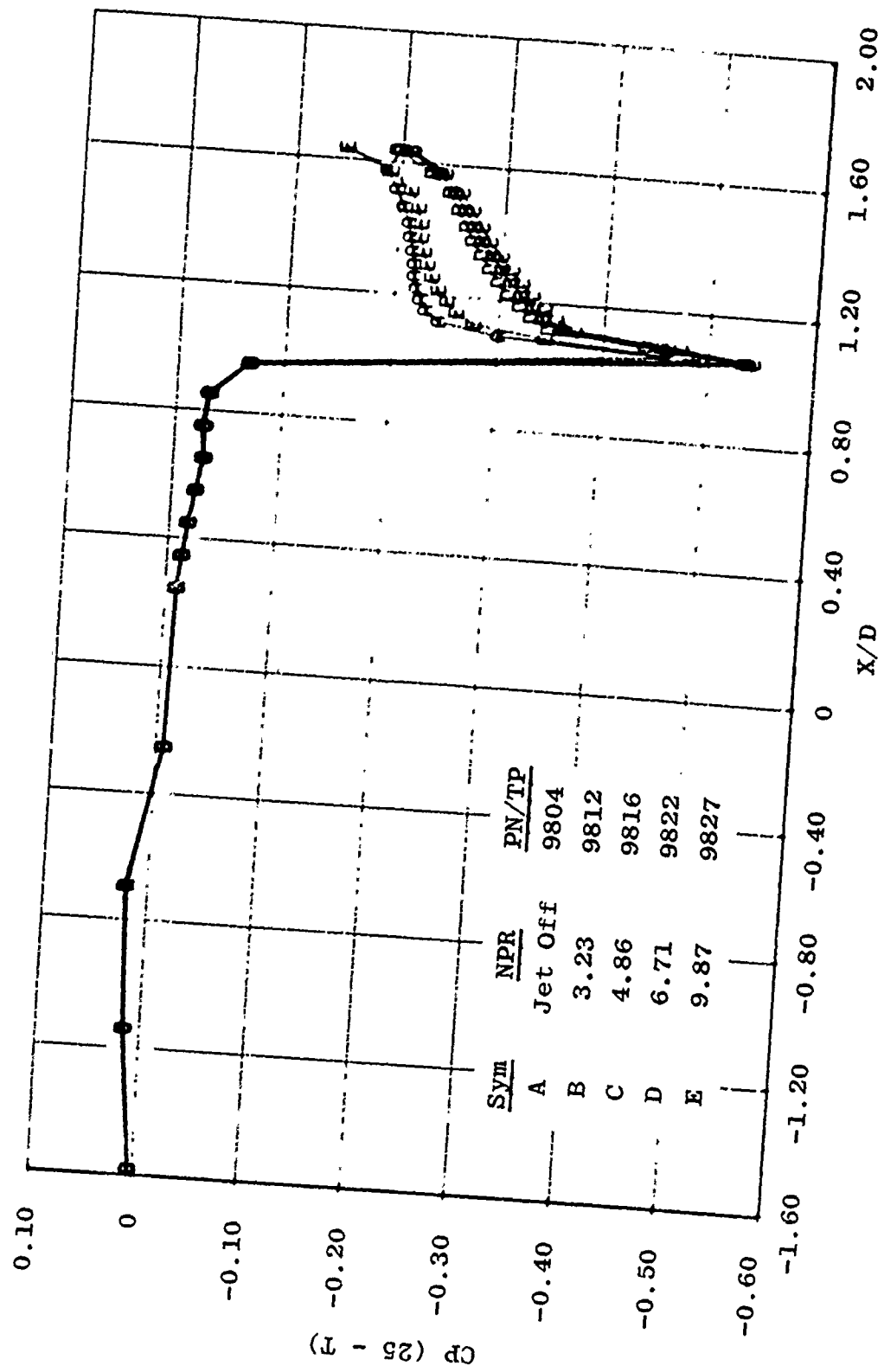
b. $M_{\infty} = 0.80$
Figure 15. Continued.



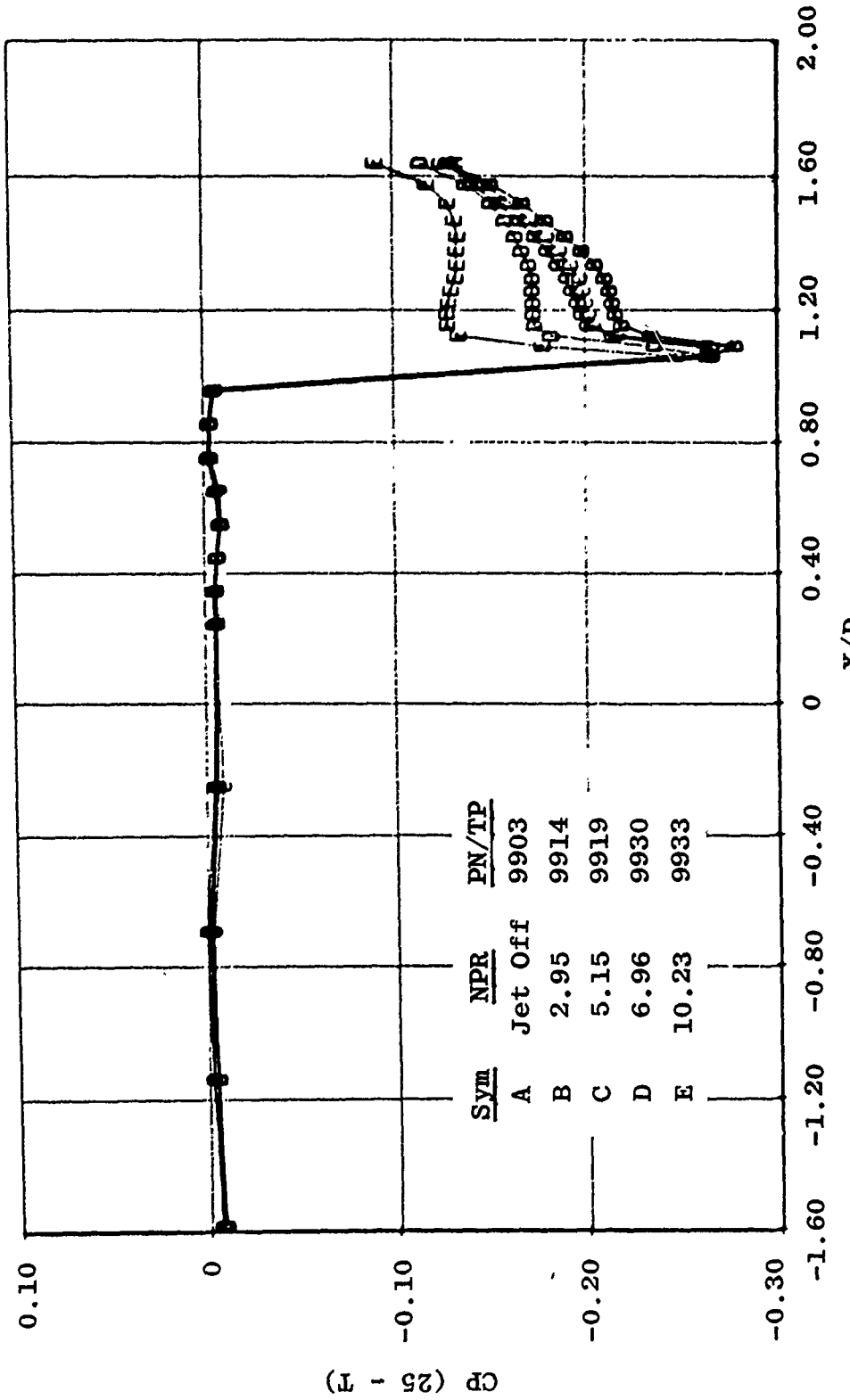
c. $M_{\infty} = 0.90$
Figure 15. Continued.



d. $M_\infty = 0.95$
Figure 15. Continued.



e. $M_\infty = 1.10$
Figure 15. Continued.



f. $M_{\infty} = 1.50$
Figure 15. Concluded.



10-deg boattail, $NPR = 6.83$



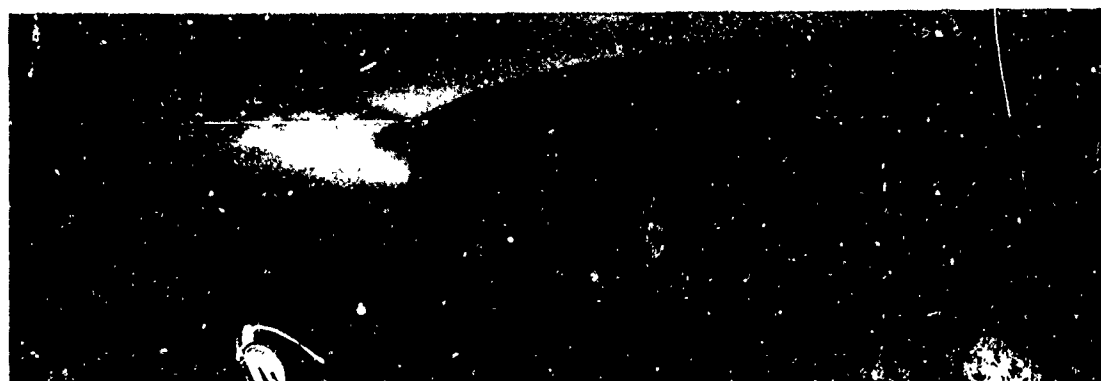
15-deg boattail, $NPR = 5.7$



25-deg boattail $NPR = 6.09$

a. $M_\infty = 0.60$

Figure 16. Schlieren photographs of 10-, 15-, and 25-deg boattail geometries at selected Mach numbers.



10-deg boattail, $NPR = 6.87$



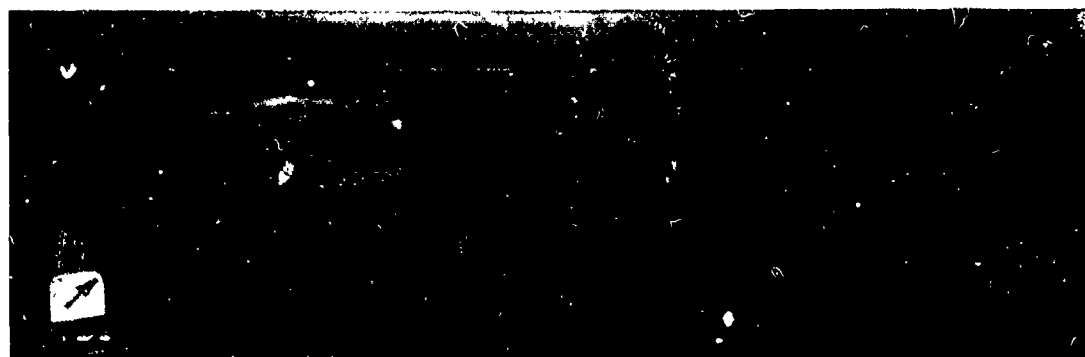
15-deg boattail $NPR = 1.99$



25-deg boattail, $NPR = 2.09$

b. $M_\infty = 0.95$

Figure 16. Continued.



10-deg boattail, $NPR = 15.86$



15-deg boattail, $NPR = 6.91$



25-deg boattail, $NPR = 5.2$

c. $M_\infty = 1.50$
Figure 16. Concluded.

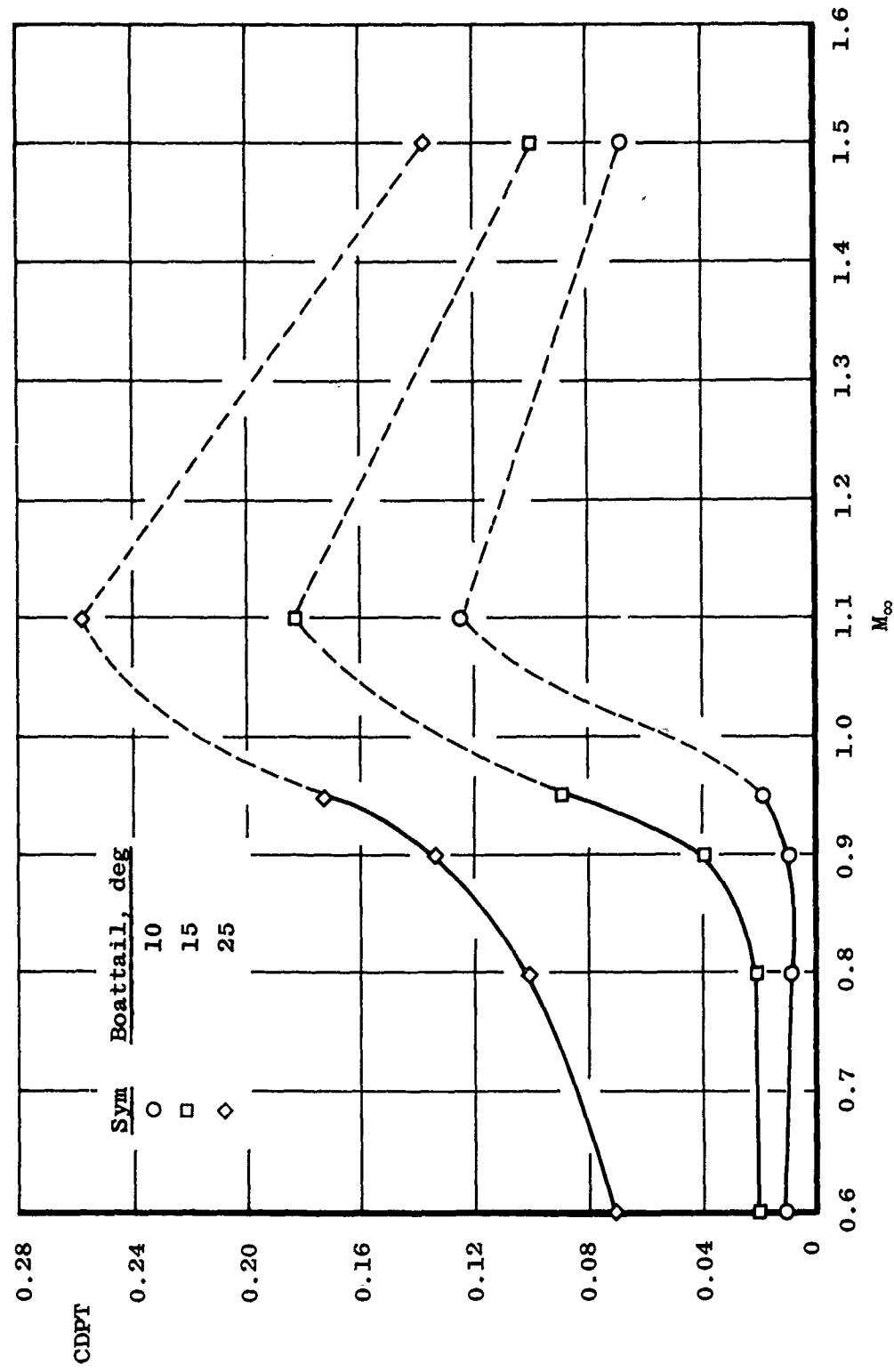


Figure 17. Variation of boattail pressure drag coefficient with Mach number.

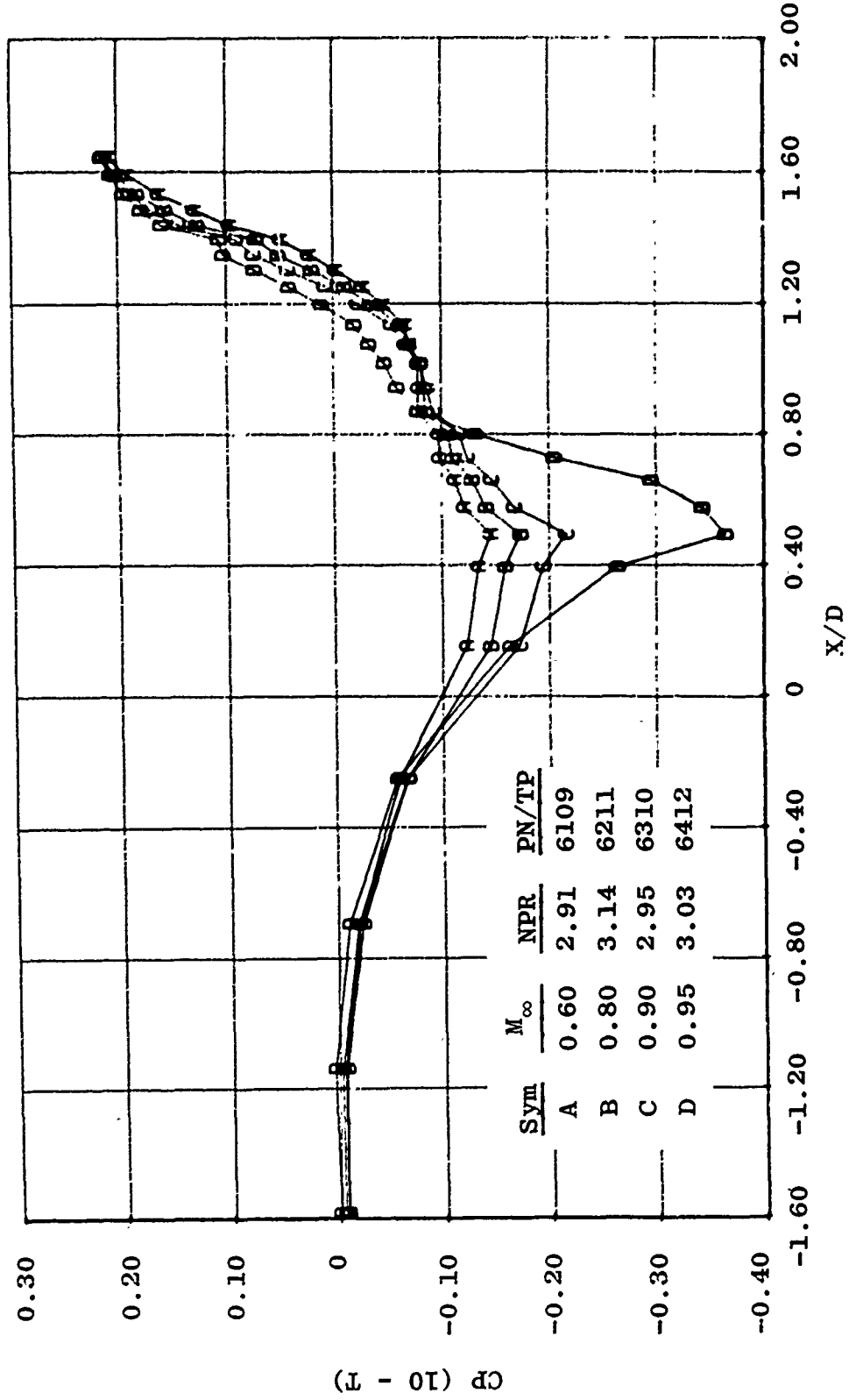
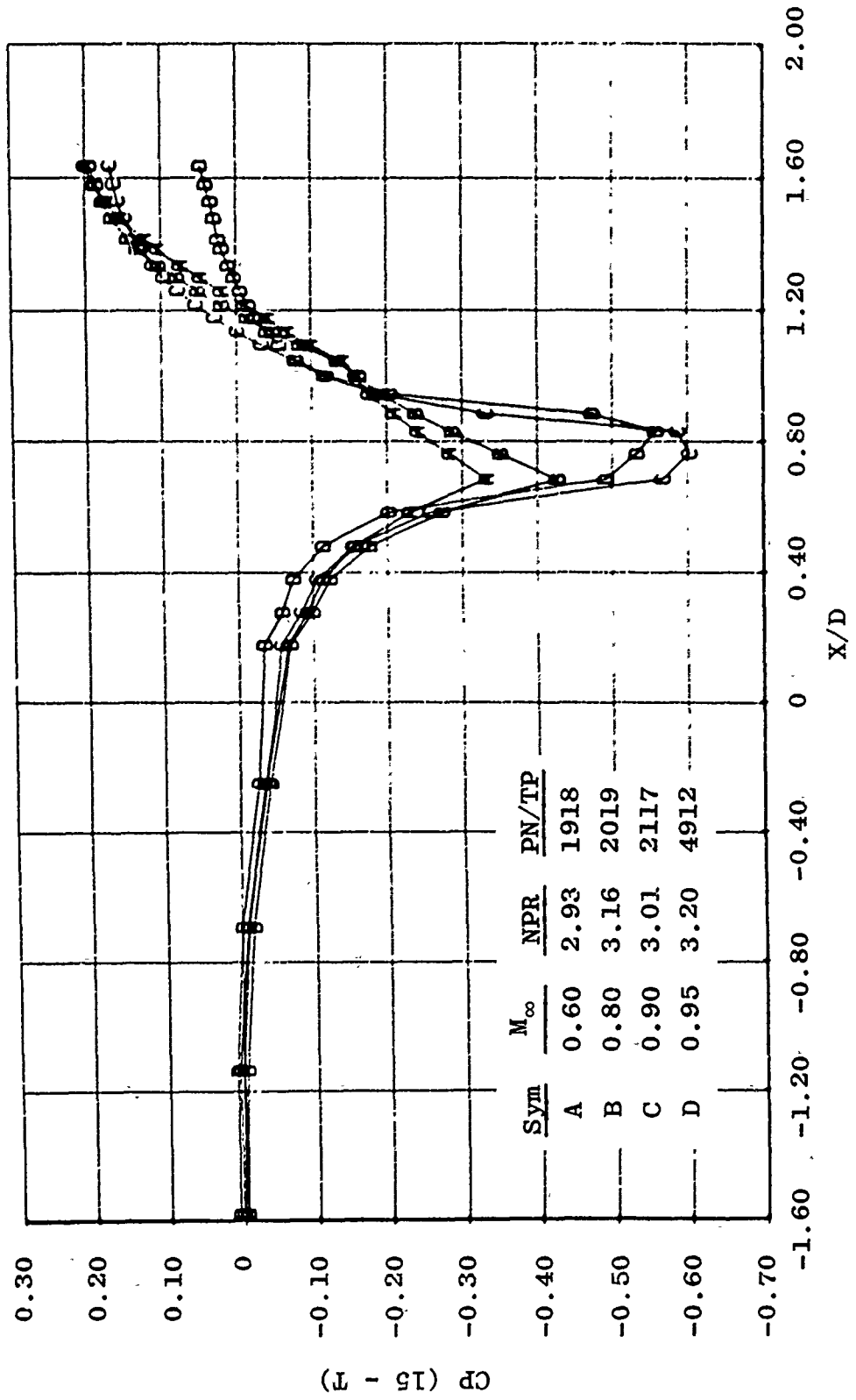
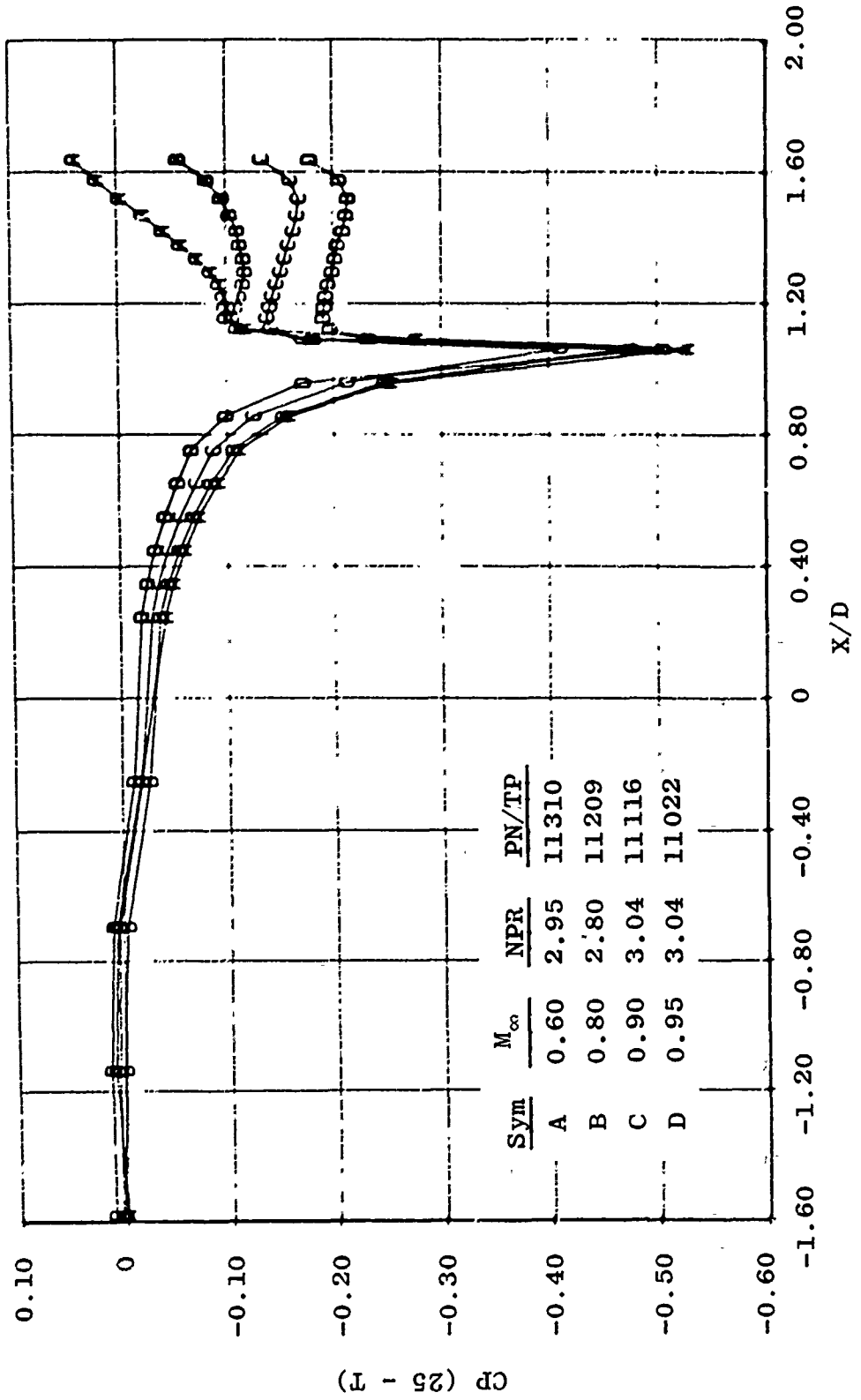


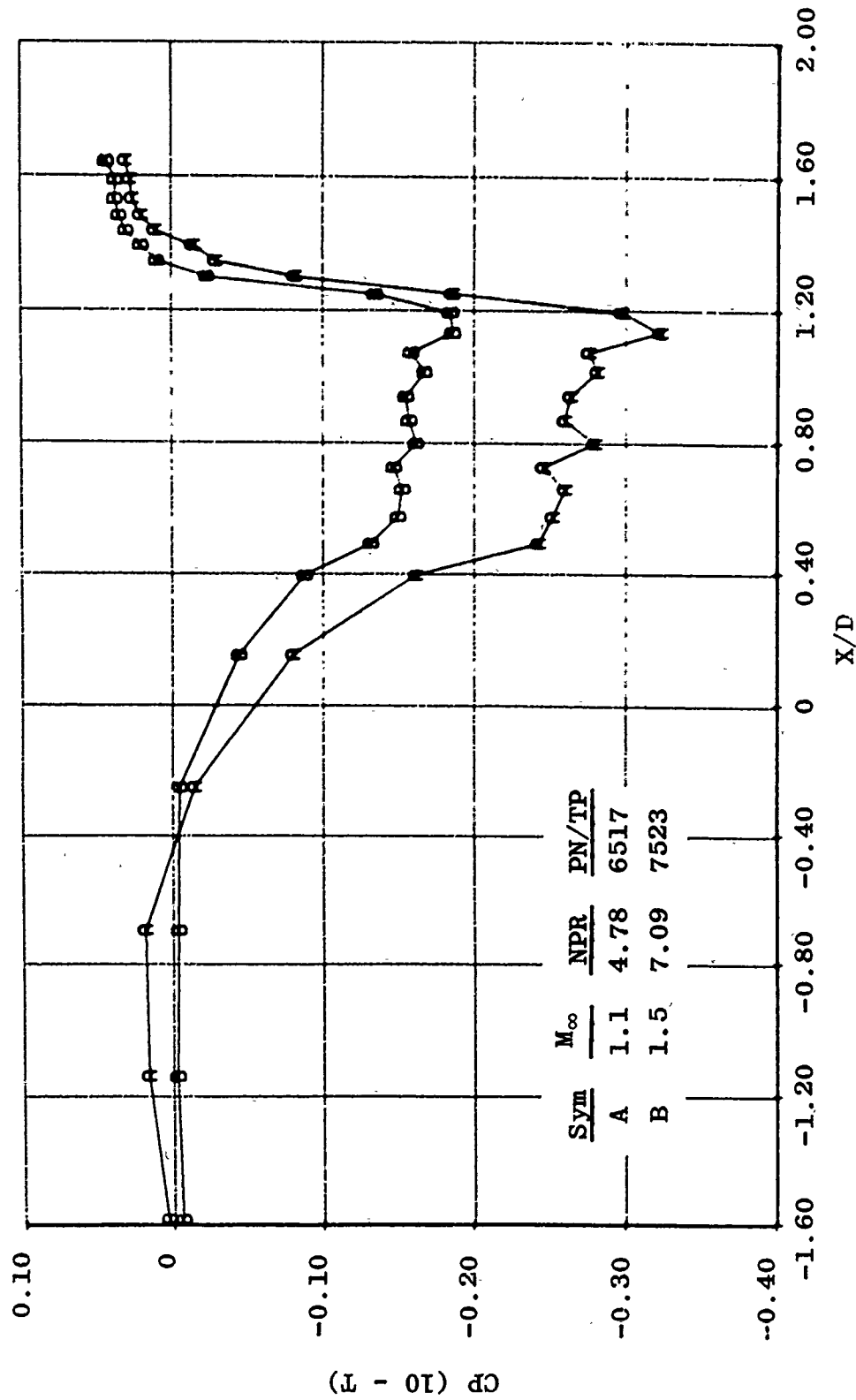
Figure 18. Subsonic Mach number effects on boattail pressure distribution.
a. 10-deg boattail



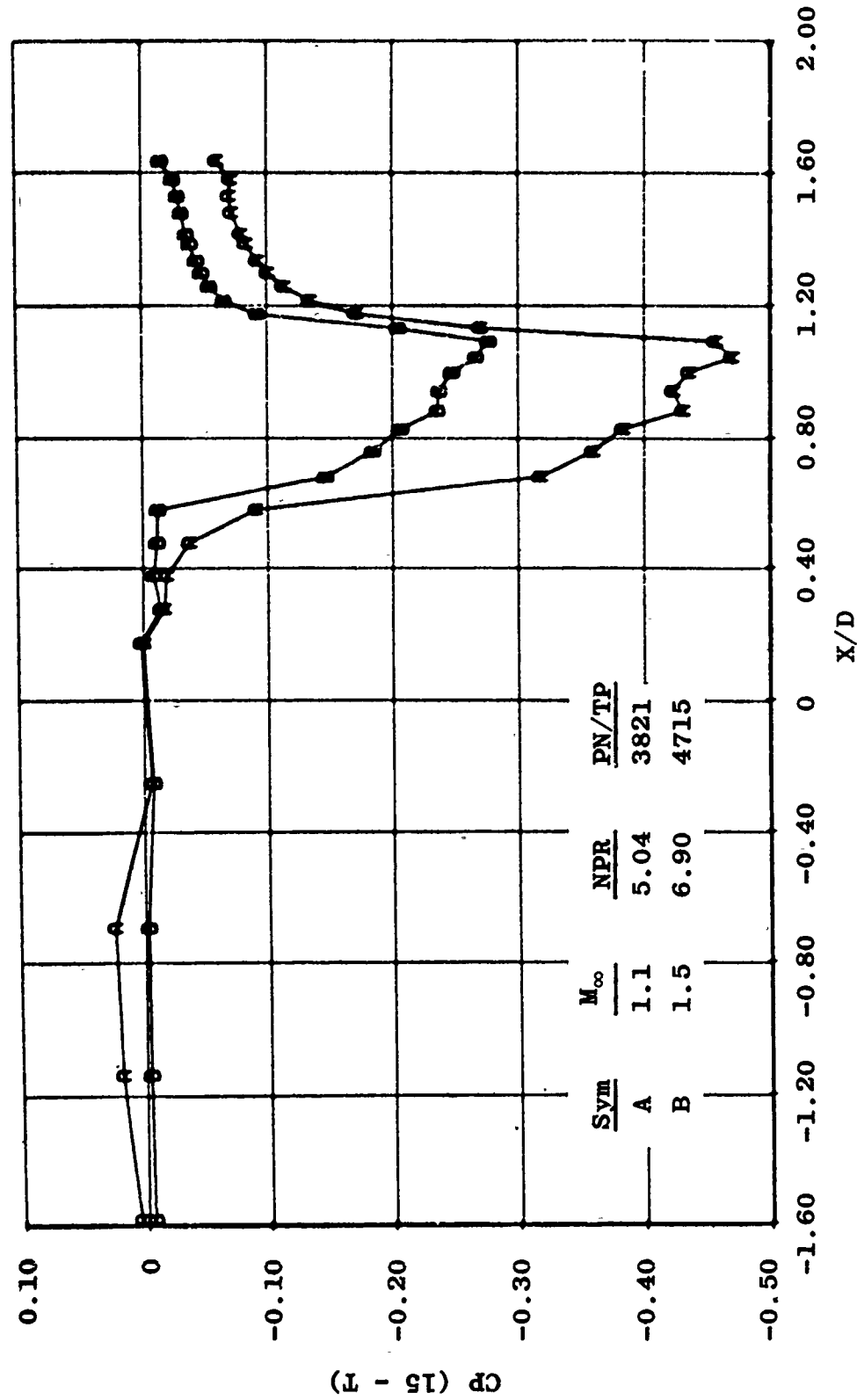
b. 15-deg boattail
Figure 18. Continued.



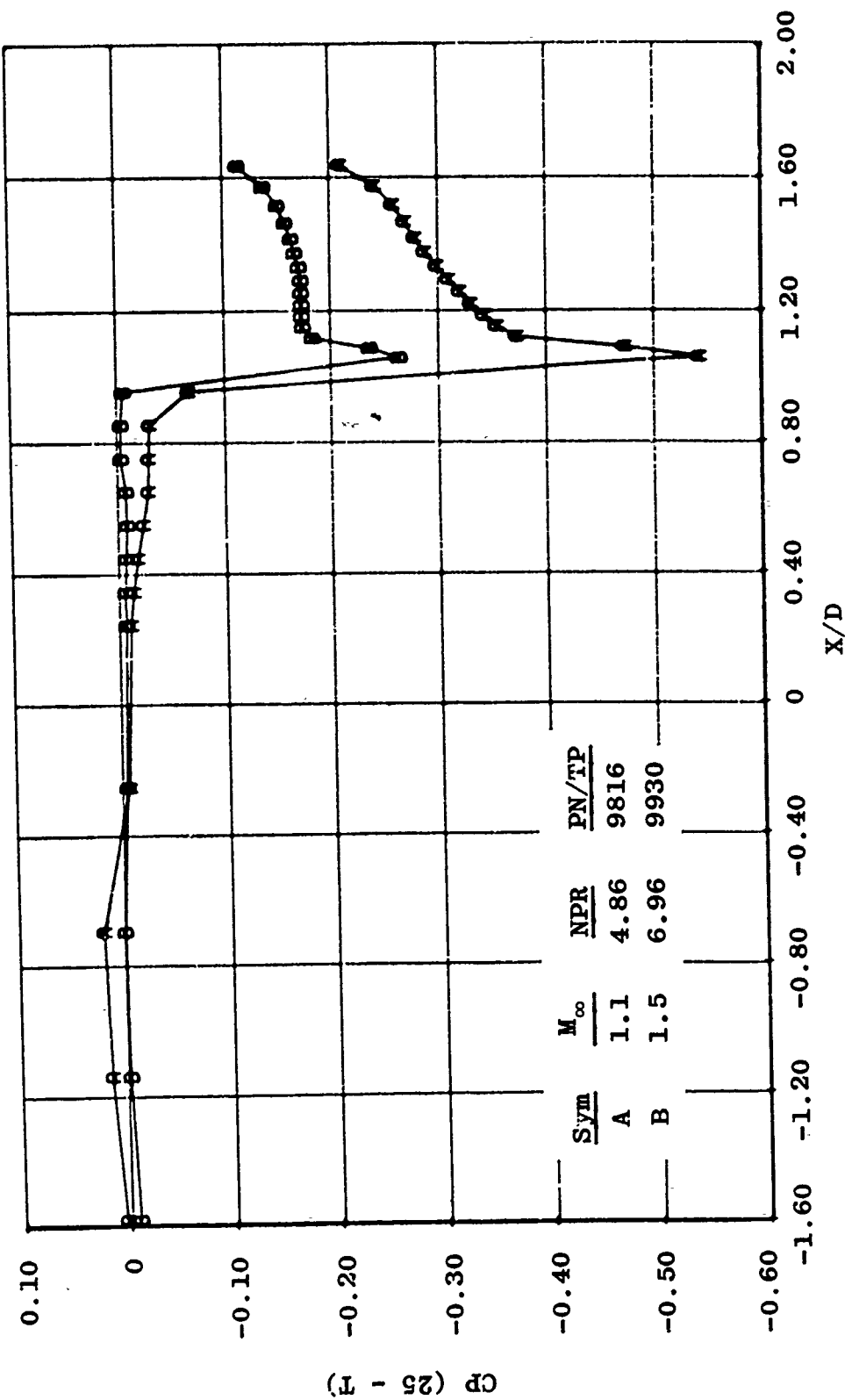
c. 25-deg boattail
Figure 18. Concluded.



a. 10-deg boattail
Figure 19. Supersonic Mach number effects on boattail pressure distribution.



b. 15-deg flat-tail
Figure 19. Continued.



c. 25-deg boattail
Figure 19. Concluded.

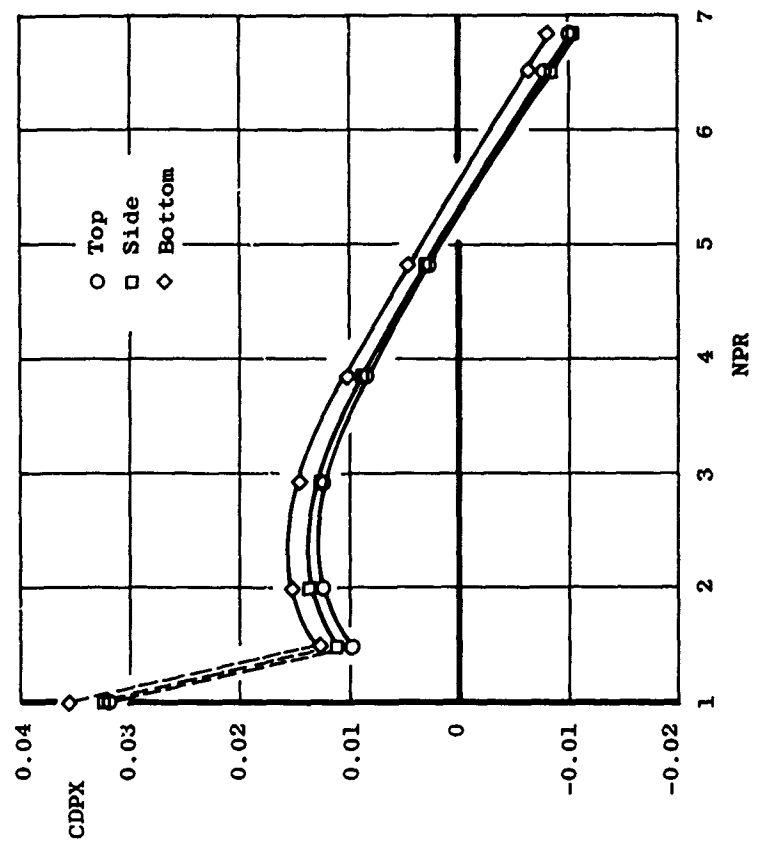
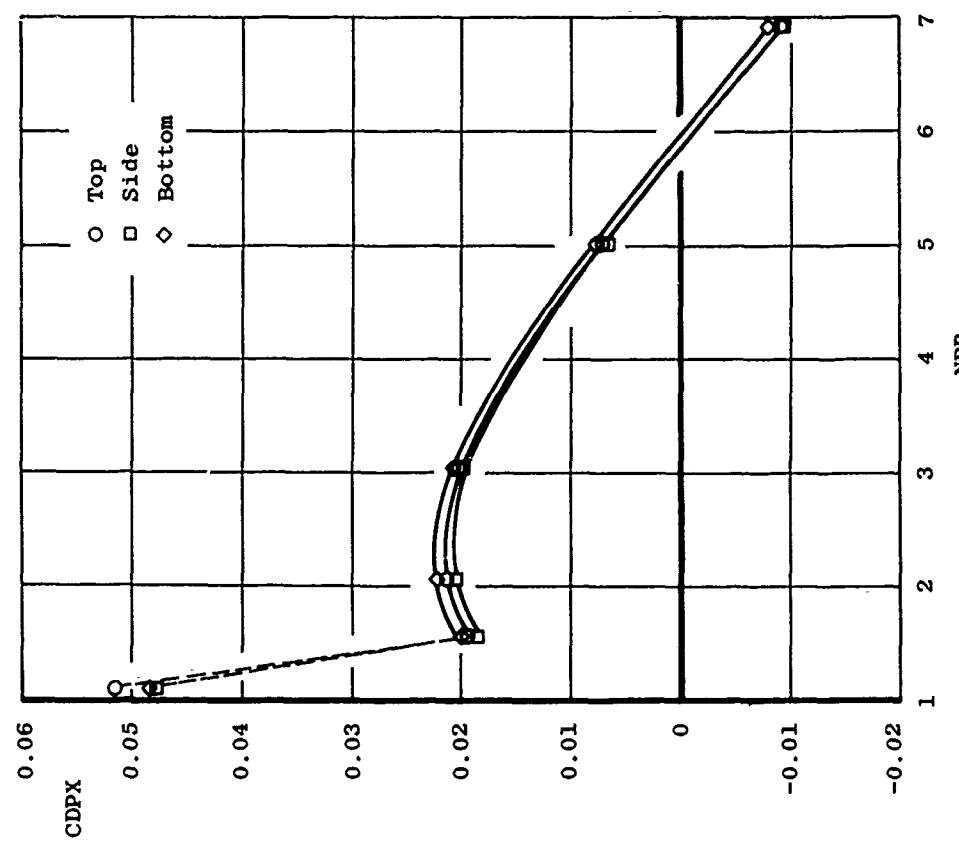
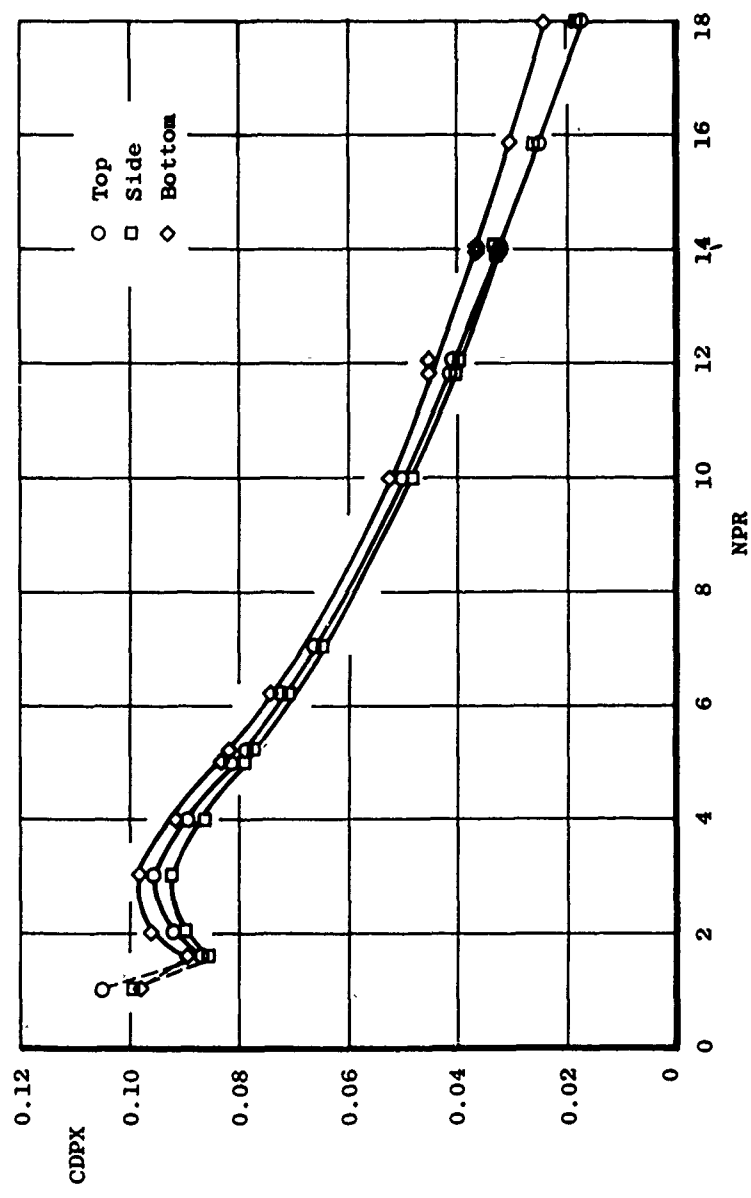


Figure 20. Flow asymmetry effects on 10-deg boat-tail pressure drag coefficient.
a. $M_{\infty} = 0.60$



b. $M_{\infty} = 0.95$
Figure 20. Continued.



c. $M_{\infty} = 1.50$
Figure 20. Concluded.

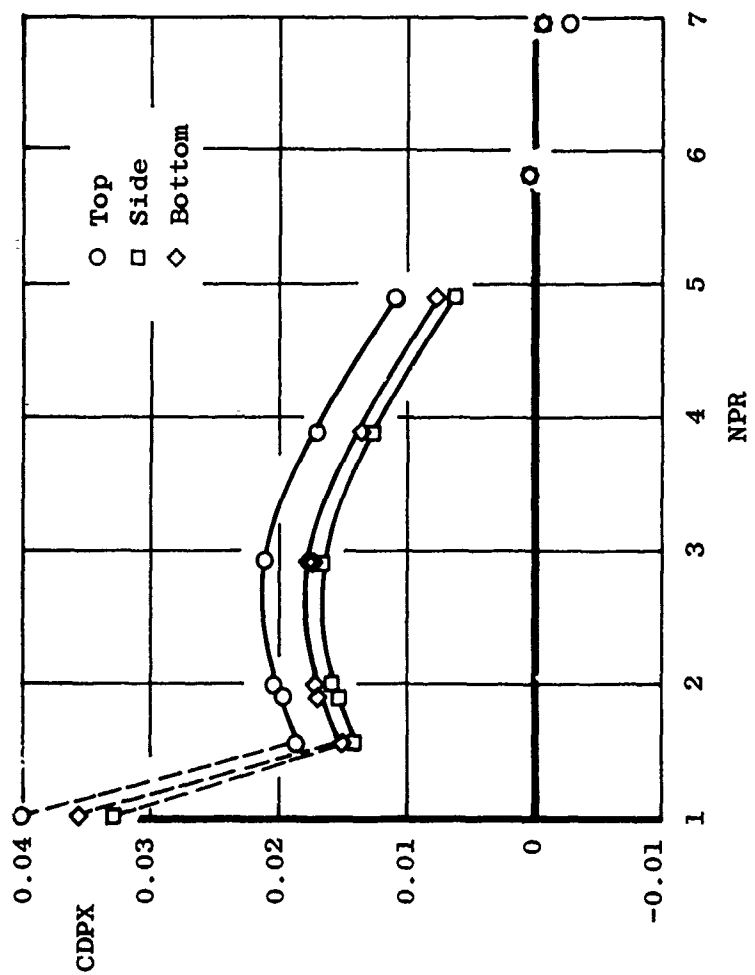
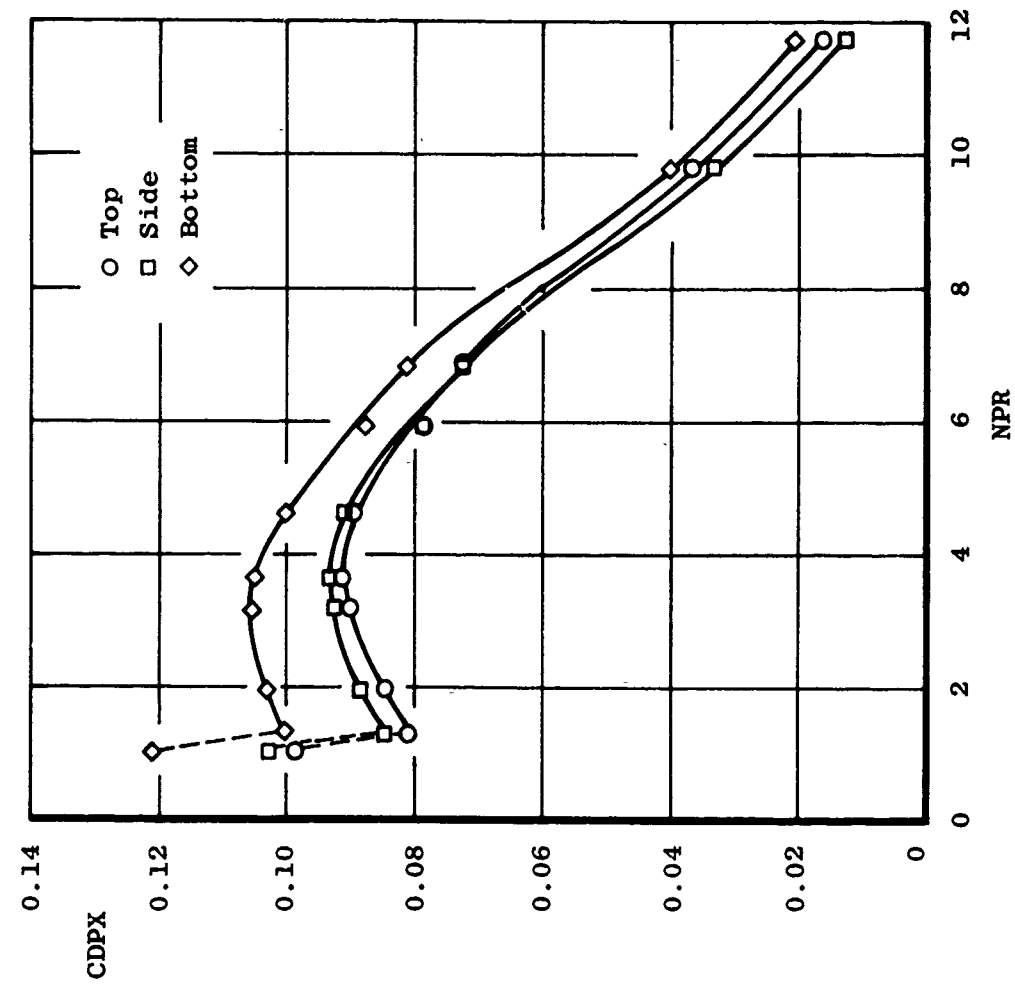
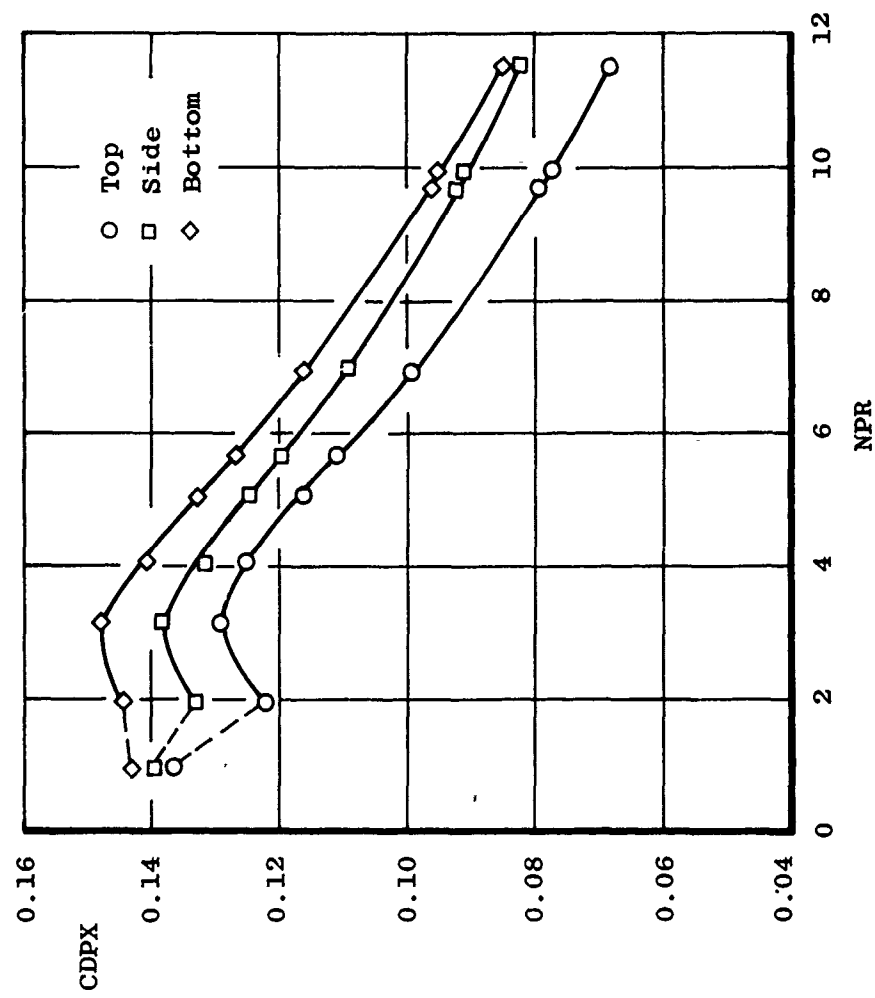


Figure 21. Flow asymmetry effects on 15-deg boattail pressure drag coefficient.
 a. $M_\infty = 0.60$



b. $M_{\infty} = 0.95$
Figure 21. Continued.



c. $M_{\infty} = 1.50$
Figure 21. Concluded.

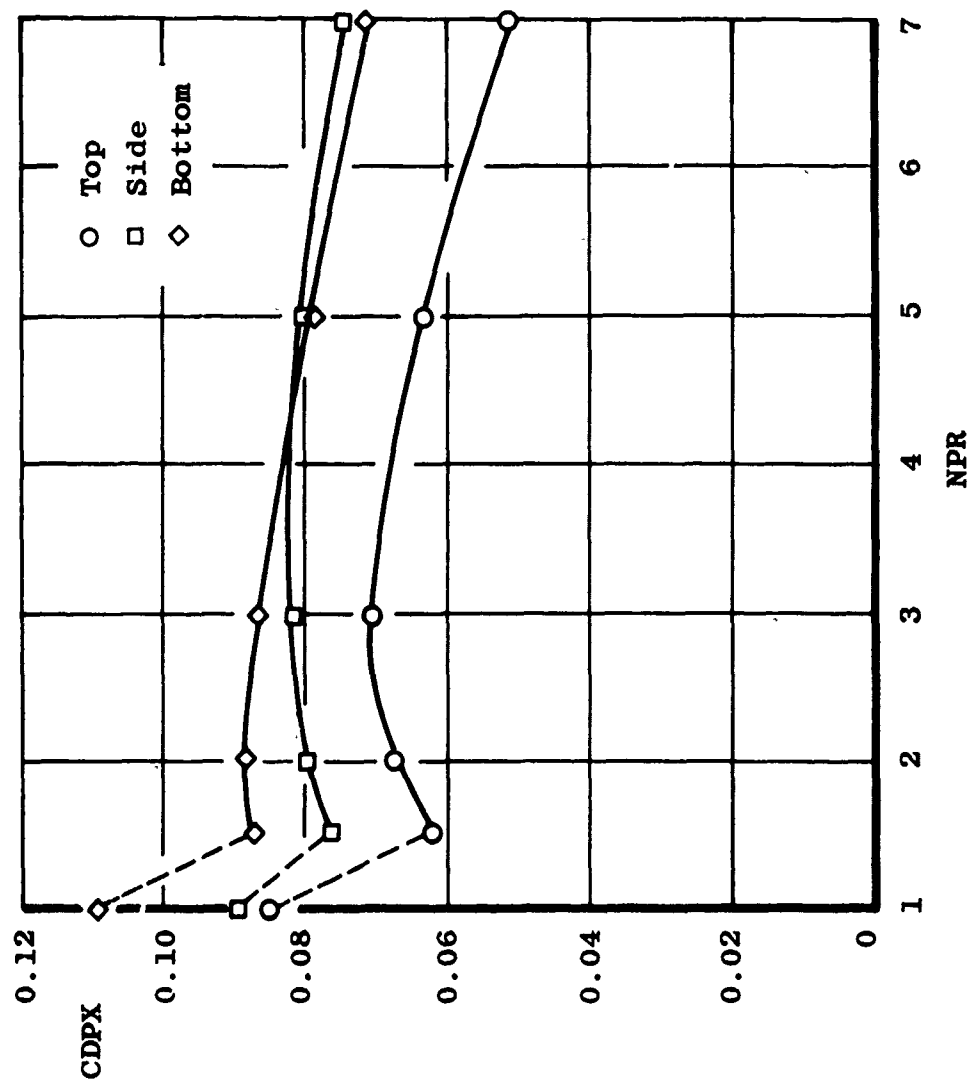
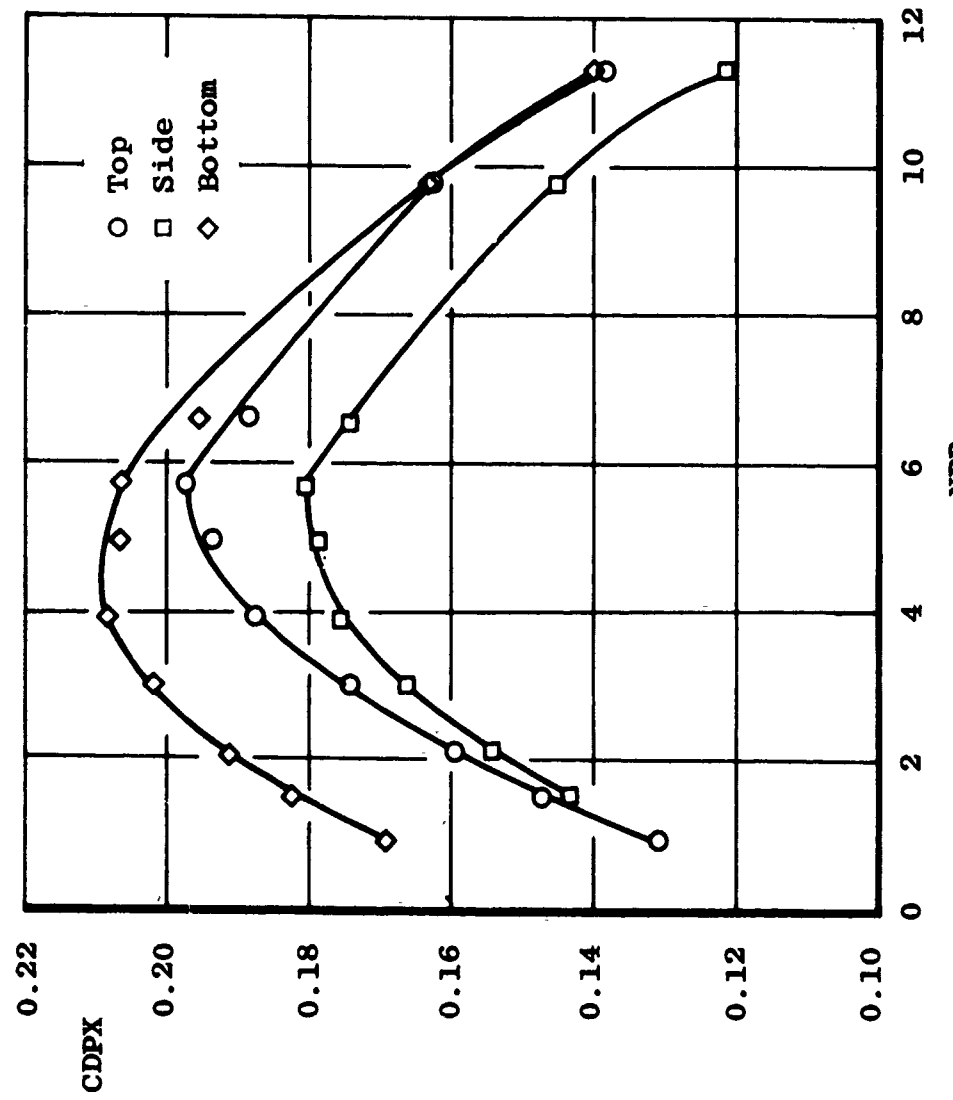
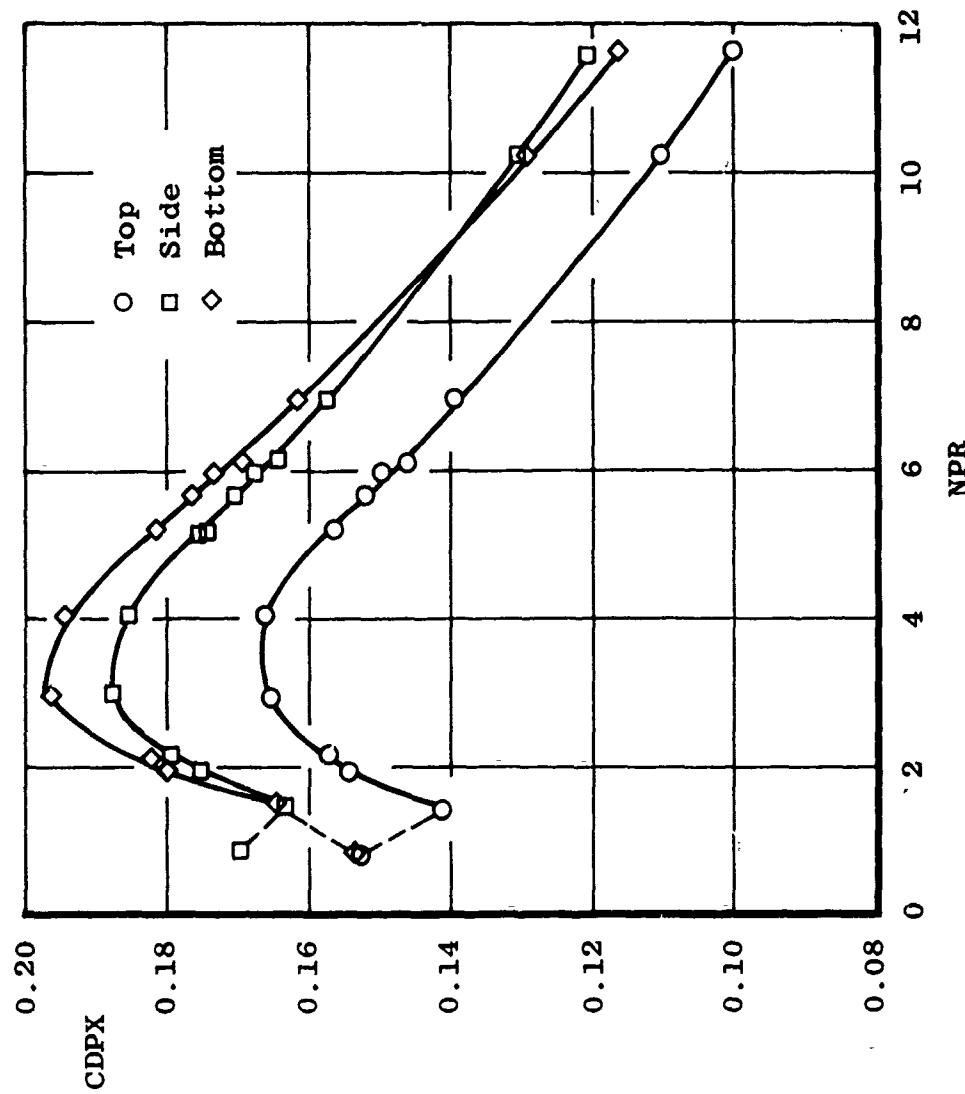


Figure 22. Flow asymmetry effects on 25-deg boattail pressure drag coefficient.
 a. $M_\infty = 0.60$



b. $M_{\infty} = 0.95$
Figure 22. Continued.



c. $M_{\infty} = 1.50$
Figure 22. Concluded.

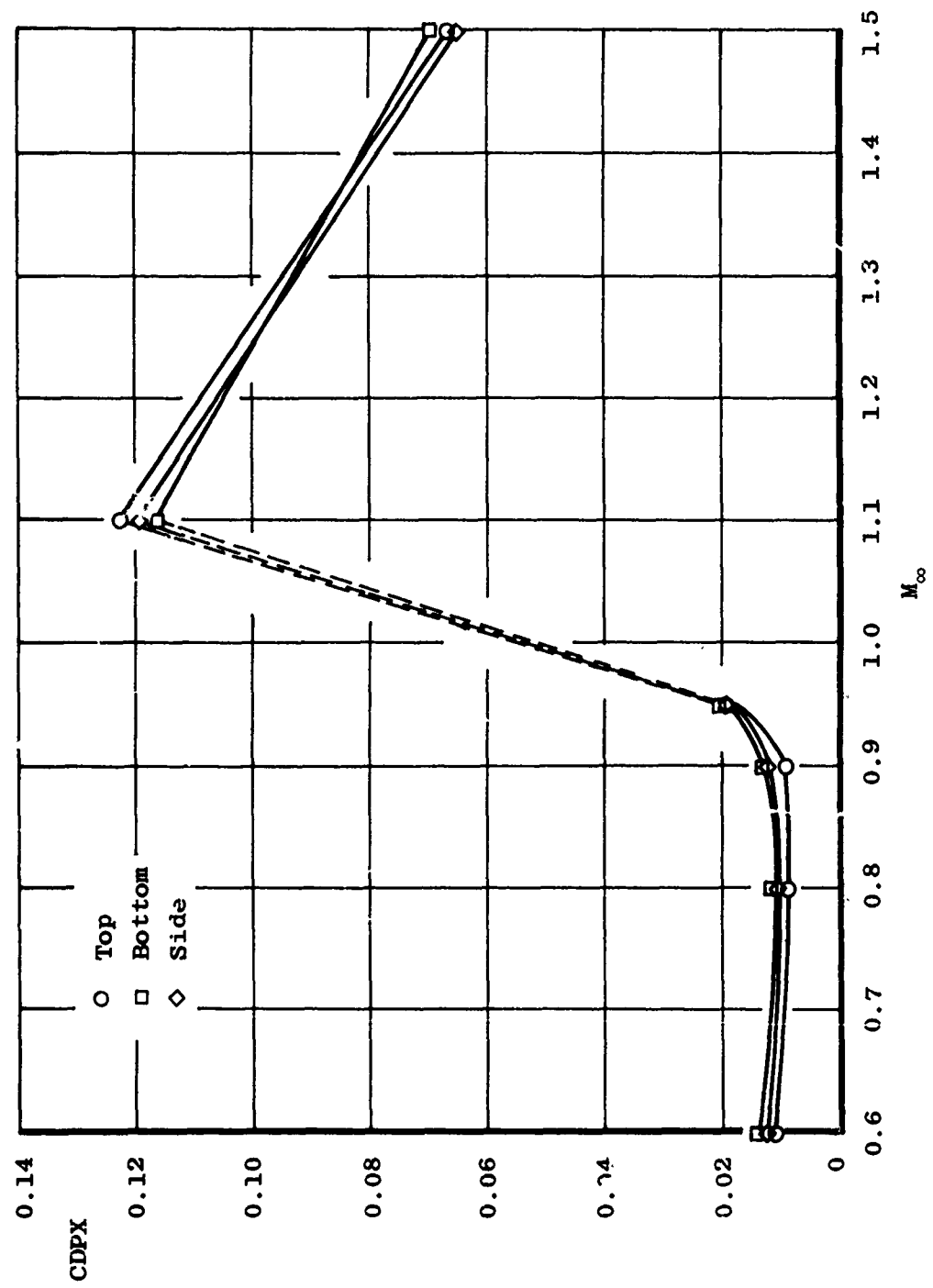
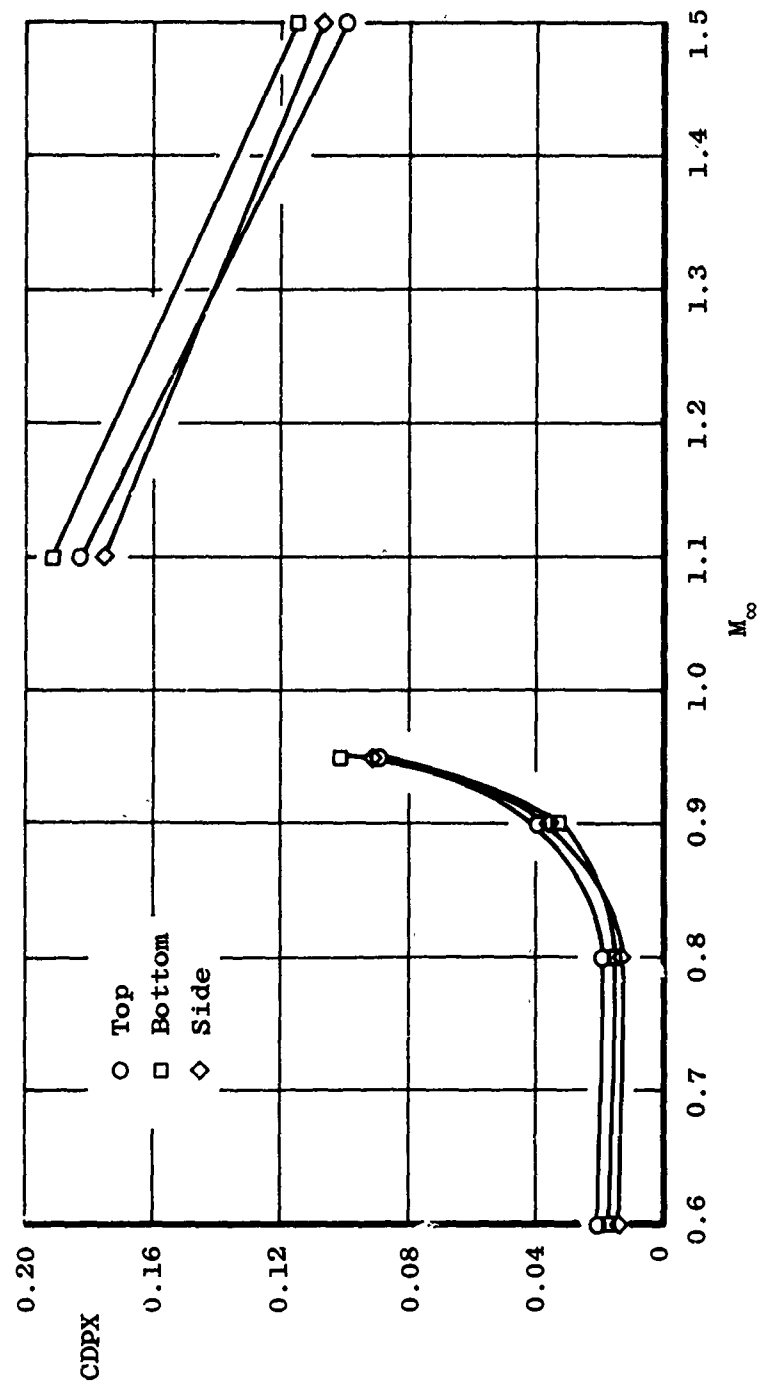
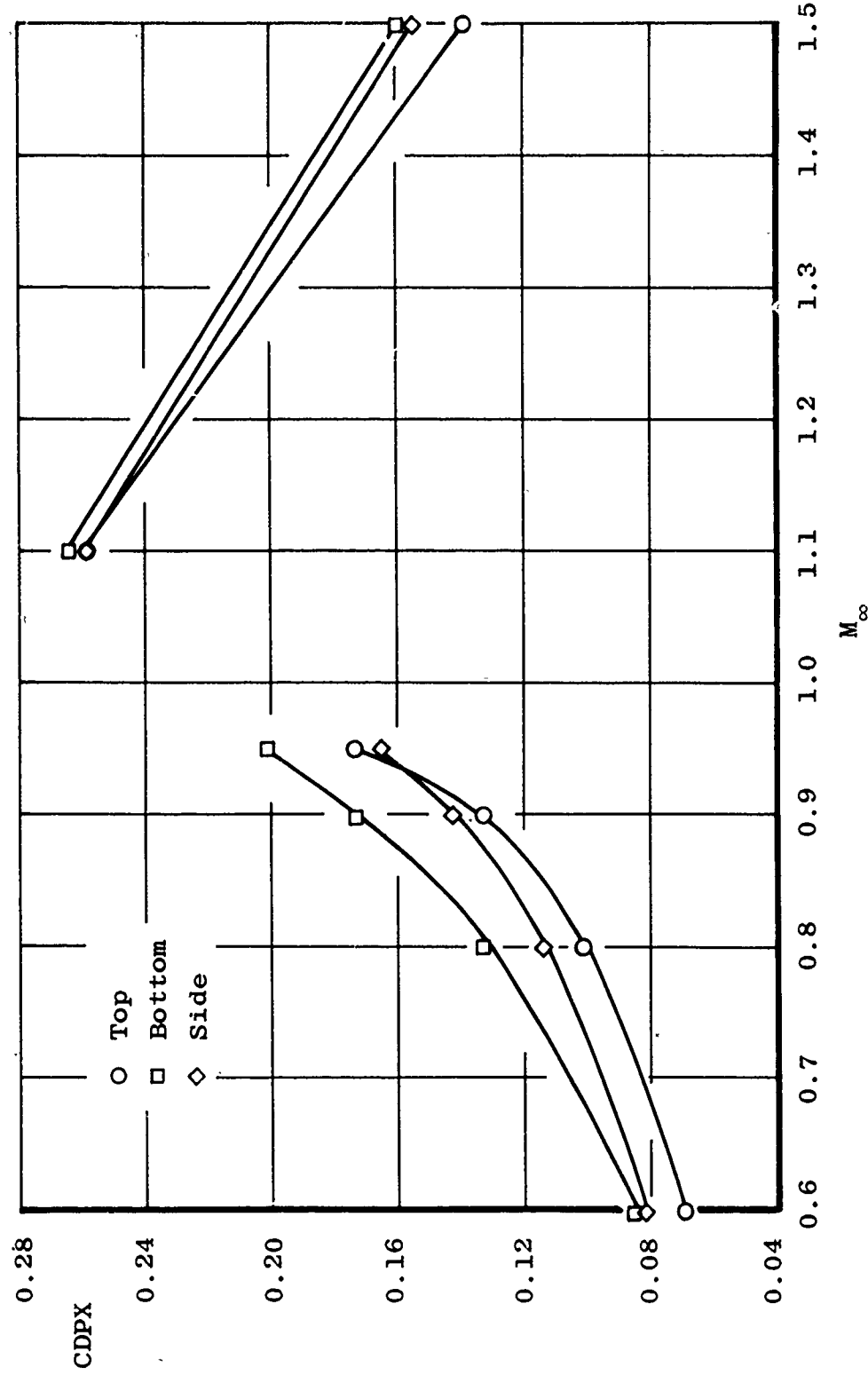


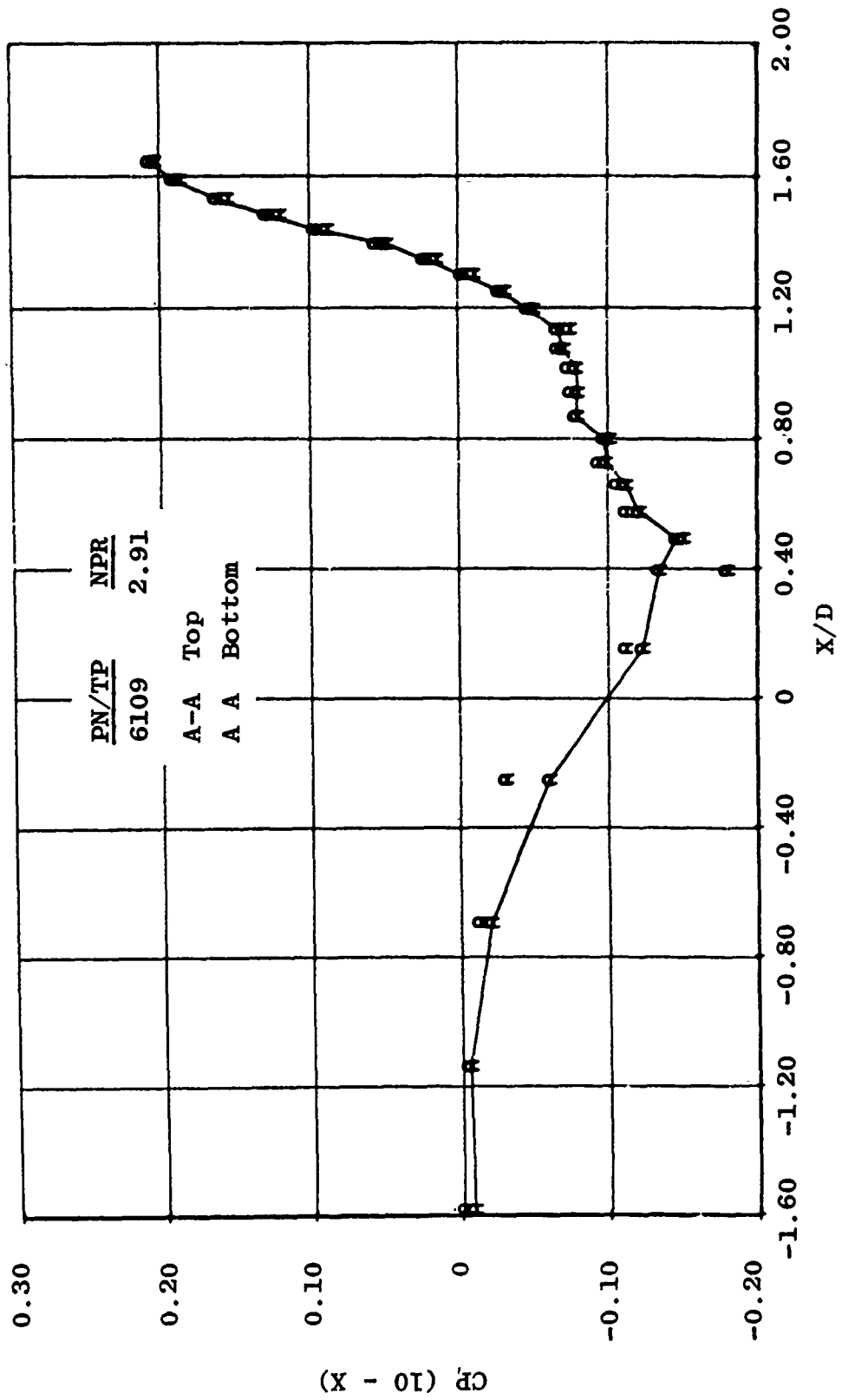
Figure 23. Flow asymmetry effects as a function of Mach number.
a. 10-deg boattail



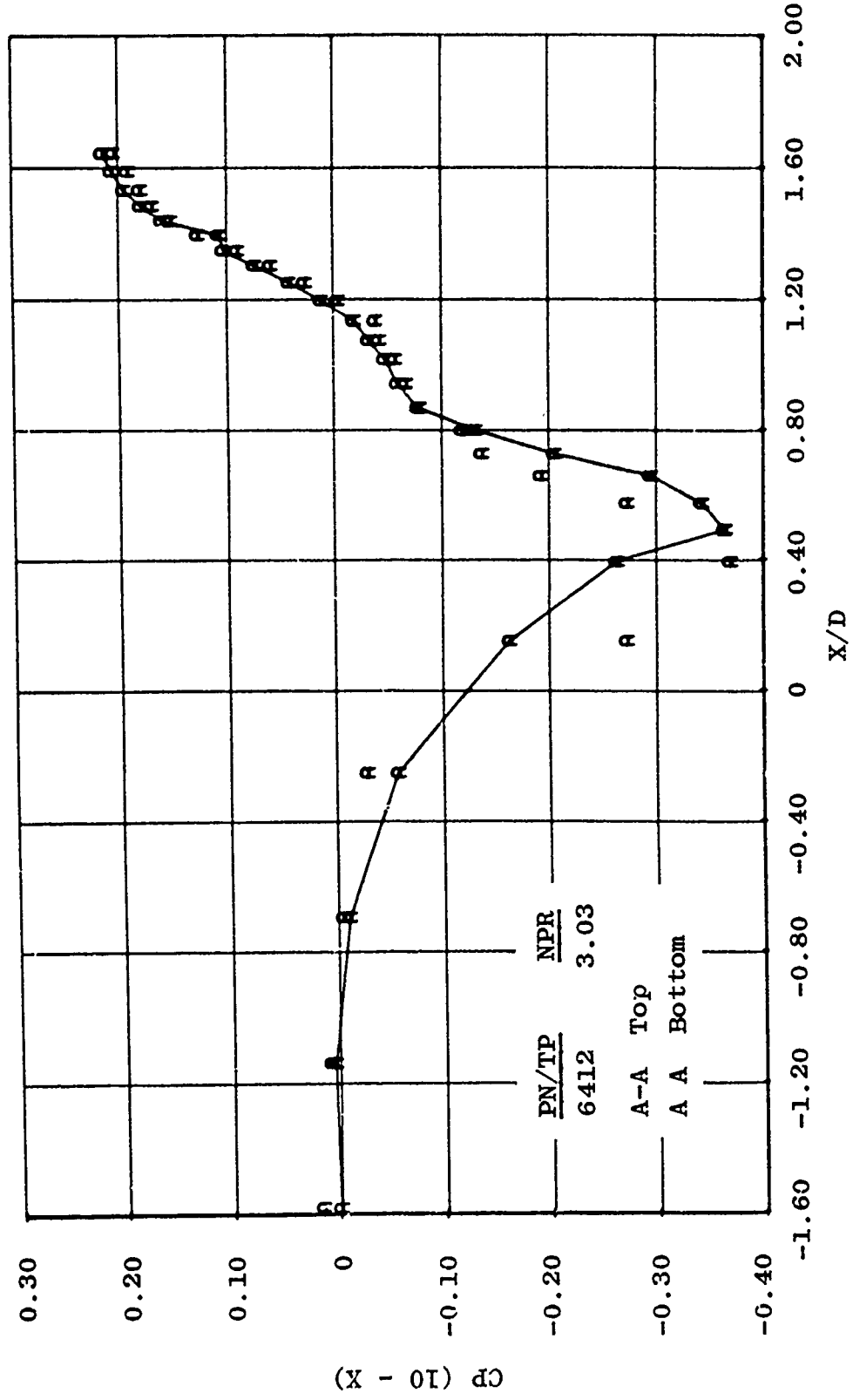
b. 15-deg boattail
Figure 23. Continued.



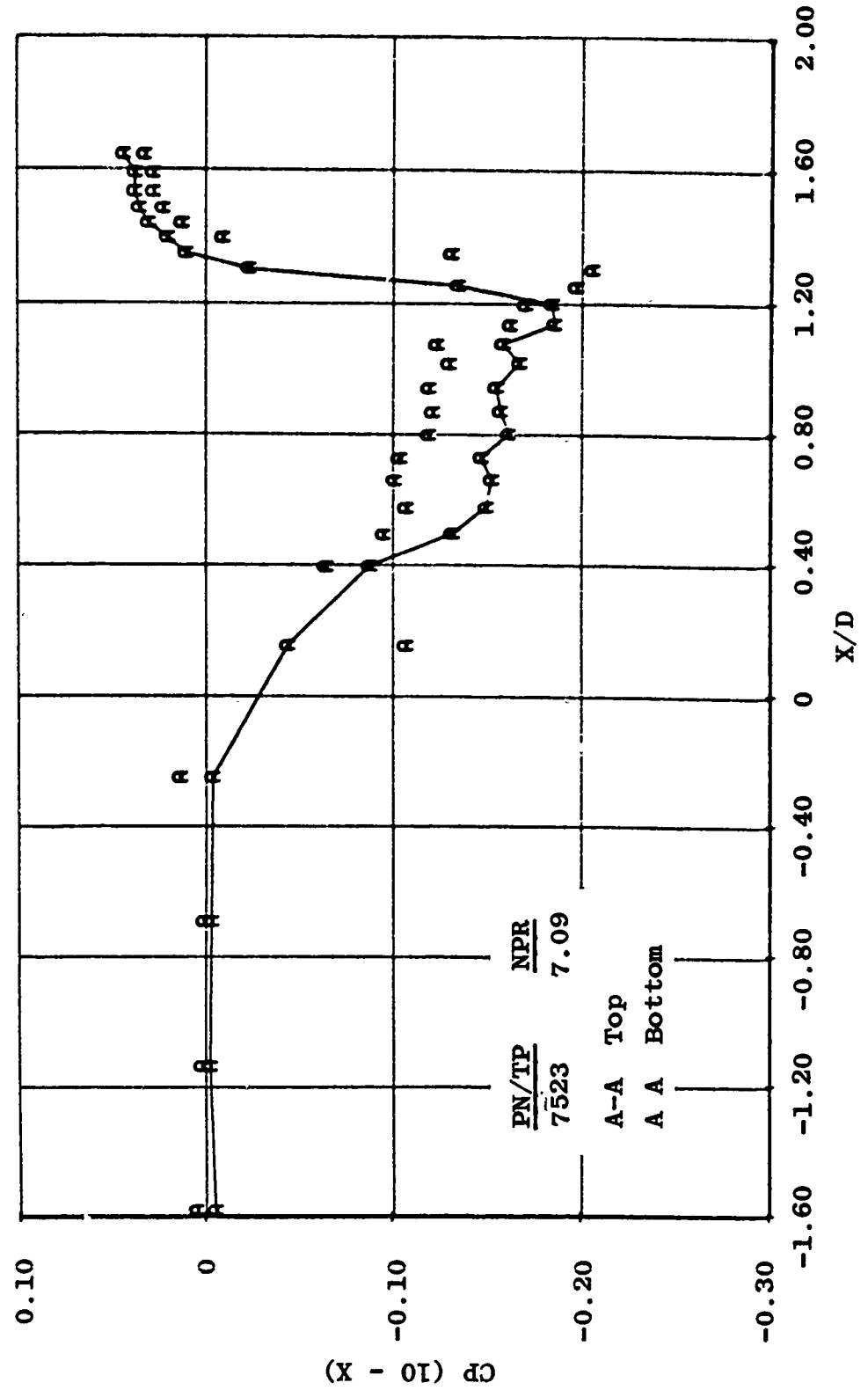
c. 25-deg boattail
Figure 23. Concluded.



a. $M_{\infty} = 0.60$
Figure 24. Flow asymmetry effects on 10-deg boattail pressure distribution.



b. $M_\infty = 0.95$
Figure 24. Continued.



c. $M_{\infty} = 1.50$
Figure 24. Concluded.

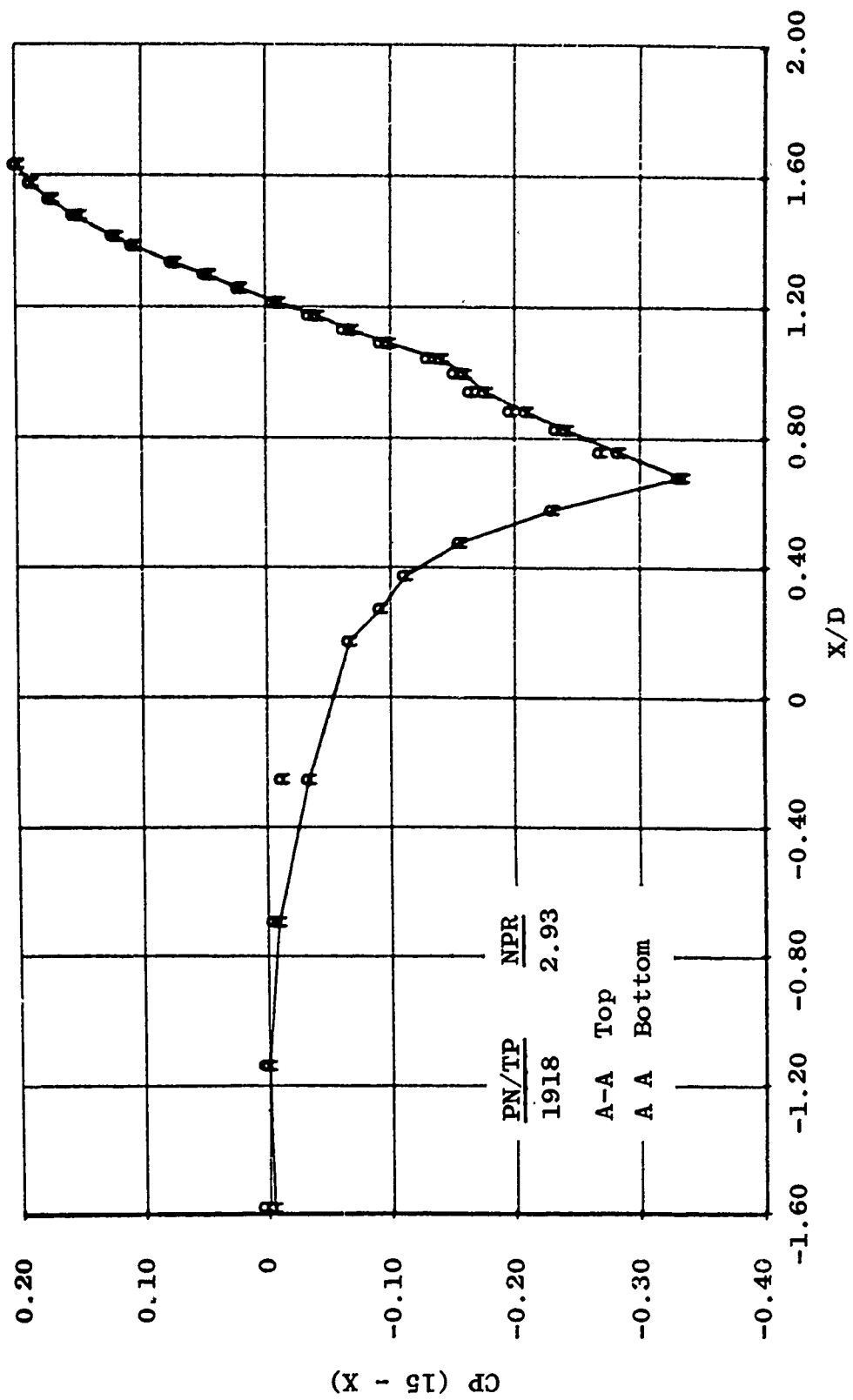
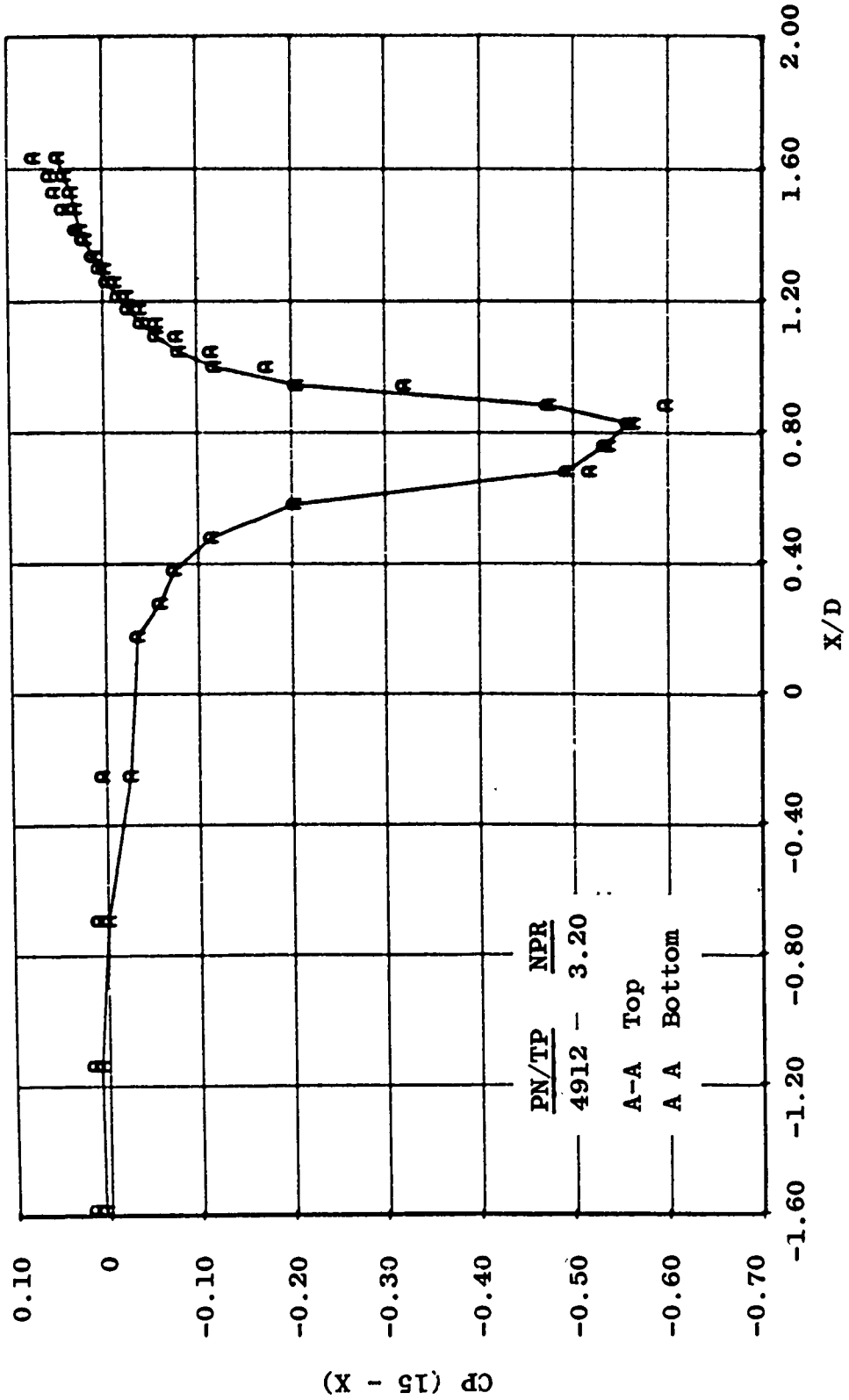
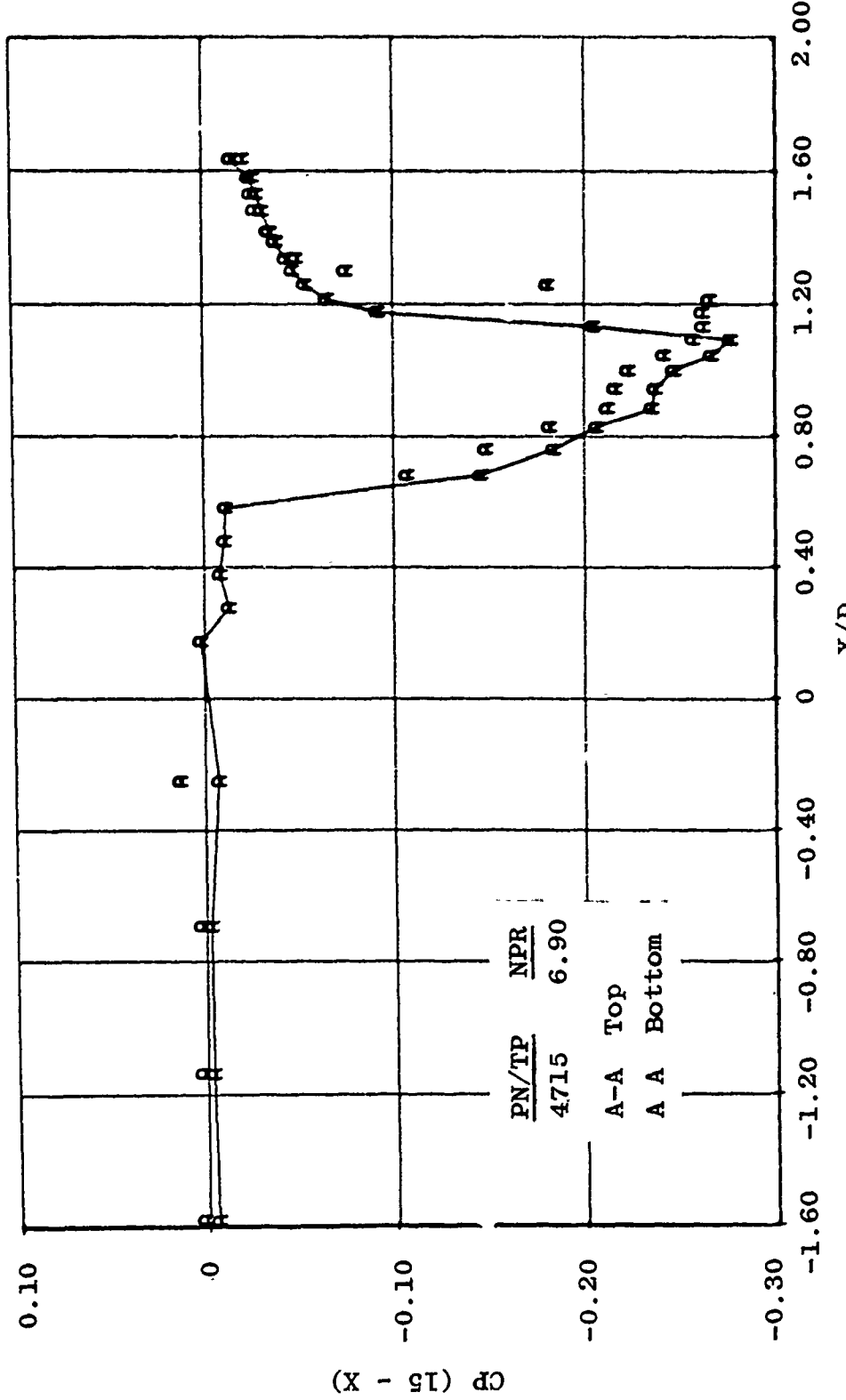


Figure 25. Flow asymmetry effects on 15-deg boattail pressure distribution.
a. $M_{\infty} = 0.60$



b. $M_{\infty} = 0.95$
Figure 25. Continued.



c. $M_{\infty} = 1.50$
Figure 25. Concluded.

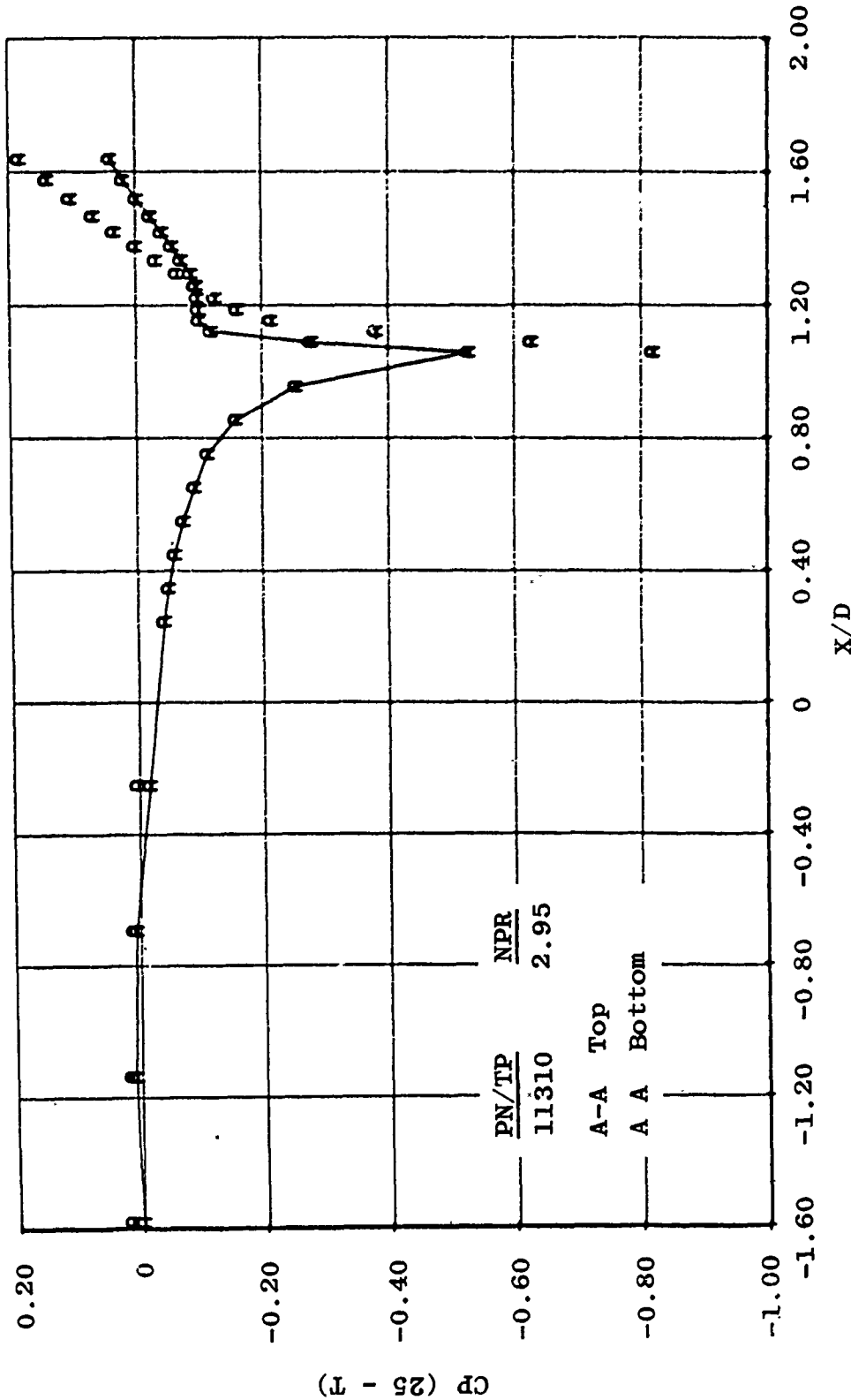
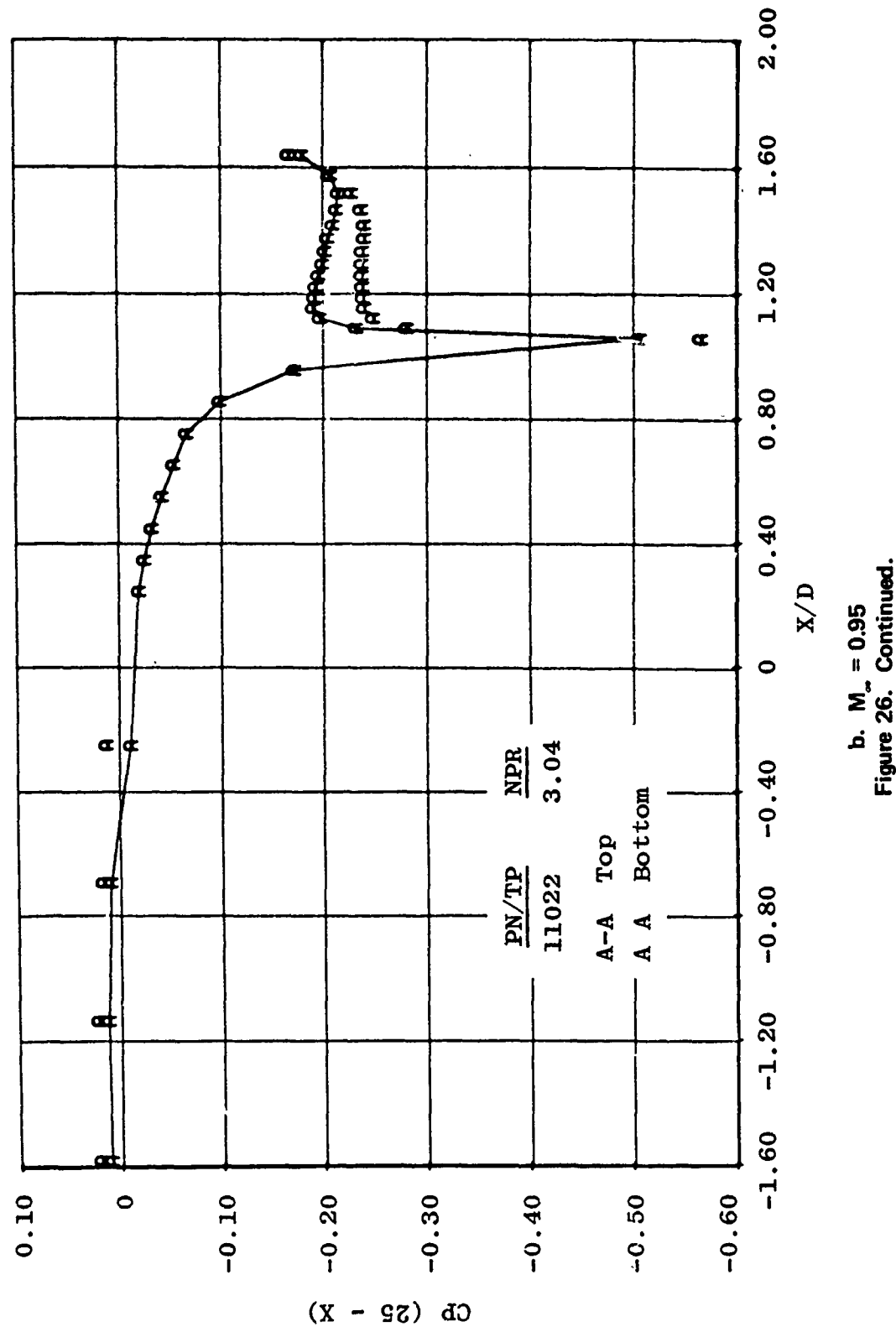
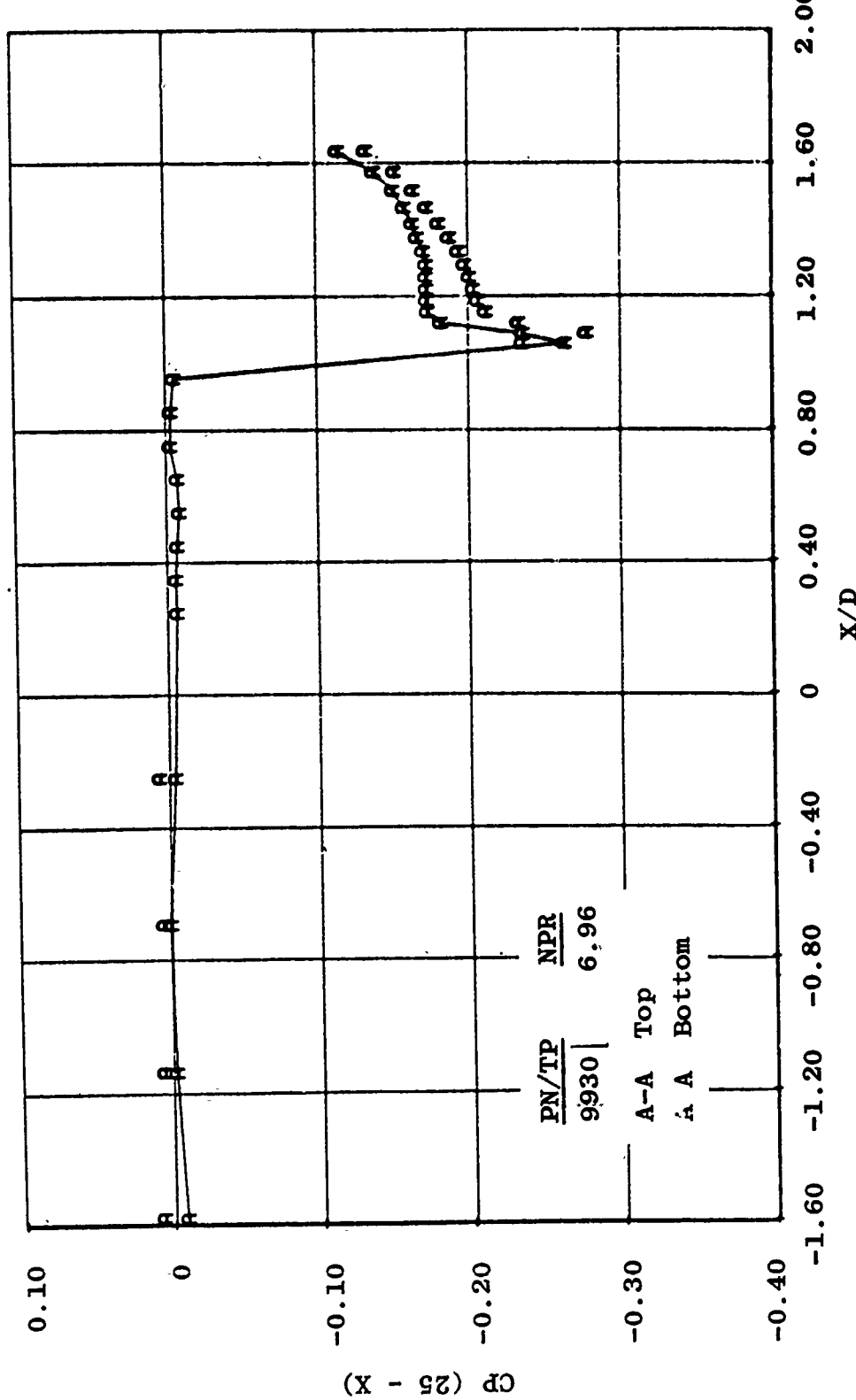


Figure 26. Flow asymmetry effects on 25-deg boattail pressure distribution.
 a. $M_{\infty} = 0.60$



b. $M_\infty = 0.95$
Figure 26. Continued.



c. $M_\infty = 1.50$
Figure 26. Concluded.

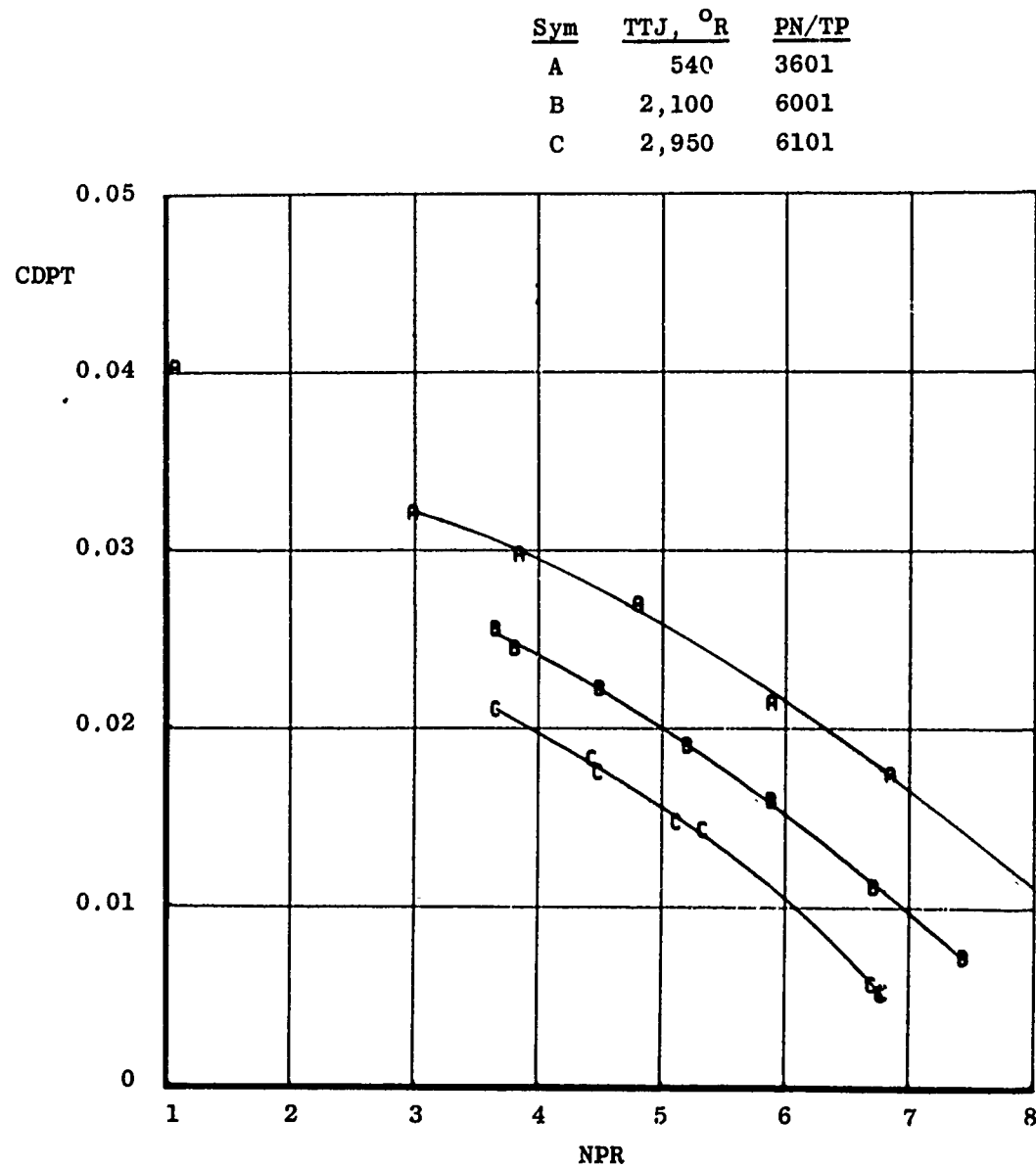
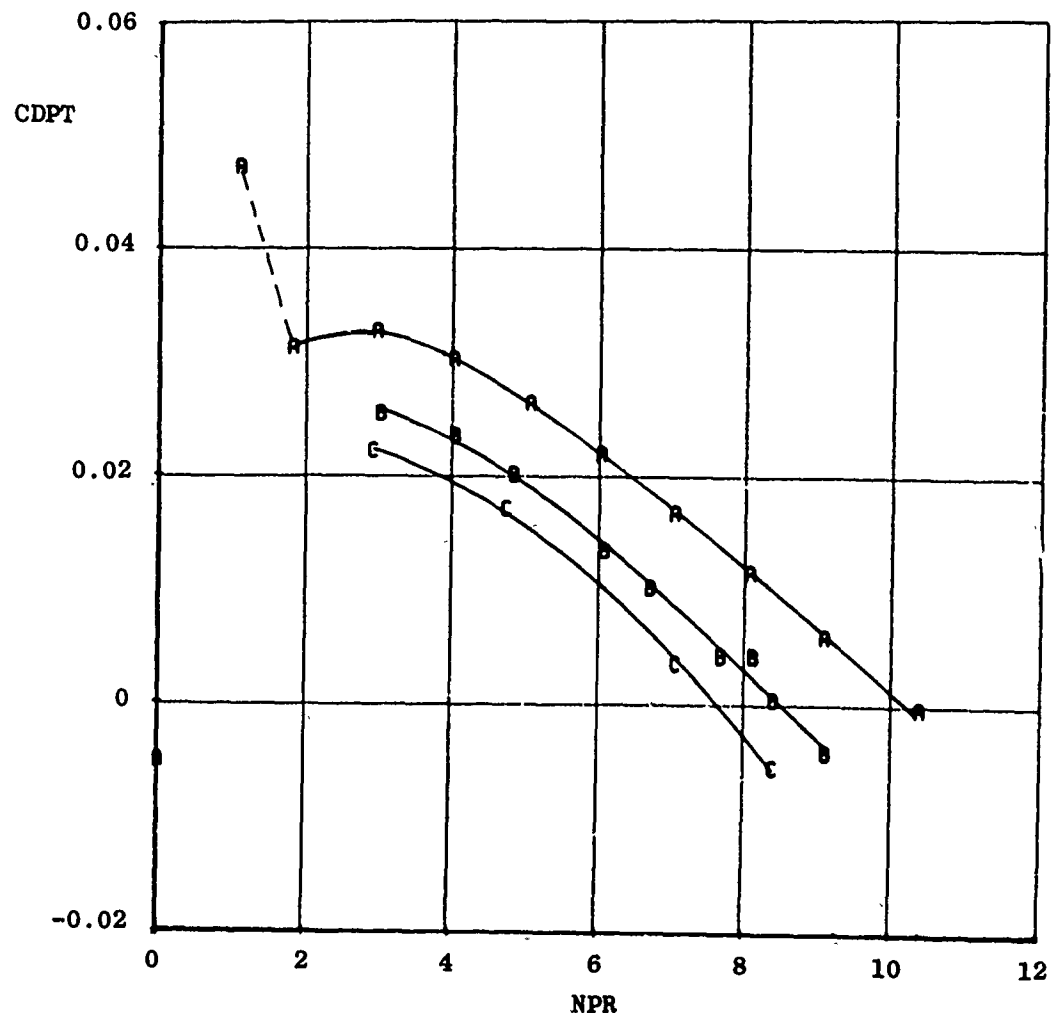


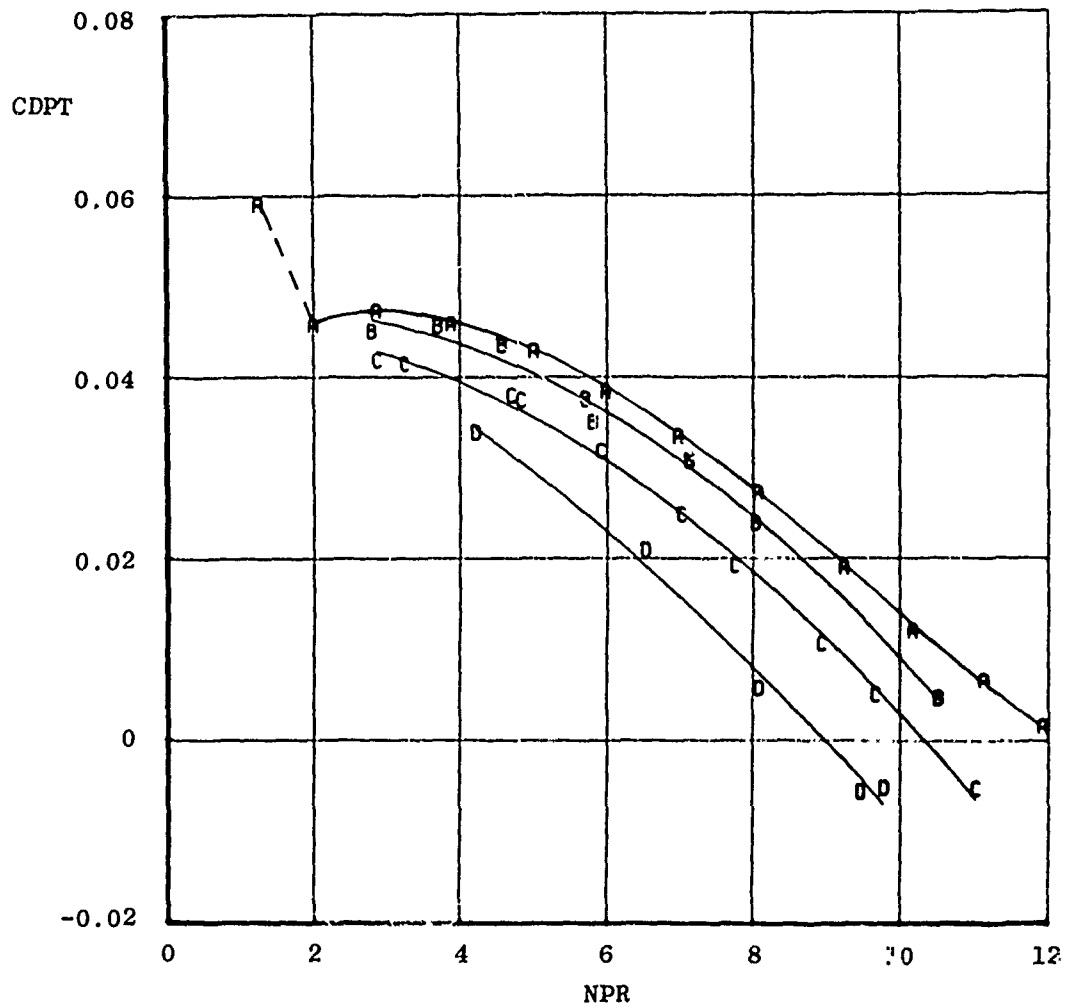
Figure 27. Exhaust plume temperature effects on 15-deg boattail configuration.

| Sym | TTJ, $^{\circ}$ R | PN/TP |
|-----|-------------------|-------|
| A | 540 | 501 |
| B | 2,125 | 4701 |
| C | 3,100 | 601 |



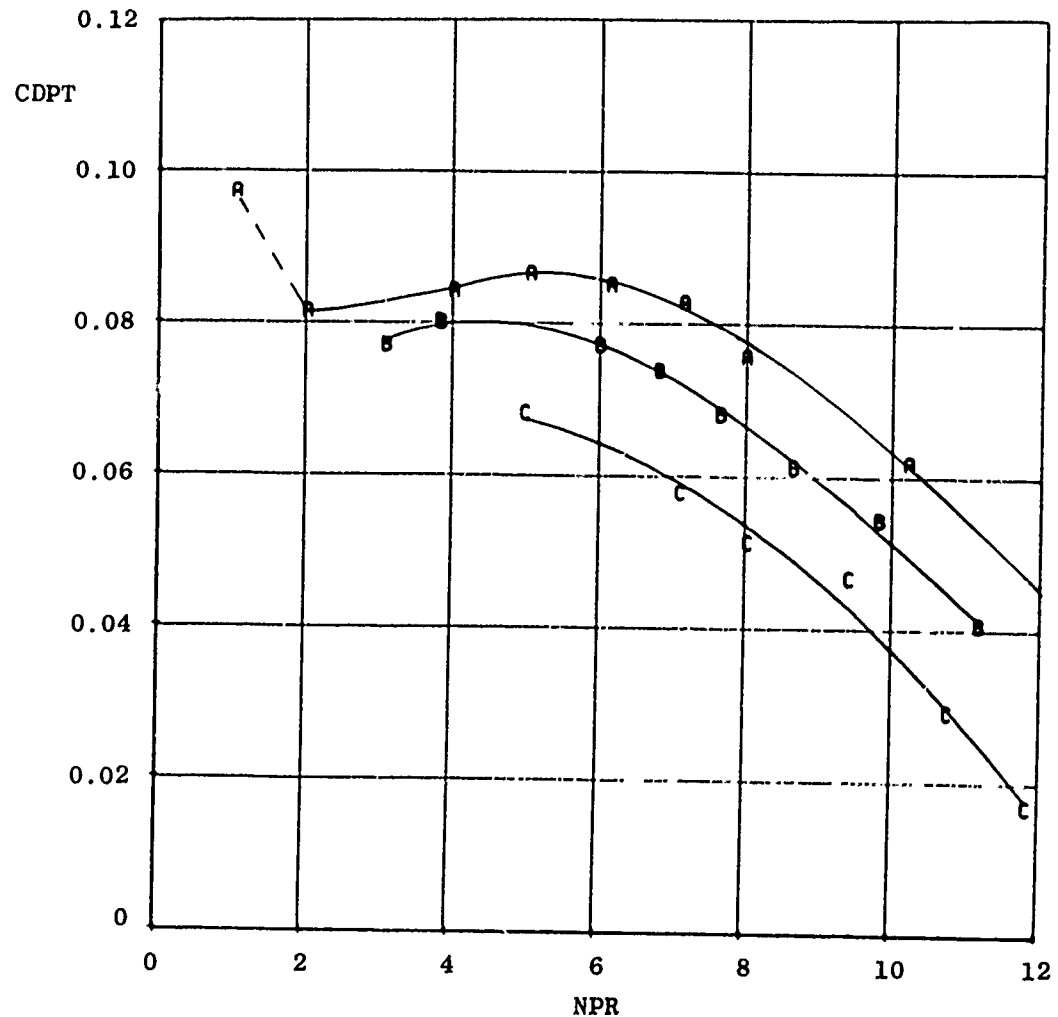
b. $M_{\infty} = 0.80$
Figure 27. Continued.

| Sym | <u>TTJ, °R</u> | <u>PN/TP</u> |
|-----|----------------|--------------|
| A | 535 | 1101 |
| B | 1,550 | 1001 |
| C | 2,100 | 4401 |
| D | 2,925 | 1301 |



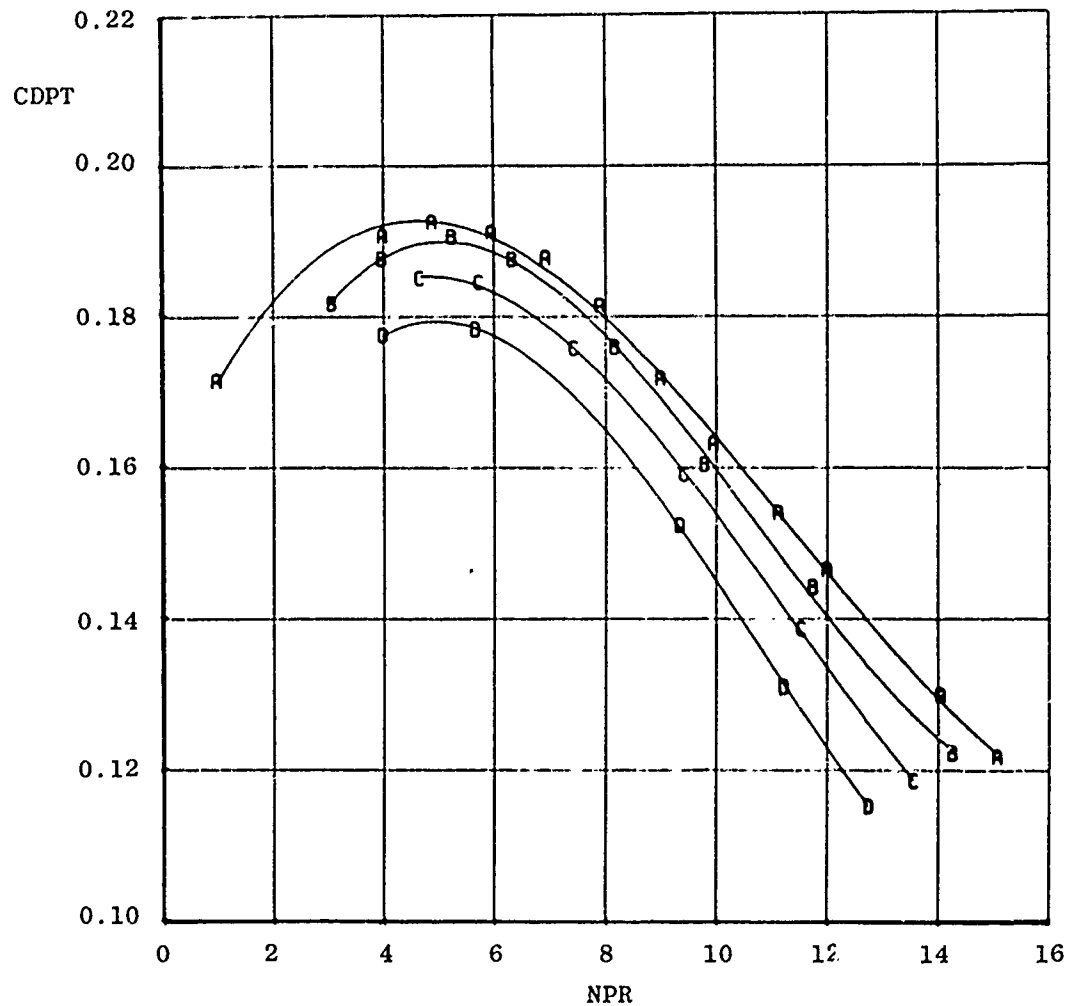
c. $M_{\infty} = 0.90$
Figure 27. Continued.

| Sym | TTJ, $^{\circ}$ R | PN/TP |
|-----|-------------------|-------|
| A | 540 | 2001 |
| B | 2,150 | 4601 |
| C | 3,025 | 1901 |



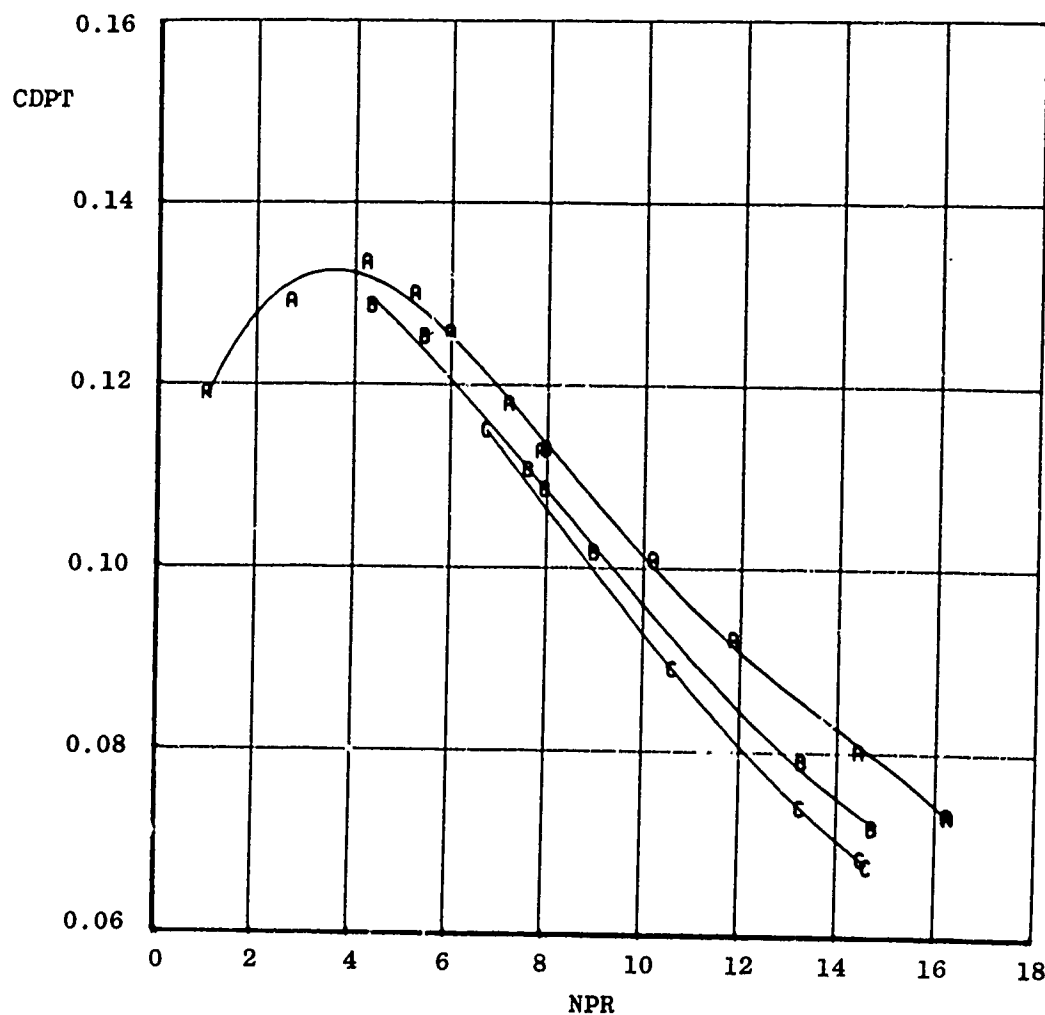
d. $M_{\infty} = 0.95$
Figure 27. Continued.

| Sym | TTJ, $^{\circ}$ R | PN/TP |
|-----|-------------------|-------|
| A | 540 | 2101 |
| B | 1,500 | 5301 |
| C | 2,125 | 5101 |
| D | 2,900 | 5201 |



e. $M_{\infty} = 1.10$
Figure 27. Continued.

| Sym | TTJ, $^{\circ}$ R | PN/TP |
|-----|-------------------|-------|
| A | 540 | 5801 |
| B | 1,950 | 5601 |
| C | 2,700 | 5701 |



f. $M_{\infty} = 1.50$
Figure 27. Concluded.

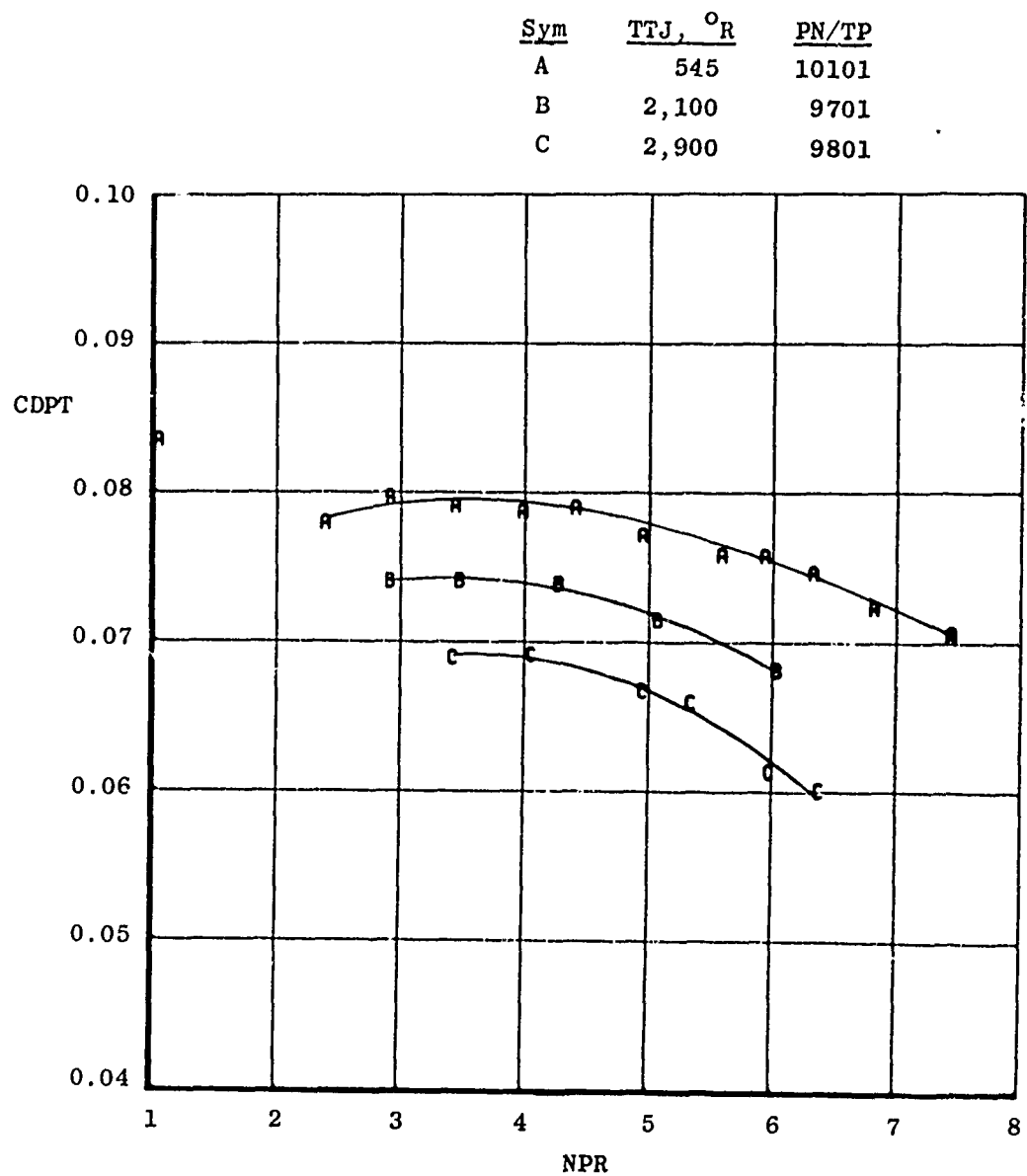
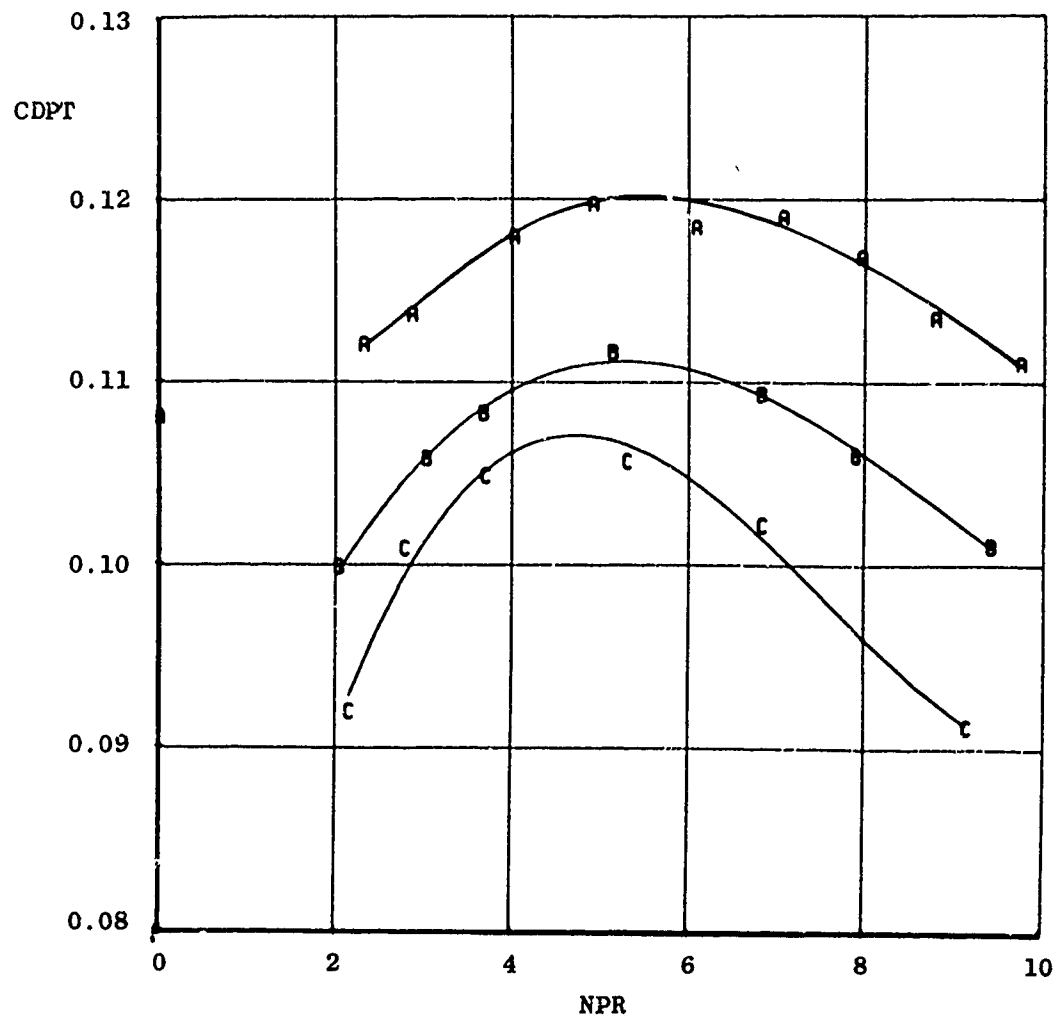
a. $M_{\infty} = 0.60$

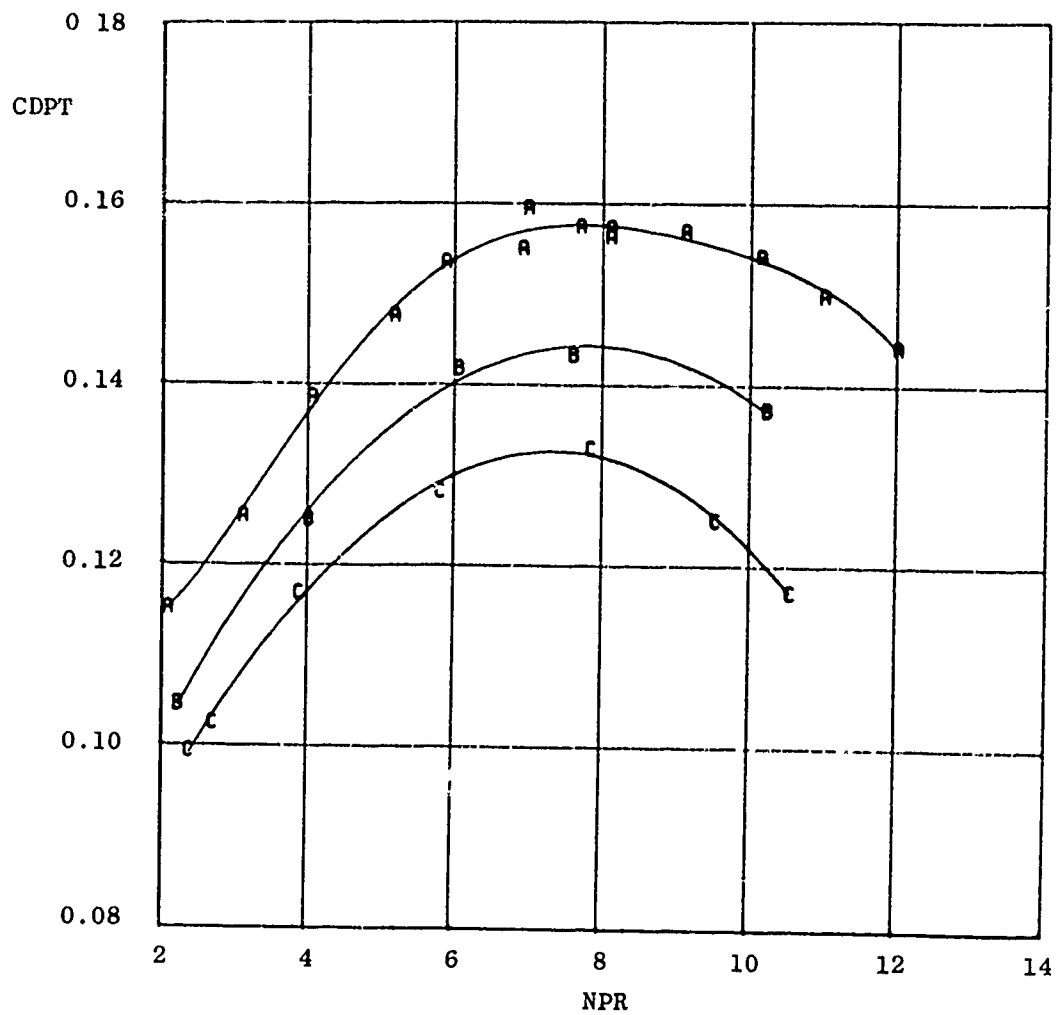
Figure 28. Exhaust plume temperature effects on 25-deg boattail configuration.

| Sym | TTJ, $^{\circ}$ R | PN/TP |
|-----|-------------------|-------|
| A | 545 | 7201 |
| B | 2,075 | 7401 |
| C | 2,900 | 7301 |



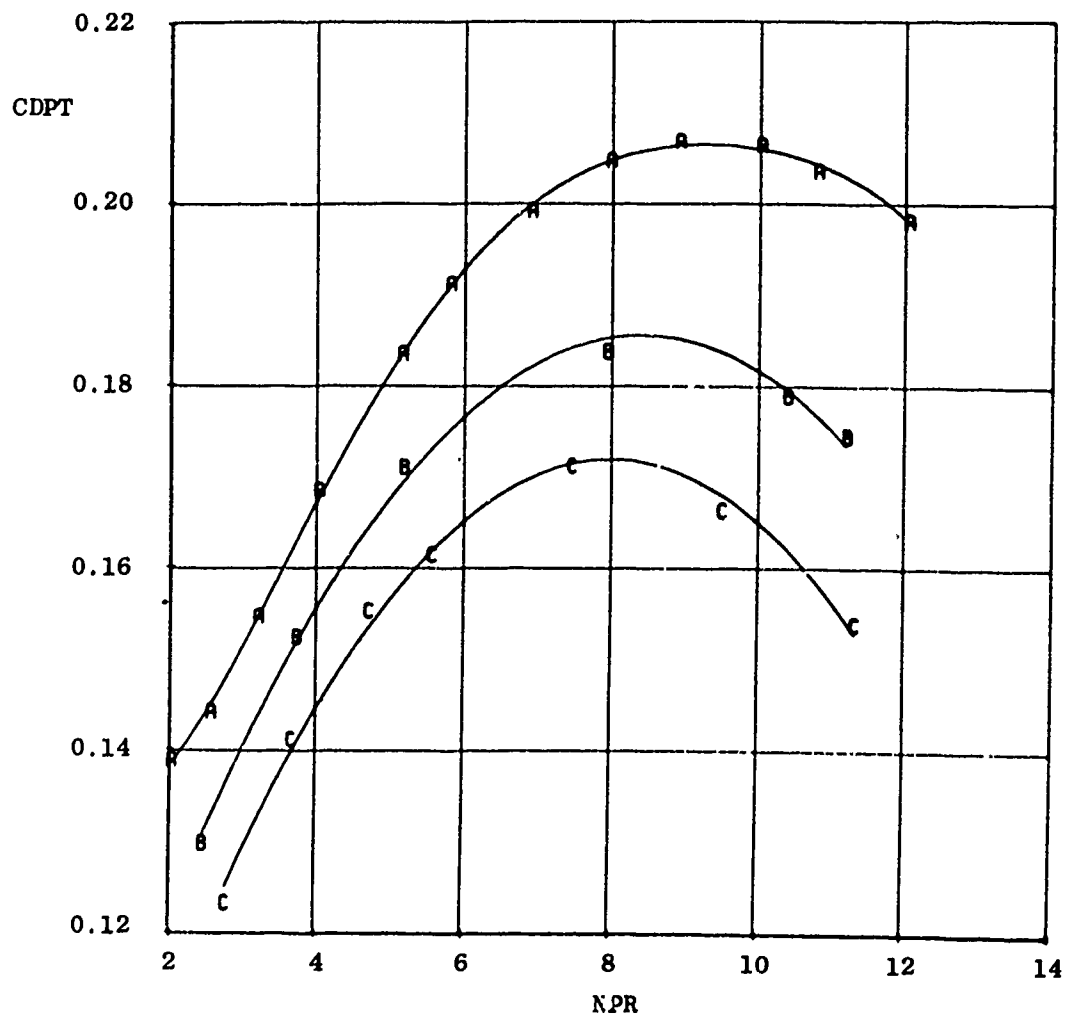
b. $M_{\infty} = 0.80$
Figure 28. Continued.

| Sym | TTJ, $^{\circ}$ R | PT |
|-----|-------------------|------|
| A | 535 | 7101 |
| B | 2,100 | 7001 |
| C | 2,850 | 6901 |



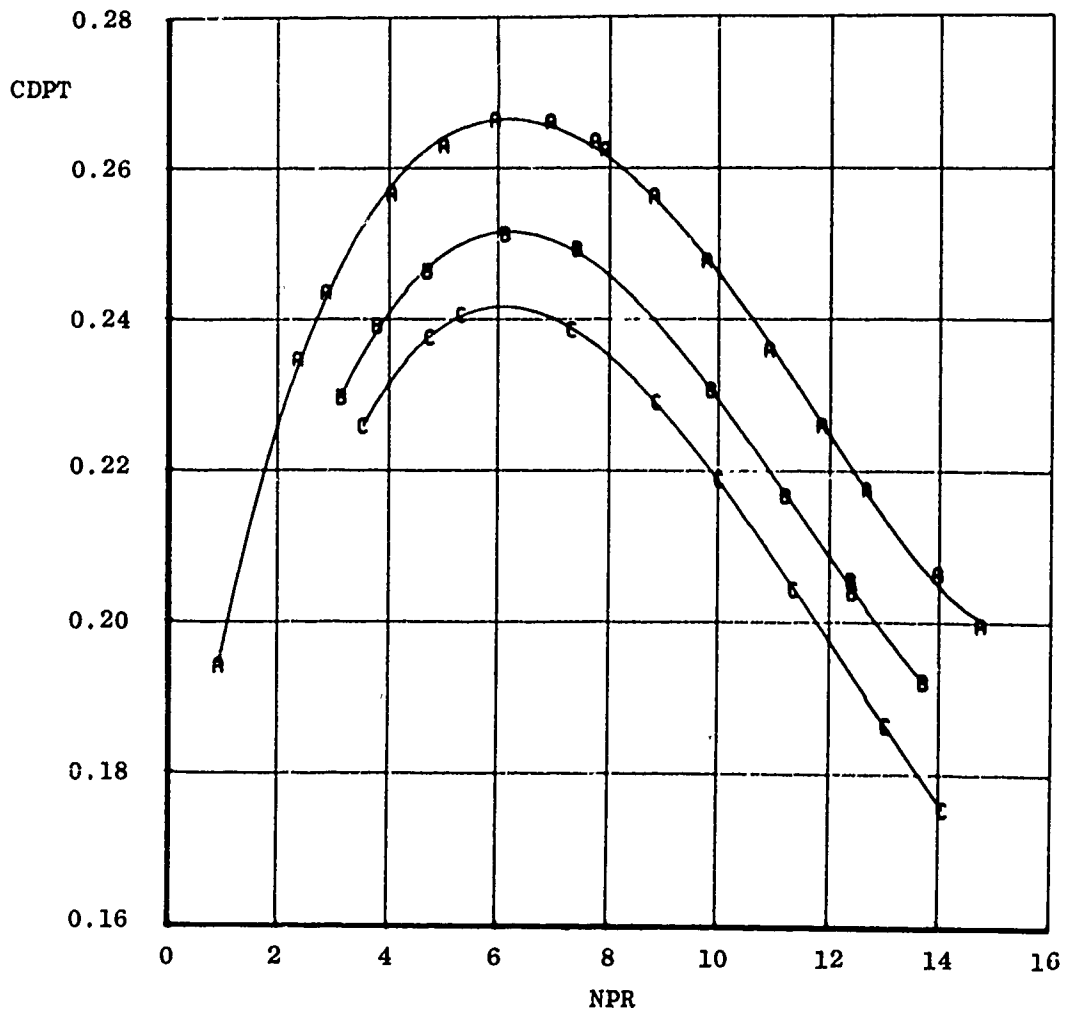
c. $M_{\infty} = 0.90$
Figure 28. Continued.

| Sym | TTJ, $^{\circ}$ R | PT |
|-----|-------------------|------|
| A | 545 | 8101 |
| B | 2,100 | 7801 |
| C | 2,850 | 7701 |



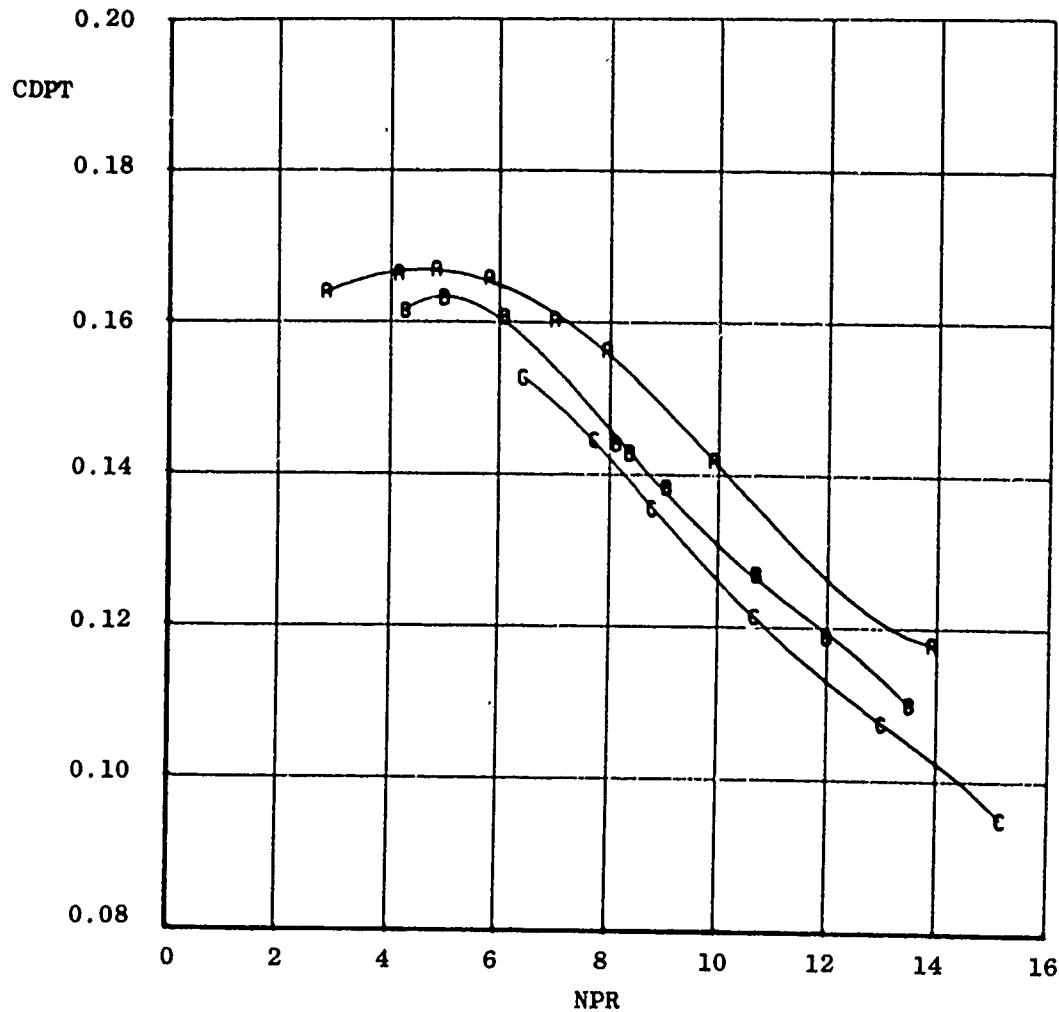
d. $M_{\infty} = 0.95$
Figure 28. Continued.

| Sym | <u>TTJ, °R</u> | <u>PT</u> |
|-----|----------------|-----------|
| A | 545 | 8201 |
| B | 2,100 | 8401 |
| C | 2,800 | 8301 |



e. $M_{\infty} = 1.10$
Figure 28. Continued.

| Sym | TTJ, °R | PN/TP |
|-----|---------|-------|
| A | 550 | 9101 |
| B | 2,125 | 8701 |
| C | 2,750 | 8801 |



f. $M_{\infty} = 1.50$
Figure 28. Concluded.

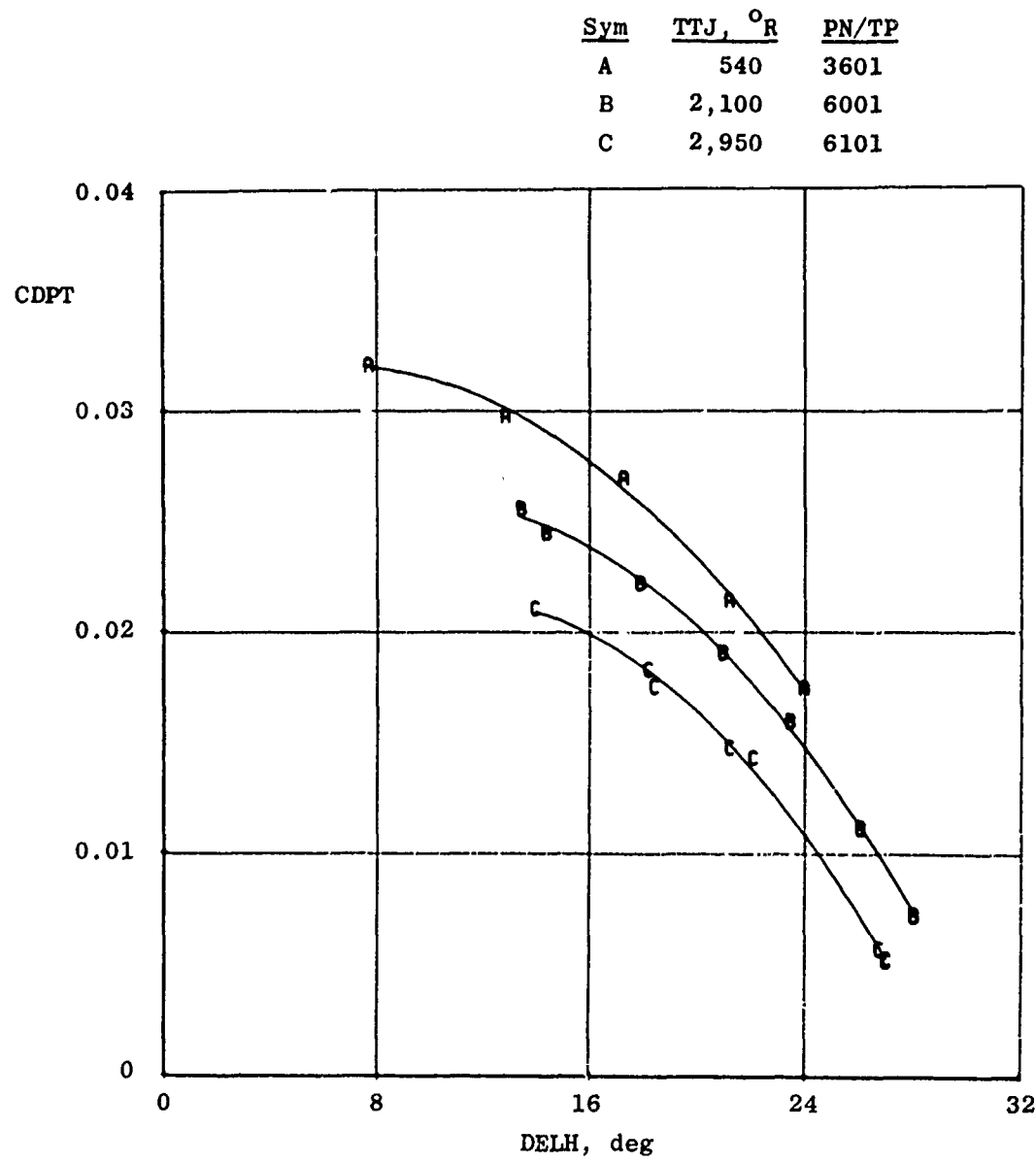
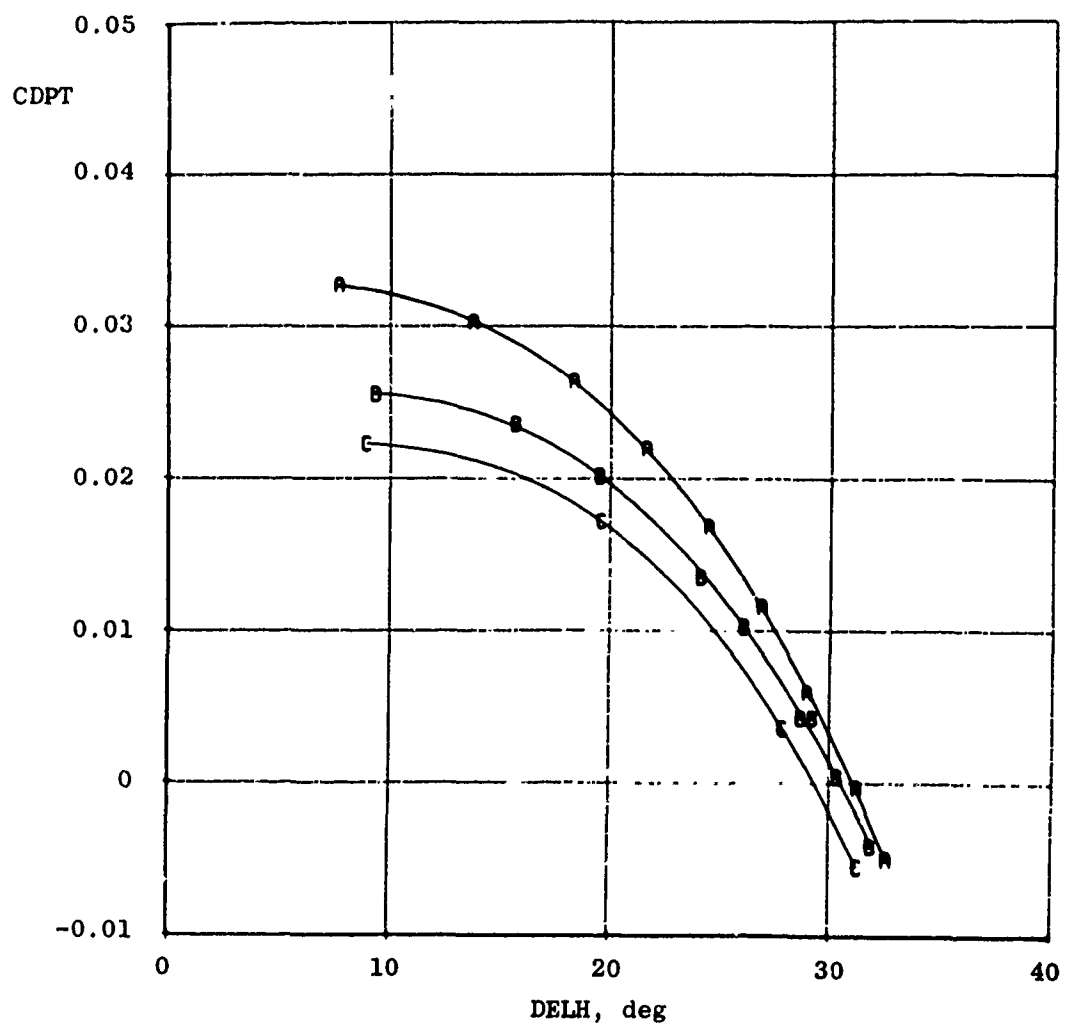
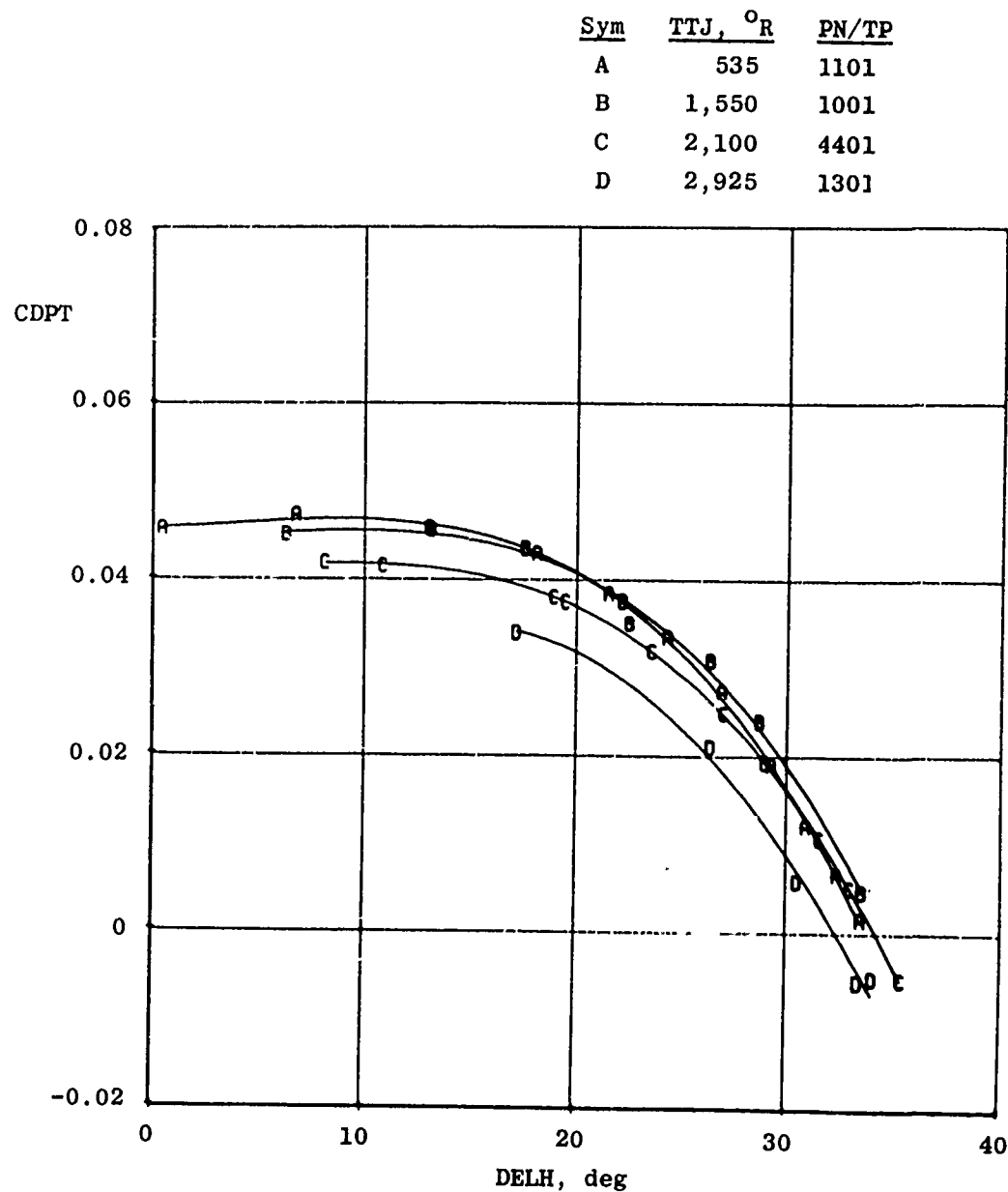


Figure 29. Exhaust plume temperature effects on 15-deg boattail as a function of jet inclination angle.

| <u>Sym</u> | <u>TTJ, $^{\circ}$R</u> | <u>PN/TP</u> |
|------------|------------------------------------|--------------|
| A | 540 | 501 |
| B | 2,125 | 4701 |
| C | 3,100 | 601 |

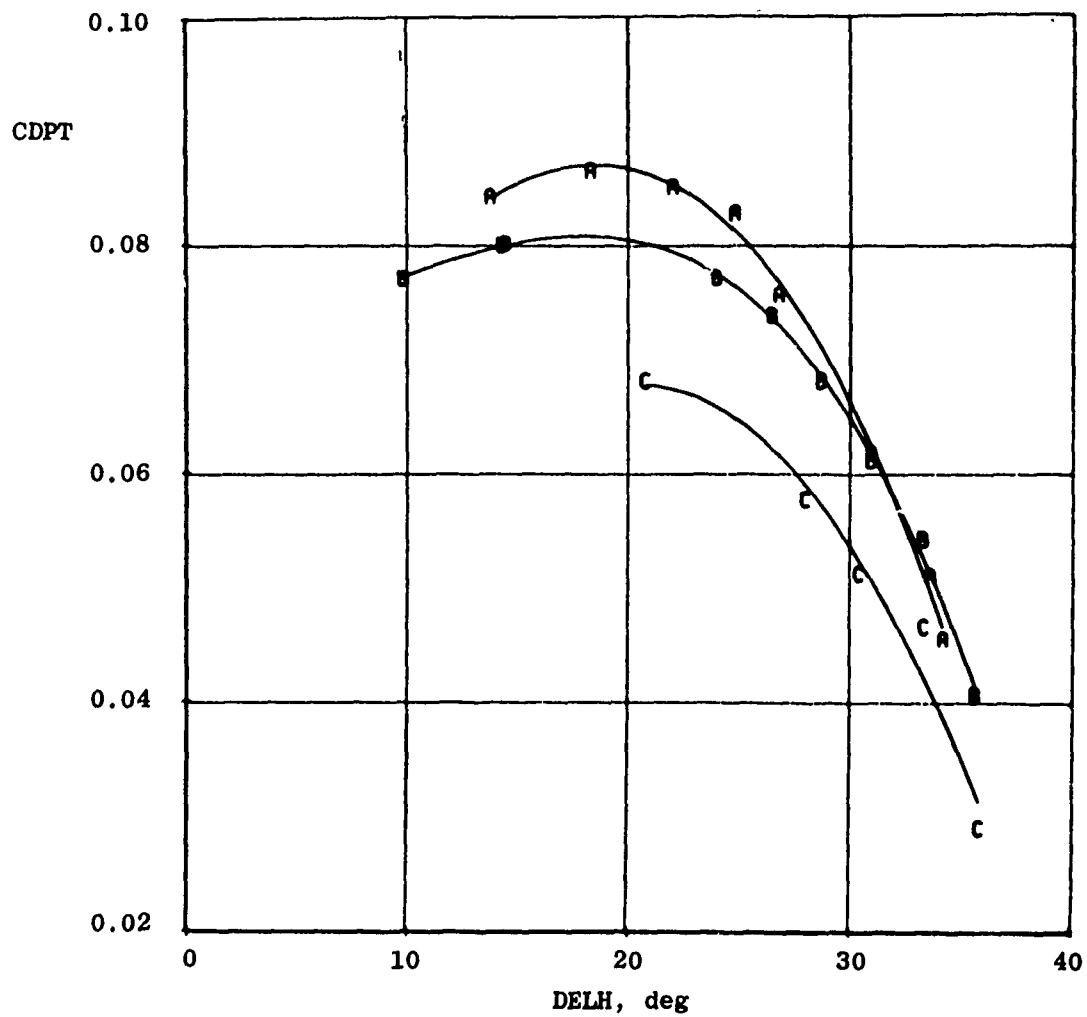


b. $M_{\infty} = 0.80$
Figure 29. Continued.



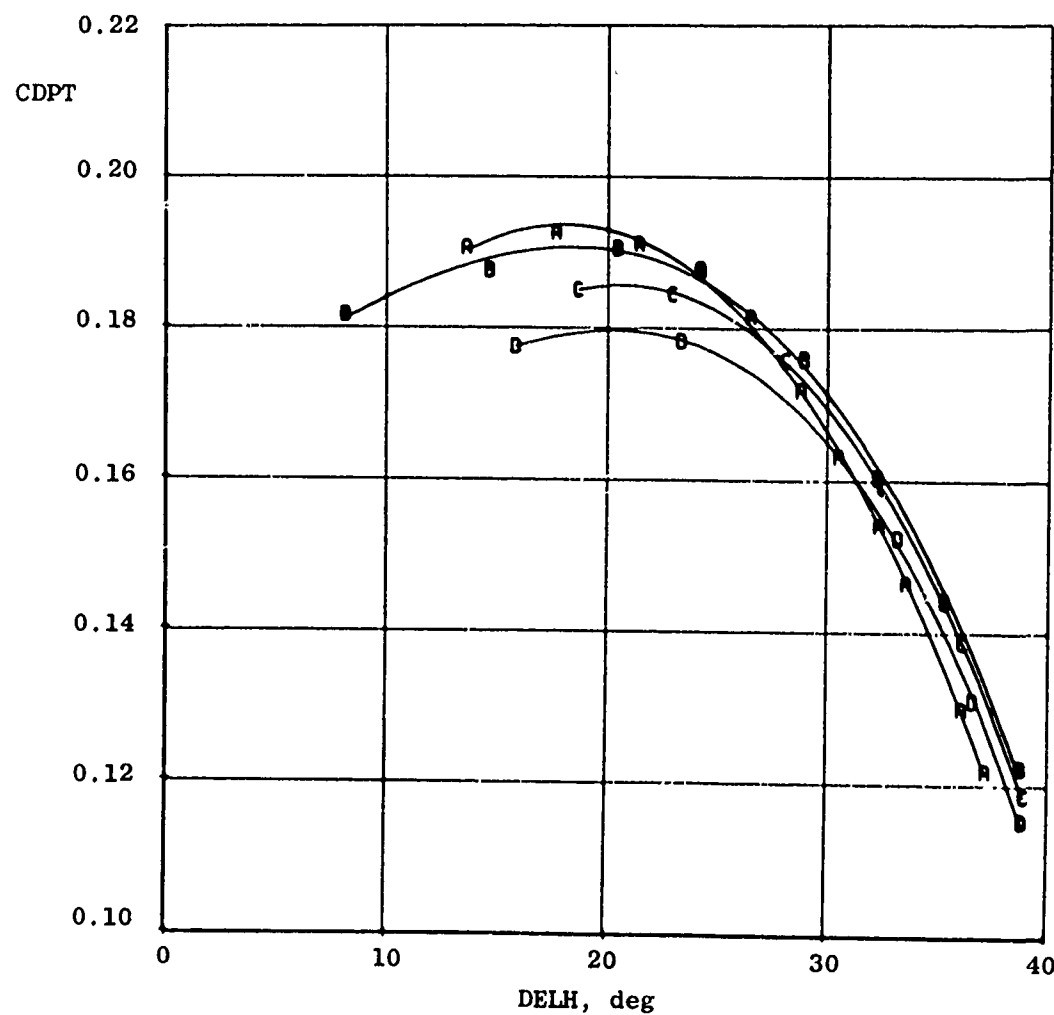
c. $M_{\infty} = 0.90$
Figure 29. Continued.

| Sym | TTJ, $^{\circ}$ R | PN/TP |
|-----|-------------------|-------|
| A | 540 | 2001 |
| B | 2,150 | 4601 |
| C | 3,025 | 1901 |



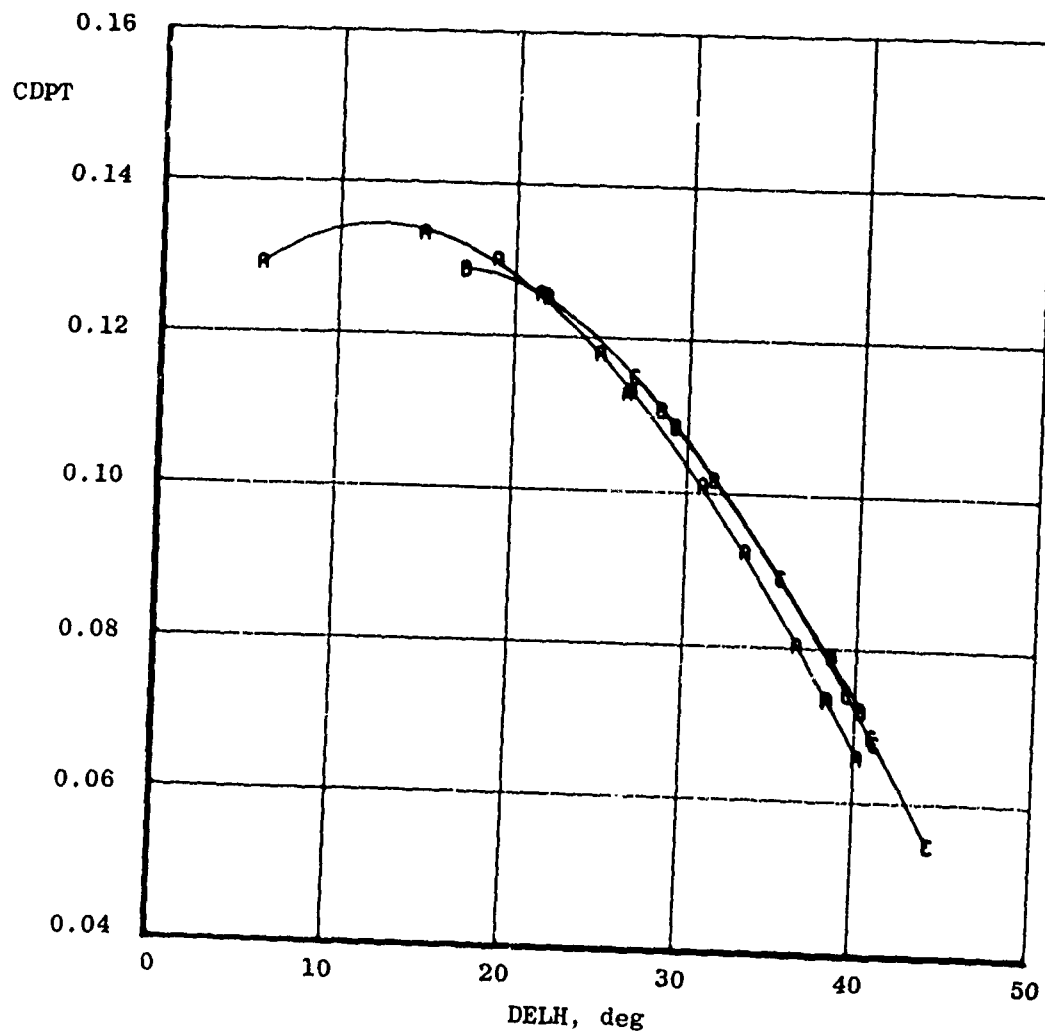
d. $M_{\infty} = 0.95$
Figure 29. Continued.

| Sym | TTJ, $^{\circ}$ R | PN/TP |
|-----|-------------------|-------|
| A | 540 | 2101 |
| B | 1,500 | 5301 |
| C | 2,125 | 5101 |
| D | 2,900 | 5201 |



e. $M_{\infty} = 1.10$
Figure 29. Continued.

| Sym | TTJ, $^{\circ}$ R | PN/TP |
|-----|-------------------|-------|
| A | 540 | 5801 |
| B | 1,950 | 5601 |
| C | 2,700 | 5701 |



f. $M_{\infty} = 1.50$
Figure 29. Concluded.

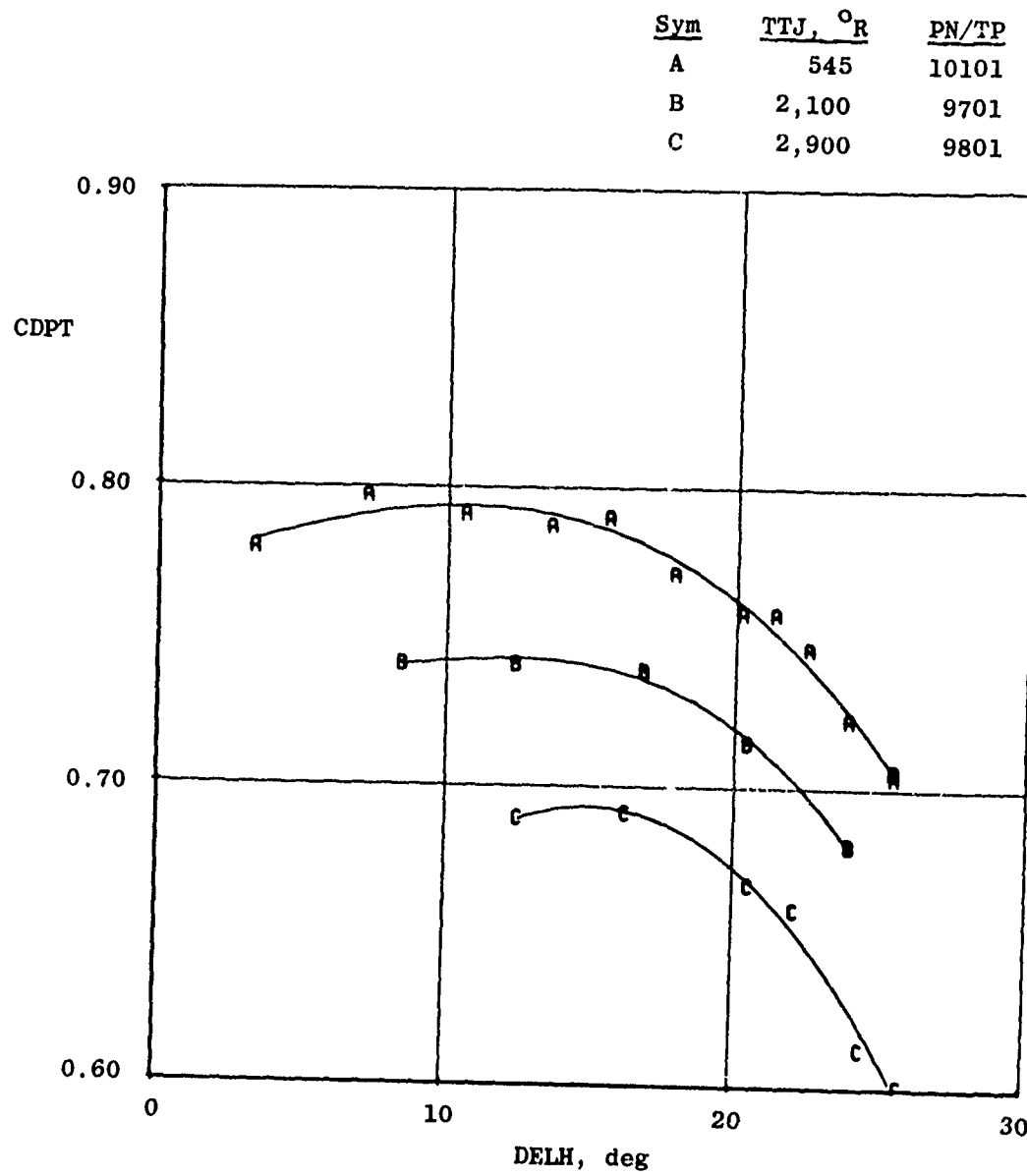
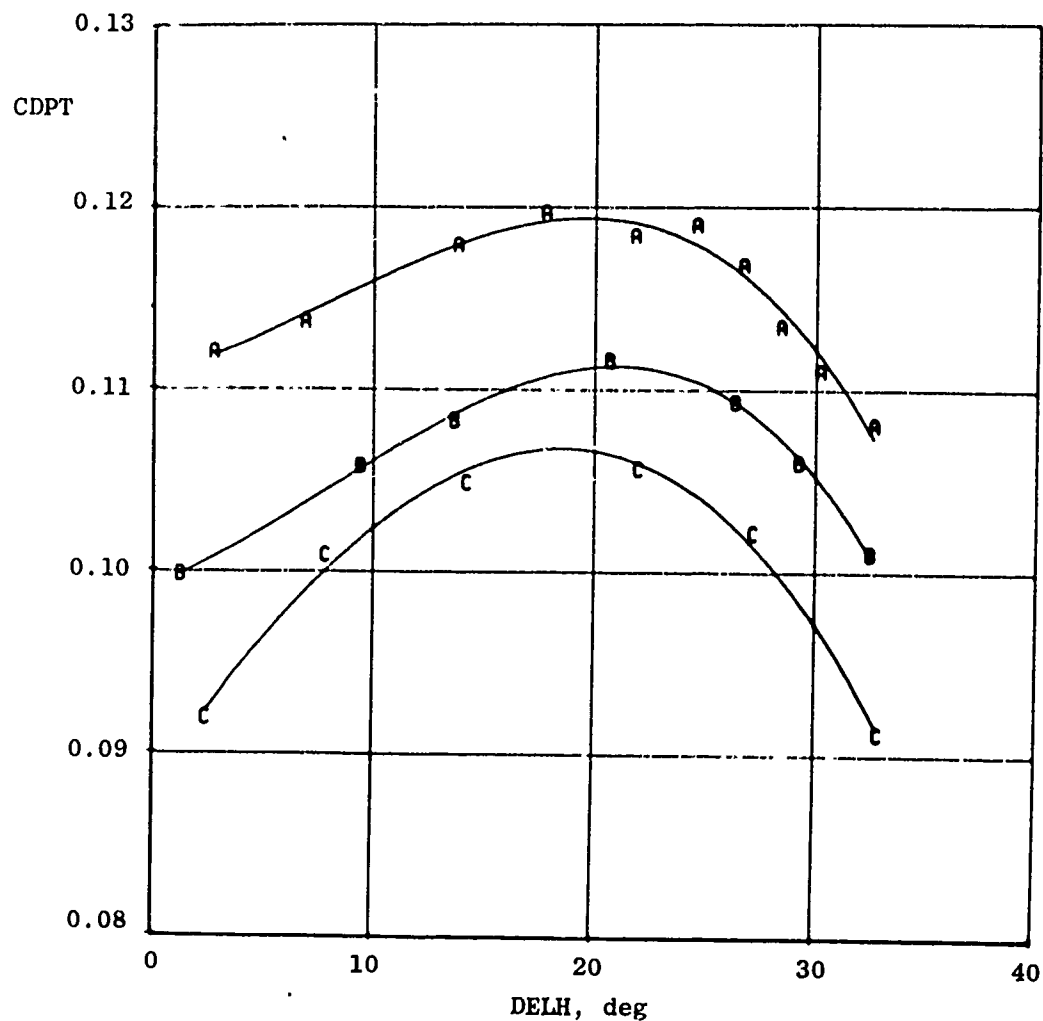
a. $M_{\infty} = 0.60$

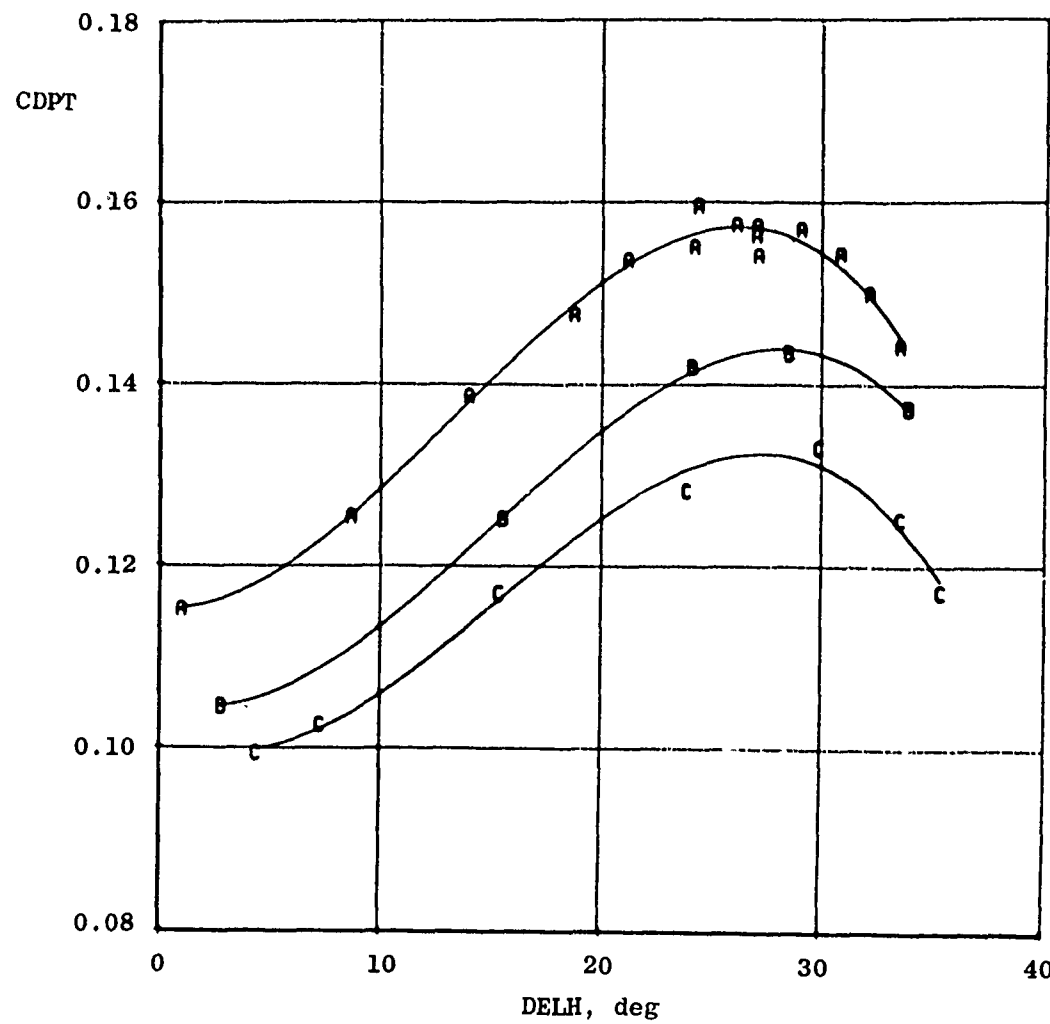
Figure 30. Exhaust plume temperature effects on 25-deg boattail as a function of jet inclination angle.

| Sym | TTJ, $^{\circ}$ R | PN/PT |
|-----|-------------------|-------|
| A | 545 | 7201 |
| B | 2,075 | 7401 |
| C | 2,900 | 7301 |



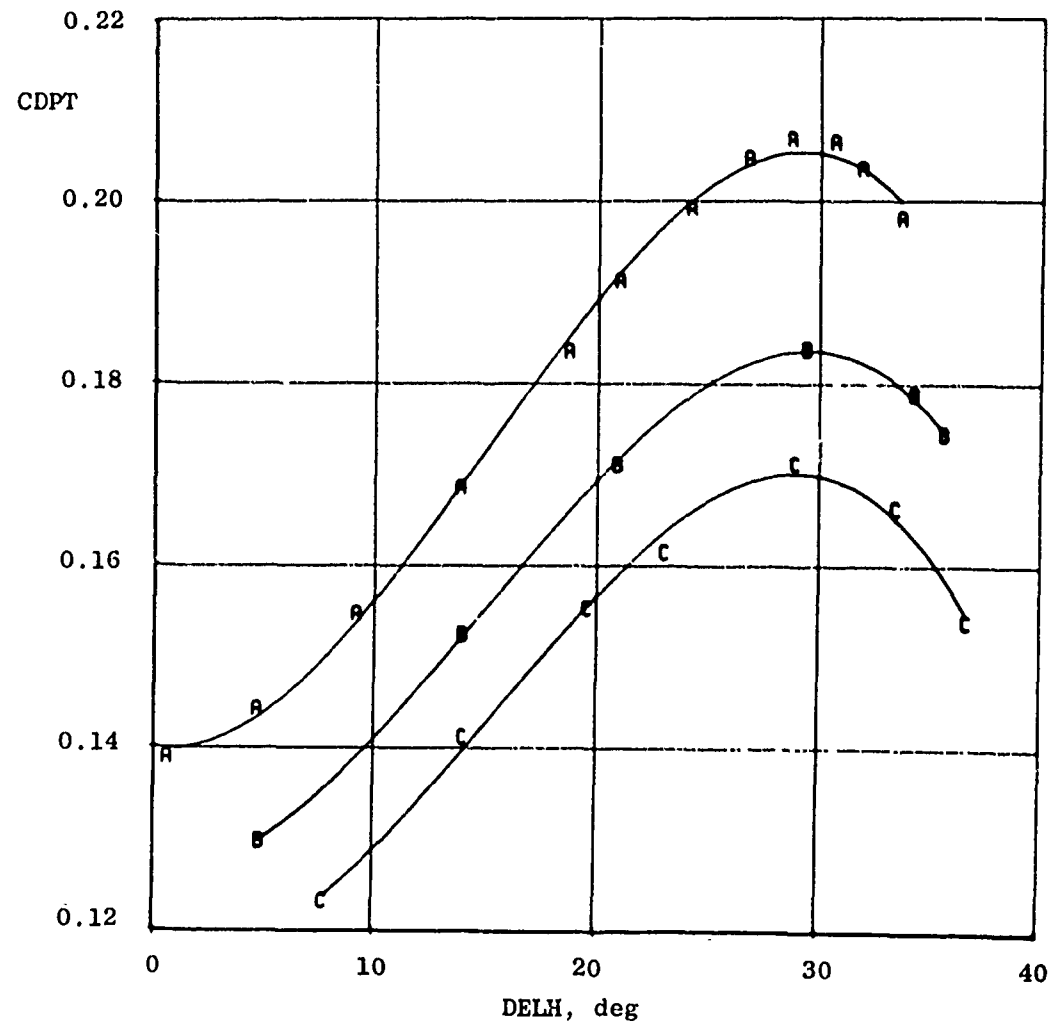
b. $M_{\infty} = 0.80$
Figure 30. Continued.

| Sym | TTJ, $^{\circ}$ R | PN/PT |
|-----|-------------------|-------|
| A | 535 | 7101 |
| B | 2,100 | 7001 |
| C | 2,850 | 6901 |



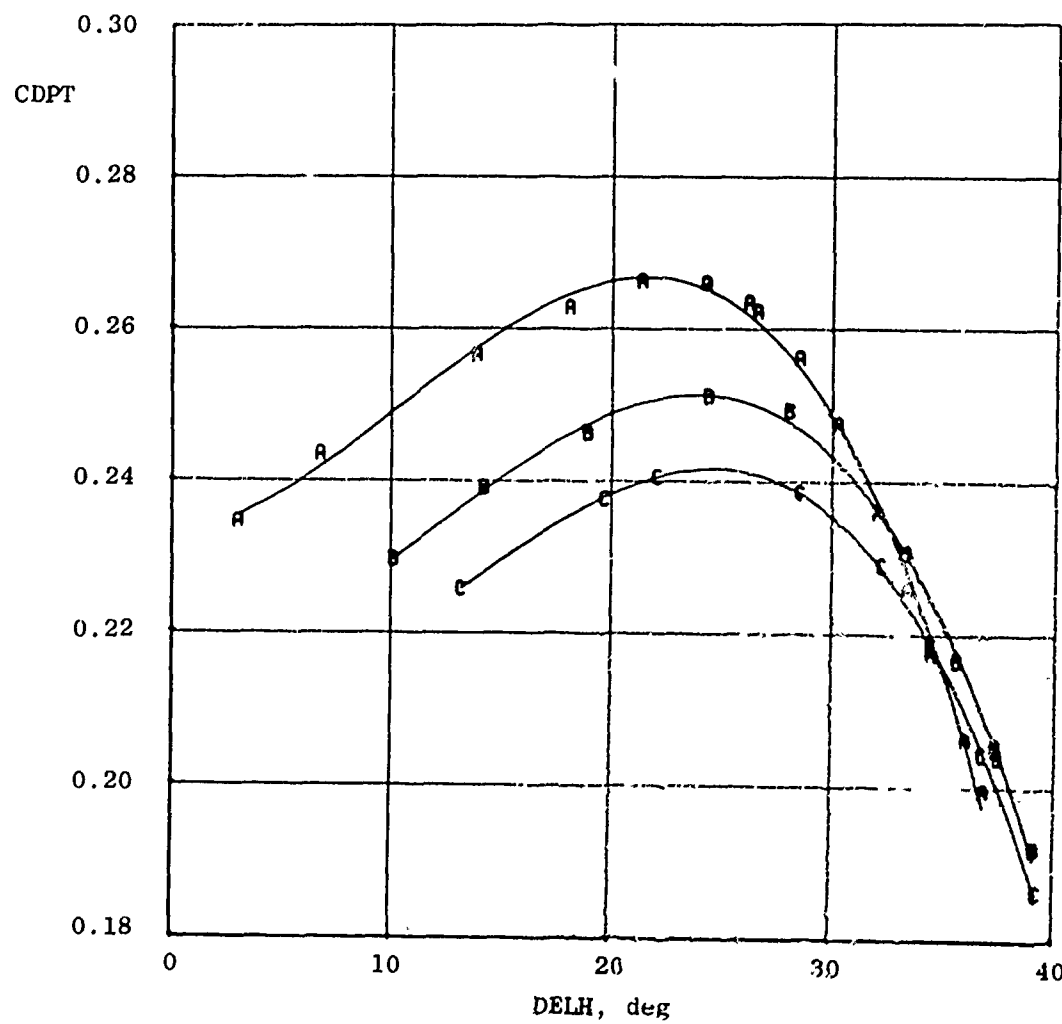
c. $M_{\infty} = 0.90$
Figure 30. Continued.

| Sym | TTJ, $^{\circ}$ R | PN/TP |
|-----|-------------------|-------|
| A | 545 | 8101 |
| B | 2,100 | 7801 |
| C | 2,850 | 7701 |



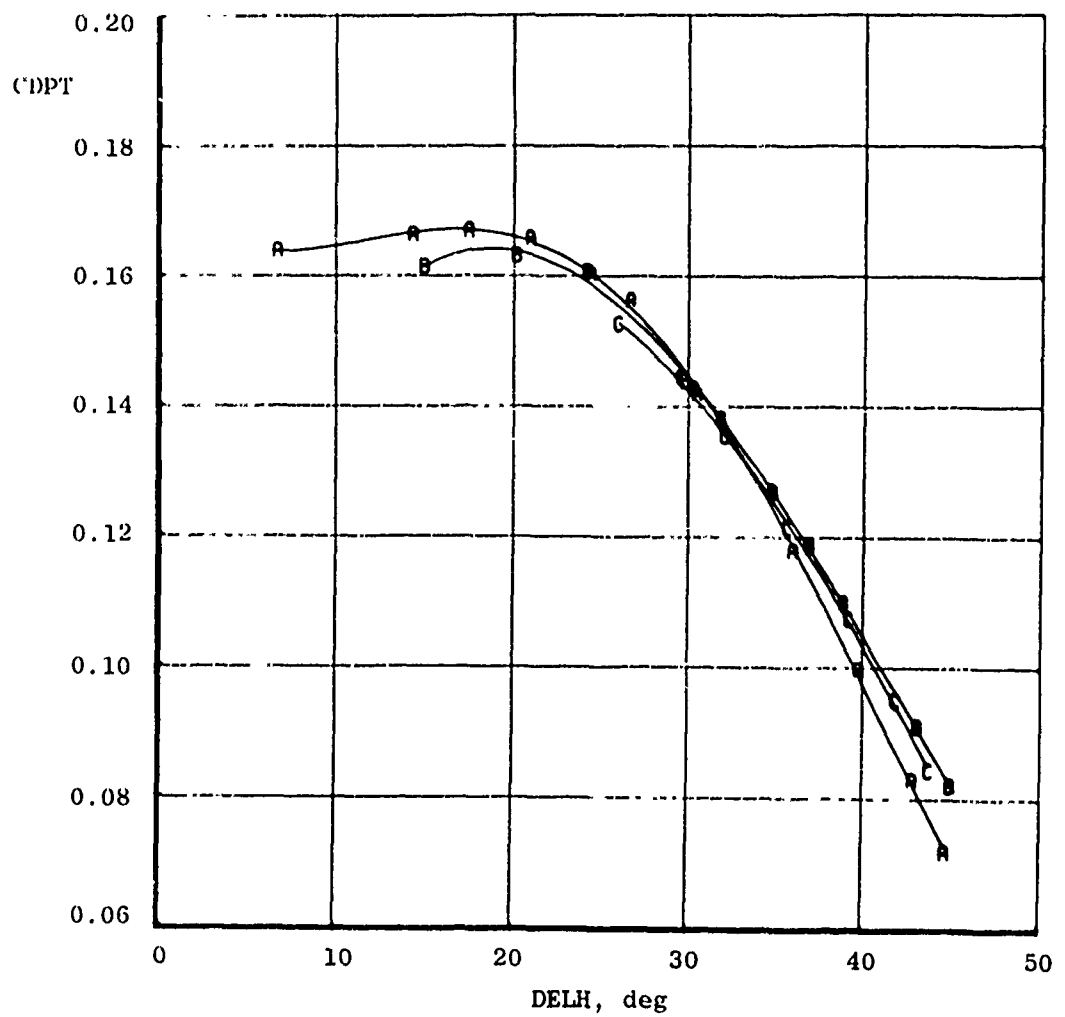
d. $M_{\infty} = 0.95$
Figure 30. Continued.

| Sym | <u>TTJ, $^{\circ}$R</u> | <u>PN/TP</u> |
|-----|------------------------------------|--------------|
| A | 545 | 8201 |
| B | 2,100 | 8401 |
| C | 2,800 | 8301 |

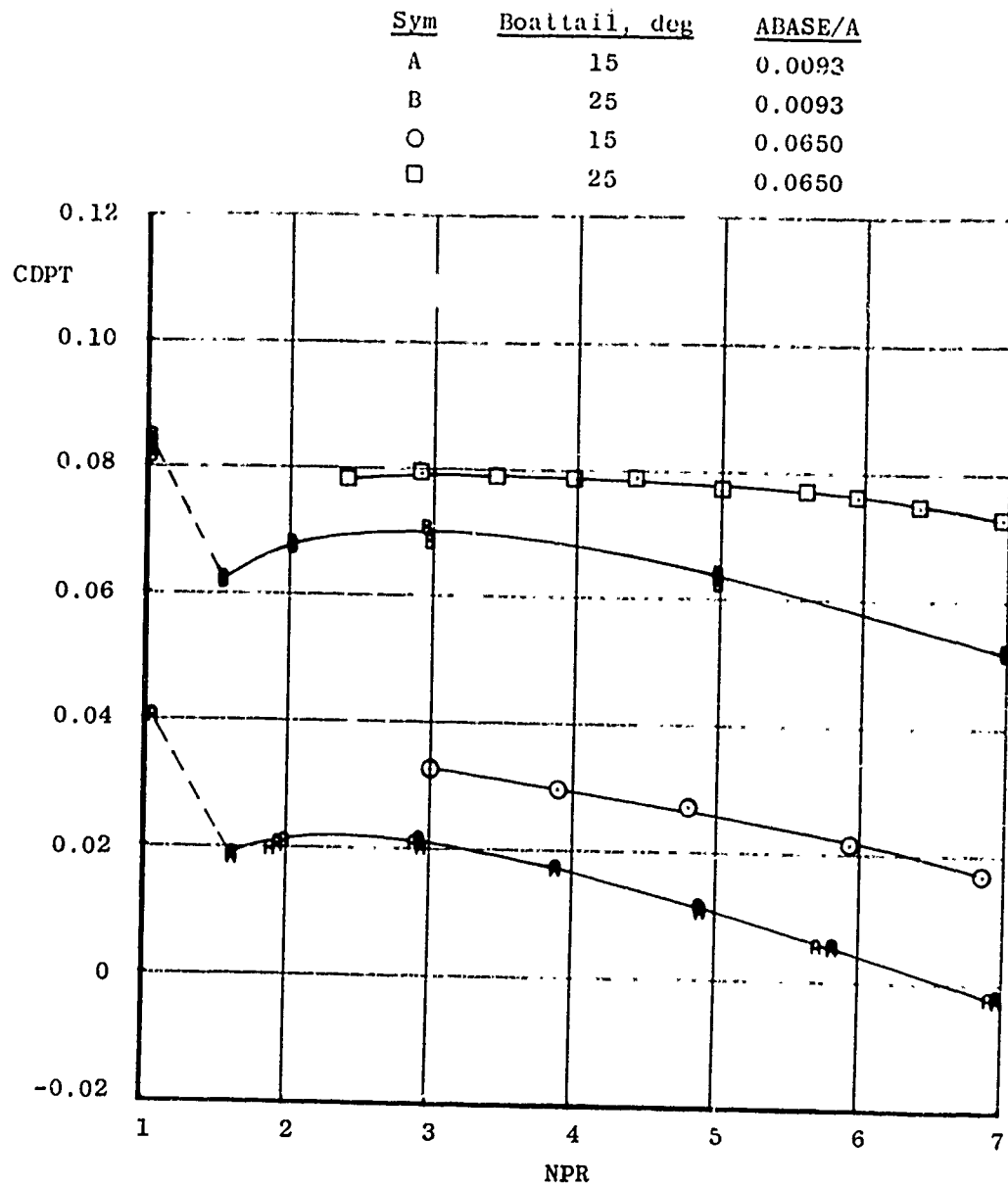


e. $M_{\infty} = 1.10$
Figure 30. Continued.

| <u>Sym</u> | <u>TTJ, $^{\circ}$R</u> | <u>PN/TP</u> |
|------------|------------------------------------|--------------|
| A | 550 | 9101 |
| B | 2,125 | 8701 |
| C | 2,750 | 8801 |

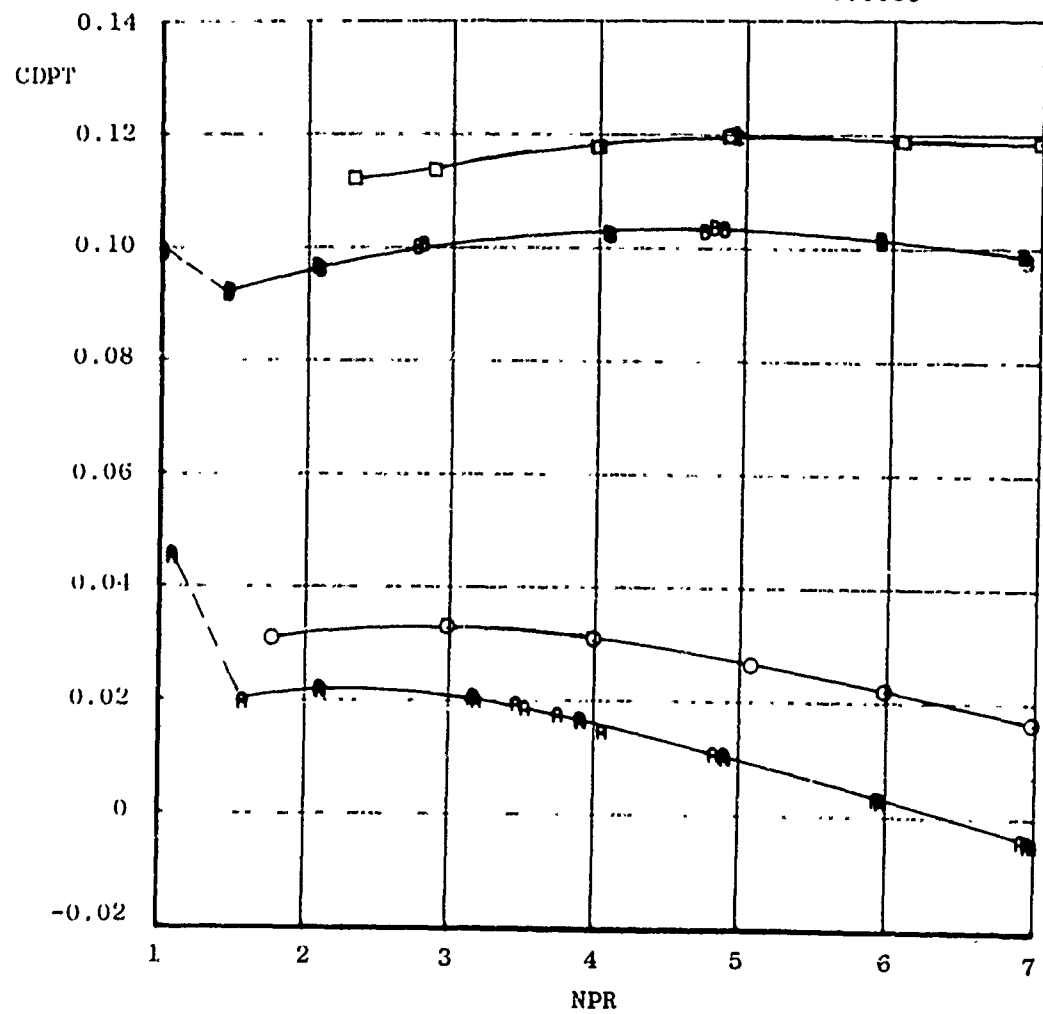


f. $M_{\infty} = 1.50$
Figure 30. Concluded.

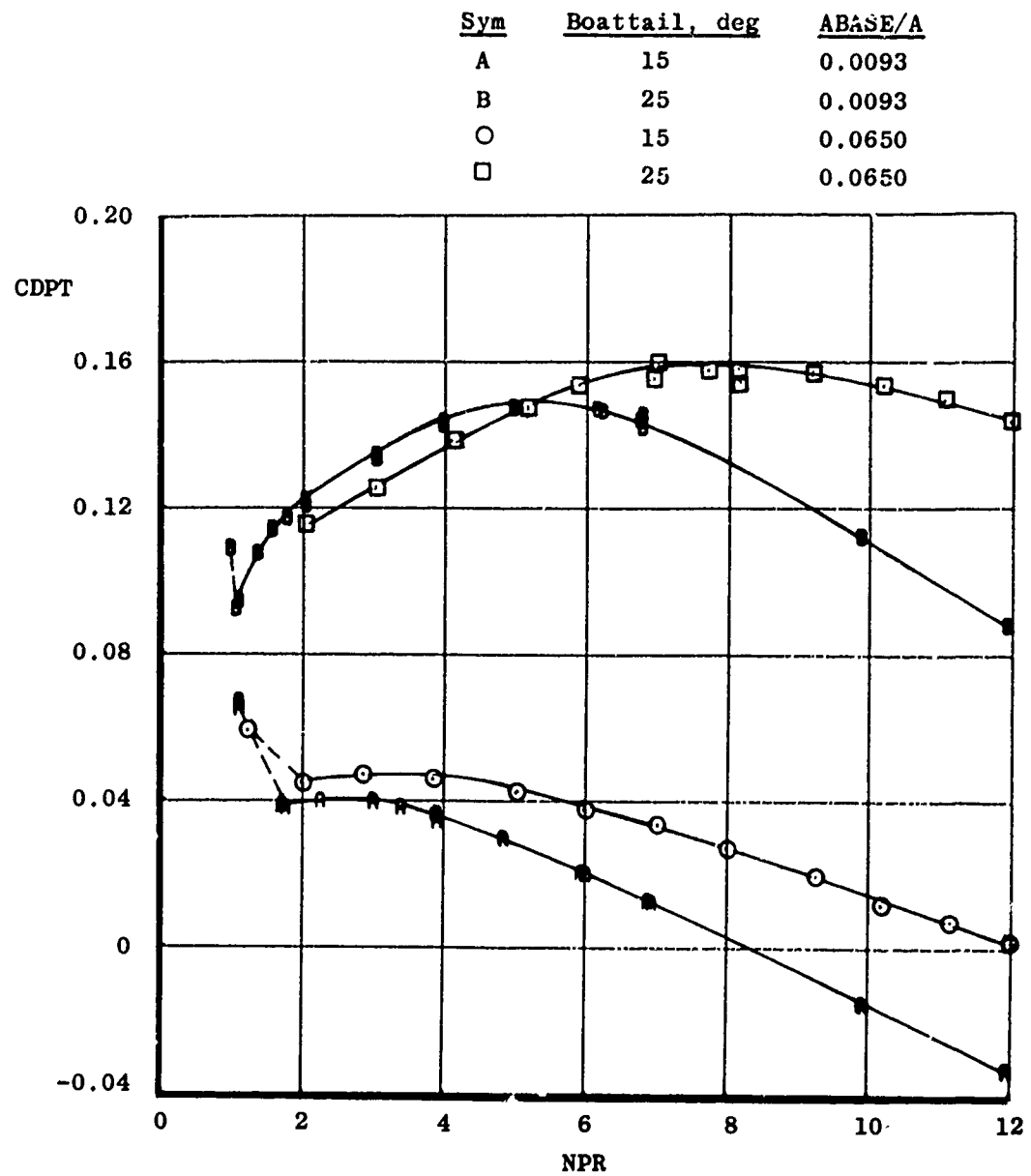


a. $M_\infty = 0.60$
Figure 31. Nozzle base area effects on 15- and 25-deg boattail configurations.

| Sym | Boattail, deg | <u>A_{BASE}/A</u> |
|-----|---------------|---------------------------|
| A | 15 | 0.0093 |
| B | 25 | 0.0093 |
| O | 15 | 0.0650 |
| □ | 25 | 0.0650 |

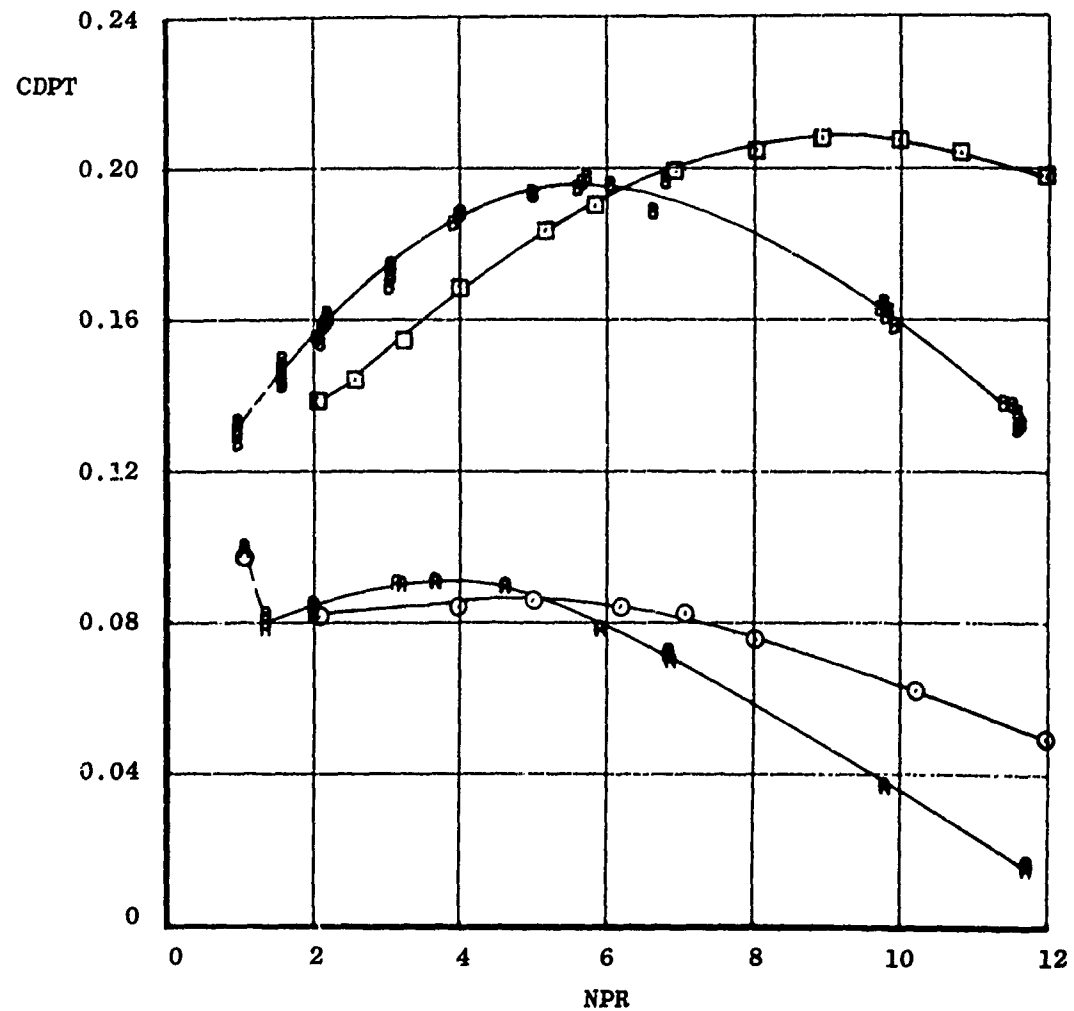


b. $M_{\infty} = 0.80$
Figure 31. Continued.



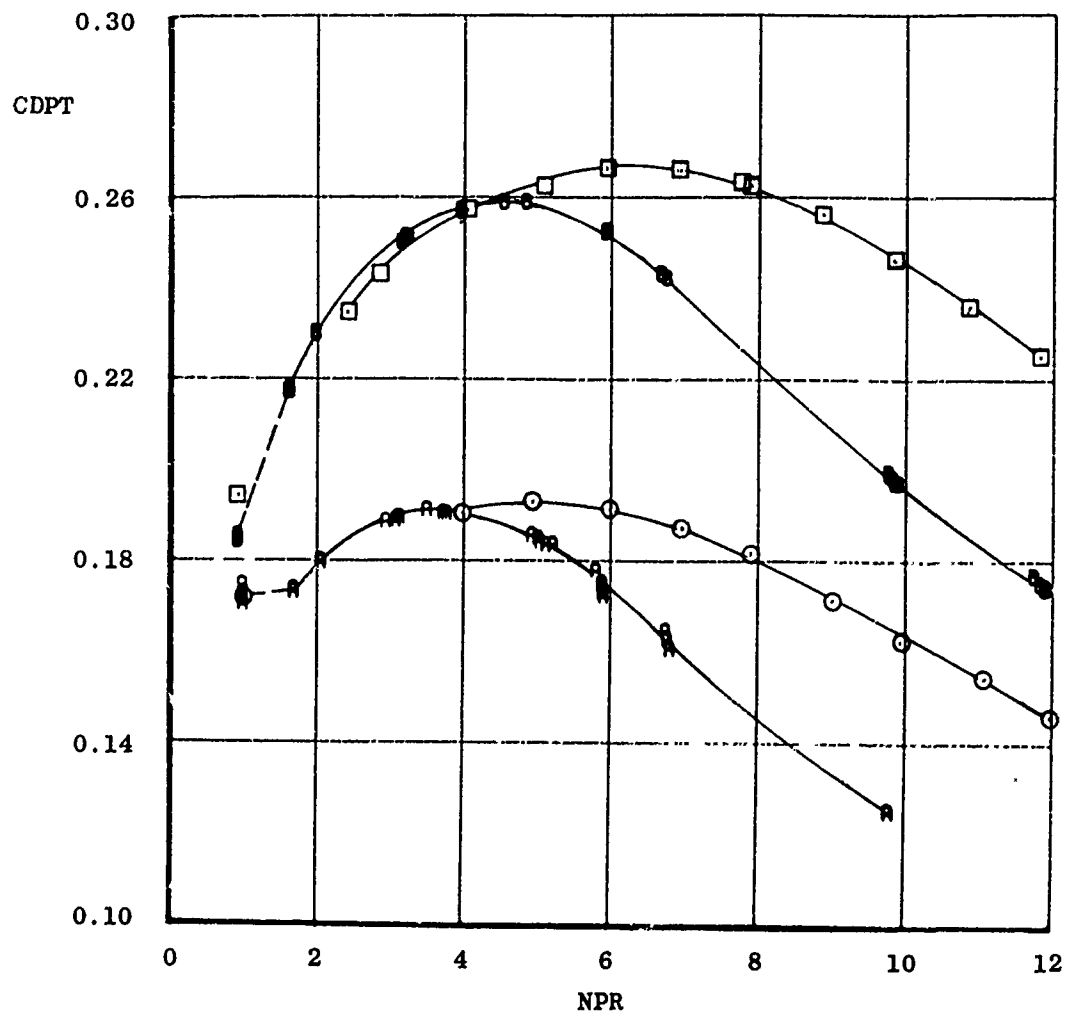
c. $M_{\infty} = 0.90$
 Figure 31. Continued.

| Sym | <u>Boattail, deg</u> | <u>A_{BASE}/A</u> |
|-----|----------------------|---------------------------|
| A | 15 | 0.0093 |
| B | 25 | 0.0093 |
| O | 15 | 0.0650 |
| □ | 25 | 0.0650 |



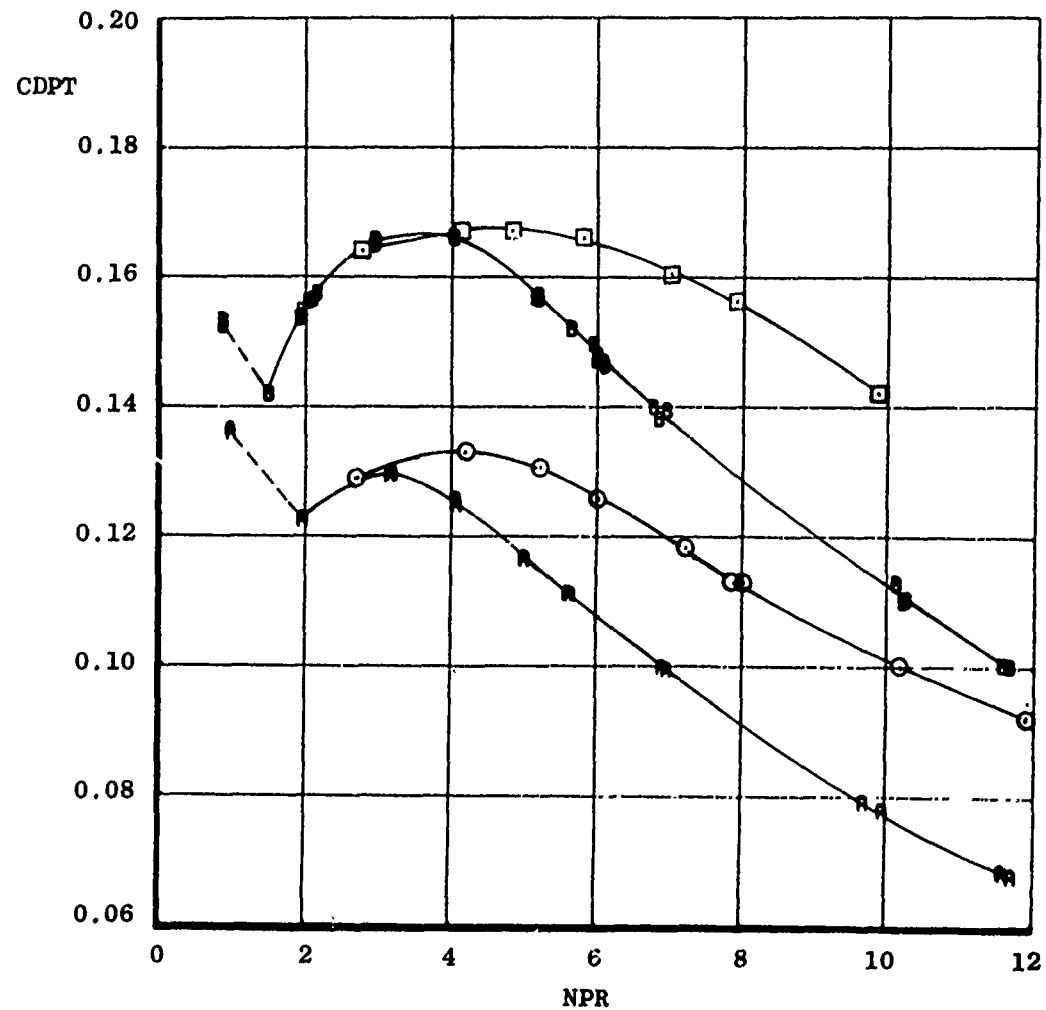
d. $M_{\infty} = 0.95$
Figure 31. Continued.

| Sym | <u>Boattail, deg</u> | <u>A_{BASE}/A</u> |
|-----|----------------------|---------------------------|
| A | 15 | 0.0093 |
| B | 25 | 0.0093 |
| O | 15 | 0.0650 |
| □ | 25 | 0.0650 |



e. $M_{\infty} = 1.10$
Figure 31. Continued.

| Sym | Boattail, deg | <u>A_{BASE}/A</u> |
|-----|---------------|---------------------------|
| A | 15 | 0.0093 |
| B | 25 | 0.0093 |
| O | 15 | 0.0650 |
| □ | 25 | 0.0650 |



f. $M_{\infty} = 1.50$
 Figure 31. Concluded.

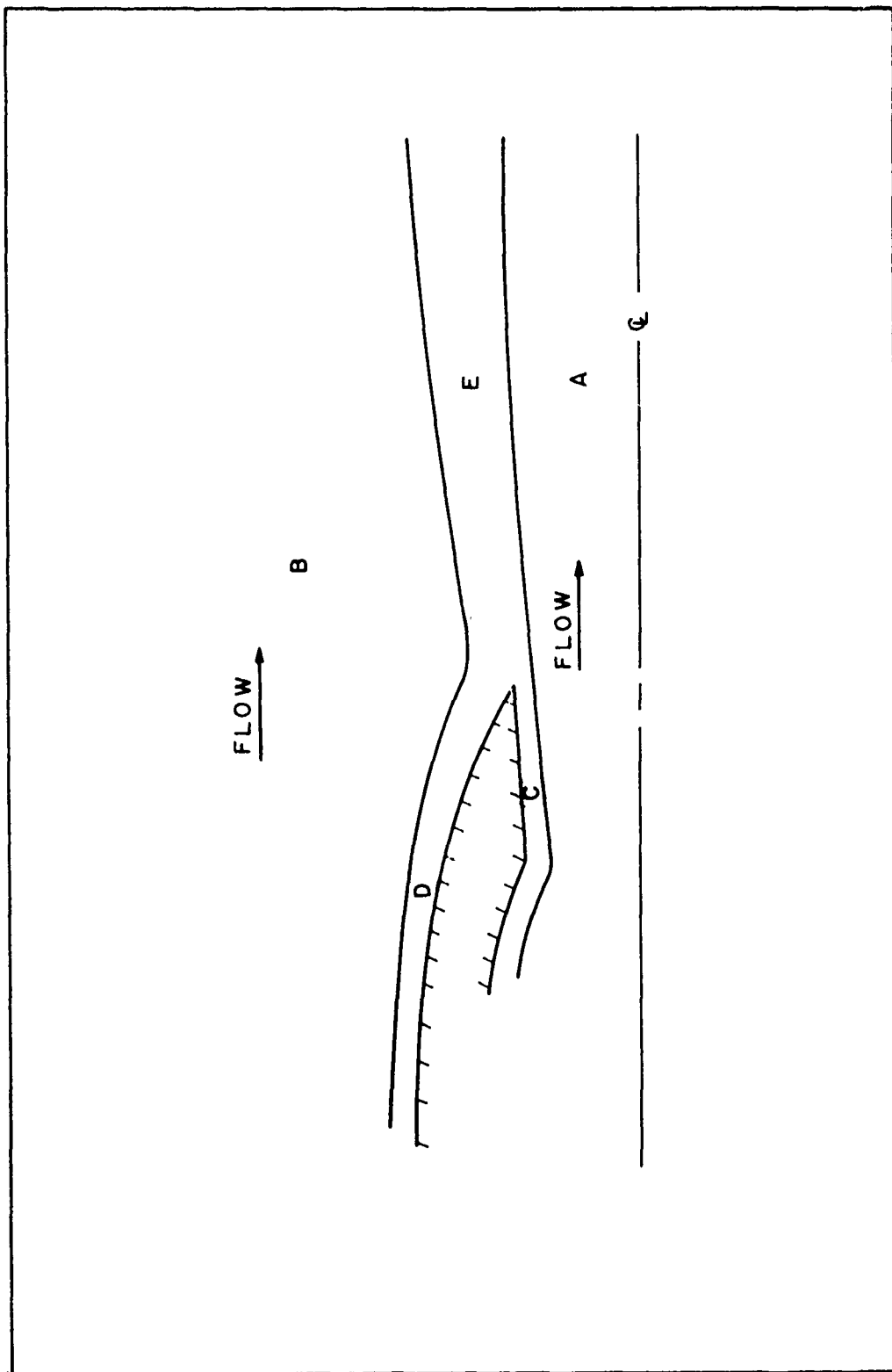


Figure 32. Schematic of the various flow regions involved in the afterbody problem.

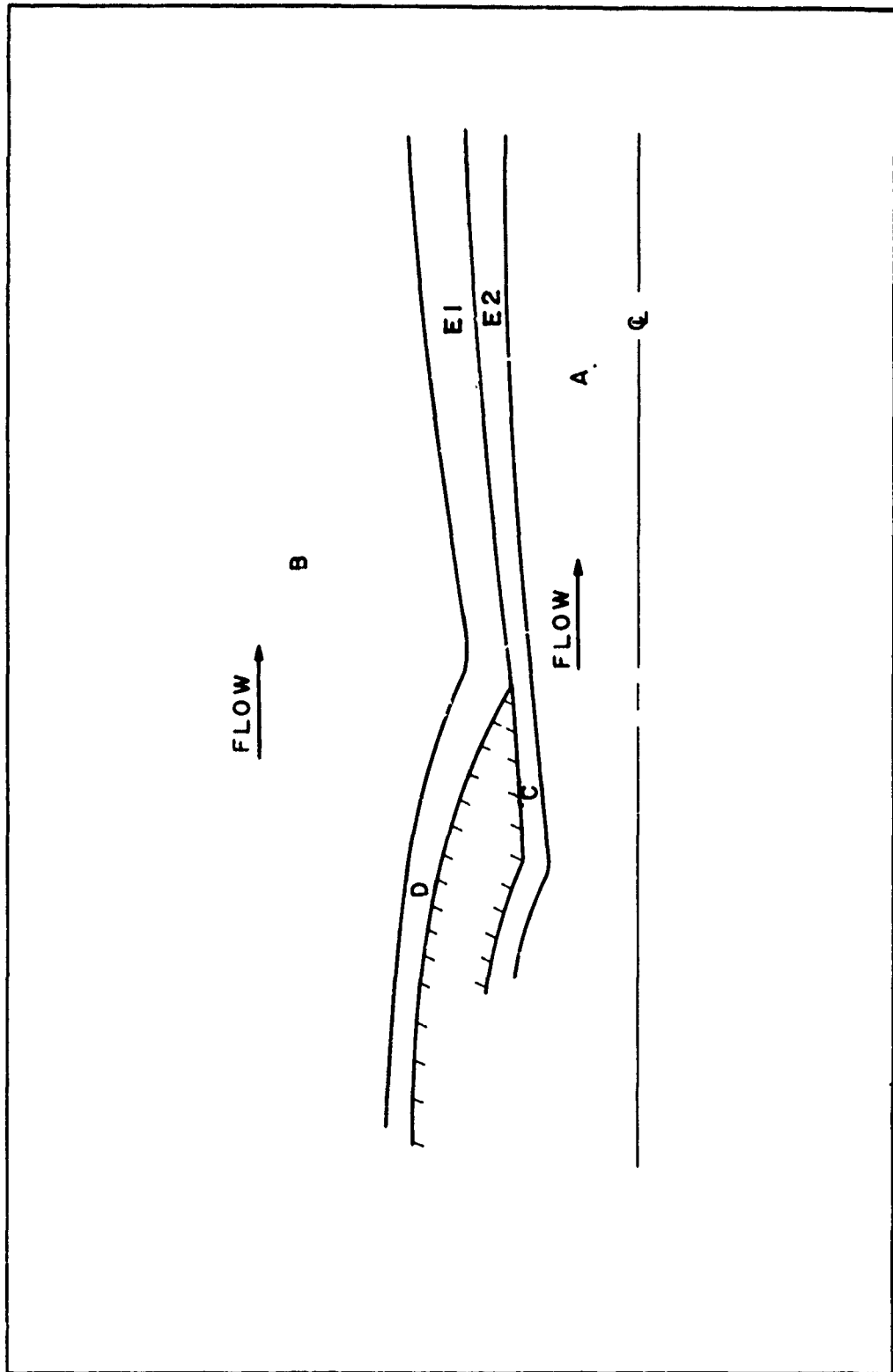


Figure 33. Schematic of the various flow regions involved in the modeling of the afterbody problem.

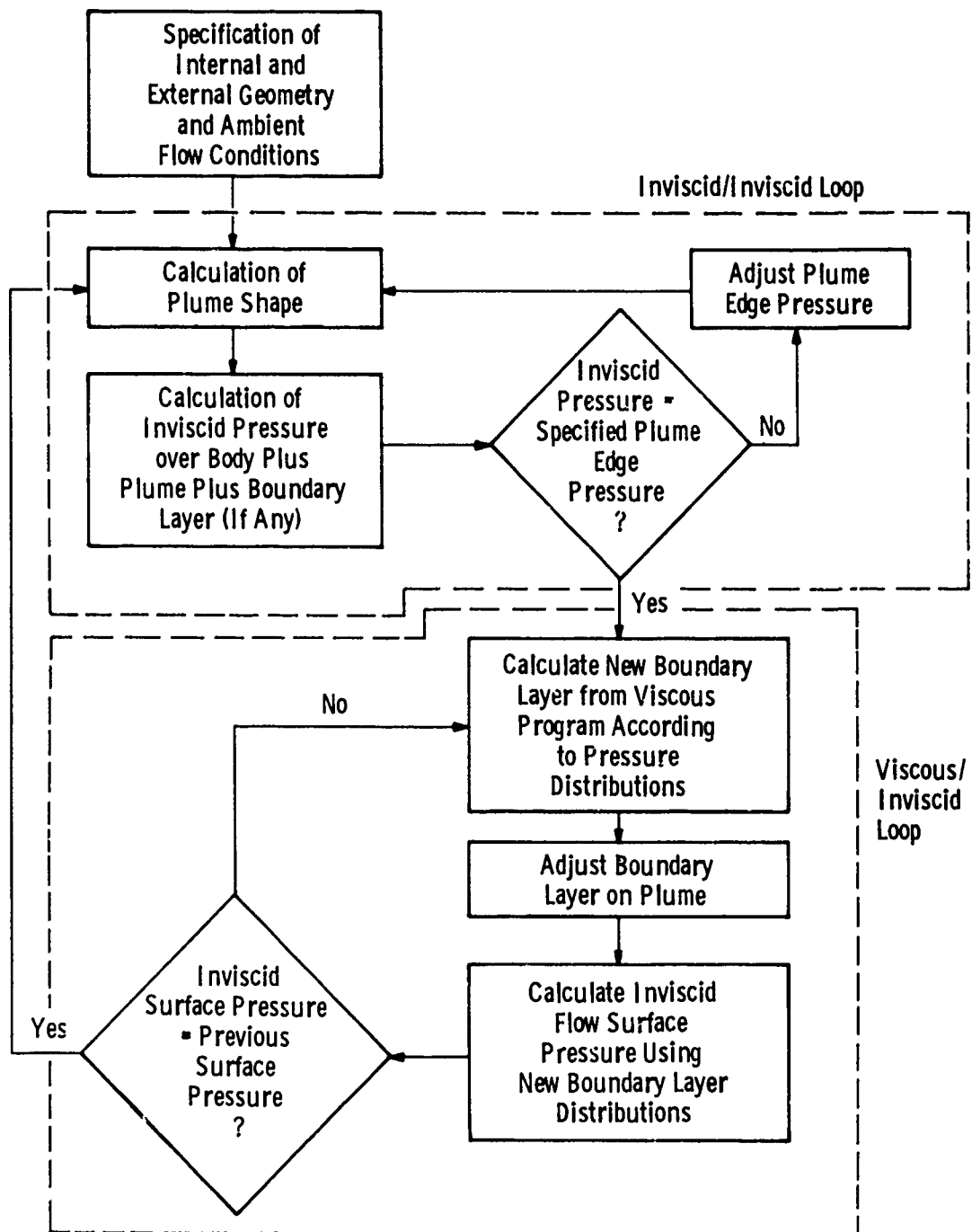


Figure 34. General iteration flow plan.

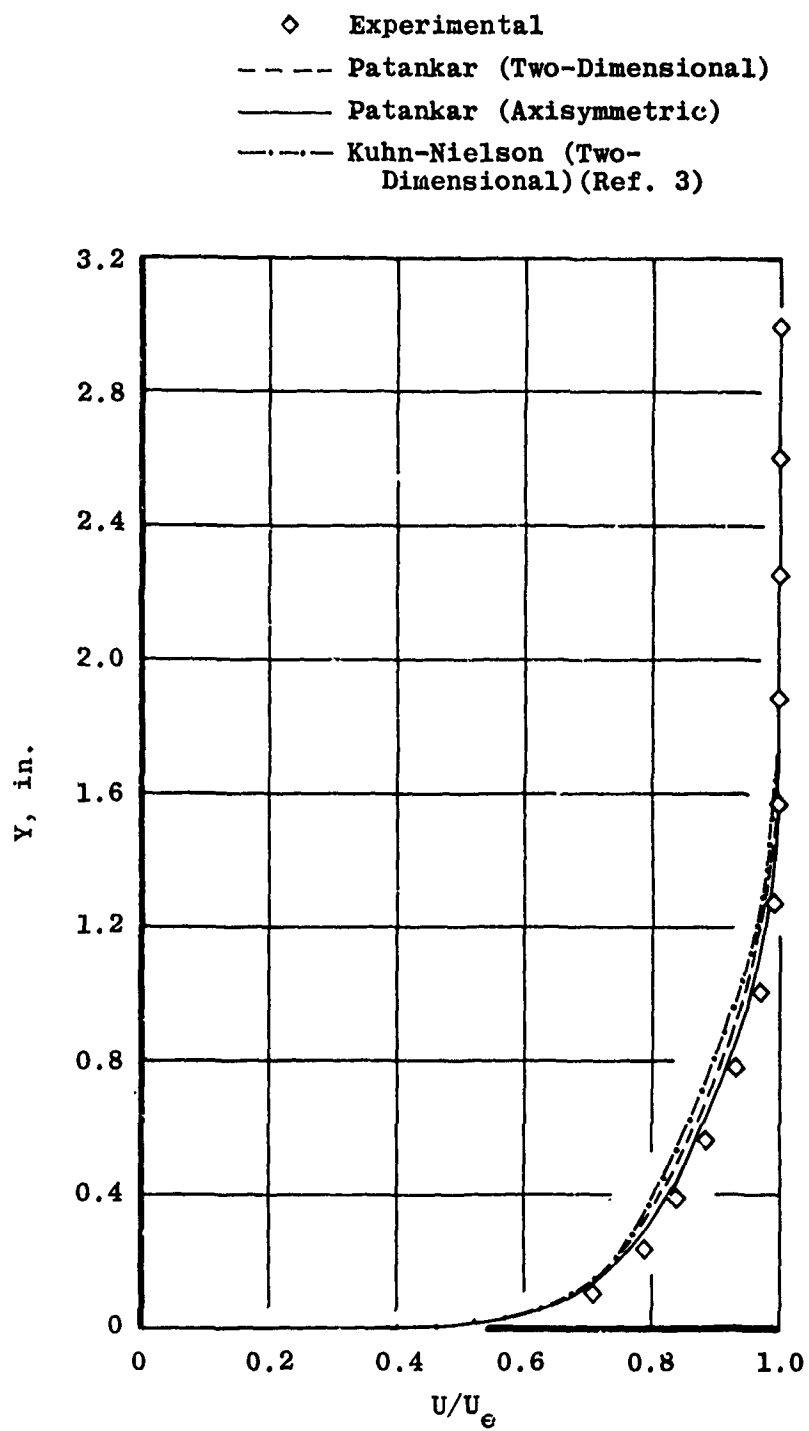


Figure 35. Comparison of computed and measured boundary layer at Mach number 0.9, model station 115.46.

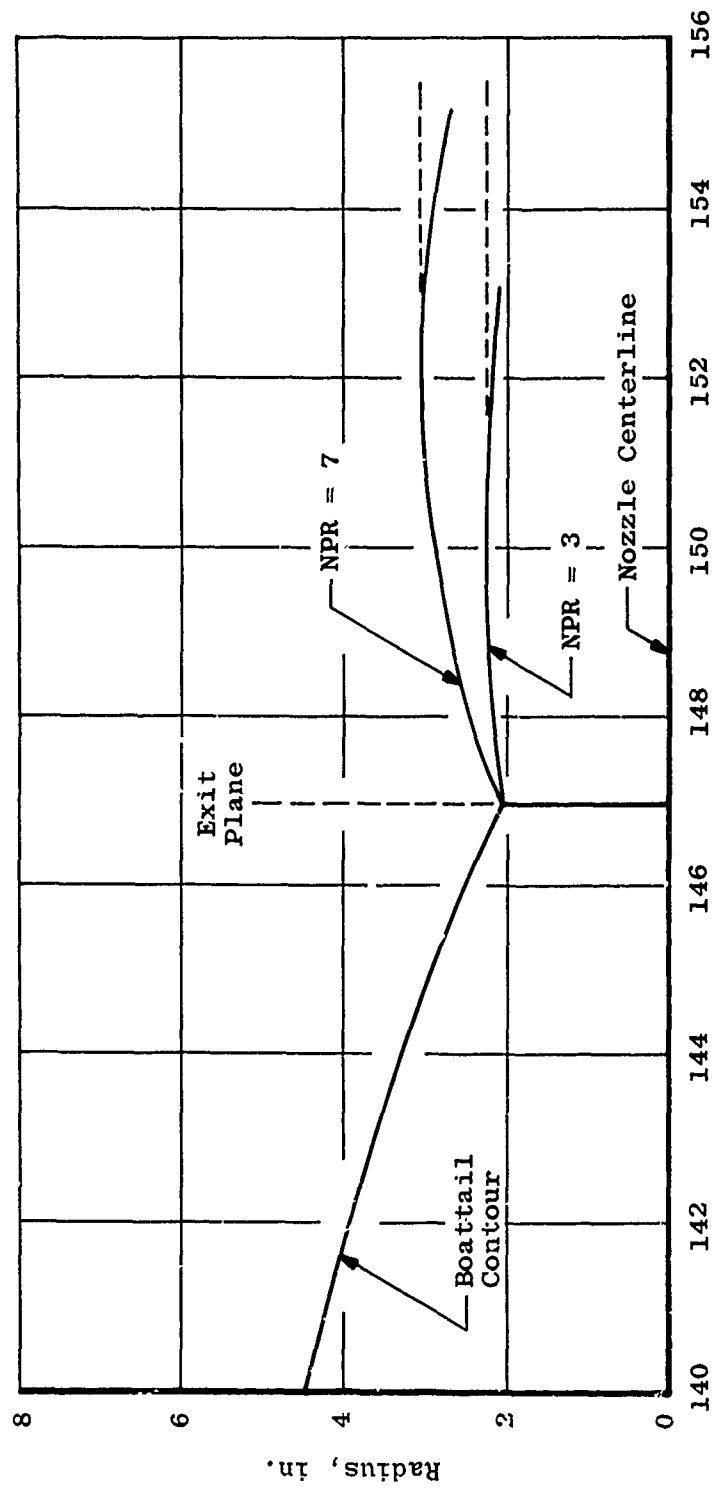
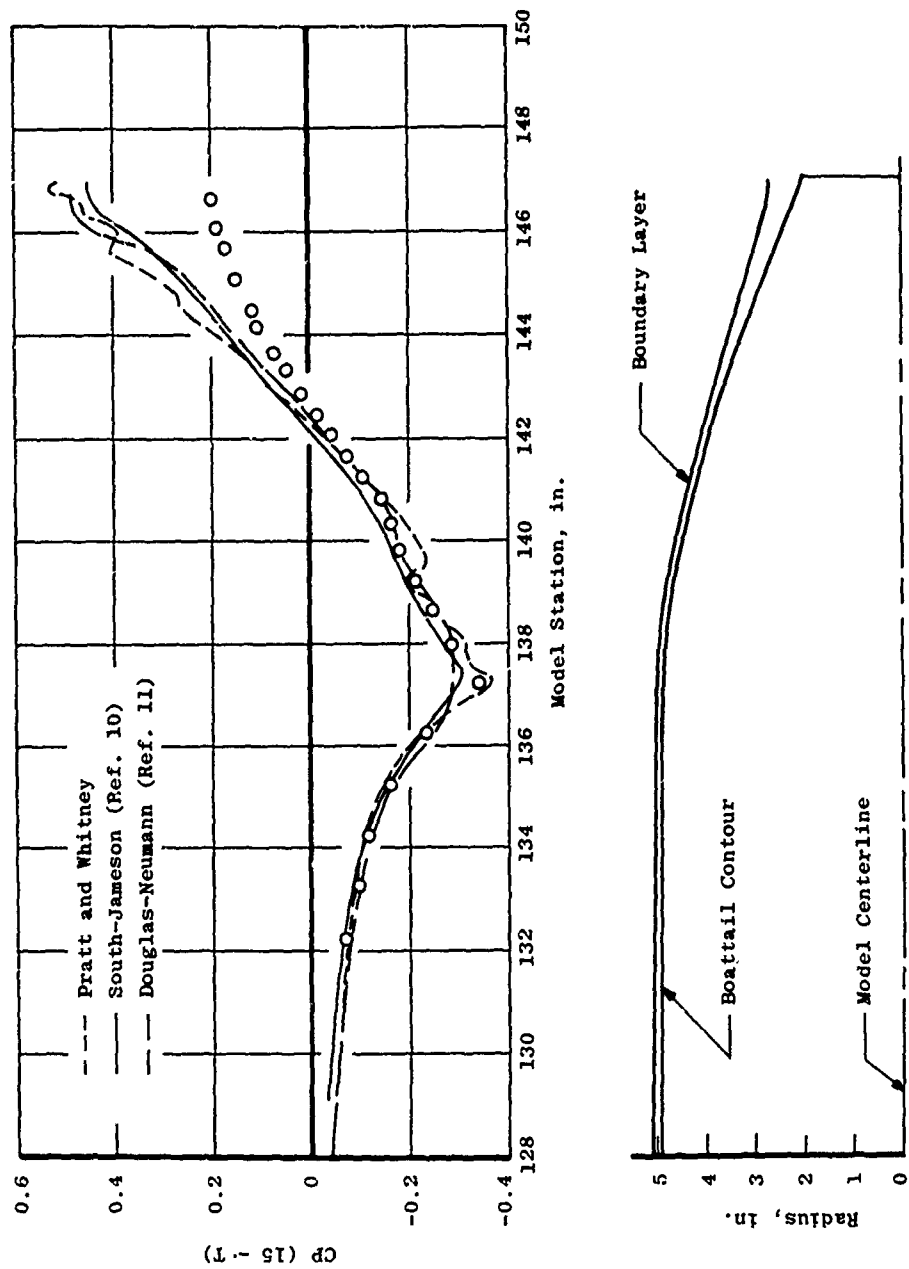
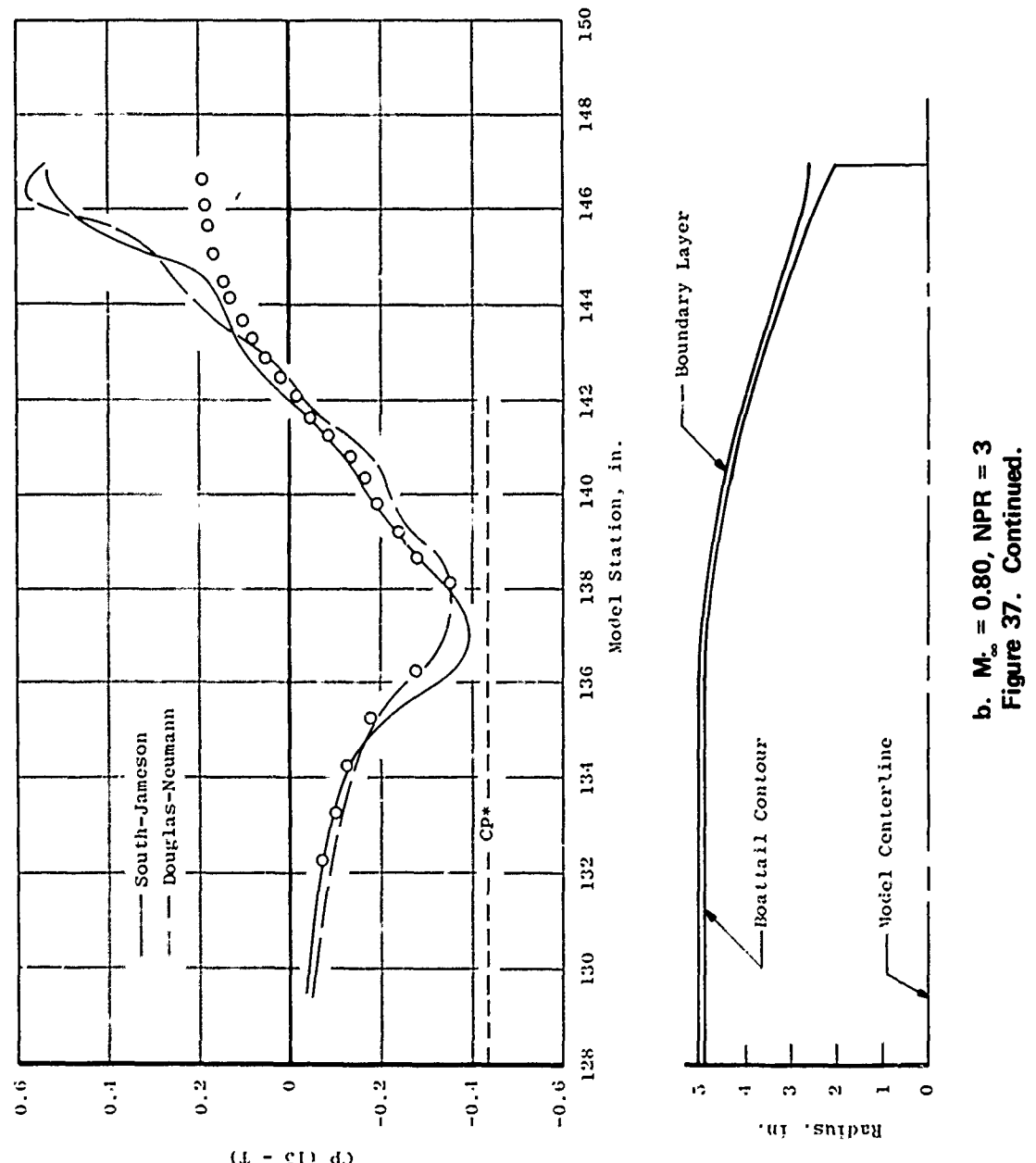


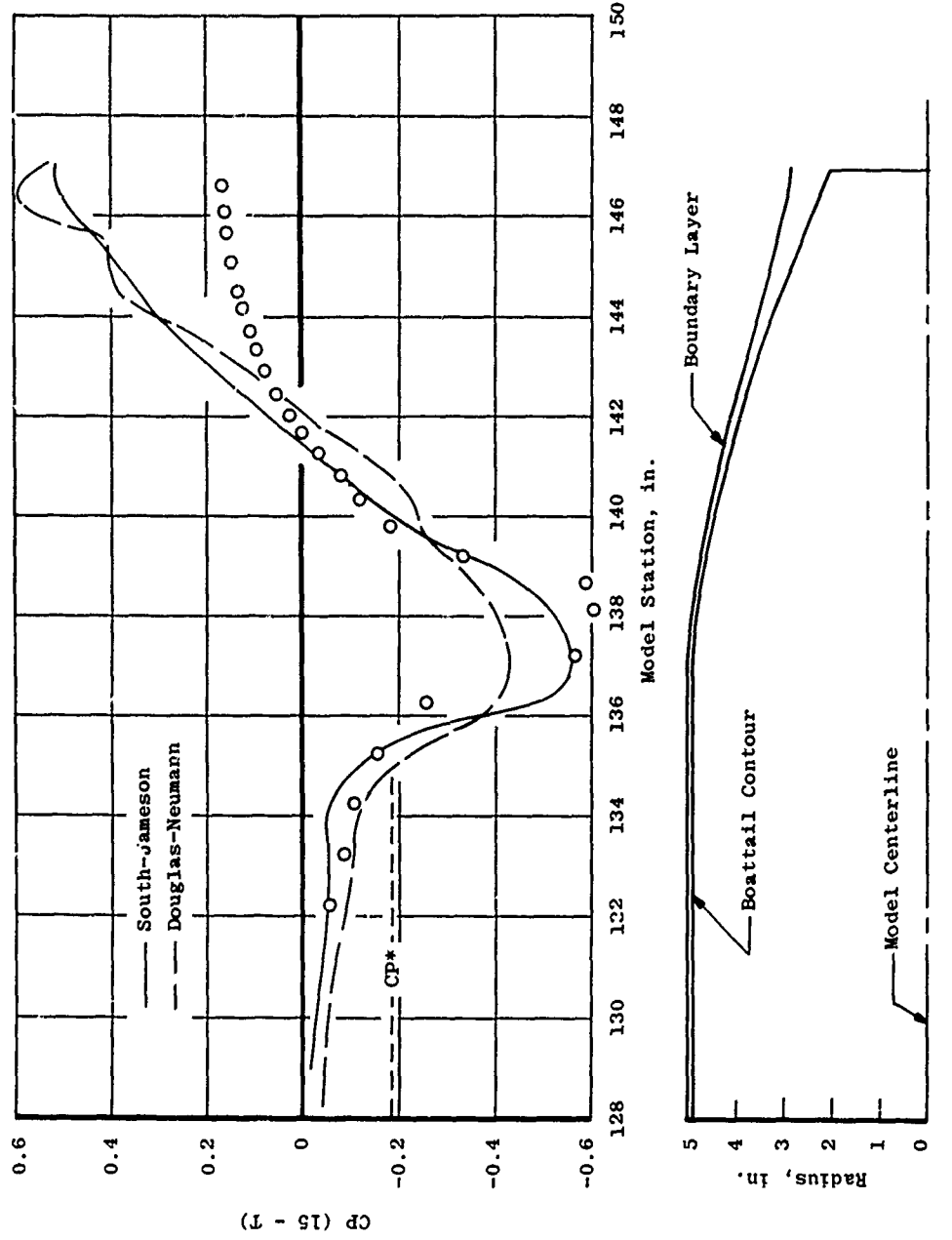
Figure 36. Characteristic plume shapes.



a. $M_\infty = 0.60$, $NPR = 3$
Figure 37. Comparison of computed and measured boattail pressure distributions for the 15-deg boattail configuration.



b. $M_{\infty} = 0.80$, $NPr = 3$
Figure 37. Continued.



c. $M_\infty = 0.90$, $NPR = 3$
Figure 37. Concluded.

Table 1. External Pressure Orifice Locations
a. 10-deg Boattail Configuration

| X | X/D | R | Pressure Orifices | | |
|---------|--------|-------|-------------------|--------|------|
| | | | Top | Bottom | Side |
| -15.581 | -1.580 | 4.930 | 602 | 607 | --- |
| -11.211 | -1.137 | | 603 | 608 | --- |
| -6.831 | -0.693 | | 604 | 609 | --- |
| -2.461 | -0.250 | | 605 | 610 | --- |
| 1.522 | 0.154 | | 401 | 442 | 464 |
| 3.914 | 0.397 | 4.799 | 402 | 443 | 465 |
| 4.874 | 0.494 | 4.706 | 403 | 444 | 466 |
| 5.683 | 0.576 | 4.613 | 404 | 445 | 467 |
| 6.509 | 0.660 | 4.514 | 405 | 446 | 468 |
| 7.178 | 0.728 | 4.426 | 406 | 447 | 469 |
| 7.893 | 0.801 | 4.332 | 407 | 448 | 470 |
| 8.570 | 0.869 | 4.229 | 408 | 449 | 471 |
| 9.292 | 0.942 | 4.120 | 409 | 450 | 472 |
| 10.023 | 1.017 | 4.000 | 410 | 451 | 473 |
| 10.596 | 1.075 | 3.896 | 411 | 452 | 474 |
| 11.186 | 1.134 | 3.780 | 412 | 453 | 475 |
| 11.789 | 1.196 | 3.646 | 413 | 454 | 476 |
| 12.336 | 1.251 | 3.513 | 414 | 455 | 477 |
| 12.834 | 1.302 | 3.379 | 415 | 456 | 478 |
| 13.288 | 1.348 | 3.246 | 416 | 457 | 479 |
| 13.750 | 1.395 | 3.094 | 417 | 458 | 480 |
| 14.180 | 1.438 | 2.941 | 418 | 459 | 481 |
| 14.628 | 1.484 | 2.773 | 419 | 460 | 482 |
| 15.105 | 1.532 | 2.584 | 420 | 461 | 483 |
| 15.670 | 1.589 | 2.342 | 421 | 462 | 484 |
| 16.210 | 1.644 | 2.134 | 422 | 463 | 485 |

X - Location Forward and Aft
MS 130.471

D - Model Maximum Diameter, 9.86 in.

R - Radius

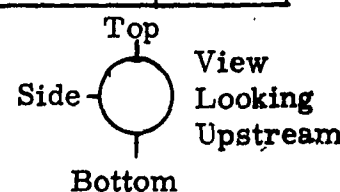


Table 1. Continued
b. 15-deg Boattail Configuration

| X | X/D | R | Pressure Orifices | | |
|---------|--------|-------|-------------------|--------|------|
| | | | Top | Bottom | Side |
| -15.581 | -1.580 | 4.930 | 602 | 607 | --- |
| -11.211 | -1.137 | | 603 | 608 | --- |
| -6.831 | -0.693 | | 604 | 609 | --- |
| -2.461 | -0.250 | | 605 | 610 | --- |
| 1.730 | 0.175 | | 401 | --- | --- |
| 2.725 | 0.276 | 4.925 | 402 | --- | --- |
| 3.727 | 0.378 | 4.921 | 403 | --- | --- |
| 4.725 | 0.479 | 4.920 | 404 | --- | --- |
| 5.725 | 0.581 | 4.919 | 405 | --- | --- |
| 6.725 | 0.682 | 4.884 | 406 | 442 | 464 |
| 7.503 | 0.761 | 4.795 | 407 | 443 | 465 |
| 8.156 | 0.827 | 4.693 | 408 | 444 | 466 |
| 8.707 | 0.883 | 4.591 | 409 | 445 | 467 |
| 9.302 | 0.943 | 4.470 | 410 | 446 | 468 |
| 9.850 | 0.999 | 4.352 | 411 | 447 | 469 |
| 10.294 | 1.044 | 4.245 | 412 | 448 | 470 |
| 10.764 | 1.092 | 4.117 | 413 | 449 | 471 |
| 11.154 | 1.131 | 4.004 | 414 | 450 | 472 |
| 11.565 | 1.173 | 3.882 | 415 | 451 | 473 |
| 11.958 | 1.213 | 3.756 | 416 | 452 | 474 |
| 12.385 | 1.256 | 3.615 | 417 | 453 | 475 |
| 12.787 | 1.297 | 3.447 | 418 | 454 | 476 |
| 13.155 | 1.334 | 3.345 | 419 | 455 | 477 |
| 13.657 | 1.385 | 3.160 | 420 | 456 | 478 |
| 13.960 | 1.416 | 3.042 | 421 | 457 | 479 |
| 14.581 | 1.479 | 2.795 | 422 | 458 | 480 |
| 15.069 | 1.528 | 2.584 | 423 | 459 | 481 |
| 15.560 | 1.578 | 2.364 | 424 | 460 | 482 |
| 16.120 | 1.635 | 2.144 | 425 | 461 | 483 |

X - Location Forward and Aft

MS 130.471

D - Model Maximum Diameter,
9.86 in.

R - Radius

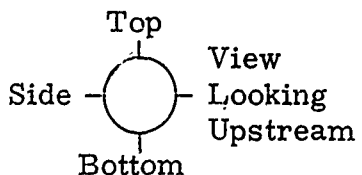


Table 1. Concluded
c. 25-deg Boat tail Configuration

| X | X/D | R | Pressure Orifices | | |
|---------|--------|-------|-------------------|--------|------|
| | | | Top | Bottom | Side |
| -15.581 | -1.580 | 4.930 | 602 | 607 | --- |
| -11.211 | -1.137 | | 603 | 608 | --- |
| -6.831 | -0.693 | | 604 | 609 | --- |
| -2.461 | -0.250 | | 605 | 610 | --- |
| 2.433 | 0.247 | | 401 | --- | --- |
| 3.433 | 0.348 | | 402 | --- | --- |
| 4.433 | 0.450 | | 403 | --- | --- |
| 5.433 | 0.551 | | 404 | --- | --- |
| 6.433 | 0.652 | | 405 | --- | --- |
| 7.433 | 0.754 | | 406 | --- | --- |
| 8.433 | 0.855 | | 407 | --- | --- |
| 9.431 | 0.956 | ↓ | 408 | --- | --- |
| 10.430 | 1.058 | 4.886 | 409 | 442 | 464 |
| 10.730 | 1.088 | 4.800 | 410 | 443 | 465 |
| 11.040 | 1.120 | 4.672 | 411 | 444 | 466 |
| 11.358 | 1.152 | 4.509 | 412 | 445 | 467 |
| 11.682 | 1.185 | 4.342 | 413 | 446 | 468 |
| 12.029 | 1.220 | 4.167 | 414 | 447 | 469 |
| 12.381 | 1.256 | 3.986 | 415 | 448 | 470 |
| 12.761 | 1.294 | 3.798 | 416 | 449 | 471 |
| 13.151 | 1.334 | 3.602 | 417 | 450 | 472 |
| 13.562 | 1.375 | 3.403 | 418 | 451 | 473 |
| 13.995 | 1.419 | 3.200 | 419 | 452 | 474 |
| 14.461 | 1.467 | 2.982 | 420 | 453 | 475 |
| 14.969 | 1.518 | 2.747 | 421 | 454 | 476 |
| 15.516 | 1.574 | 2.485 | 422 | 455 | 477 |
| 16.138 | 1.637 | 2.198 | 423 | 456 | 478 |

X - Location Forward and Aft

MS 130.471

D - Model Maximum Diameter,
9.86 in.

R - Radius

Top
View
Looking
Upstream
Side
Bottom

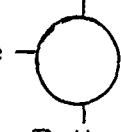
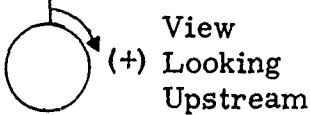


Table 2. Cold Flow Nozzle Assembly Instrumentation

Total Pressure Rake (MS 133.587)

| <u>Pressure</u> | <u>Position (Radius, in.)</u> |
|-----------------|-------------------------------|
| PTJ 1 | Nozzle Centerline |
| 2 | 0.389 |
| 3 | 0.778 |
| 4 | 1.167 |
| 5 | 1.556 |
| 6 | 1.945 |
| 7 | 2.334 |
| 8 | 2.723 |
| 9 | 3.112 |
| 10 | 3.501 |

Wall Static Pressures (MS 133.57)

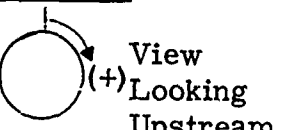
| <u>Pressure</u> | <u>Position, deg</u> |  |
|-----------------|----------------------|--------------------------------------------------------------------------------------|
| PW 1 | 45 | (+) View Looking Upstream |
| 2 | 135 | |
| 3 | 225 | |
| 4 | 315 | |

Total Temperature Probes (MS 135.70)

| <u>Temperature</u> | <u>Position, deg</u> |
|--------------------|----------------------|
| TD 1 | 120 |
| TD 2 | 240 |

Table 3. Hot Flow Nozzle Assembly Instrumentation

Chamber Wall Static Pressures (MS 136.47)

| <u>Pressure</u> | <u>Position, deg</u> |  |
|-----------------|----------------------|-------------------------------------------------------------------------------------|
| PW 1 | 45 | |
| 2 | 135 | |
| 3 | 225 | |
| 4 | 315 | |

Nozzle Exit Static Pressures (MS 146.895)

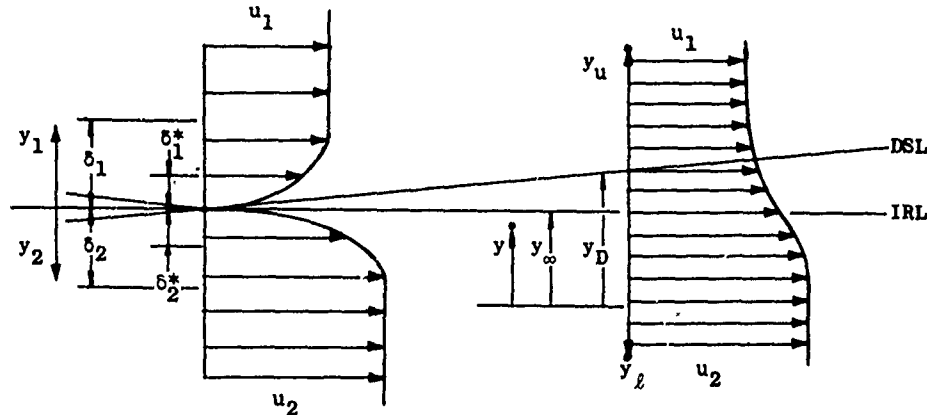
| <u>Pressure</u> | <u>Position, deg</u> |
|-----------------|----------------------|
| PE 1 | 45 |
| 2 | 135 |
| 3 | 225 |
| 4 | 315 |

Chamber Liner Temperatures (MS 146.895)

| <u>Temperature</u> | <u>Position, deg</u> |
|--------------------|----------------------|
| TL 1 | 0 |
| TL 2 | 180 |

APPENDIX A
PLUME DISPLACEMENT THICKNESS CALCULATION

Assume that the static pressure is everywhere constant and that the flow direction is parallel to the inviscid reference line (IRL); that is, transverse (y -direction) flow may be neglected.



Mass is conserved above the DSL.

$$\begin{aligned}
 \int_0^{y_u - y_\infty} \rho u dy_1 &= \int_{y_D}^{y_u} \rho u dy \\
 \int_0^{\delta_1} \rho u dy_1 + \int_{\delta_1}^{y_u - y_\infty} \rho_1 u_1 dy_1 &= \int_{y_D}^{y_u} \rho u dy \quad (1) \\
 \int_0^{\delta_1} \rho u dy_1 + \rho_1 u_1 (y_u - y_\infty - \delta_1) &= \int_{y_D}^{y_u} \rho u dy
 \end{aligned}$$

Apply the definition of δ^* at the downstream position assuming the DSL as the surface, as follows:

$$\begin{aligned}
 \delta_p^* &= \int_{y_D}^{y_u} \left(1 - \frac{\rho u}{\rho_1 u_1}\right) dy \\
 \int_{y_D}^{y_u} \rho u dy &= -\rho_1 u_1 (\delta_p^* - y_u + y_D) \quad (2)
 \end{aligned}$$

Combining (1) and (2) gives

$$\int_0^{\delta_1} \rho u dy_1 + \rho_1 u_1 (y_D + \delta_p^* - y_\infty - \delta_1) = 0 \quad (3)$$

Apply the definition of δ^* to the upstream position, as follows:

$$\begin{aligned} \delta_1^* &= \int_0^{\delta_1} \left(1 - \frac{\rho u}{\rho_1 u_1}\right) dy_1 \\ \int_0^{\delta_1} \rho u dy_1 &= \rho_1 u_1 (\delta_1 - \delta_1^*) \end{aligned} \quad (4)$$

Substitution of (4) into (3) gives

$$\delta_p^* = \delta_1^* + (y_\infty - y_D) \quad (5)$$

The displacement relative to the IRL boundary is, by definition

$$\delta_{IRL}^* = (y_D - y_\infty) + \delta_p^* \quad (6)$$

Combining Eqs. (5) and (6) yields

$$\delta_{IRL}^* = \delta_1^*$$

Thus, the "plume displacement thickness" relative to the IRL is simply the displacement thickness of the boundary layer at the afterbody/plume junction.

NOMENCLATURE

| | |
|-----------------|-------------------------------------------------------------------------------------------------------------------------------------------------|
| A | Model cross-sectional area, 0.5303 ft ² |
| ABASE | Nozzle annular base area, 0.03450 ft ² (hot flow nozzle) and 0.00492 ft ² (cold flow nozzle) |
| AT | Nozzle throat area, 0.05683 ft ² (hot flow nozzle) and 0.08648 ft ² (cold flow nozzle) |
| CDND | Nozzle discharge coefficient |
| CDPX | Boattail pressure drag coefficient, X = T(top), B(bottom), or S(side) |
| CP _i | Pressure coefficient, $(P_i - P_\infty)/q_\infty$ |
| CP(10-X) | Pressure coefficient for 10-deg boattail configuration, X = T(top), B(bottom), or S(side) |
| CP(15-X) | Pressure coefficient for 15-deg boattail configuration, X = T(top), B(bottom), or S(side) |
| CP(25-X) | Pressure coefficient for 25-deg boattail configuration, X = T(top), B(bottom), or S(side) |
| CP* | Pressure coefficient at sonic Mach number |
| D | Model maximum diameter 0.82166 ft |
| DELH | Nozzle jet initial inclination angle, deg |
| DSL | Dividing streamline |
| FTA | Fuel/air ratio |
| IRL | Inviscid reference line |
| I/I | Inviscid/inviscid iteration loop |
| K _γ | Specific heat ratio function, $0.77658 (\gamma)^{0.5} \left[\frac{\gamma + 1}{2} \exp \left(- \frac{\gamma + 1}{2\gamma - 2} \right) \right]$ |
| dot{M}_a | Air mass flow, lbm/sec |
| dot{M}_f | Fuel mass flow, lbm/sec |

| | |
|------------|----------------------------------------------------------------------|
| MOC | Method of characteristics |
| MS | Model station, in. |
| M_∞ | Free-stream Mach number |
| NPR | Nozzle total pressure to free-stream static pressure ratio |
| NPRB | Nozzle total pressure to free-stream static pressure ratio, backup |
| P_i | Static pressure, psfa |
| P_{wall} | Nozzle flow duct static pressure forward of throat contraction, psfa |
| P_∞ | Free-stream static pressure, psfa |
| PN/TP | Part number/test point |
| PT_{ave} | Nozzle flow duct rake average total pressure, psfa |
| PTJ | Nozzle flow duct calculated total pressure, psfa |
| PTX | Nozzle flow duct rake total pressure, psfa |
| $(PT/P)_i$ | Isentropic pressure ratio |
| q_∞ | Free-stream dynamic pressure, psf |
| Re/ℓ | Free-stream Reynolds number per foot, 1/ft |
| RET | Nozzle throat Reynolds number |
| R | Cold flow nozzle duct radius 0.3004 ft |
| R_i | Nozzle boattail radius, ft |
| TTJ | Nozzle exhaust average total temperature, °R |
| U_e | External velocity |
| U_i | Local velocity, ft/sec |
| U_∞ | Free-stream velocity, ft/sec |
| V/I | Viscous/inviscid iteration loop |

| | |
|------------|-----------------------------------------------------------|
| X/D | External pressure orifice location relative to MS 130.471 |
| Y_i | Transverse coordinate |
| Y/R | Total pressure probe location from nozzle flow duct wall |
| γ | Ratio of specific heats |
| δ | Boundary-layer thickness, ft |
| δ^* | Boundary-layer displacement thickness, ft |
| ρ | Density, lbm/ft ³ |